

Design and Synthesis of Covalent Organic  
Frameworks for Electrochemical Energy  
Storage and Conversion

XU QING

Doctor of Philosophy

Department of Structural Molecular Science

School of Physical Sciences

SOKENDAI (The Graduate University for

Advanced Studies)

**Design and Synthesis of Covalent Organic  
Frameworks for Electrochemical Energy Storage and  
Conversion**

**XU Qing**

**Doctor of Philosophy**

**Department of Structural Molecular Science  
School of Physical Sciences  
The Graduate University for Advanced Studies**

**January 2018**



# Contents

<b>Chapter 1. General Introduction</b> .....	1
1.1 Introduction of Covalent Organic Frameworks.....	2
1.1.1 Design Principle .....	2
1.1.2 Synthesis Conditions and Methods.....	6
1.2 COFs for Electrochemical Energy Storage and Conversion .....	9
1.2.1 COFs Used in Capacitors .....	10
1.2.2 COFs Used in Batteries .....	15
1.2.3 COFs Used in Fuel Cells .....	20
1.2.4 COFs Used in Other Electrochemical Reactions.....	23
1.3 COF-derived Carbon Materials .....	25
References .....	32
<b>Chapter 2. A Template Strategy to Convert Conventional Covalent Organic Frameworks into High-Performance Carbons for Capacitors</b> .....	37
Abstract .....	38
2.1 Introduction .....	39
2.2 Design and Synthesis of Core-Shell Carbons.....	40
2.3 Characterization of Core-Shell Precursors .....	41
2.4 Characterization of Core-Shell Carbons.....	47
2.4 Capacitive Energy Storage Performance of Carbons .....	53
2.5 Conclusion.....	58
2.6 Experimental Sections.....	59
References .....	67
<b>Chapter 3. Template Conversion of Covalent Organic Frameworks into Two-Dimensional Conducting Nanocarbons for Catalyzing Oxygen Reduction Reaction</b> .....	69
Abstract .....	70
3.1 Introduction .....	71
3.2 Materials and Methods .....	72
3.3 Molecular Design and Structural Characterization .....	74
3.4 Electrocatalytic Performance.....	84
3.5 Conclusion.....	92
3.6 Experimental Sections.....	93
Reference.....	97
<b>Chapter 4. Design and Synthesis of Covalent Organic Frameworks for Lithium Ion Conduction</b> .....	100
Abstract .....	101

4.1 Introduction .....	102
4.2 Materials and Methods .....	103
4.3 Characterization of COFs and Li@COFs.....	105
4.4 Results and Discussion.....	112
4.5 Conclusion.....	119
4.6 Experimental Sections .....	120
References .....	127
<b>Chapter 5. Design and Synthesis of Covalent Organic Frameworks for Polymer Electrolytes by Pore Surface Engineering Method.....</b>	<b>129</b>
Abstract .....	130
5.1 Introduction .....	131
5.2 Materials and Methods .....	132
5.3 Characterization of Polymer Electrolytes.....	135
5.5 Results and Discussion.....	146
5.6 Conclusion.....	157
5.6 Experimental Sections .....	157
References .....	161
<b>Chapter 6. Summary and Perspectives .....</b>	<b>163</b>
<b>List of Publications .....</b>	<b>166</b>
<b>Acknowledgements .....</b>	<b>168</b>

## **Chapter 1. General Introduction**

## 1.1 Introduction of Covalent Organic Frameworks

Porous materials have been well developed, because of their outstanding character and broad applications, including gas capture, gas separation, optoelectronics, ion detection, catalysts and energy storage.<sup>1</sup> Among porous polymers, covalent organic frameworks (COFs), a kind of crystalline polymers, are getting more and more attentions since the first examples were successfully synthesized from 2005.<sup>2</sup>

COFs are composed of light weight elements and linked by covalent bond, which makes COFs possess excellent chemical and thermal stability.<sup>3</sup> Additionally, they are precisely integrated into extended structures with ordered pore channels. This places them in contrast to other types of porous material, such as zeolites, mesoporous silica, organosilica, metal–organic frameworks (MOFs), conjugated microporous polymers (CMPs), porous carbons, and metal–organic and organic cages. COFs are classified into two-dimensional (2D) or three-dimensional (3D) COFs, controlled by the geometries of the building blocks. In 3D COFs, the building blocks are covalently connected, and the lattice structures are maintained by covalent bonds. 3D COFs have high surface areas, numerous open sites, and low densities, making them ideal candidates for gas capture.<sup>4</sup> By contrast, in 2D COFs, the organic units are linked into 2D atomic layers that further stack via  $\pi$ – $\pi$  interactions to crystallize layered structures, and the frameworks are locked by intralayer covalent bonds and controlled by interlayer non-covalent forces. 2D COFs have a well-defined alignment of  $\pi$  building units in their atomic layers and segregated arrays of  $\pi$  columns in their frameworks. The elegant  $\pi$  skeletons of 2D COFs provide a fundamental basis for structural design. Meanwhile, the sizes, shapes and environments of their one-dimensional (1D) channels are fully controllable.

### 1.1.1 Design Principle

The synthesis of COFs generally depends on kinetically controlled reactions. Dynamic covalent chemistry (DCC) deals with reversible covalent reactions that allows the free exchange of molecular components to achieve thermodynamic minimum of the system at equilibrium.<sup>5</sup> Different from noncovalent interactions and conventional covalent bond formation utilized in supramolecular chemistry, DCC enables efficient thermodynamic equilibrium, and exhibits “error checking” and “proof-reading” characteristics. Thus, the DCC is favor for forming ordered, crystalline and thermodynamic stability structure COFs. From the concept of DCC, those issues must

be considered in the design and synthesis of COFs: the first is the linkages, which should be synthesized from reversible reaction; the second is the suitable building blocks.

### 1.1.1.1 Linkage Diversities

Linkages of COFs connect the building blocks to ordered and crystalline polymers, which play key roles in the COFs field. To afford COFs, the formation of linkages should be reversible. Till now, many linkages, including boronate,<sup>6</sup> boroxine,<sup>7</sup> spiroborate,<sup>8</sup> imine,<sup>9</sup> hydrazone,<sup>10</sup> azine,<sup>11</sup> phenazine,<sup>12</sup> squaraine,<sup>13</sup> imide,<sup>14</sup> triazine,<sup>15</sup> boron-nitrogen linkage<sup>16</sup> and double-stage connections<sup>17</sup> have been developed in COFs (shown in Figure 1). And these linkages could be summarized in three categories: boron-based linkages, nitrogen-involved linkages, and carbon-based linkages.

The linkage of the first COF (COF-1) is boron-linkage, by the self-condensation of 1,4-phenylenediboronic acid (BDDBA). In addition to self-condensed boroxine-linkages COFs, boronic acids can be also co-condensed with dialcohols to obtain five-membered boroxine. However, the low solubility and oxidative sensitivity of planar polyfunctional catechols hampers large-scale synthesis and storage. To overcome the drawback of catechols, a modified method was developed, in which acetonide-protected catechols were used as alternative. The acetonide-protected catechols reacted with boronic acid building blocks under the condition of Lewis acid ( $\text{BF}_3 \cdot \text{OEt}_2$ ).<sup>18</sup> Moreover, an ionic covalent organic framework (ICOF), which contains  $\text{sp}^3$  hybridized boron anionic centers and tunable counteractions, was constructed by formation of spiroborate linkages.<sup>19</sup> The ICOF showed great thermal stabilities and excellent resistance to hydrolysis, even keep stable in water or basic solution for over two days.

Although the boron-based linkages possess high thermal stability, most of them have a high susceptibility to water, even vapor in the air.<sup>20</sup> Unlike boron-based linked COFs, nitrogen-involved linkages COFs often exhibit much more enhanced stability. For example, A COF (TPB-DMTP-COF) synthesized from TPB (5'-(4-aminophenyl)-[1,1':3',1''-terphenyl]-4,4''-diamine) and DMTP (2,5-dimethoxyterephthalaldehyde), can keep crystallinity and porosity under harsh conditions like water, strong acids and strong bases.<sup>21</sup> Nitrogen-involved linkages cover imine, hydrazone, azine, phenazine, squaraine, imide, triazine, boron-nitrogen linkage, salen-based linkage, Michael additional-elimination based linkage and double-stage linkage. Among them, most of covalent triazine frameworks (CTF) possess low crystallinity because of the poor reversibility of trimerization reaction.

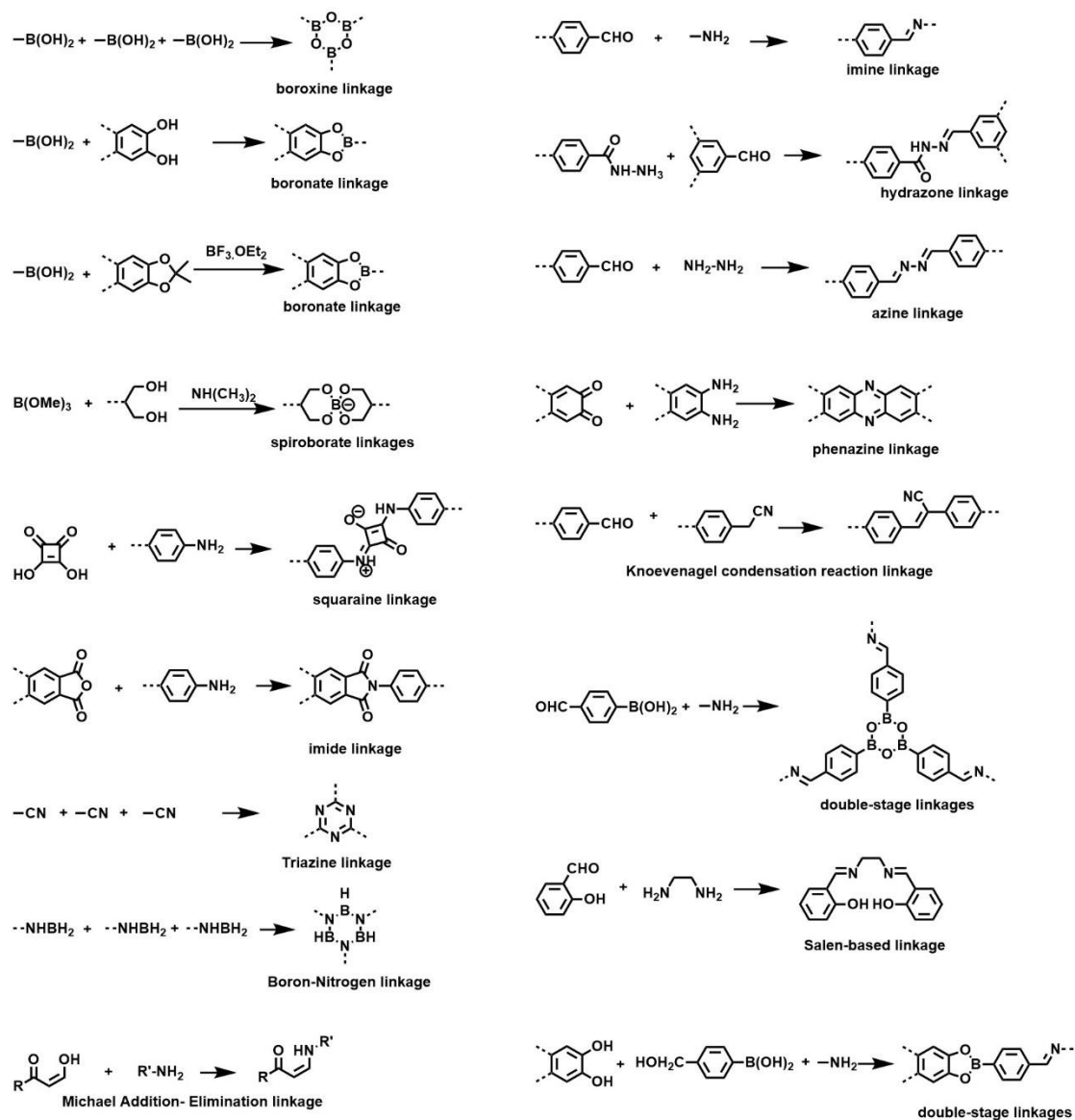


**Figure 1.** Diversities of linkages for the formation of COFs, including boron-based, nitrogen-based, and carbon-based linkages.

Apart from boron-based, nitrogen-based linkages, a 2D fully conjugated COF ( $sp^2c$ -COF) has been reported recently.<sup>22</sup> The COF was obtained from 1,3,6,8-tetrakis(4-formylphenyl)pyrene (TFPPy) and 1,4-phenylenediacetonitrile (PDAN) by Knoevenagel condensation reaction in alkaline condition (4 M NaOH) under solvothermal method.  $sp^2c$ -COF was a semiconductor with a band gap of 1.9 eV. The conductivity of  $sp^2c$ -COF was enhanced by 12 orders of magnitude after chemical oxidized.

### 1.1.1.2 Building Blocks Diversities

The building blocks generate the topological design of COFs, and could be classified into 2D or 3D based on simplified symmetry notation. The 2D or 3D refers to the

directional symmetry of the reactive groups, as summarized in Figure 2 (2D- $C_2$ , 2D- $C_3$ , 2D- $C_4$ , 2D- $C_6$  and 3D- $T_d$ ).

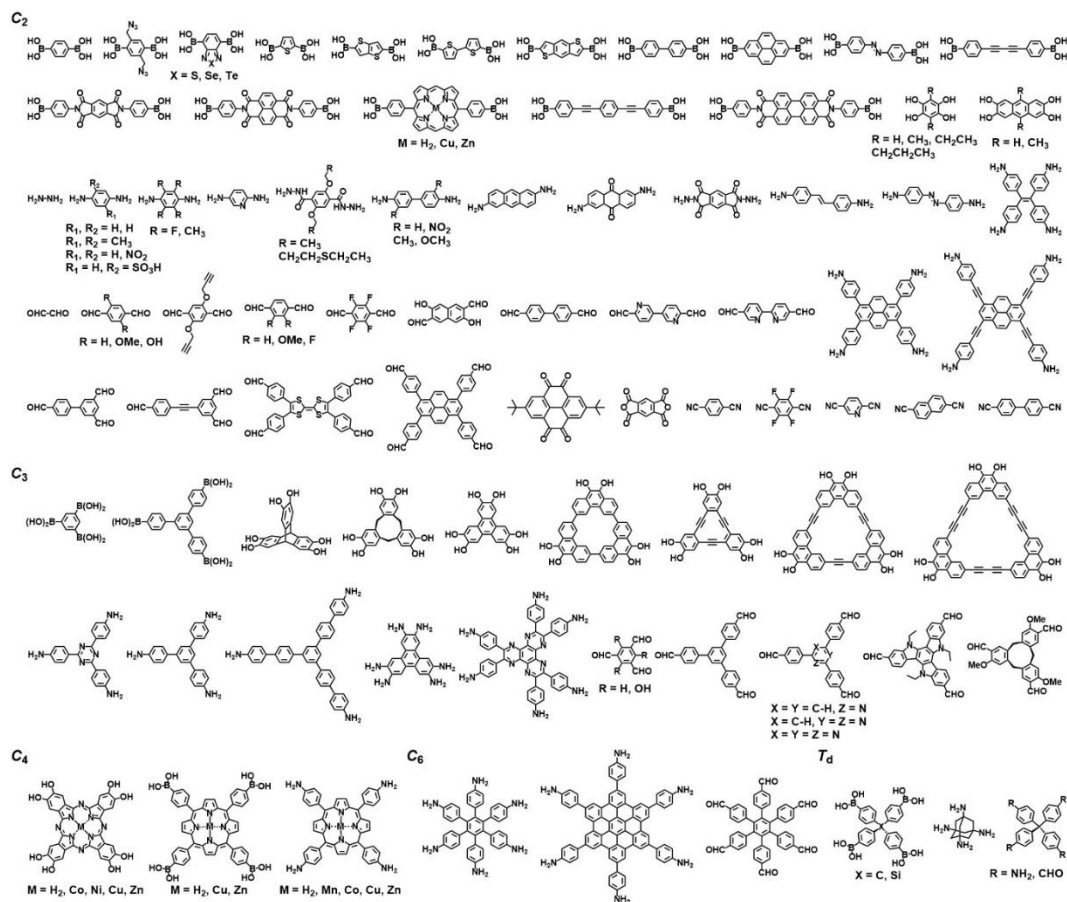


**Figure 2.** Typical examples of  $C_2$ ,  $C_3$ ,  $C_4$ ,  $C_6$ , and  $T_d$ -symmetric monomers used for the synthesis of COFs.

The geometry of the building blocks determines the resulting structure. Therefore, the combinations such as 3D- $T_d$  + 3D- $T_d$ , 3D- $T_d$  + 2D- $C_2$ , 3D- $T_d$  + 2D- $C_3$ , 3D- $T_d$  + 2D- $C_4$  can lead to the construction of 3D COFs with different building blocks. And the 2D COFs are combined by 2D building blocks (e.g., 2D- $C_2$  + 2D- $C_3$ , 2D- $C_2$  + 2D- $C_4$ , 2D- $C_2$  + 2D- $C_6$ , 2D- $C_3$  + 2D- $C_3$  and 2D- $C_6$ + $C_3$ ). Different from the other linkages of COFs, the CTF based linkage COFs can be constructed by every 2D or 3D building blocks. The variety of building blocks results in the diversity of the COFs (Figure 3).

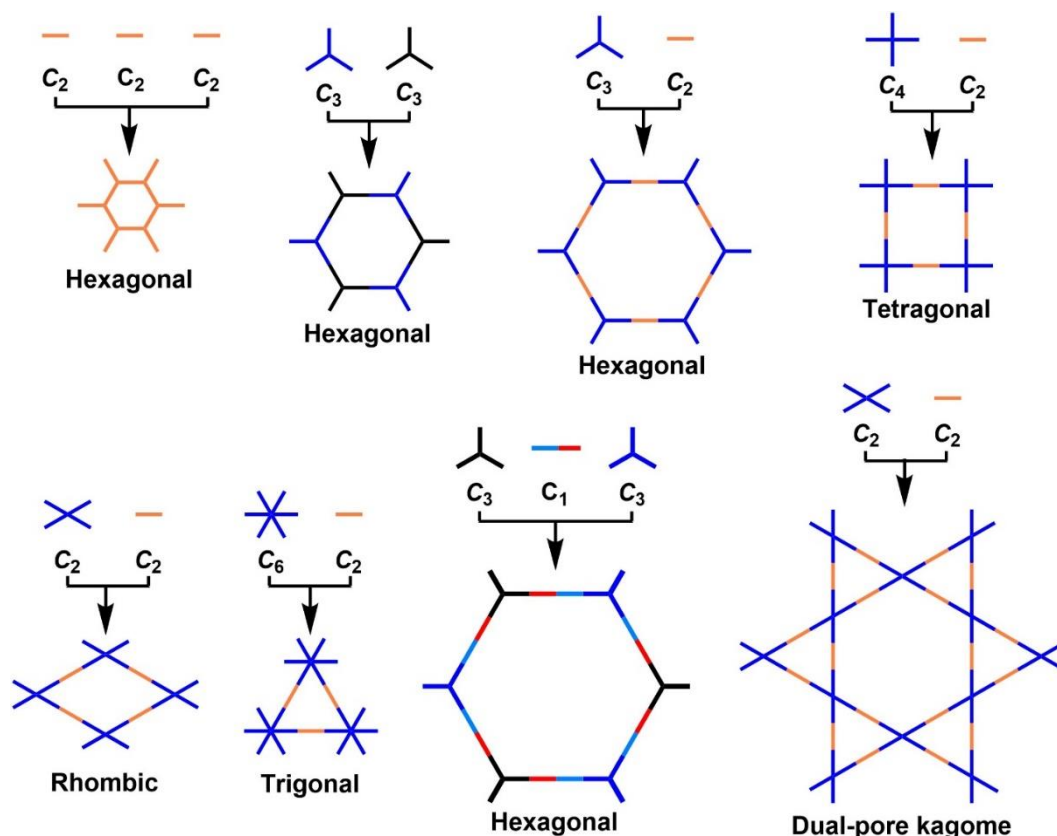


**Figure 3.** Topology diagrams represent the polygon skeletons of COFs.

## 1.1.2 Synthesis Conditions and Methods

### 1.1.2.1 Solvothermal Synthesis

Most COFs have been synthesized by solvothermal method in which reaction conditions are highly dependent on the solubility and reactivity of building blocks and the reversibility of the reactions. Moreover, the reaction time, the reaction temperature, the solvent conditions, and the catalytic concentration are key factors in the solvothermal method to prepare crystalline porous COFs successfully. As a general synthetic protocol, the mixture of suitable monomers for vertices and edges, solvents or a mixture of solvents and catalyst were placed in a Pyrex tube with suitable volume. The mixture was sonicated for a short period, degassed *via* freeze-pump-thaw cycles, sealed with gas burner and kept at suitable temperature for a certain of period. The tube was cooled down to room temperature and the crude products were then obtained by centrifugation or filtration, and washed with appropriate solvents at room temperature or by Soxhlet extraction to exchange high boiling-point solvents and/or remove oligomers. The residue was then dried under vacuum at 80 – 120 °C and kept under nitrogen or argon in dark. Notably, by this method, some COFs can be prepared in large scale. For example, TPT-COF-1 from 2,4,6-tris(4-aminophenoxy)-1,3,5-triazine (TPT-

NH<sub>2</sub>) and 2,4,6-tris-(4-formylphenoxy)-1,3,5-triazine (TPT-CHO) could be easily prepared on gram scale, and the TPT-COF-1 possessed high BET surface area of 1589 m<sup>2</sup> g<sup>-1</sup> and high crystallinity.<sup>23</sup>

#### 1.1.2.2 Microwave Methods

Considering the fact that the solvothermal method often requires long reaction time, microwave method has been explored as a rapid method to prepare crystalline porous COFs. Till now, boronate-ester linked COF-5, COF-102,<sup>24,25</sup> and imine-linked TpPa-COF,<sup>26</sup> have been synthesized successfully by using microwave method. A general microwave synthetic method is described as follow. A mixture of monomers in a suitable solvent was sealed in a microwave tube under nitrogen or vacuum and heated with stirring for 60 min at a designated temperature such as 100 °C. To synthesize the boron-based COF-5 and COF-102, the crude products were collected, mixed with acetone, and reacted at 65 °C with stirring for another 20 min as a process of solvent extraction. The resulting precipitate was collected by filtration and dried under vacuum. A feature of the microwave solvent extraction method is that it can remove oligomers in the COFs more efficiently and the resulting COFs possess better porosity. Different from the boron-based COFs, after microwave reaction, the resulting imine-linked COFs were collected by filtration, washed with mesitylene and acetone, extracted with THF by using Soxhlet to remove any oligomers adsorbed in the pores, and then dried at 100 °C under vacuum. In addition, three CTFs (P1M, P2M and P4M) have been synthesized by using microwave methods.<sup>27</sup> The synthetic protocol is described as follow. Firstly, a mixture of trifluoromethanesulfonic acid and monomers in a reaction vessel was sealed and stirred at 110 °C for 30 min. Secondly, the precipitate was collected, grounded carefully into powder, and washed with ammonia solution. Finally, the powder was washed with water, ethanol, acetone and THF, and dried under vacuum to yield the CTFs.

#### 1.1.2.3 Ionothermal Synthesis

Although there is a diversity of monomers for the synthesis of triazine-based networks, most of them are amorphous materials and lacking long-range molecular ordering. Nevertheless, two CTFs, i.e. CTF-1 and CTF-2, synthesized under ionothermal conditions are crystalline porous materials.<sup>28</sup> In a typical method, the monomer and ZnCl<sub>2</sub> in a Pyrex ampoule were evacuated, sealed, and heated at 400 °C for 40 h. The mixture was cooled at room temperature, grounded, and washed thoroughly with water to remove ZnCl<sub>2</sub>. The powder was further stirred in a diluted

HCl solution for 15 h, collected by filtration, washed with water and THF, and dried under vacuum to yield CTF-1 and CTF-2 (Figure 4). During the synthetic process, the molten salt acts as the solvent and catalyst for the trimerization reaction, which is likely reversible at this temperature.

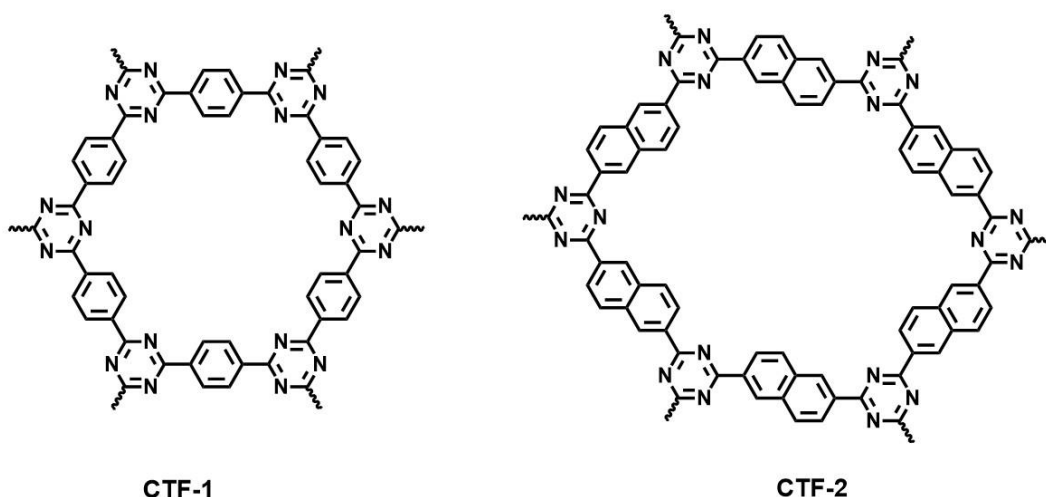


**Figure 4.** CTF-1 and CTF-2 synthesized by the ionothermal method.

#### 1.1.2.4 Mechanochemical Synthesis

Because solvothermal and microwave reactions must be conducted under complicated experimental conditions (e.g., reaction in a sealed Pyrex tube, inert atmosphere, suitable solvents and temperature for crystallization, etc.), the exploration of simple synthetic method is highly desired. Especially, mechanochemical synthesis that constructs bonds through the simple, economical, and environmental friendly route, could overcome the limitations of other synthetic methods. Till now, many COFs have been synthesized by this feasible method (Figure 5). In the mechanochemical synthesis, the monomers were placed in a mortar and grounded by using a pestle at room temperature for 40 min to yield the COFs.<sup>29</sup> To explore the full potential of this method with appropriate optimized mechanochemical conditions, the liquid-assisted grinding method has been developed. While grinding the monomers, a small amount of catalyst solution was added to the mortar; the addition of catalyst solution enhances the reaction rate by facilitating the homogeneity of reactants, which also leads to improved crystallinity of the COFs.

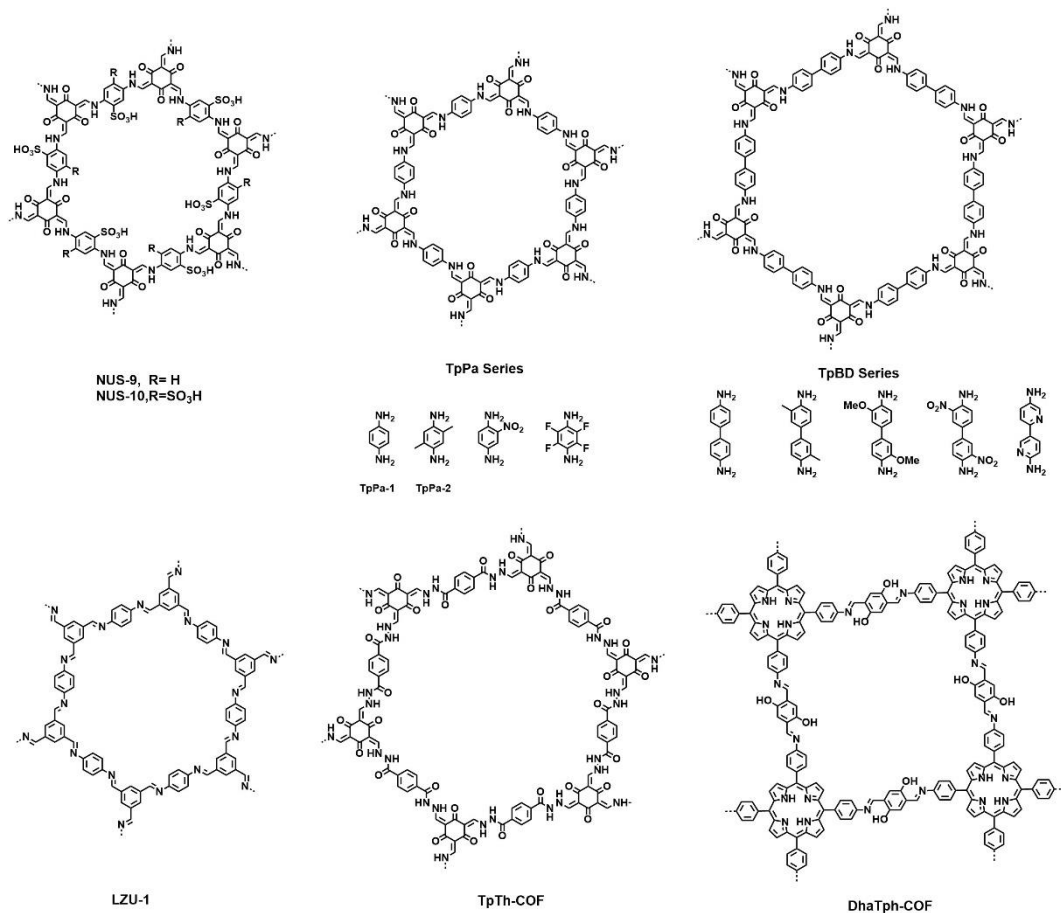


**Figure 5.** COFs synthesized by mechanochemical synthesis method.

## 1.2 COFs for Electrochemical Energy Storage and Conversion

As the skeletons and pores of COFs can be systematically designed according to the topological design principle and can be synthetically controlled by judicious choice of building blocks, the functions of COFs can be designed and managed; this designability in both structures and functions is the significant feature of COFs that makes a sharp contrast to other extended porous materials. The design of COFs to create porous structures includes the design and control of pore shape, pore size and pore environment, which are key parameters that determine sorption, separation, catalysis, and energy conversion and storage applications. Apart from the designable, the other important feature of COFs is pore surface engineering. The pore channels of COFs are able to be modified by different functional groups for different applications. The designable character and pore surface engineer features endow the frameworks with outstanding physicochemical properties, including optoelectronic,<sup>30</sup> chemical sensor,<sup>31</sup> and catalysts.<sup>21,32</sup> Especially, various electric functional building blocks, excellent thermal stability, and 1D fast pore channels, make COFs show superior performance in

electrochemical energy storage and conversion devices, such as capacitors, fuel cells and batteries.

### 1.2.1 COFs Used in Capacitors

Energy storage is necessary for a sustainable development. Capacitors are a class of ideal energy storage devices that are able to combine high power density, short charging time, and long cycle stability. The capacitors are classified into electrical faradaic supercapacitors (FS) and electrical double-layer supercapacitors (EDLS).<sup>33</sup>

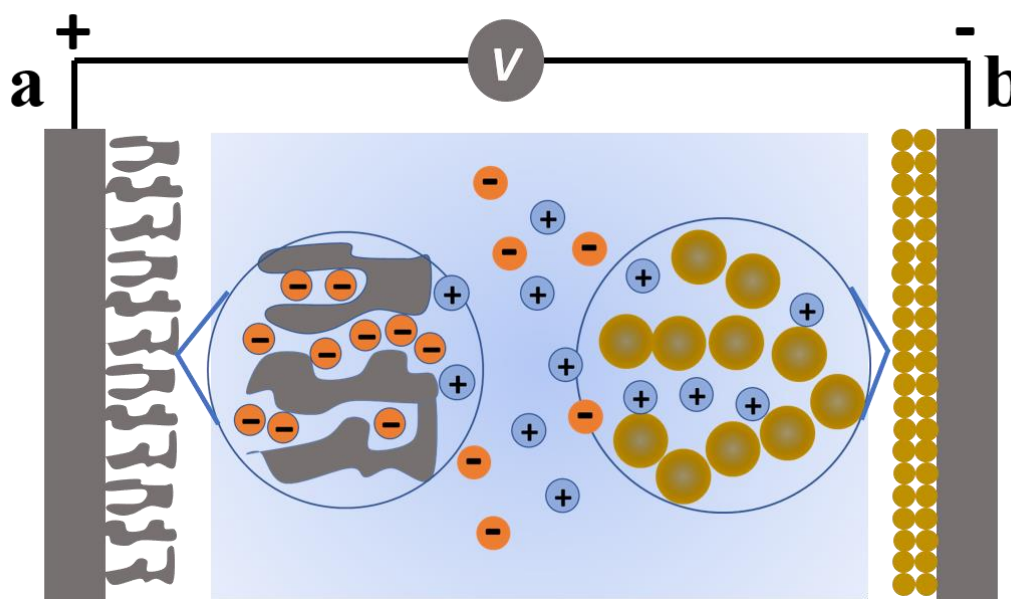


**Figure 6.** Illustration of different capacitors, a) electrical double-layer supercapacitors and b) electrical faradaic capacitors.

In EDLS, the electrode materials, such as porous carbon materials, are not electrochemically active. During charge and discharge process of EDLS, pure physical charge accumulation occurs at the electrode/electrolyte interface (Figure 6a). Different from EDLS, the electrode materials of FS are electrochemically active, e.g. metal oxides and conducting polymers, charges are stored in the charging and discharging processes (Figure 6b) by faradaic reactions (redox reactions). As a result, the EDLS possess better cyclic stability performance than FS, whereas FS exhibit higher capacitances.

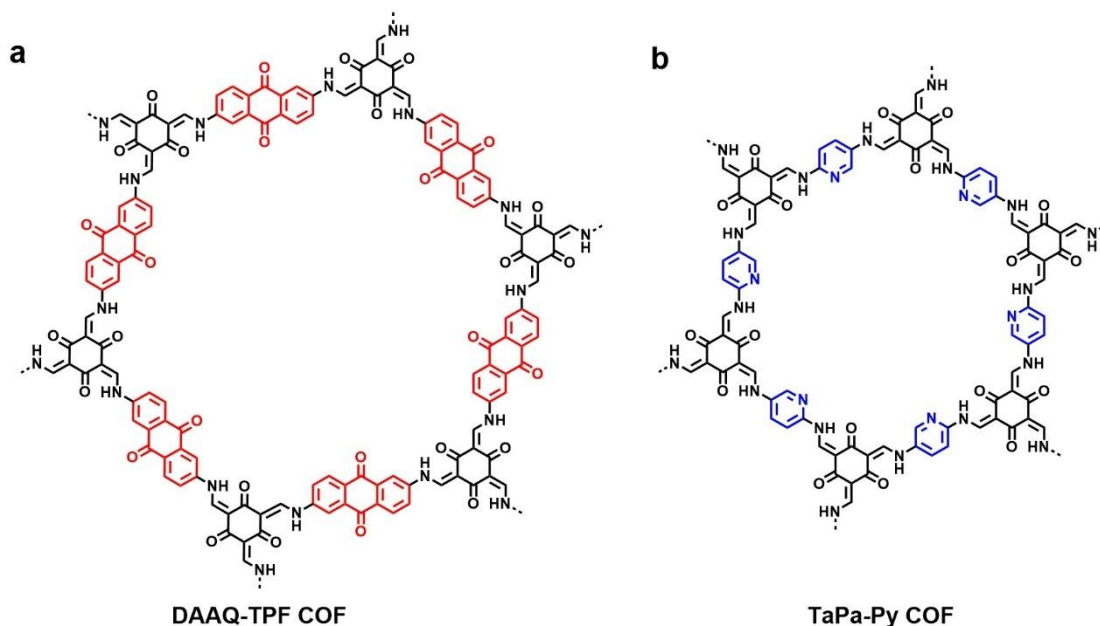


**Figure 7.** COF structure of a) DAAQ-TPF COF, and b) TaPa-Py COF for capacitive energy storage.

The skeleton of 2D COFs is linked by redox-active building blocks, and 1D pore channels benefit charge and ion transport and fast diffusion, which make 2D COFs be an ideal candidate as capacitors. The first COF-based capacitor is DAAQ-TPF COF.<sup>34</sup> Redox active 2,6-diaminoanthraquinone (DAAQ) units were successfully introduced to the edges of the imine-linked DAAQ-TPF COF (Figure 7) via the condensation with 1,3,5-triformylphloroglucinol (TFP) as the knot units. Reversible redox reaction between anthraquinone and 9,10-dihydroxyanthracenes involves a two-electron and two-proton process that endows the COF with pseudocapacity. The redox peak separation of the DAAQ-TPF COF was only 4 mV, which was much lower than that of the DAAQ monomer (160 mV), indicating facilitated electron transfer between electrode and the redox sites in the COF skeleton. In the galvanostatic charge-discharge experiments, the DAAQ-TPF COF exhibited a capacitance of  $48 \pm 10 \text{ F g}^{-1}$  and was stable after 5000 charge-discharge cycles. By contrast, the DAB-TPF COF analogue (DAB: 4-diaminobenzene) without redox active DAAQ units in the COF skeleton exhibited a lower specific capacitance ( $15 \pm 6 \text{ F g}^{-1}$ ), under the same conditions. Owing to the randomly oriented DAAQ-TPF COF crystallites in the electrode, only 2.5% of the redox-active units contributed to the capacitive energy storage. This situation can be greatly improved by growing oriented COF thin films on gold. In this case, 80% – 99% of the redox-active sites were involved in the energy storage.<sup>35</sup> For example, the capacitance of a 200-nm thick film was drastically increased to  $3.0 \text{ mF cm}^{-2}$  compared

with that of ( $0.40 \text{ mF cm}^{-2}$ ) COF powder. The film was stable for cycle use with only 7% loss of capacity after 5000 cycles, indicating that the  $\beta$ -ketoenamine-linked framework is robust in charge-discharge cycles. Integrating conducting polymer, such as polyethylenedioxythiophene (PEDOT), into the 1D channels of redox-active COF films can further increase the conductivity as demonstrated by the DAAQ-TFP COF for high-rate energy storage device with high volumetric energy density.<sup>36</sup> The COF composite films exhibited faradaic charge storage capacity up to 9.3 mC, corresponding to 97% accessible anthraquinone redox-active sites. The COF composite film exhibited 40-fold enhanced charge storage capacity compared to the unmodified COF film. Moreover, the COF composite film enabled high-rate charge-discharge performance at 100 C, which requires only 36 s for a full charge or discharge. The COF composite film retained 50% of its maximum capacitance ( $350 \text{ F cm}^{-3}$ ) at a rate of even 1600 C, corresponding to a time of only 2.25 s for a complete charging. Importantly, the COF composite film exhibited stable capacity over 10,000 charge-discharge cycles. The enhanced current response and exceptional volumetric capacitance of the COF composite film most likely originates from the wire effect of specially confined conducting PEDOT within the 1D channels that facilitates the accessibility of the redox active sites as well as promoting ion conduction. A similar approach based on the COF<sub>DAAQ-BTA</sub> thin films grown on 3D graphene substrate showed that the capacitance of the COF-graphene composite can reach  $31.7 \text{ mF cm}^{-2}$ , indicating good conduction with graphene enables improved contribution of the redox-active anthraquinones sites to the energy storage.<sup>37</sup>

Apart from the DAAQ building blocks, pyridine was another redox active units used in COFs (Figure 7b).<sup>38</sup> The specific capacitance of TaPa-Py COF calculated from CV in 1 M H<sub>2</sub>SO<sub>4</sub> solution, was  $180.5 \text{ F g}^{-1}$ , far superior to that of DAB-TFP COF ( $79.1 \text{ F g}^{-1}$ ) without pyridine group at  $20 \text{ mV s}^{-1}$ . More importantly, the specific capacitance was high to  $139.4 \text{ F g}^{-1}$  even at  $20 \text{ mV s}^{-1}$ . From the galvanostatic charge-discharge curves, the capacitance of TaPa-Py COF was  $209 \text{ F g}^{-1}$  higher than that of DAB-TFP COF ( $98 \text{ F g}^{-1}$ ) at  $0.5 \text{ A g}^{-1}$ . The outperformance of the prepared COF was due to combination of faradaic capacitance from the pyridine units and double-layer capacitance from ordered porous structure.

One of the defects of the FS is the poor cyclical stability, to overcome the disadvantage, a novel COF, TpPa-(OH)<sub>2</sub> (Figure 8a), was synthesized based on redox-

active groups hydroquinone (H<sub>2</sub>Q) by solvothermal method.<sup>39</sup> TpPa-(OH)<sub>2</sub> exhibited high surface area of 369 m<sup>2</sup> g<sup>-1</sup>, with the pore size from 1.0 to 1.8 nm. The capacitive performance was measured in 1 M phosphate buffer. From the CV curves, the specific capacitance was 396 F g<sup>-1</sup> at a scan rate of 2 mV s<sup>-1</sup>, which was in accordance with the results calculated by galvanostatic results, 416 F g<sup>-1</sup> at 0.5 A g<sup>-1</sup>. The values is the highest among COF-based capacitors. The high capacitance was from the low molecular weight of COFs units. Additionally, 66% specific capacitance was maintained even after 10 000 cycles at a current density of 5 A g<sup>-1</sup>. Thus, the prepared COF possessed both high capacitance, and excellent cyclic stability. The good cyclic stability is from the H-bonding in the COFs: carbonyl oxygen (C=O) of the benzoquinone (Q) functionality is involved in H-bonding with the neighboring amine, which inhibits the decomposition of Q (Figure 8b).

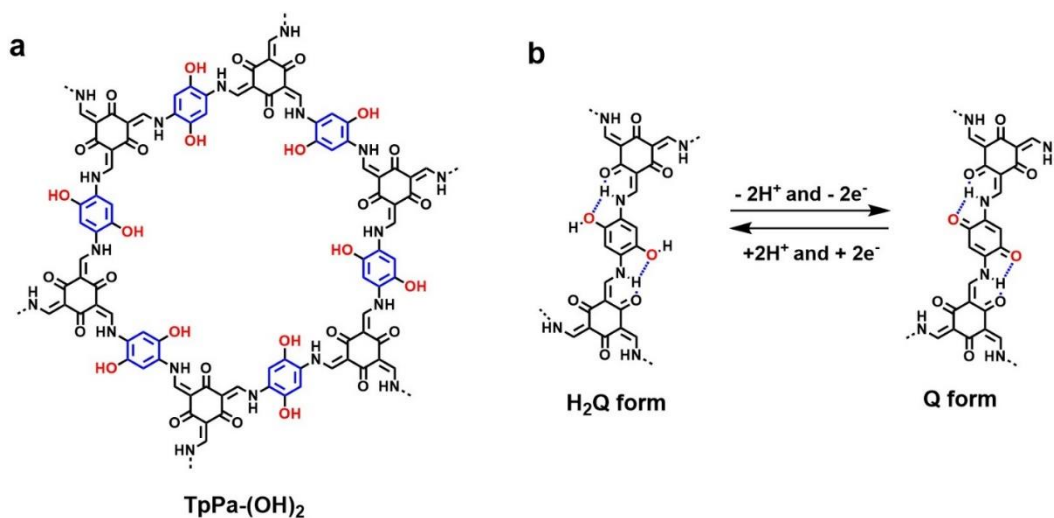


**Figure 8.** a) COF structure of TpPa-(OH)<sub>2</sub>. b) H-bonding stabilized both the hydroquinone (H<sub>2</sub>Q) and benzoquinone (Q).

The poor conductivity of the COFs is another severe problem, which limits the widely application in the electrodes of capacitors. To overcome the disadvantage, the COF was grown on the amino-functionalized carbon nanotubes (NH<sub>2</sub>-f-MWCNTs), the resultant materials exhibited enhanced performance as the electrode of capacitor (Figure 9), due to the enhanced conductivity.<sup>40</sup> The COF (TA-DHTA COF) exhibited high BET surface area (1591 m<sup>2</sup> g<sup>-1</sup>), with 1D mesoporous channels. After grown on the NH<sub>2</sub>-f-MWCNTs, the BET surface area showed decrease, about 1157 m<sup>2</sup> g<sup>-1</sup>, because of the low surface area of NH<sub>2</sub>-f-MWCNTs. The electrochemical performance of NH<sub>2</sub>-f-MWCNT@TTA-DHTA-COF was investigated by using a typical three-

electrode system in 1 M Na<sub>2</sub>SO<sub>4</sub> aqueous electrolyte. The specific capacitances of NH<sub>2</sub>-f-MWCNT@TTA-DHTA-COF were calculated to be 127.5 F g<sup>-1</sup> at 0.4 A g<sup>-1</sup> and 98.7 F g<sup>-1</sup> at 2 A g<sup>-1</sup>, whereas the specific capacitances of TTA-DHTA-COF and NH<sub>2</sub>-f-MWCNT were 10 F g<sup>-1</sup> at 0.1 A g<sup>-1</sup> and 65 F g<sup>-1</sup> at 0.5 A g<sup>-1</sup>, respectively. Moreover, a retention of specific capacitance was 96% even after 1000 charge and discharge cycles.

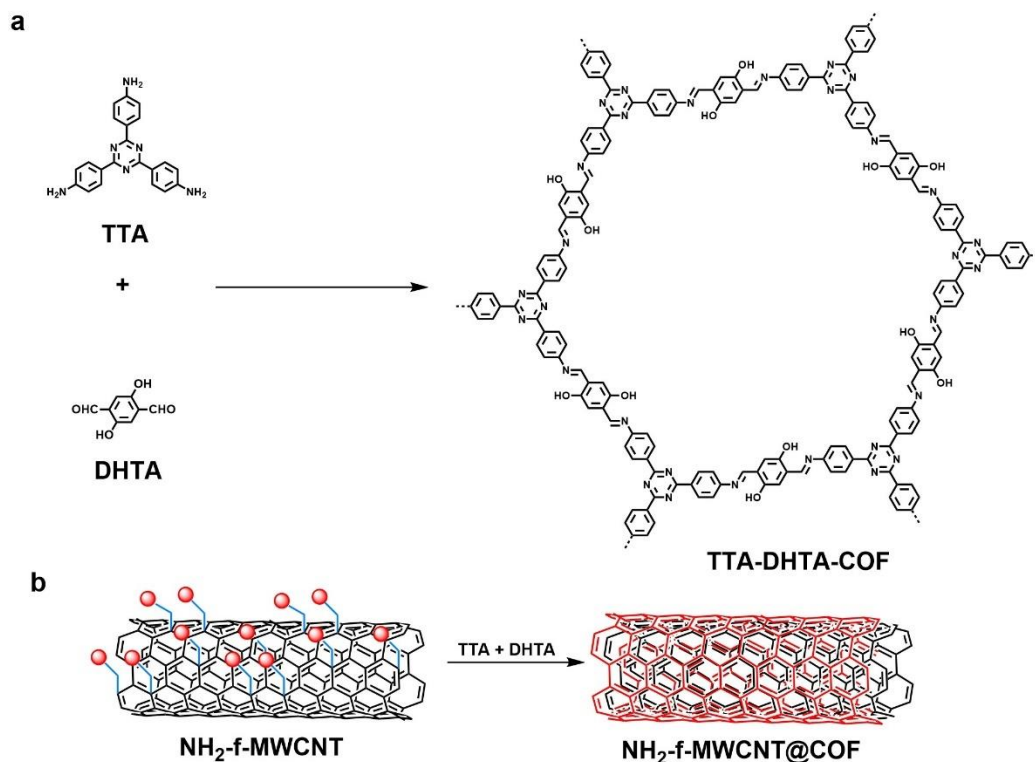


**Figure 9.** a) TTA-DHTA-COF was synthesized from TTA and DHTA. b) Illustration of growth COF on the NH<sub>2</sub>-f-MWCNT.

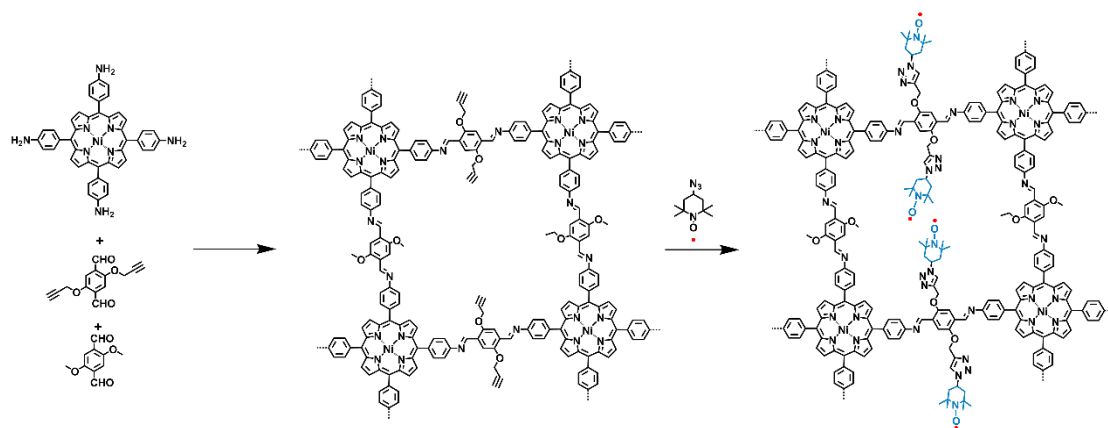


**Figure 10.** Pore surface engineering strategy for the synthesis of radical COFs toward energy storage.

Although COFs with redox-active skeletons are attractive for energy storage, however, their further development is restricted to the limited availability of redox-

active monomers. As an alternative, the conventional COFs can be successfully converted into redox-active supercapacitor electrode materials via pore surface engineering. The open lattice of NiP-COF was converted to segregated redox-active phases via a click reaction with 4-azido-2,2,6,6-tetramethyl-1-piperidinyloxy (TEMPO) and yielded [TEMPO]<sub>x</sub>-NiP-COFs (X = 0, 50% and 100%, Figure 10) that bearing electrochemically active radicals (TEMPO) on the pore walls.<sup>41</sup> The [TEMPO]<sub>x</sub>-NiP-COFs exhibited a pair of reversible peaks in CV diagram, which were assigned to the one-electron redox reaction of the TEMPO radical switching between neutral radical and the oxoammonium cation. The specific capacitance of [TEMPO]<sub>100%</sub>-NiP-COF was higher than that of [TEMPO]<sub>50%</sub>-NiP-COF owing to the denser radical distribution in the former. On the other hand, [TEMPO]<sub>50%</sub>-NiP-COF showed faster reversible charge-discharge reaction, as evidenced by a narrower separation between the oxidative and reductive peaks. The capacitances of [TEMPO]<sub>50%</sub>-NiP-COF and [TEMPO]<sub>100%</sub>-NiP-COF were 167 and 124 F g<sup>-1</sup>, respectively, which were much higher than that of the redox-active DAAQ-TFP COF (40 ± 9 F g<sup>-1</sup>). The robust covalent bonds between COF skeletons and redox active sites on the walls led to structural stability that accounts for the improved cycle performance in the galvanostatic charge-discharge process. [TEMPO]<sub>50%</sub>-NiP-COF retained its high capacitance over 100 cycles at a current density of 500 mA g<sup>-1</sup>.

### 1.2.2 COFs Used in Batteries

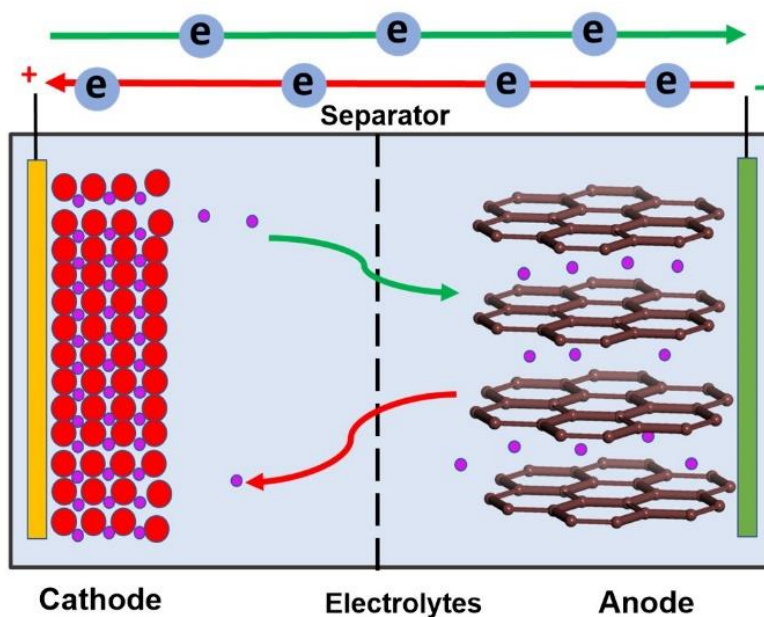


**Figure 11.** Illustration of lithium ion batteries, where the carbons work as anodes, and organic materials with redox-active functions work as cathodes.

Lithium ion batteries (LIBs) are widely used in our life, including our mobile phones, computers, and vehicles, because of their unique advantages, high energy density, energy efficiency, and rapid charge and discharge ability.<sup>42</sup> Organic materials with redox-active sites are promising candidates for the next generation of rechargeable LIBs, since they are heavy-metal free and can be prepared from widespread resources and feature high rate performance stemmed from simple redox reaction. In this class of LIBs, carbons work as the anode electrodes, and the organic materials work as cathode electrodes, and electrolytes play roles in transporting lithium in the batteries (Figure 11).

However, organic electrodes for the LIBs usually have poor rate performance and cycle stability – the main hurdles to be addressed. Anchoring redox-active monomers on COF skeletons via covalent bonds is expected to enhance the cycle performance by avoiding the leak of active materials during lithiation and delithiation process. Moreover, the open channels can facilitate ion transport that responsible for high-rate performance. Nevertheless, the limited electric conductivity of COFs remains an obstacle for a quick electrochemical process in LIBs. Hybrids of redox-active COF with carbon nanotubes (CNTs) or conducting polymers have a chance to boost electric conductivity and achieve high-rate performance in LIBs.

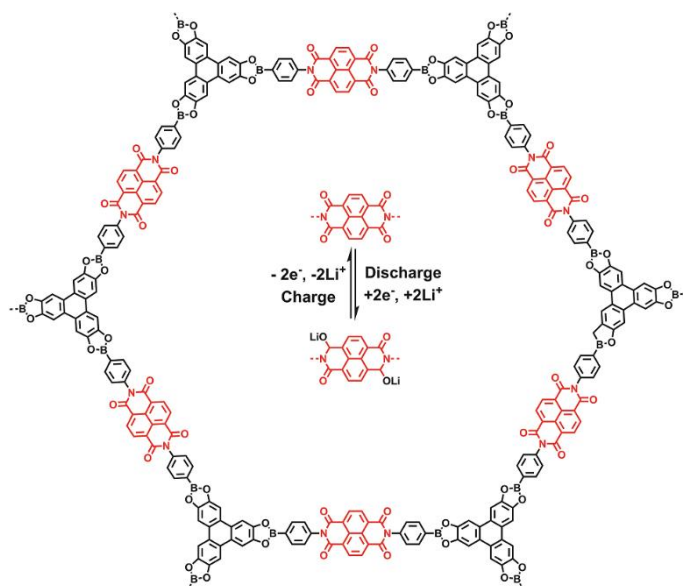


**Figure 12.** Chemical structure of donor-acceptor D<sub>TP</sub>-ANDI-COF, the inserted was redox reaction of NDI edge units.

As a proof of concept, the COF-CNTs composites have been developed as the cathode for LIBs by *in-situ* growing the mesoporous redox-active D<sub>TP</sub>-ANDI-COF

(Figure 12) containing redox-active naphthalene diimide (NDI) units on CNTs; the NDI units underwent a reversible two-electron redox reaction during lithiation and delithiation process.<sup>43</sup> Indeed, the discharge-charge curve for LIBs with D<sub>TP</sub>-A<sub>NDI</sub>-COF@CNTs cathode was symmetric, indicating the reversibility of oxidation and reduction processes. The Coulombic efficiency retained the maximum value of 100% even after 100 cycles. The capacity of D<sub>TP</sub>-A<sub>NDI</sub>-COF@CNTs was as high as 67 mA h g<sup>-1</sup> at 2.4 C, corresponding to an efficiency of 82% in utilizing the redox-active sites. At 12 C, the capacity was 58 mA h g<sup>-1</sup>, corresponding to the 71% utilization of the redox-active sites. In the long-term stability test at 2.4 C, the capacity retained even after 700 cycles and stabilized at 74 mA h g<sup>-1</sup> with the redox-active site utilization efficiency of 90%. The charge transfer resistance was decreased from 129 Ω for COF to 8.3 Ω for D<sub>TP</sub>-A<sub>NDI</sub>-COF@CNTs hybrid, which accounts for the outstanding performance.

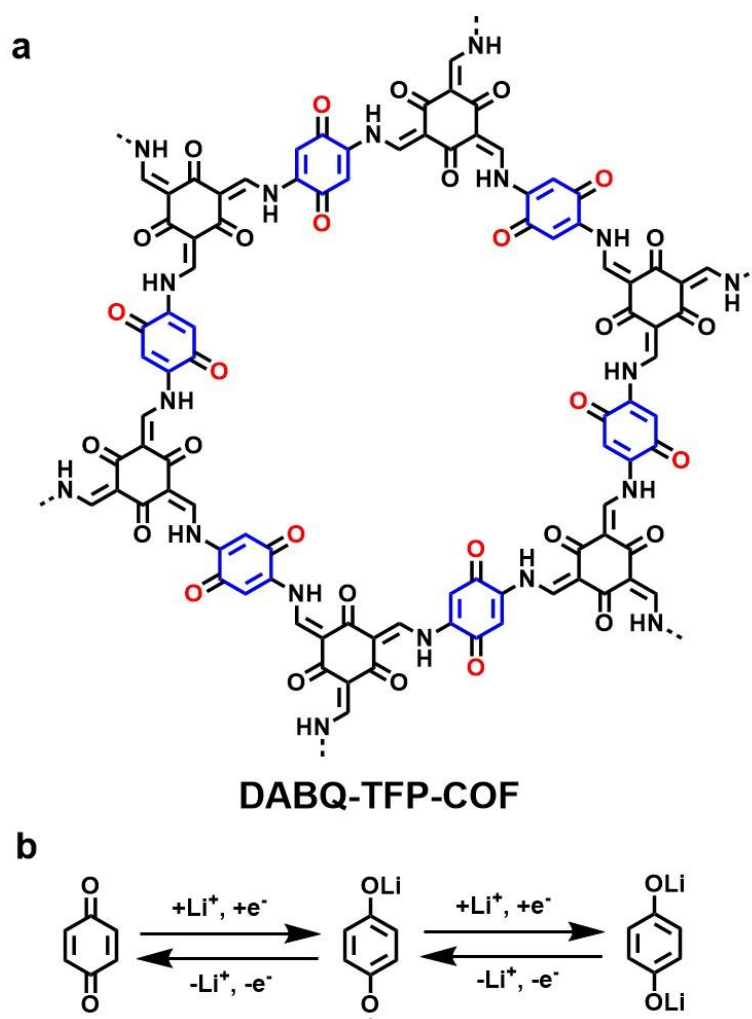


**Figure 13.** a) COF structure of DABQ-TFP-COF. b) Redox reaction of DABQ units.

Considering 2D layers of COFs are stacked close layer-by-layer because of strong  $\pi$  -  $\pi$  interaction, the redox-active sites are difficult to reach in charge and discharge process in batteries. The long pore channels make it difficult for the redox-active sites to be fully used, which lowers their capacity and rate performance. Thus, shortening the pore channels enables to short the lithium ion transport distance, leads to enhance the performance. Accordingly, a novel strategy that exfoliating COFs layer by ball milling method was used in cathodes has been reported.<sup>44</sup> The exfoliated COF (ECOF (DAAQ-ECOF)) exhibited approximately 5 nm, and possessed ultrathin, transparent and slightly wrinkled layer structure, whereas the DAAQ-TFP-COF (structure shown in Figure 7) was in bulk morphology (Figure 13). From powder X-ray diffraction (PXRD) and nitrogen sorption isotherm measurements, the crystallinity and pore structure of the COF was maintained after conducting exfoliating. These coin cells were proceeded charge/discharge cycles between 1.5 and 4 V at a rate of 20 mA g<sup>-1</sup>. the DAAQ-ECOF showed a high capacity of 145 mA h g<sup>-1</sup>, whereas the capacity of bulk COF was 110 mA h g<sup>-1</sup>. The higher capacity of DAAQ-ECOF confirmed that limited few layers were beneficial to enable ultrafast discharge/charge process and fully utilization of its active sites. Moreover, the retention of capacities were high to 107 and 76 mA g<sup>-1</sup> even at rates of 500 and 3000 mA g<sup>-1</sup>. And the reversible capacity of the DAAQ-ECOF was retained at 104 mA g<sup>-1</sup> after 1800 cycles, with a Coulombic efficiency of 99%. The superior cycle performance was caused by the stable framework reinforced by covalent and H-bonding. By replacing the DAAQ with DABQ (Figure 13), the discharge voltage was increased by 0.5 V, because of the electronic effect. And the capacity reached high to 210 mA h g<sup>-1</sup>, 35% higher than bulk DABQ-TFP-COF, which is potential in practical applications.

Sulfur is an attractive electrode because of its high capacity and low cost. However, sulfur cannot be directly used as electrodes because of its insulating character and dissolving issue. Moreover, the shuttling loss of intermediate lithium polysulfides eventually causes the deterioration of cycle performance. To address these drawbacks, trapping sulfur into porous materials opens a promising way, whereas the pore size and pore volume are key factors to be considered.

The long-term charge-discharge stability of Li-S batteries is highly affected by the accumulation of electron inert Li<sub>2</sub>S<sub>2</sub>/Li<sub>2</sub>S intermediates that are generated in the redox process. To solve this problem, iCOF-CNT hybrid papers were constructed by *in-situ* growing COF-1 (Figure 14a) on CNT papers and used as an interlayer between the

sulfur cathode and separator membrane.<sup>45</sup> As a result, the cell maintains 84% of its original capacity after 300 cycles at 2 C. The interlayer can trap  $\text{Li}_2\text{S}$  by the micropores of COF-1 and the S-B bonding between  $\text{Li}_2\text{S}$  and COF-1 mitigates the electrostatic repulsion between  $\text{Li}_2\text{S}$  and  $\text{S}_6^{2-}$  ( $\text{S}_3^*$ ). These effects facilitate the reversion from insoluble  $\text{Li}_2\text{S}$  to soluble  $\text{Li}_2\text{S}_x$ , thus preventing the aggregation of insulating  $\text{Li}_2\text{S}$  on the CNTs and enhancing the cycle stability.

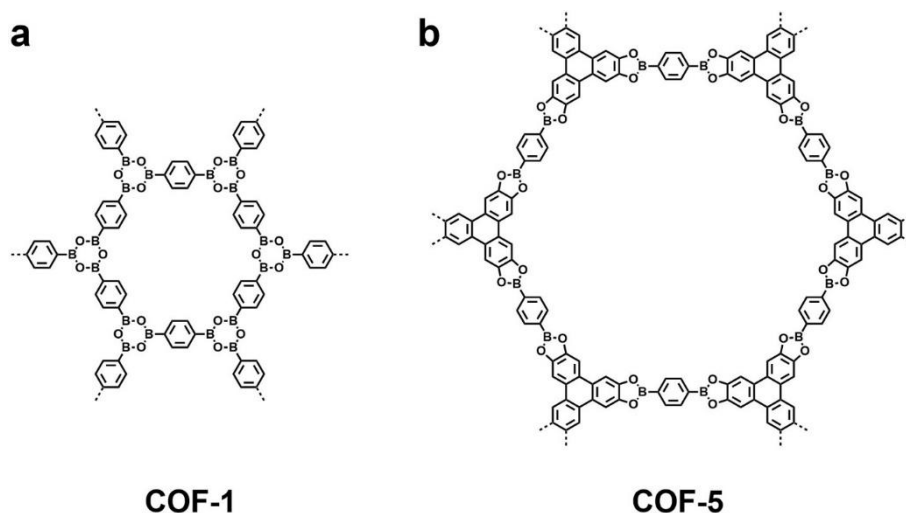


**Figure 14.** Chemical structure of COF-1 for Li-S battery and b) COF-5 for lithium ion conduction.

In LIBs, electrolytes play important roles in lithium ion transport between electrodes. Most batteries use organic liquid electrolytes, which cause many problems, because they are leaked and combustible. And the low work potential of liquid electrolytes limits the practical application. Moreover, the thermal stability is another severe problem. To solve the critical problems, the best method is to replace liquid electrolytes by all solid electrolytes. Preferred orientation of 2D COF layers have been developed by pressing the COF powders, which facilitate mass transfer within the aligned cylindrical pores in the COF pellets.<sup>46</sup> For example, the powder samples of COF-5 (Figure 14b) and TpPa-1 COFs were treated with 1M  $\text{LiClO}_4/\text{THF}$  for 48 h to load 3.77 mol% lithium ion. The resulting pellets exhibited ionic conductivities of 0.26 and 0.15  $\text{mS cm}^{-1}$ , at room temperature. The pellets without lithium salts were inactive for ion conduction. Moreover, by using linear Arrhenius plot, the activation energy was evaluated to be  $0.037 \pm 0.004$  eV for COF-5. The low activation energy indicates that the ion conductivity retains over a wide temperature range. Thus, the outcome portends use of COFs as solid-state electrolytes in batteries.

## 1.2.3 COFs Used in Fuel Cells

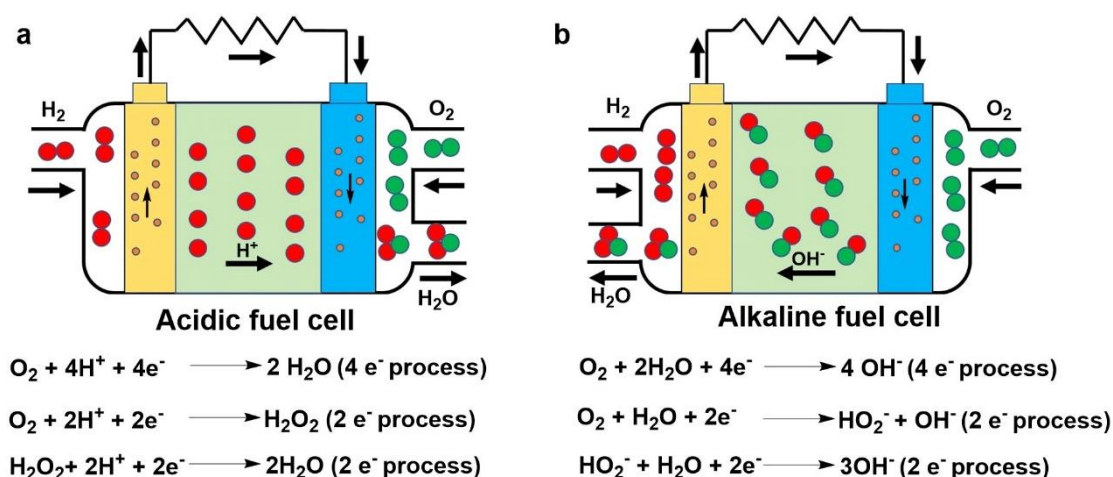


**Figure 15.** Illustration of mechanism of fuel cells, a) acidic fuel cells and b) alkaline fuel cells.

Fuel cells, an important class energy conversion devices, convert the chemical energy from a fuel into electricity through electrochemical reactions.<sup>47</sup> Fuel cells are a class of high efficiency and green energy storage and conversion devices. These advantages make them used in fuel cell electric vehicles. In acidic fuels, H<sub>2</sub> was oxidized into H<sup>+</sup> at the anode, then transport to the cathode by proton exchange membranes, and react with O<sub>2</sub>. In alkaline fuel cells, the OH<sup>-</sup> transports to the anode by KOH, and react with H<sub>2</sub> (Figure 15).<sup>48</sup>

Development of proton conducting materials is key to fuel cells. Pentafluorinated sulfonic acid functionalized polymer membrane, i.e., Nafion, is the benchmark material for proton conduction. Due to the unique morphological and structural characteristics, Nafion exhibits high proton conductivity (e.g. 10<sup>-1</sup> S cm<sup>-1</sup>) at moderate temperature (60 – 80 °C) under high relative humid condition (98% RH).<sup>49</sup> Due to high costs and low efficiency at high operating temperature (120 – 200 °C), long-term efforts over the past 5 decades have been made with an aim to explore new materials that can replace Nafion.

Materials with inherent pores are promising to provide a pathway for ion conduction across the nanopores. The combination of well-defined structural ordering, tunable porosity and functionality, and robust thermal and chemical stability in one extended COF structure is hardly achieved by other porous materials; recent advances demonstrated that COFs offer a new platform for molecular design of proton conducting materials. Especially, the ordered 1D channels of the 2D COFs are

accessible to proton carriers and are important for improving the proton conductivity beyond the level of Nafion through rational structural design.

By developing a stable skeleton, TPB-DMTP-COF (Figure 16) showed its high capability of loading organic proton carriers in the mesoporous channels of 3.2 nm.<sup>50</sup> TPB-DMTP-COF can accommodate 180 wt% triazole (trz) and 155 wt% imidazole (im) within its mesopores, which are close to the theoretical loading amounts of 186 wt% and 164 wt%, respectively. The anhydrous proton conductivities of them were as high as  $1.1 \times 10^{-3}$  and  $4.37 \times 10^{-3}$  S cm<sup>-1</sup>, respectively at 403 K. The high proton conductivity of im@TPB-DMTP-COF compared with trz@TPB-DMTP-COF indicated a great influence of different proton carriers on the proton conductivity. By decreasing the loading content of im or trz, the resulting materials greatly decreased the proton conduction. For example, the conductivity of im@TPB-DMTP-COF with a half theoretical loading amount, was  $2.03 \times 10^{-4}$  S cm<sup>-1</sup> at 403 K. Notably, the conductivity of im@TPB-DMTP-COF was four orders of magnitude higher than that of amorphous analogue im@TPB-TP-COF under otherwise same conditions, indicating the 1D channels promoted proton conduction in pores. Clearly, the activation energy ( $E_a$ ) for im@TPB-DMTP-COF was 0.38 V, which was much lower than amorphous im@TPB-TP-COF (0.91 eV). The low activation energy indicated the proton conduction was dominated by hopping mechanism, whereas the im and trz molecules in the mesopores form H-bonding networks and the protons move forward through these networks.

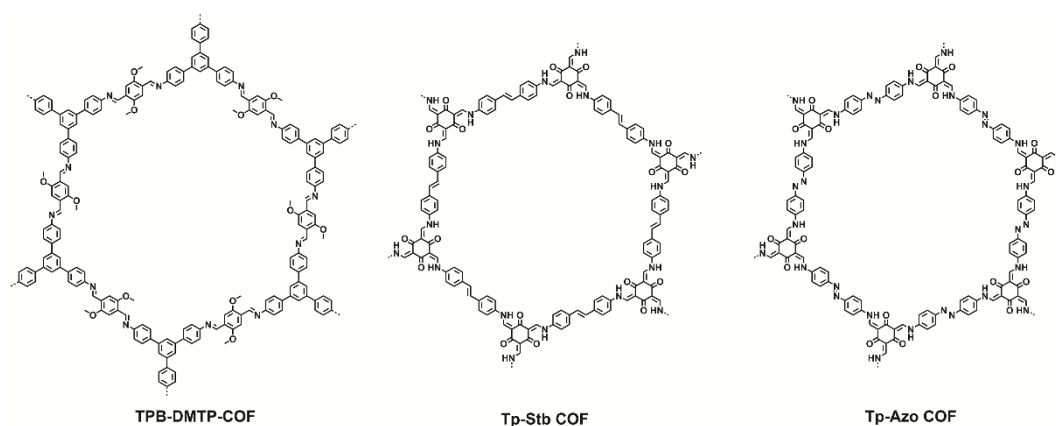


**Figure 16.** Chemical structure of TPB-DMTP-COF, Tp-Stb COF and Tp-Azo COF for proton conduction.

Similarly, phosphoric acid ( $H_3PO_4$ , PA) loaded Tp-Azo COF (Figure 16) has been investigated for proton conduction under humid and anhydrous condition from 295 to 415 K.<sup>49</sup> The PA@Tp-Azo COF with a PA content of 5.4 wt% exhibited proton

conductivity of  $6.7 \times 10^{-5} \text{ S cm}^{-1}$  at 340 K under anhydrous condition. In contrast, PA@Tp-Stb COF (2.8 wt% PA) without azo units exhibited almost no proton conductivity under otherwise same conditions. The conductivity of both COFs was increased by increasing the humidity. For example, PA@Tp-Azo and PA@Tp-Stb COFs exhibited the proton conductivity of  $9.9 \times 10^{-4}$  and  $2.3 \times 10^{-5} \text{ S cm}^{-1}$ , respectively, at 332 K under 98% RH. The different behaviors for azo ( $-\text{N}=\text{N}-$ ) and non-azo ( $-\text{C}=\text{C}-$ ) functionalized COFs clearly demonstrated that the presence of azo unit had remarkable contribution to the proton conduction. The protonated azo units on the 1D channel walls of the Tp-Azo COF under humid conditions form hydrogen-bonding network that promotes proton conduction.

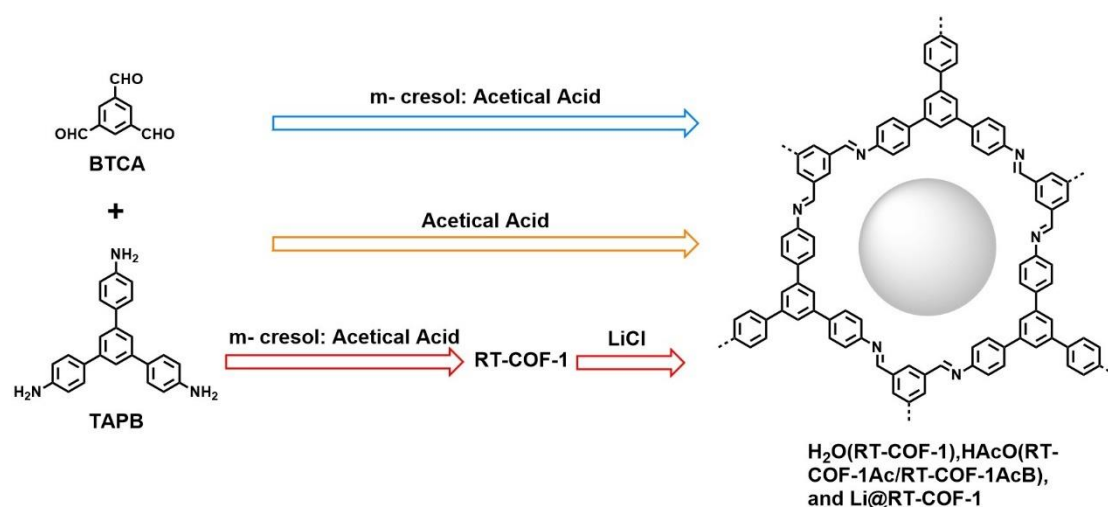


**Figure 17.** Synthesis of LiCl@RT-COF-1, RT-COF-1AcB, RT-COF-1Ac, and RT-COF-1 from BTCA and TAPB.

Apart from  $\text{H}_3\text{PO}_4$ , loading lithium ion within the pore channels is another effective method to improve  $\text{H}^+$  transport.<sup>51</sup> Addition of lithium ion provides a higher concentration of water in the channels, because of highly hydrophilic nature of lithium ion. The prepared COFs were synthesized from the same building blocks in different condition, which led to the different host in the pore channels (Figure 17).<sup>52</sup> By treating the gel (RT-COF-1) with LiCl aqueous solution, lithium ion was successfully incorporated in COFs. From the water absorption curves, LiCl@RT-COF-1 exhibited  $635 \text{ cm}^3 \text{ g}^{-1}$  at 90% RH. The prepared powder was upon a stress of 400 MP for 5 mins to obtain films with 0.03 to 0.05 cm. The prepared materials exhibited conductivities of  $10^{-10}$  to  $10^{-9} \text{ S cm}^{-1}$  at 22% RH, indicating no ionic conduction. With increasing RH to 100%, the conductivities of LiCl@RT-COF-1, RT-COF-1AcB, RTCOF-1Ac, RT-COF-1 were  $6.45 \times 10^{-3}$ ,  $5.25 \times 10^{-4}$ ,  $1.07 \times 10^{-4}$  and  $1.83 \times 10^{-5} \text{ S cm}^{-1}$ . The conduction

performance was in accordance with the absorption ability of H<sub>2</sub>O. Especially, LiCl@RT-COF-1 possessed the highest conductivity at 100% RH and 313 K among all the COFs and MOFs. The prepared materials were fabricated into membrane electrode assemblies (MEAs). The maximum power and current density of LiCl@RT-COF-1 were 12.95 mW cm<sup>-2</sup> and 53.1 mA cm<sup>-2</sup> at 323 K.

#### 1.2.4 COFs Used in Other Electrochemical Reactions

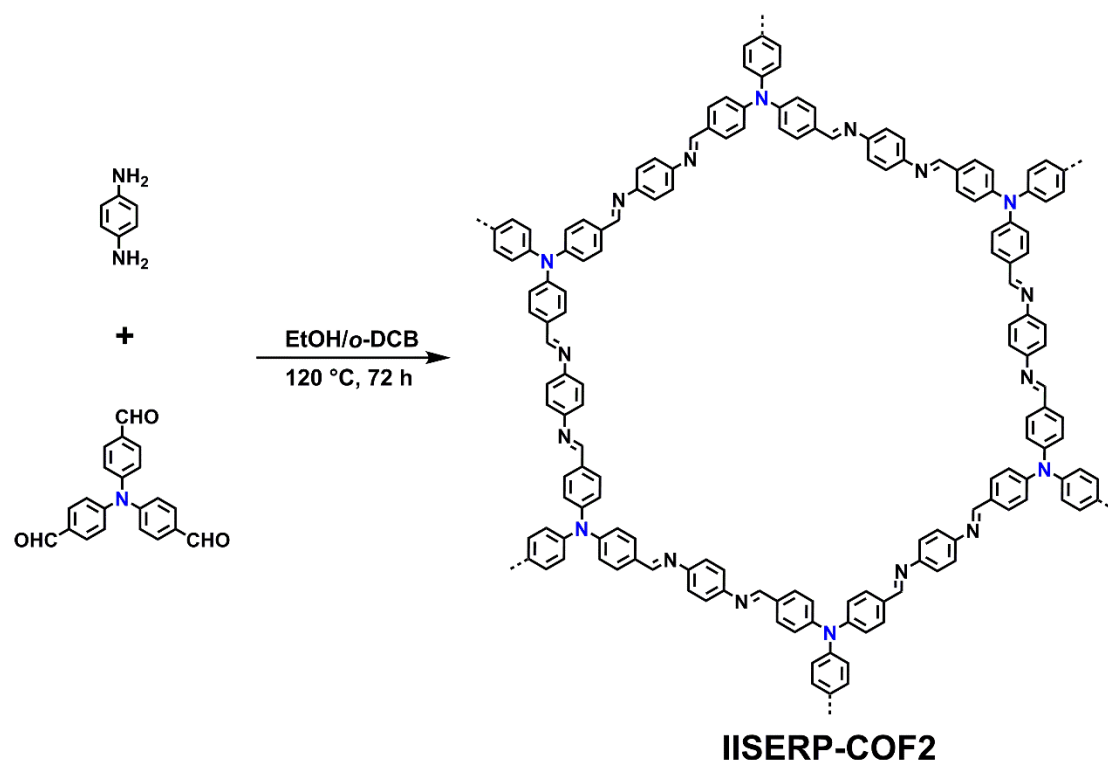


**Figure 18.** Synthesis of IISERP-COF2 for loading NiN<sub>3</sub> to split H<sub>2</sub>O.

**Water Splitting.** COFs can affect the electronic properties of the metal-based catalysts and thus have a chance to facilitate the OER process. For example, using an *sp*<sup>3</sup>-nitrogen rich COF (IISERP-COF2) (Figure 18) as a matrix to isolate the nickel metal nanoparticles can enhance the catalytic performance.<sup>53</sup> This method was further developed by a hybrid composite based on a benzimidazole COF (IISERP-COF3); a hybrid system with the Ni<sub>3</sub>N nanoparticles was prepared by heating a mixture of IISERP-COF3, nickel acetate, and urea at 350 °C for 6 h. The Ni<sub>3</sub>N nanoparticles were distributed between the COF layers and confined inside the COF channels as evidenced by FE-SEM and HR-TEM images. The electrochemical performance in an aqueous KOH solution (1 M) saturated with H<sub>2</sub>, the hybrid catalyst exhibited an onset potential at 1.43 V and overpotential of 230 mV at a current density of 10 mA cm<sup>-2</sup>. A Faradaic efficiency of 98% at 1 mA cm<sup>-2</sup> was confirmed by the rotating ring disk electrode

(RRDE) experiments. The oxygen evolution rate was as high as  $230 \text{ mmol h}^{-1} \text{ g}^{-1}$  with a TOF value of  $0.52 \text{ s}^{-1}$  at an over potential of 300 mV, which was superior to those of other catalysts reported under similar conditions. The spatial confinement of the  $\text{Ni}_3\text{N}$  nanoparticles between the ordered nitrogen-rich COF layers accounts for the high performance.

**Oxygen Evolution Reaction (OER).** The development of efficient OER catalyst for oxidizing water molecule is a challenging issue, due to its poor reaction kinetics at a neutral pH. The bipyridine-containing TpBpy COF (Figure 19) has been developed as an OER catalyst by coordinating cobalt (Co) (II) ions to the bipyridine edges.<sup>54</sup> The electrochemical property of Co-TpBpy COF (12% Co) was studied by cyclic voltammetry (CV) and linear sweep voltammetry (LSV) with Co-TpBpy-COF-coated glassy carbon working electrodes in 0.1 M aqueous phosphate buffer at pH = 7. The CV profile showed the onset potential at 1.63 V and an over potential of 400 mV at  $1 \text{ mA cm}^{-2}$ . The Co-TpBpy COF retained similar LSV patterns and roughness factor (1.46) even after 1000 scans and achieves 94% retention in the OER current. ICP analysis of the electrolyte revealed that there was no cobalt ion leaked from the Co-TpBpy COF electrode. The SEM and X-ray photoelectron spectral (XPS) analysis also confirmed the intact structure of the Co-TpBpy COF after OER process.

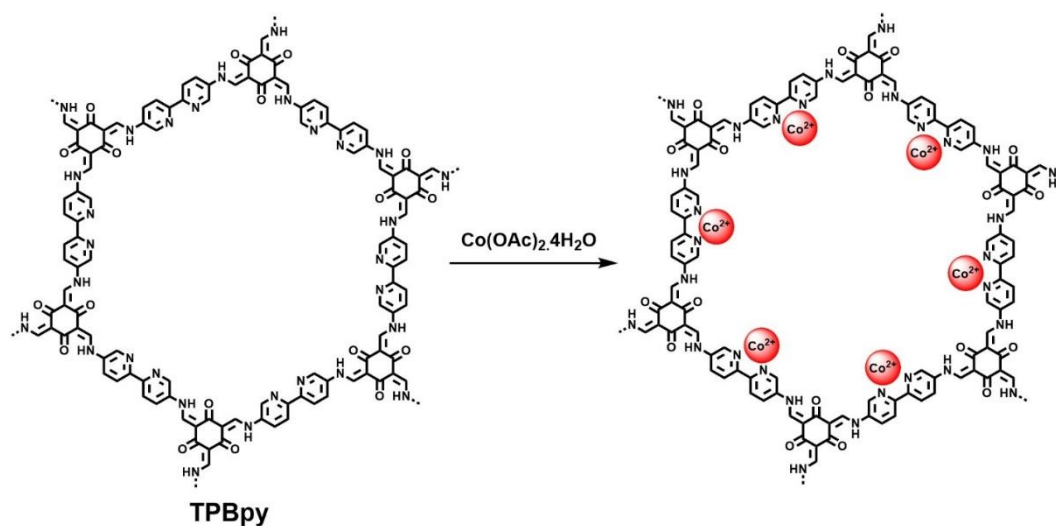


**Figure 19.** Synthesis of the Co-TpBpy COF via ligation of Co (II) to the bipyridine edge units as the OER catalyst.

**Carbon Dioxide Reduction.** Porphyrin-based electrocatalytic COF has been developed for carbon dioxide reduction to carbon monoxide. The imine-linked COF-366-Co and COF-367-Co (Figure 20) consisting of cobalt porphyrin units at the vertices,

terephthalaldehyde (BDA) and biphenyl-4,4'-dicarboxaldehyde (BPDA) at the edges, respectively, served as an electrocatalyst for the reduction of  $\text{CO}_2$  to  $\text{CO}$ .<sup>55</sup> The COF-366-Co exhibited 10% enhanced catalytic performance compared with the molecular cobalt porphyrin unit and achieved a turnover number (TON) of 1352 (TON per electroactive cobalt,  $\text{TON}_{\text{EA}} = 34000$ ) and an initial turnover frequency of  $98 \text{ h}^{-1}$  (TOF per electroactive cobalt,  $\text{TOF}_{\text{EA}} = 2500$ ). The Faradaic efficiency for  $\text{CO}$  ( $\text{FE}_{\text{CO}}$ ) was as high as 90%. By contrast, the large-pore COF-367-Co promoted the  $\text{CO}$  evolution with a TON of 3901 ( $\text{TON}_{\text{EA}} = 48000$ ) during 24 h and afforded a high selectivity of competing proton reduction ( $\text{FE}_{\text{CO}} = 91\%$ ). A multivariate strategy to dilute cobalt component by introducing copper porphyrin units was developed and the  $\text{TON}_{\text{EA}}$  for these multivariate Co/Cu COF-367 catalysts exhibited substantial improvement with each 10-fold dilution of cobalt loading. The hybrid COF (COF-367-Co (1%)) with optimum active content achieved excellent performance with very high  $\text{TON}_{\text{EA}}$  of 296000 ( $\text{TON} > 24000$ ) and an initial TOF of  $9400 \text{ h}^{-1}$ . Notably, this hybrid COF is one of the most efficient electrochemical  $\text{CO}_2$  reduction catalysts reported to date.

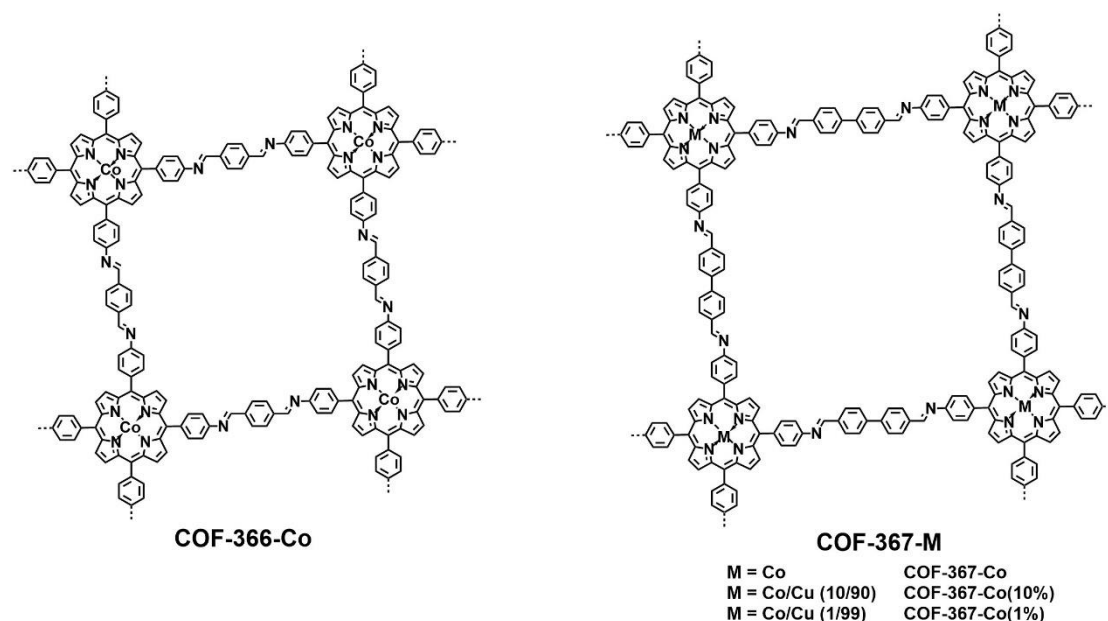


**Figure 20.** Porphyrin-based COFs for the reduction of  $\text{CO}_2$  to  $\text{CO}$ .

### 1.3 COF-derived Carbon Materials

COFs are a unique kind of porous polymers, with broad structural diversities and enable synthetic control over their topologies, building blocks and pores. COFs comprise mainly of carbons and are versatile for integrating heteroatoms such as B, O and N to the skeletons. The designable structure and abundant composition render

COFs useful as precursors for the pyrolytic synthesis of heteroatom-doped carbons. However, the structure and morphology of COFs will be collapsed, which enhances the difficulties for preparing functional carbons from COFs.

**Oxygen Reduction Reaction (ORR).** ORR is the key reaction in the fuel cells. To replace the platinum catalyst for ORR in fuel cells, various porous carbons from porous precursors have been developed, including MOFs, CMP, and COFs. A cobalt porphyrin COF (Co-COF) (Figure 21a) has been utilized as a precursor for the pyrolysis preparation of a nanocomposite of well-distributed Co (0) nanoparticles and graphitized carbon structures, as a new kind of Co, N-containing precursor to produce Co/N/C catalysts for ORR.<sup>56</sup> In an aqueous solution of KOH (0.1 M), both the potential and current responses obtained from pyrolyzed Co-COF-900 were comparable to those of the commercial 20% Pt/C catalyst. Based on RRDE, there were 3.85 electrons involved in the ORR, demonstrating that the oxygen reduction catalyzed by pyrolyzed Co-COF-900 involved a four-electron process. In addition to the metal-contained COFs, another metal-free COF (2DPPV) based on olefin (C=C) linkage was used as a precursor for porous carbon (Figure 16 b).<sup>57</sup> 2DPPV was synthesized from 1,4-phenylenediacetonitrile and three-armed aromatic aldehyde. The BET surface area of 2DPPV was  $472 \text{ m}^2 \text{ g}^{-1}$ , and the pore volume was  $0.37 \text{ cm}^3 \text{ g}^{-1}$ . And the corresponding pore size was 1.6 nm. The SEM and AFM images showed 2DPPV were in sheet-like flakes, and thickness was from 50 to 300 nm. 2DPPV was pyrolyzed at 700, 800 and 900 °C under an argon atmosphere. The 800 °C pyrolyzed carbon was further treated at 800 °C under an ammonia atmosphere for 15 min to produce activated pores. The resulting porous carbons were denoted as 2DPPV-X (X = 700, 800, 900 and 800a, respectively). The resultant carbon exhibited higher surface areas from 529 to  $880 \text{ m}^2 \text{ g}^{-1}$  (2DPPV-800a). As a metal-free ORR catalyst, the resultant 2DPPV-800a exhibited a low onset potential at 0.85 V (*vs.* RHE) and a four-electron pathway in alkaline condition (0.1 M KOH). Apart from ORR performance, 2DPPV-X showed good performance as capacitors. The specific capacitance of 2DPPV-800 was high to  $334 \text{ F g}^{-1}$  at  $0.5 \text{ A g}^{-1}$ , which was about 85% and 27% higher than those of 2DPPV-700 and 2DPPV-900, respectively. The capacitance was retained after 10000 cycles by galvanostatic charge–discharge measurement at current density of  $0.5 \text{ A g}^{-1}$ .

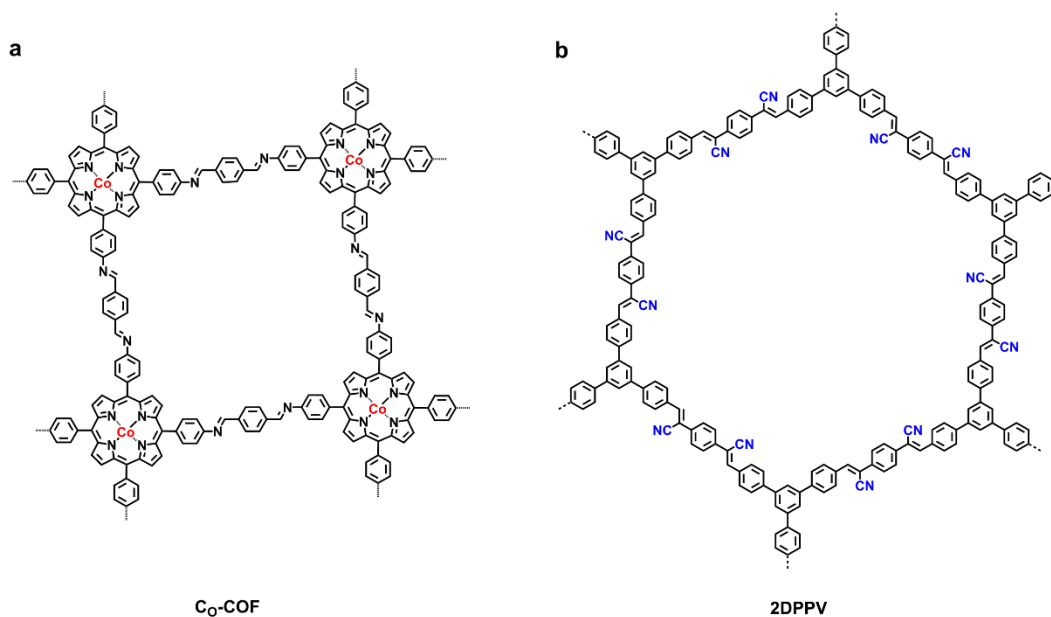


**Figure 21.** The structure of a) Co-COF and b) 2DPPV as porous precursors for ORR catalysts.

**Capacitive Energy Storage.** Different from COF-based faradaic capacitors, EDLS possess high power density, short charging time, excellent reversibility and long cycle stability. Additionally, EDLS do not need redox active monomers and groups as faradaic capacitor. Heteroatom (oxygen, nitrogen, fluorine or phosphorus) doping has been demonstrated as an effective strategy to enhance the capacitive energy storage performance of a carbon electrode, through affecting the electron distribution of carbon material, further ameliorating the surface wettability, facilitating rapid electrolyte ion transport within the micropores and enhancing the pseudocapacitance effect. Thus, COF-derived carbon is a promising electrode material as EDLS. However, direct carbonization of COFs always leads to carbon with low surface areas because of collapsed skeleton and structure.<sup>58</sup> To overcome the bottleneck, an effective method has been explored. The dried COF-5 was mixed with  $\text{ZnCl}_2$ , and then grinded uniformly. The resultant mixture was pyrolysis at  $700\text{ }^\circ\text{C}$ , to obtain B-doped carbon (Figure 22). The prepared carbon (BC-MS-700-14) exhibited a high surface area of  $1460\text{ m}^2\text{ g}^{-1}$ , with the pore volume of  $1.76\text{ cm}^3\text{ g}^{-1}$ , whereas the direct carbonization product (BC-700) had a surface area of  $449\text{ m}^2\text{ g}^{-1}$ . And the corresponding pore volume was  $0.26\text{ cm}^3\text{ g}^{-1}$ . BC-MS-700-14 showed the best capacitive performance, whose specific capacitance was  $160\text{ F g}^{-1}$  at  $10\text{ mV s}^{-1}$  in  $1\text{ M H}_2\text{SO}_4$  aqueous solution.



storage performance. Moreover, the capacitance of (N)G2 was retained high than 90% after 10,000 charge/discharge cycles, indicated good cyclic stability of the carbon.

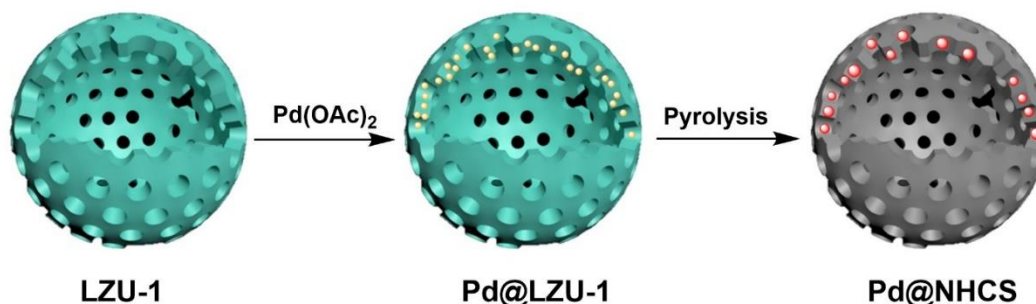


**Figure 24.** Schematic illustration of fabrication Pd@NHCS from LZU-1.

**Catalysts.** Hollow carbon spheres are very attractive due to their outstanding features, including low density, good thermal stability and permeability. The traditional method to synthesis of hollow carbon spheres includes three steps: firstly, grow precursors on the hard template, then pyrolysis the materials, thirdly, remove the template. LZU-1 (structure shown in Figure 5) possesses hollow sphere morphology, which could converse to hollow carbon sphere by thermal treatment.<sup>60</sup> The distance of eclipsed nitrogen atoms in adjacent layers of LZU-1 was about 3.7 Å, which benefited incorporating of metal ions. After binding with Pd<sup>2+</sup> in the COF, the prepared Pd@LZU-1 was pyrolysis at 500 or 600 °C to yield Pd nanoparticles in the N-doped hollow carbon spheres (Pd@NHCS (500) or Pd@NHCS (600)) (Figure 24). Pd@NHCS materials had BET surface areas of 468 and 527 m<sup>2</sup> g<sup>-1</sup>, respectively. The Pd@NHCS was used to catalyse the hydrogenation of nitrobenzene to aniline as a model reaction. Compared with Pd@NHCS (600), Pd@NHCS (500) was of higher activity, which was because some hollow structure of Pd@NHCS (600) was broken, that leading to aggregated Pd nanoparticles. Moreover, Pd@NHCS (500) could be regenerated and reused at least five times in subsequent reactions without obvious loss of catalytic activity and selectivity.

### 1.5 Scope of This Thesis

2D COFs, as a unique class of 2D materials, enable precisely atom integration of organic units into extended structures with periodic skeletons and ordered channels. The geometry and dimensions of the building blocks can be designed and controlled to direct the topological evolution of structural periodicity. The diversity of the building blocks and topology schemes make COFs a promising materials platform for structural and functional designs. Apart from the designable, the other important feature of COFs

was pore surface engineering. The pore channels of COFs could be modified by different functional groups for different applications. The designable character and pore surface engineer features endow the frameworks with outstanding physicochemical properties, including optoelectronic, chemical sensor, charge separation and charge carrier conduction, and catalyst. Especially, various electric functional building blocks, excellent thermal stability, and 1D fast pore channels, make COFs show superior performance in electrochemical energy storage and conversion devices, such as capacitors, fuel cells and batteries.

In chapter 1, I summarized the field of COFs. I illustrated the design principle, the diversity of building blocks, and the availability of linkages. I also outlined the progress of COFs for electrochemical energy storage and conversion, including capacitor, lithium-ion batteries, lithium-sulfur batteries, and fuel cells. Furthermore, I reviewed the recent progress on the synthesis of COF-derived carbons, which target for supercapacitors, catalysts, and electrochemical catalysts.

In chapter 2, I described a novel strategy for converting COFs into carbon for supercapacitor based on template pyrolysis. COFs were grown as a shell on crosslinked polymer spheres to form a thickness-tunable core-shell structure. This core-shell structure enables a synergistic structural effect to produce carbons that integrated microporous structure, high conductivity, and abundant heteroatom content, which are attractive in energy storage and conversion field. The capacitors thus fabricated achieved exceptional capacitance ( $411 \text{ F g}^{-1}$  at  $0.5 \text{ A g}^{-1}$  and  $287 \text{ F g}^{-1}$  at  $1 \text{ A g}^{-1}$ ), high-rate charge and discharge, and stable performance over 10000 cycles.

In chapter 3, I demonstrated a methodology for the synthesis of an ideal carbon catalyst for oxygen reduction reactions by combining two strategies: the use of COFs as a carbon precursor and the development of a suitable template to guide the pyrolysis. This methodology yields carbon sheets with high conductivity, hierarchical porosity and abundant heteroatom catalytic edges. These carbons serve as metal-free electrochemical catalysts for oxygen reduction reactions, and achieve ultrahigh performance with exceptional onset (about  $0 \text{ V}$  vs  $\text{Ag}/\text{AgCl}$ ) and half-wave potentials of  $-0.11 \text{ V}$ , and high limit current density of  $7.2 \text{ mA cm}^{-1}$ . These results outperformed the state-of-the-art Pt catalysts and reveal a novel materials platform based on COFs for designing catalytic energy conversion systems.

In chapter 4, I described the design and synthesis of all-solid lithium electrolytes based on 2D COFs in which the one-dimensional pore walls are functionalized with

oligoethylene oxide chains that formed a pre-organized pathway for lithium ion conduction. The targeted COF (TPB-BMTP-COF) was synthesized from TPB and 2,5-bis ((2-methoxyethoxy) methoxy) terephthalaldehyde (BMTP) under solvothermal conditions. TPB-BMTP-COF exhibited a high BET surface of  $1750 \text{ m}^2 \text{ g}^{-1}$ . And the pore size was 3.0 nm, with a pore volume of  $0.96 \text{ cm}^3 \text{ g}^{-1}$ . Moreover, TPB-BMTP-COF was thermally stable up to  $300 \text{ }^\circ\text{C}$  under nitrogen. TPB-BMTP-COF enables the load of  $\text{LiClO}_4$  in the pores to form  $\text{LiClO}_4@\text{TPB-BMTP-COF}$  that achieved an ion conductivity as high as  $6.9 \times 10^{-3} \text{ S cm}^{-1}$  at  $100 \text{ }^\circ\text{C}$ .  $\text{LiClO}_4@\text{TPB-BMTP-COF}$  shows excellent cyclic stability to retain a high conductivity after 24 h continuous operation at  $100 \text{ }^\circ\text{C}$ .

In chapter 5, I described the design and synthesis of a series of solid polymer electrolytes based on COFs by pore surface engineering method. The frameworks were designed to possess short ethylene oxide chains that are free of crystallinity by click reactions. The ethylene oxide chains on the pore walls retain high motion flexibility that can facilitate ion transport across the channels. Moreover, the COFs allow for the precise tune of and control over the length and content of ethylene oxide chains on the pore walls. The resulting COFs, upon load of lithium ions, serve as polyelectrolytes that enable high rate transport of lithium ions, demonstrating the importance of ordered channels and ordered electrolyte sites in facilitating ion conduction.

In chapter 6, I summarized the results of this work and showed the perspectives of COFs for energy storage and conversion.

**References**

1. (a) N. Stock, S. Biswas, *Chem. Rev.* **2012**, *112*, 933-969. (b) D. Wu, F. Xu, B. Sun, R. Fu, H. He, K. Matyjaszewski, *Chem. Rev.* **2012**, *112*, 3959-4015. (c) S. Das, P. Heasman, T. Ben, S. Qiu, *Chem. Rev.* **2017**, *117*, 1515-1563. (d) W. Lu, Z. Wei, Z.-Y. Gu, T.-F. Liu, J. Park, J. Tian, M. Zhang, Q. Zhang, T. Gentle Iii, M. Bosch, H.-C. Zhou, *Chem. Soc. Rev.* **2014**, *43*, 5561-5593. (e) A. G. Slater, A. I. Cooper, *Science* **2015**, *348*, aaa8075, doi: 10.1126/science.aaa8075. (f) Y. Xu, S. Jin, H. Xu, A. Nagai, D. Jiang, *Chem. Soc. Rev.* **2013**, *42*, 8012-8031. (g) L. Tan, B. Tan, *Chem. Soc. Rev.* **2017**, *46*, 3322-3356.
2. A. P. Côté, A. I. Benin, N. W. Ockwig, M. Keefe, A. J. Matzger, O. M. Yaghi, *Science* **2005**, *310*, 1166-1170.
3. (a) N. Huang, P. Wang, D. Jiang, *Nat. Rev. Mater.* **2016**, *1*, 16068, doi: 10.1038/natrevmats 2016.68. (b) X. Feng, X. Ding, D. Jiang, *Chem. Soc. Rev.* **2012**, *41*, 6010-6022. (c) J. L. Segura, M. J. Mancheno, F. Zamora, *Chem. Soc. Rev.* **2016**, *45*, 5635-5671. (d) P. J. Waller, F. Gándara, O. M. Yaghi, *Acc. Chem. Res.* **2015**, *48*, 3053-3063. (e) C. S. Diercks, O. M. Yaghi, *Science* **2017**, *355*, eaal1585, doi: 10.1126/science.aal1585.
4. (a) H. Furukawa, O. M. Yaghi, *J. Am. Chem. Soc.* **2009**, *131*, 8875-8883. (b) Z. Kahveci, T. Islamoglu, G. A. Shar, R. Ding, H. M. El-Kaderi, *CrystEngComm.* **2013**, *15*, 1524-1527.
5. (a) S. J. Rowan, S. J. Cantrill, G. R. L. Cousins, J. K. M. Sanders, J. F. Stoddart, *Angew. Chem. Int. Ed.* **2002**, *41*, 898-952. (b) Y. Jin, C. Yu, R. J. Denman, W. Zhang, *Chem. Soc. Rev.* **2013**, *42*, 6634-6654. (c) Y. Jin, Q. Wang, P. Taynton, W. Zhang, *Acc. Chem. Res.* **2014**, *47*, 1575-1586.
6. A. P. Côté, H. M. El-Kaderi, H. Furukawa, J. R. Hunt, O. M. Yaghi, *J. Am. Chem. Soc.* **2007**, *129*, 12914-12915.
7. A. P. Cote, A. I. Benin, N. W. Ockwig, M. O'Keefe, A. J. Matzger, O. M. Yaghi, *Science* **2005**, *310*, 1166-1170.
8. Y. Du, H. S. Yang, J. M. Whiteley, S. Wan, Y. H. Jin, S. H. Lee, W. Zhang, *Angew. Chem. Int. Ed.* **2016**, *55*, 1737-1741.
9. X. Chen, M. Addicoat, S. Irle, A. Nagai, D. Jiang, *J. Am. Chem. Soc.* **2013**, *135*, 546-549.

10. F. J. Uribe-Romo, C. J. Doonan, H. Furukawa, K. Oisaki, O. M. Yaghi, *J. Am. Chem. Soc.* **2011**, *133*, 11478-11481.
11. S. Dalapati, S. Jin, J. Gao, Y. Xu, A. Nagai, D. Jiang, *J. Am. Chem. Soc.* **2013**, *135*, 17310-17313.
12. J. Guo, Y. Xu, S. Jin, L. Chen, T. Kaji, Y. Honsho, M. A. Addicoat, J. Kim, A. Saeki, H. Ihee, S. Seki, S. Irle, M. Hiramoto, J. Gao, D. Jiang, *Nat. Commun.* **2013**, *4*, 2736, doi: 10.1038/ncomms3736.
13. A. Nagai, X. Chen, X. Feng, X. Ding, Z. Guo, D. Jiang, *Angew. Chem. Int. Ed.* **2013**, *52*, 3770-3774.
14. Q. Fang, Z. Zhuang, S. Gu, R. B. Kaspar, J. Zheng, J. Wang, S. Qiu, Y. Yan, *Nat. Commun.* **2014**, *5*, 4503, doi: 10.1038/ncomms5503.
15. P. Kuhn, M. Antonietti, A. Thomas, *Angew. Chem. Int. Ed.* **2008**, *47*, 3450-3453.
16. K. T. Jackson, T. E. Reich, H. M. El-Kaderi, *Chem. Commun.* **2012**, *48*, 8823-8825.
17. X. Chen, M. Addicoat, E. Jin, H. Xu, T. Hayashi, F. Xu, N. Huang, S. Irle, D. Jiang, *Sci. Rep.* **2015**, *5*, 14650, doi: 10.1038/srep14650.
18. E. L. Spitler, M. R. Giovino, S. L. White, W. R. Dichtel, *Chem. Sci.* **2011**, *2*, 1588-1593.
19. Y. Du, H. Yang, J. M. Whiteley, S. Wan, Y. Jin, S.-H. Lee, W. Zhang, *Angew. Chem. Int. Ed.* **2016**, *55*, 1737-1741.
20. L. M. Lanni, R. W. Tilford, M. Bharathy, J. J. Lavigne, *J. Am. Chem. Soc.* **2011**, *133*, 13975-13983.
21. H. Xu, J. Gao, D. Jiang, *Nat. Chem.* **2015**, *7*, 905-912.
22. E. Jin, M. Asada, Q. Xu, S. Dalapati, M. A. Addicoat, M. A. Brady, H. Xu, T. Nakamura, T. Heine, Q. Chen, D. Jiang, *Science* **2017**, *357*, 673-676.
23. L. Q. Xu, S. Y. Ding, J. M. Liu, J. L. Sun, W. Wang, Q. Y. Zheng, *Chem. Commun.* **2016**, *52*, 4706-4709.
24. N. L. Campbell, R. Clowes, L. K. Ritchie, A. I. Cooper, *Chem. Mater.* **2009**, *21*, 204-206.
25. L. K. Ritchie, A. Trewin, A. Reguera-Galan, T. Hasell, A. I. Cooper, *Microporous Mesoporous Mater.* **2010**, *132*, 132-136.
26. H. Wei, S. Chai, N. Hu, Z. Yang, L. Wei, L. Wang, *Chem. Commun.* **2015**, *51*, 12178-12181.
27. S. Ren, M. J. Bojdys, R. Dawson, A. Laybourn, Y. Z. Khimyak, D. J. Adams, A. I. Cooper, *Adv. Mater.* **2012**, *24*, 2357-2361.

28. (a) P. Kuhn, M. Antonietti, A. Thomas, *Angew. Chem. Int. Ed.* **2008**, *47*, 3450-3453. (b) M. J. Bojdys, J. Jeromenok, A. Thomas, M. Antonietti, *Adv. Mater.* **2010**, *22*, 2202-2205.
29. (a) B. P. Biswal, S. Chandra, S. Kandambeth, B. Lukose, T. Heine, R. Banerjeet, *J. Am. Chem. Soc.* **2013**, *135*, 5328-5331. (b) G. Das, D. B. Shinde, S. Kandambeth, B. P. Biswal, R. Banerjee, *Chem. Commun.* **2014**, *50*, 12615-12618.
30. (a) X. S. Ding, L. Chen, Y. Honsho, X. Feng, O. Saenpawang, J. D. Guo, A. Saeki, S. Seki, S. Irle, S. Nagase, V. Parasuk, D. Jiang, *J. Am. Chem. Soc.* **2011**, *133*, 14510-14513. (b) X. Ding, J. Guo, X. Feng, Y. Honsho, S. Seki, P. Maitarad, A. Saeki, S. Nagase, D. Jiang, *Angew. Chem. Int. Ed.* **2011**, *50*, 1289-1293.
31. N. Huang, L. Zhai, H. Xu, D. Jiang, *J. Am. Chem. Soc.* **2017**, *139*, 2428-2434. (b) Q. Sun, B. Aguila, J. Perman, L. D. Earl, C. W. Abney, Y. Cheng, H. Wei, N. Nguyen, L. Wojtas, S. Ma, *J. Am. Chem. Soc.* **2017**, *139*, 2786-2793.
32. (a) X. Wang, X. Han, J. Zhang, X. Wu, Y. Liu, Y. Cui, *J. Am. Chem. Soc.* **2016**, *138*, 12332-12335. (b) H. S. Xu, S. Y. Ding, W. K. An, H. Wu, W. Wang, *J. Am. Chem. Soc.* **2016**, *138*, 11489-11492.
33. (a) P. Simon, Y. Gogotsi, *Nat. Mater.* **2008**, *7*, 845-854. (b) Y. Wang, Y. Song, Y. Xia, *Chem. Soc. Rev.* **2016**, *45*, 5925-5950. (c) G. Wang, L. Zhang, J. Zhang, *Chem. Soc. Rev.* **2012**, *41*, 797-828. (d) X. Peng, L. L. Peng, C. Z. Wu, Y. Xie, *Chem. Soc. Rev.* **2014**, *43*, 3303-3323. (e) Z. Yang, J. Ren, Z. Zhang, X. Chen, G. Guan, L. Qiu, Y. Zhang, H. Peng, *Chem. Rev.* **2015**, *115*, 5159-5223.
34. C. R. DeBlase, K. E. Silberstein, T. T. Truong, H. D. Abruna, W. R. Dichtel, *J. Am. Chem. Soc.* **2013**, *135*, 16821-16824.
35. C. R. DeBlase, K. Hernández-Burgos, K. E. Silberstein, G. G. Rodríguez-Calero, R. P. Bisbey, H. D. Abruña, W. R. Dichtel, *ACS Nano* **2015**, *9*, 3178-3183.
36. C. R. Mulzer, L. Shen, R. P. Bisbey, J. R. McKone, N. Zhang, H. D. Abruña, W. R. Dichtel, *ACS Cent. Sci.* **2016**, *2*, 667-673.
37. Z. Zha, L. Xu, Z. Wang, X. Li, Q. Pan, P. Hu, S. Lei, *ACS Appl. Mater. Interfaces* **2015**, *7*, 17837-17843.
38. A. M. Khattak, Z. A. Ghazi, B. Liang, N. A. Khan, A. Iqbal, L. Li, Z. Tang, *J. Mater. Chem. A*, **2016**, *4*, 16312-16317.
39. S. Chandra, D. Roy Chowdhury, M. Addicoat, T. Heine, A. Paul, R. Banerjee, *Chem. Mater.* **2017**, *29*, 2074-2080.
40. B. Sun, J. Liu, A. Cao, W. Song, D. Wang, *Chem. Commun.* **2017**, *53*, 6303-6306.

41. F. Xu, H. Xu, X. Chen, D. Wu, Y. Wu, H. Liu, C. Gu, R. Fu, D. Jiang, *Angew. Chem. Int. Ed.* **2015**, *54*, 6814-6818.
42. (a) H.-J. Peng, J.-Q. Huang, Q. Zhang, *Chem. Soc. Rev.* **2017**, *46*, 5237-5288. (b) Z. W. Seh, Y. Sun, Q. Zhang, Y. Cui, *Chem. Soc. Rev.* **2016**, *45*, 5605-5634. (c) N. Nitta, F. Wu, J. T. Lee, G. Yushin, *Mater. Today* **2015**, *18*, 252-264.
43. F. Xu, S. Jin, H. Zhong, D. Wu, X. Yang, X. Chen, H. Wei, R. Fu, D. Jiang, *Sci. Rep.* **2015**, *5*, 8225, doi: 10.1038/srep08225.
44. S. Wang, Q. Wang, P. Shao, Y. Han, X. Gao, L. Ma, S. Yuan, X. Ma, J. Zhou, X. Feng, B. Wang, *J. Am. Chem. Soc.* **2017**, *139*, 4258-4261.
45. J. Yoo, S. J. Cho, G. Y. Jung, S. H. Kim, K. H. Choi, J. H. Kim, C. K. Lee, S. K. Kwak, S. Y. Lee, *Nano Lett.* **2016**, *16*, 3292-3300.
46. D. A. Vazquez-Molina, G. S. Mohammad-Pour, C. Lee, M. W. Logan, X. Duan, J. K. Harper, F. J. Uribe-Romo, *J. Am. Chem. Soc.* **2016**, *138*, 9767-9770.
47. R. K. Shah, In *Recent Trends in Fuel Cell Science and Technology*, Basu, S., Ed. Springer New York: New York, NY, **2007**, 1-9.
48. (a) L. Dai, Y. Xue, L. Qu, H.-J. Choi, J.-B. Baek, *Chem. Rev.* **2015**, *115*, 4823-4892. (b) X. Ge, A. Sumboja, D. Wu, T. An, B. Li, F. W. T. Goh, T. S. A. Hor, Y. Zong, Z. Liu, *ACS Catal.* **2015**, *5*, 4643-4667.
49. S. Chandra, T. Kundu, S. Kandambeth, R. BabaRao, Y. Marathe, S. M. Kunjir, R. Banerjee, *J. Am. Chem. Soc.* **2014**, *136*, 6570-6573.
50. H. Xu, S. Tao, D. Jiang, *Nat. Mater.* **2016**, *15*, 722-726.
51. S. Horike, Y. Kamitsubo, M. Inukai, T. Fukushima, D. Umeyama, T. Itakura, S. Kitagawa, *J. Am. Chem. Soc.* **2013**, *135*, 4612-4615.
52. C. Montoro, D. Rodríguez-San-Miguel, E. Polo, R. Escudero-Cid, M. L. Ruiz-González, J. A. R. Navarro, P. Ocón, F. Zamora, *J. Am. Chem. Soc.* **2017**, *139*, 10079-10086.
53. D. Mullangi, V. Dhavale, S. Shalini, S. Nandi, S. Collins, T. Woo, S. Kurungot, R. Vaidhyanathan, *Adv. Energy Mater.* **2016**, doi: 10.1002/aenm.201600110.
54. H. B. Aiyappa, J. Thote, D. B. Shinde, R. Banerjee, S. Kurungot, *Chem. Mater.* **2016**, *28*, 4375-4379.
55. S. Lin, C. S. Diercks, Y. B. Zhang, N. Kornienko, E. M. Nichols, Y. B. Zhao, A. R. Paris, D. Kim, P. Yang, O. M. Yaghi, C. J. Chang, *Science* **2015**, *349*, 1208-1213.

56. W. Ma, P. Yu, T. Ohsaka, L. Mao, *Electrochem. Commun.* **2015**, *52*, 53-57.
57. X. Zhuang, W. Zhao, F. Zhang, Y. Cao, F. Liu, S. Bi, X. Feng, *Polym. Chem.* **2016**, *7*, 4176-4181.
58. Y.-B. Huang, P. Pachfule, J.-K. Sun, Q. Xu, *J. Mater. Chem. A* **2016**, *4*, 4273-4279.
59. J. Romero, D. Rodriguez-San-Miguel, A. Ribera, R. Mas-Ballesté, T. F. Otero, I. Manet, F. Licio, G. Abellán, F. Zamora, E. Coronado, *J. Mater. Chem. A* **2017**, *5*, 4343-4351.
60. L. Chen, L. Zhang, Z. Chen, H. Liu, R. Luque, Y. Li, *Chem. Sci.* **2016**, *7*, 6015-6020.

**Chapter 2. A Template Strategy to Convert Conventional  
Covalent Organic Frameworks into High-Performance  
Carbons for Capacitors**

*Chemical Communications*, 2017, 53, 11690 – 11693

Q. Xu, Y. Tang, L. Zhai, Q. Chen, and D. Jiang

## **Abstract**

Two-dimensional organic skeletons and one-dimensional porous channels found in covalent organic frameworks (COFs) render them attractive as precursors for designing porous carbon materials. Nevertheless, direct pyrolysis of COFs eventually gives rise to only low active carbons. Here, I describe a general strategy to fabricate core-shell carbons for capacitive energy storage from COFs based on template pyrolysis. COFs were grown as a shell on crosslinked polymer spheres to form a thickness-tunable core-shell structure in which a synergistic structural effect enables the pyrolysis formation of carbons that integrated microporous structure, conductivity, and heteroatom density, which are promising in energy storage fields. The capacitors thus fabricated achieve exceptional capacitance, high-rate charge and discharge, and stable cycle over 10000 times. The results offer a new platform based on COFs for designing high value-added carbons in energy storage and catalysis.

## 2.1 Introduction

Energy storage is necessary for a sustainable development. Capacitors are a class of ideal energy storage devices that possess many advantages such as high power density, short charging time, and long cycle stability. Carbon materials are promising as metal-free electrodes in capacitor.<sup>1</sup> The most widely approach of preparing carbons is via directly pyrolysis precursors such as natural polymers, linear polymers and porous polymer networks. Generally, this decomposition process is uncontrollable, and the structure and properties of the resulting carbons are difficult to be designed. Among them, crystalline materials are unique, because they are able to pre-organize the carbon skeletons, with heteroatoms, or metal species uniformly distribution into well-defined frameworks. For example, metal-organic frameworks (MOFs) have been utilized as precursors for heteroatom-doped carbons, that are useful in energy storage and conversion.<sup>2</sup>

Covalent organic frameworks (COFs), are a unique class of two-dimensional (2D) materials. The most important feature of COFs is the designable, which makes COFs designed and synthesized for different application, including semiconductor, chemical sensor, proton conduction and magnetization.<sup>3-5</sup> Their unique structures are also attractive for designing electrochemical devices for energy storage. Indeed, integration of specific redox-active units into the polygon skeletons allows for the synthesis of redox-active COFs in which electric energy could be stored via redox reactions. However, COFs are usually very low in conductivity.<sup>5</sup> To supplement this drawback, preparation of COFs on conducting substrates, such as carbon nanotube, graphene, and gold, has been investigated for the fabrication of capacitors<sup>5a-d</sup> and batteries.<sup>5e-f</sup>

COFs consist of ordered pores and carbon-rich layers, in which heteroatoms are uniformly distributed in the skeleton and layers. The designable structure and abundant composition render COFs useful as precursors for the pyrolytic synthesis of heteroatom-doped carbons. Recently, COFs have been pyrolyzed into carbons for catalysts and electrochemical catalysts in fuel cells.<sup>6</sup> However, the resulting carbons are not able to maintain their structural and morphology features of COFs. Thus, developing an effective strategy using COFs as precursors for carbon in well-maintained structure is important.

## 2.2 Design and Synthesis of Core-Shell Carbons

Herein, I described a general strategy to prepare porous carbons from conventional COFs based on template method. An imine-linked 2D COF, TAPT-DHTA-COF (Figure 1a) was as a precursor, and polycyclotriphosphazene-co-4,4'-sulfonyldiphenol (PPZS) as the template. As for the template, PPZS spheres are of high heteroatom contents and can be obtained under mild condition.<sup>7</sup> TAPT-DHTA-COF was in-situ condensation of building blocks (TAPT and DHTA), and then coated on the surface of template. The ratio of the building blocks to PPZS was controlled. As a result, TAPT-DHTA-COF<sub>X</sub>@PPZS were successfully synthesized, where X (0.05, 0.1 and 0.2) is the weight ratio between COF and PPZS. (Figure 1b).

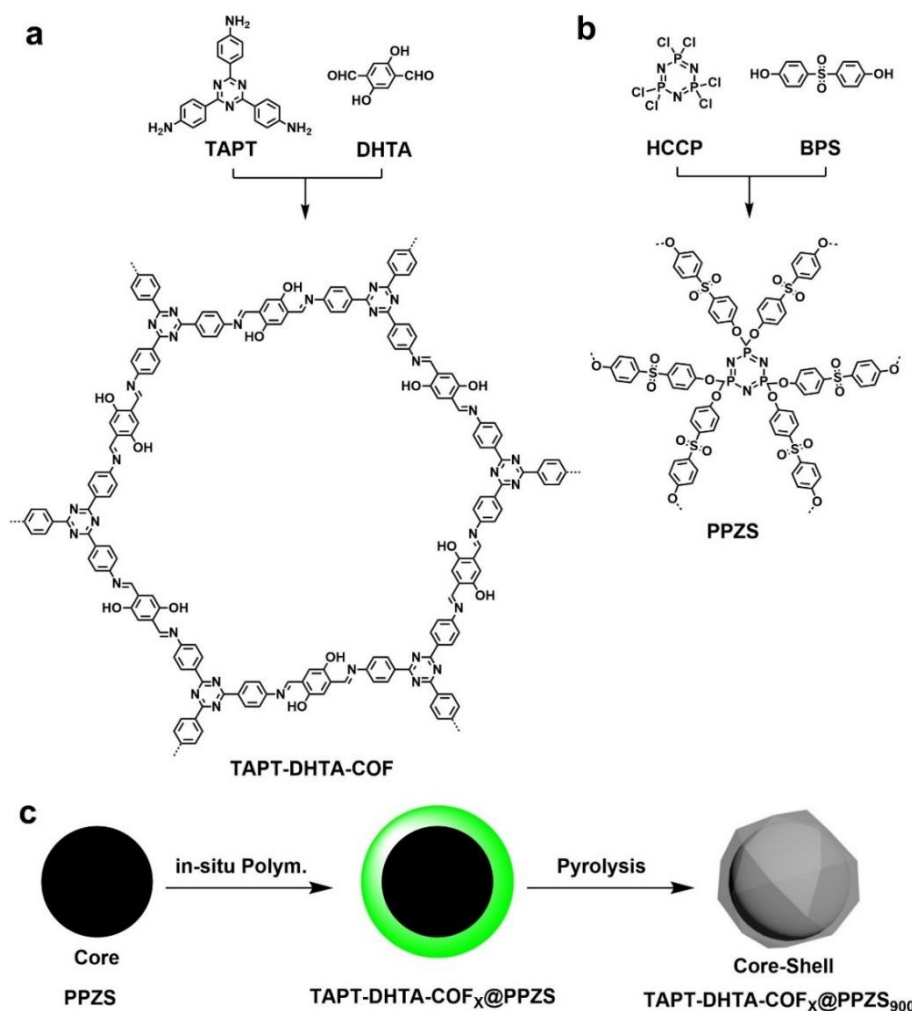


**Figure 1.** Schematic illustration for the synthesis process of TAPT-DHTA<sub>X</sub>-COF@PPZS<sub>900</sub>. a) Synthesis of crosslinked PPZS networks. b) Synthesis of TAPT-DHTA-COF. c) Schematic of the synthesis of TAPT-DHTA-COF<sub>X</sub>@PPZS and their pyrolysis to make TAPT-DHTA-COF<sub>X</sub>@PPZS<sub>900</sub>.

**PPZS Spheres.** TEA (2 mL) was added to a 300-mL round-bottom flask containing a mixture of HCCP (0.80 g), BPS (1.74 g) and acetonitrile (200 mL). The resulting mixture was supersonicated (200 W, 40 kHz) at 40 °C for 5 h. I collected the precipitate by centrifugation, then washed it three times with acetone and deionized water, respectively. The crude product was dried at 50 °C under vacuum for 24 h to give PPZS as a white powder in 92% yield.

**TAPT-DHTA-COF.** First, A mixture of mesitylene/dioxane (0.5 mL/0.5 mL), TAPT (28 mg), DHTA (20 mg), and aqueous acetic acid solution (3 M, 0.2 mL) was added into a Pyrex tube (10 mL). Then I degassed it by freeze-pump-thaw cycles for three times, sealed the tube and kept it at 120 °C for 3 days. I collected the precipitate by filtering, and then subjected to Soxhlet extraction with THF for 24 h, and dried it at 120 °C under vacuum overnight to obtain TAPT-DHTA-COF in 86 % yield.

**TAPT-DHTA-COF<sub>x</sub>@PPZS.** PPZS (30 mg for X = 0.05, 40 mg for X = 0.1, and 50 mg for X = 0.2) was dispersed in dioxane (0.5 mL) in a Pyrex tube (10 mL) and supersonicated for 10 min. The resulted mixture was added with TAPT (4.2 mg) and acetic acid (0.2 mL, 3 M), and then supersonicated for 10 min. DHTA (3 mg) in mesitylene (0.5 mL) was added to the tube, and the mixture was then degassed by freeze-pump-thaw for three cycles. After heating at 120 °C for 3 days, the mixture was cooled at room temperature and the precipitates were collected by centrifugation. The solid was washed with THF and dried at 120 °C under vacuum overnight, to obtain products, TAPT-DHTA-COF<sub>0.2</sub>@PPZS (35.7 mg), TAPT-DHTA-COF<sub>0.1</sub>@PPZS (44.2 mg) and TAPT-DHTA-COF<sub>0.05</sub>@PPZS (52.6 mg) as red powders.

**PPZS<sub>900</sub>, TAPT-DHTA-COF<sub>900</sub>, and TAPT-DHTA-COF<sub>x</sub>@PPZS<sub>900</sub>.** TAPT-DHTA-COF<sub>x</sub>@PPZS (X = 0.05, 0.1, and 0.2; 300 mg), PPZS (300 mg), or TAPT-DHTA-COF (300 mg) samples were heated at a rate of 2 °C min<sup>-1</sup> up to 900 °C and kept at 900 °C for 3 h under nitrogen, to yield TAPT-DHTA-COF<sub>x</sub>@PPZS<sub>900</sub> (X = 0.05; 63 mg, X = 0.1; 96 mg, X = 0.2; 102 mg), PPZS<sub>900</sub> (114 mg), and TAPT-DHTA-COF<sub>900</sub> (165 mg), respectively.

### 2.3 Characterization of Core-Shell Precursors

Powder X-ray diffraction (PXRD) measurements showed that TAPT-DHTA-COF is a crystalline polymer with the most intensive peak at 2.78°, and other five peaks at 4.86, 5.68, 7.48, 9.80, and 26.00°, which were from the (100), (110), (200), (120), (220), and (001) facets, respectively (Figure 2, red curve). The Pawley-refined PXRD curve

(black curve) agreed well with the experimentally observed curve as confirmed by their negligible difference (Figure 2, green curve and Table 4-6).

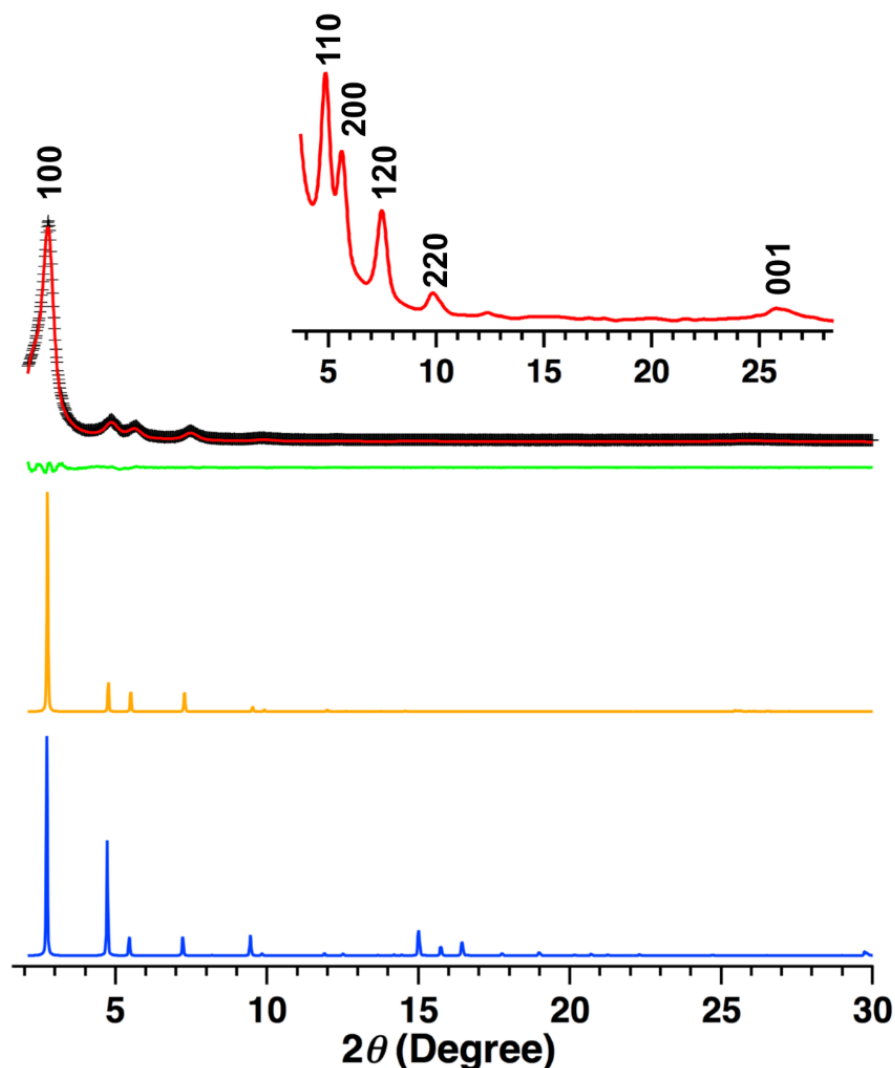


**Figure 2.** Indexed PXRD profiles of TAPT-DHTA-COF of the experimentally observed (red), the Pawley-refined (black), and their difference (green), the simulated using AA stacking model (orange) and AB stacking model (blue).  $R_{WP} = 4.92\%$  and  $R_P = 3.54\%$ .

Different from the high crystallinity of TAPT-DHTA-COF, the PPZS template exhibited no crystallinity. With TAPT-DHTA-COF on the surface of the template, the resulting TAPT-DHTA-COF<sub>x</sub>@PPZS were crystalline hybrids in the presence of crystalline TAPT-DHTA-COF on the surface. The peaks at  $2.78^\circ$  and  $26^\circ$  were in accordance with the (100) and (001) facets of TAPT-DHTA-COF, respectively (Figure 3). These peak positions were the same as those of TAPT-DHTA-COF samples. Thus, all the prepared TAPT-DHTA-COF<sub>x</sub>@PPZS possessed good crystallinity and pore structure.

TAPT-DHTA-COF at 77 K exhibited type-IV sorption isotherm curves, from which the Brunauer–Emmett–Teller (BET) surface area was evaluated to be as high as 2170  $\text{m}^2 \text{g}^{-1}$  (Figure 4a, red curves). It consisted of mesopores with size of 3.1 nm, whereas the pore volume calculated using the nonlocal density functional theory method was 1.08  $\text{cm}^3 \text{g}^{-1}$  (Figure 4b).

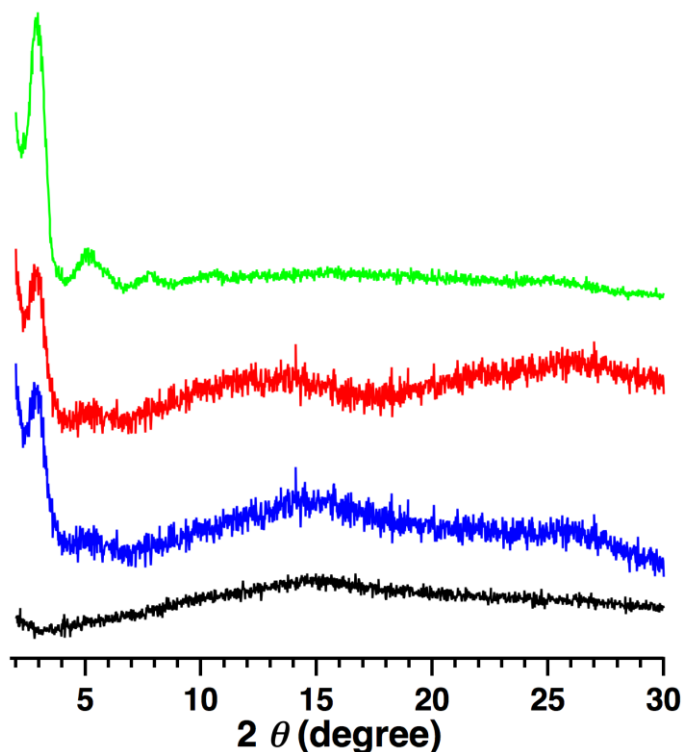


**Figure 3.** PXRD profiles of PPZS (black), TAPT-DHTA-COF<sub>0.05</sub>@PPZS (blue), TAPT-DHTA-COF<sub>0.1</sub>@PPZS (red), and TAPT-DHTA-COF<sub>0.2</sub>@PPZS (green).

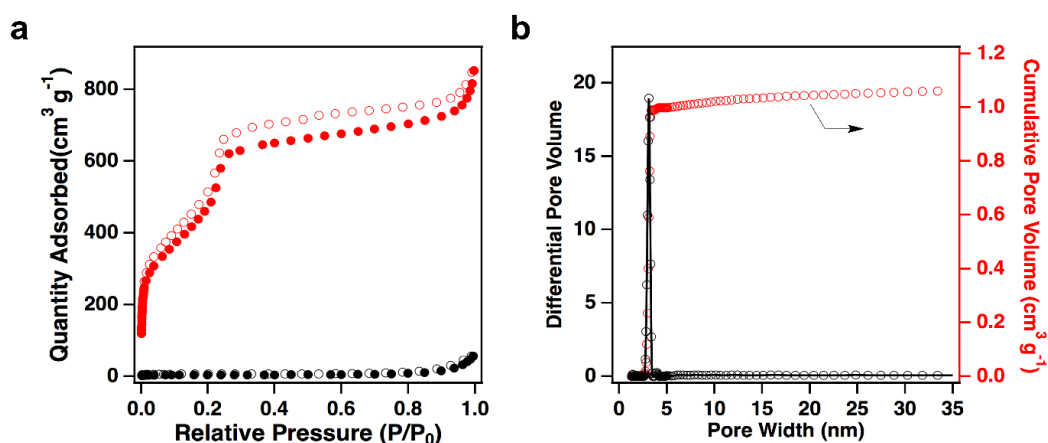


**Figure 4.** a) nitrogen adsorption-desorption isotherms for TAPT-DHTA-COF (red) and TAPT-DHTA-COF<sub>900</sub> (black) at 77 K. b) Pore size distribution curves of TAPT-DHTA-COF.

The presence of TAPT-DHTA-COF shell makes TAPT-DHTA-COF<sub>x</sub>@PPZS possess porous structure. Nitrogen sorption measurements at 77 K revealed that the PPZS spheres were almost nonporous. The corresponding BET surface area was low to 8 m<sup>2</sup> g<sup>-1</sup> (Figure 5a, black dots). Differently, the nitrogen adsorption–desorption isotherms of TAPT-DHTA-COF<sub>x</sub>@PPZS exhibited type-IV sorption curves, indicating mesoporous feature. Clearly, with increasing content of COF-shell, the BET surface areas were increased, which were 57 m<sup>2</sup> g<sup>-1</sup> (X = 0.05), 168 m<sup>2</sup> g<sup>-1</sup> (X = 0.1), and 256 m<sup>2</sup> g<sup>-1</sup> (X = 0.2), respectively. The pore size distribution profiles revealed that TAPT-DHTA-COF<sub>x</sub>@PPZS had similar pore size of 3.1 nm. And the corresponding pore volume was 0.028, 0.065, 0.147 cm<sup>3</sup> g<sup>-1</sup> (Figure 5b).

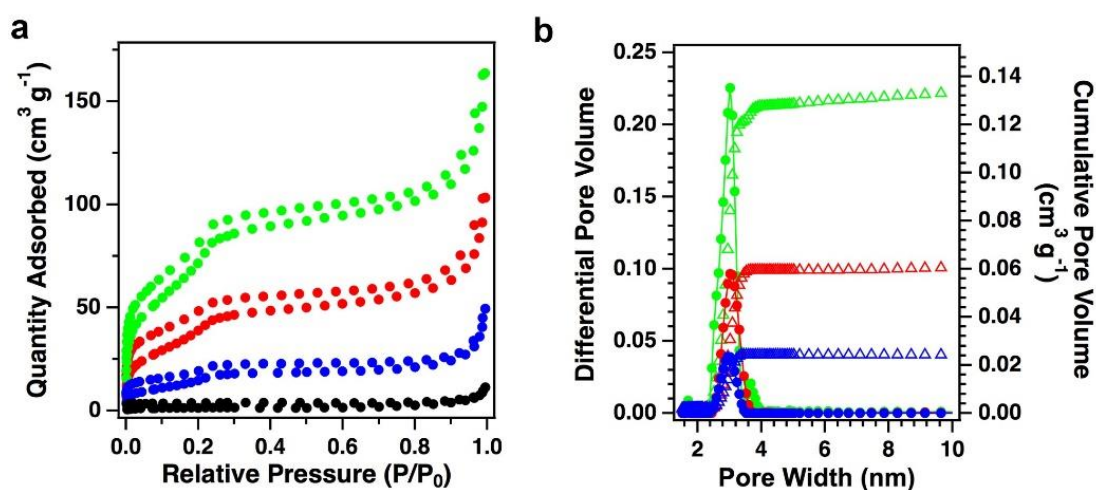


**Figure 5.** a) Nitrogen adsorption–desorption isotherms and b) pore size distribution profiles of PPZS (black), TAPT-DHTA-COF<sub>0.05</sub>@PPZS (blue), TAPT-DHTA-COF<sub>0.1</sub>@PPZS (red), and TAPT-DHTA-COF<sub>0.2</sub>@PPZS (green).

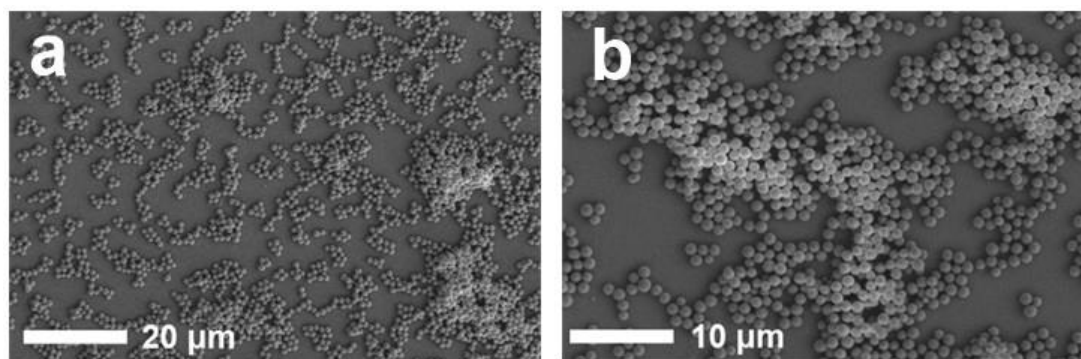


**Figure 6.** FE-SEM images of PPZS at different areas and magnifications.

The morphology of the PPZS was investigated by the Field-emission scanning electron microscopy (FE-SEM, Figure 6) images. PPZS was uniform sphere with smooth surface, and the diameters was from 830 to 1200 nm. TAPT-DHTA-COF was

in a ribbon shape (Figure 7). By contrast, with TAPT-DHTA-COF coating on PPZS yielded spheres (Figure 8), and almost no ribbon-shaped TAPT-DHTA-COF objects were observable. Different from PPZS and bulky TAPT-DHTA-COF, TAPT-DHTA-COF<sub>x</sub>@PPZS displayed spherical morphology but with quite rough surface and diameters increased by 100-200 nm compared to PPZS. These results reflected that TAPT-DHTA-COF was successfully coated on the surface of the spheres. Additionally, the surface of TAPT-DHTA-COF<sub>x</sub>@PPZS was different from that of PPZS. The surface was quite rough, which may be caused by the 2D extended hexagonal polygon nature of the COF.

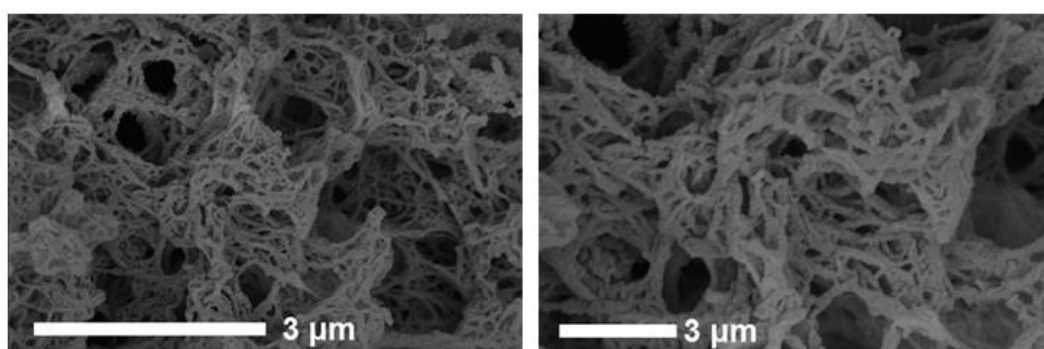


**Figure 7.** FE-SEM images of TAPT-DHTA-COF at different areas and magnifications.

From Infrared spectroscopy, the vibration bands at  $1490\text{ cm}^{-1}$  observed for TAPT-DHTA-COF<sub>x</sub>@PPZS were much broader than that of the PPZS (Figure 9), which was from the combination of two bands in TAPT-DHTA-COF<sub>x</sub>@PPZS; the band at  $1490\text{ cm}^{-1}$  was from the phenyl C=C bond of the PPZS, and another band at  $1514\text{ cm}^{-1}$  was from the phenyl C=C bond of the COF skeleton. In addition, the intensity ratio between bands at  $1302\text{ cm}^{-1}$  and  $1367\text{ cm}^{-1}$  assigned to C–O bond and C–N bond in triazine was clearly enhanced for TAPT-DHTA-COF<sub>x</sub>@PPZS.

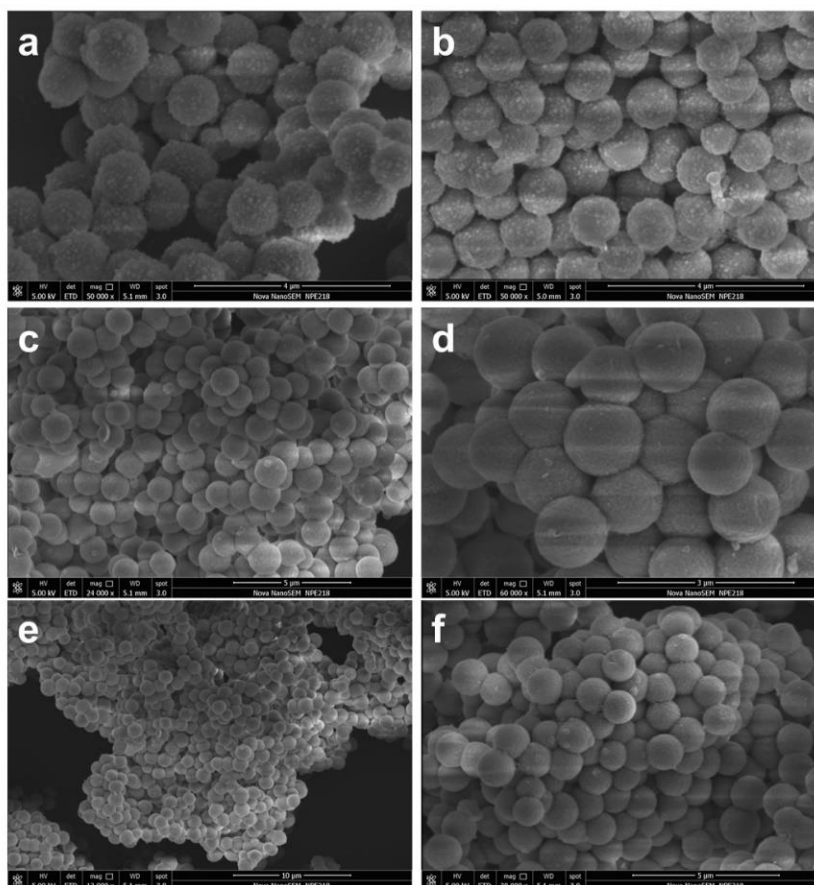


**Figure 8.** FE-SEM images of a, b) TAPT-DHTA-COF<sub>0.2</sub>@PPZS, c, d) TAPT-DHTA-COF<sub>0.1</sub>@PPZS, and e, f) TAPT-DHTA-COF<sub>0.05</sub>@PPZS at different areas and magnifications.

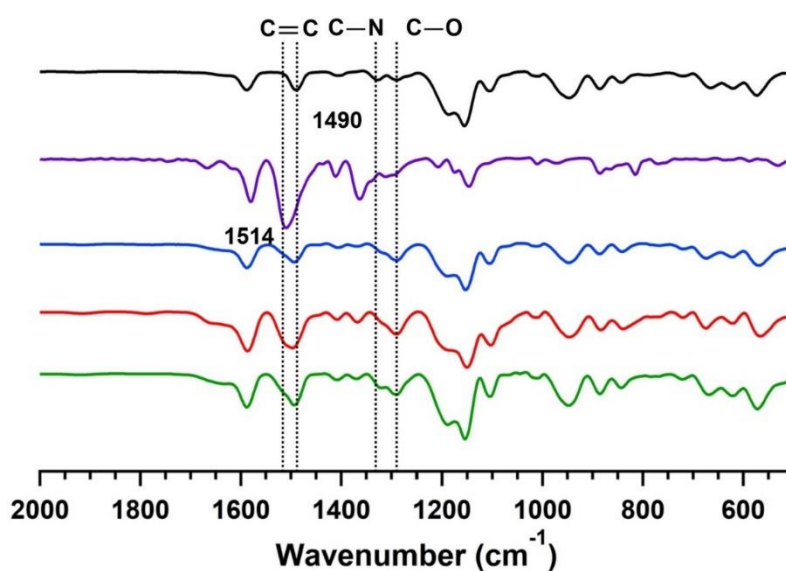


**Figure 9.** FT IR spectra of PPZS (black curve), TAPT-DHTA-COF (purple curve), TAPT-DHTA-COF<sub>0.05</sub>@PPZS (blue curve), TAPT-DHTA-COF<sub>0.1</sub>@PPZS (red curve) and TAPT-DHTA-COF<sub>0.2</sub>@PPZS (green curve).

## 2.4 Characterization of Core-Shell Carbons

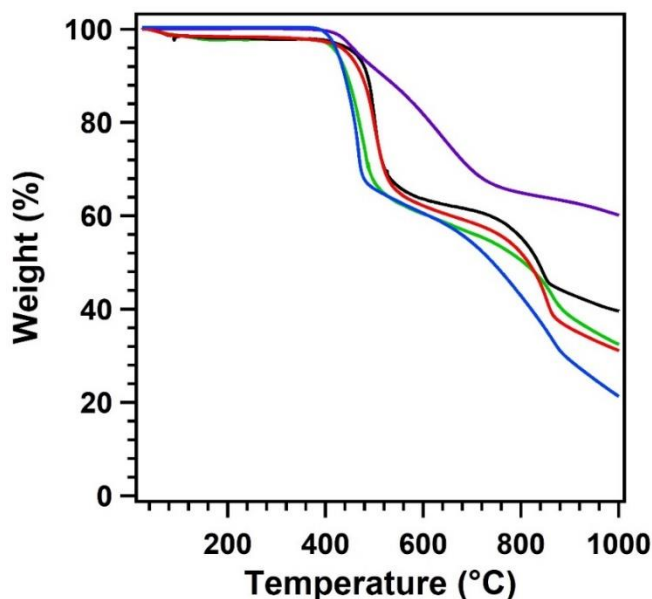


**Figure 10.** TGA curves of PPZS (black), TAPT-DHTA-COF (purple), TAPT-DHTA-COF<sub>0.05</sub>@PPZS (blue), TAPT-DHTA-COF<sub>0.1</sub>@PPZS (red) and TAPT-DHTA-COF<sub>0.2</sub>@PPZS (green).

From thermogravimetric analysis (TGA) results, a lot decomposition of PPZS and TAPT-DHTA-COF<sub>x</sub>@PPZS observed before 900 °C under nitrogen, thus, the precursors were carbonization at 900 °C (Figure 10). At 900 °C, the weight loss of TAPT-DHTA-COF<sub>x</sub>@PPZS were 60%-70%. With thermal treatment at 900 °C under nitrogen, TAPT-DHTA-COF<sub>x</sub>@PPZS were transformed into its corresponding carbons, namely TAPT-DHTA-COF<sub>x</sub>@PPZS<sub>900</sub> in yields of 34% (X = 0.2), 32% (X = 0.1), and 21% (X = 0.05) (Figure 1c). As controls, by direct pyrolysis of PPZS and TAPT-DHTA-COF under the same conditions resulted in PPZS<sub>900</sub> and TAPT-DHTA-COF<sub>900</sub> in 38% and 55% yields, respectively.

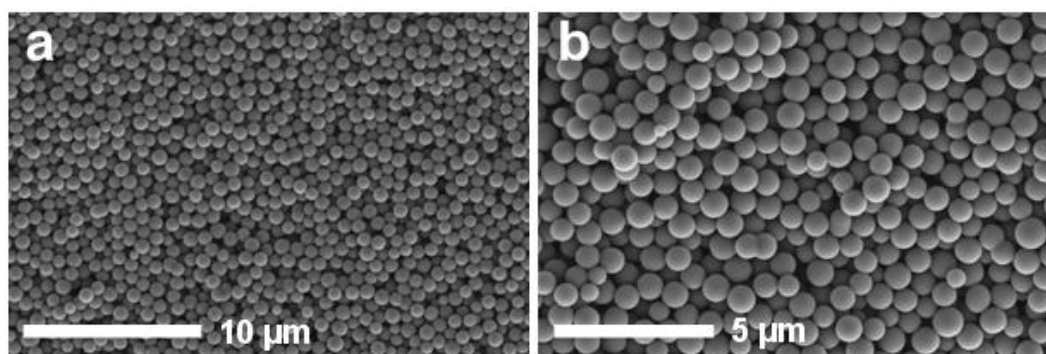


**Figure 11.** FE-SEM images of PPZS<sub>900</sub> at different magnification scales.

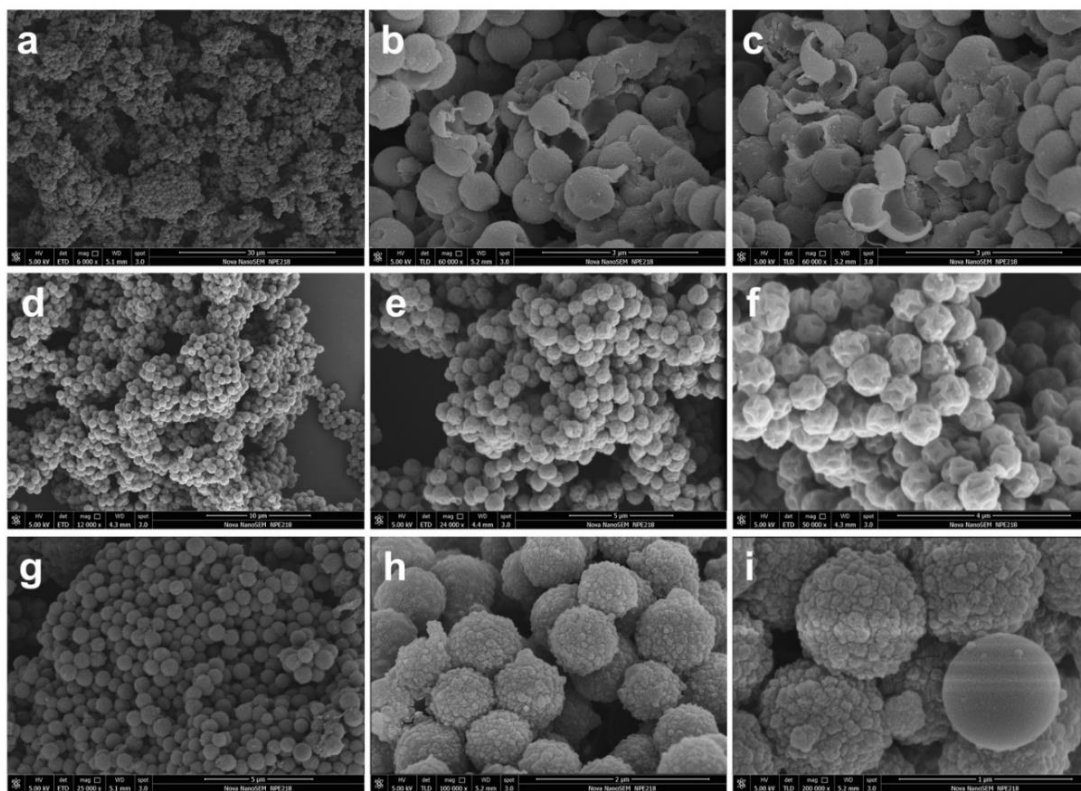


**Figure 12.** FE-SEM images of a-c) TAPT-DHTA-COF<sub>0.05</sub>@PPZS<sub>900</sub>, d-f) TAPT-DHTA-COF<sub>0.1</sub>@PPZS<sub>900</sub>, and g-i) TAPT-DHTA-COF<sub>0.2</sub>@PPZS<sub>900</sub>.

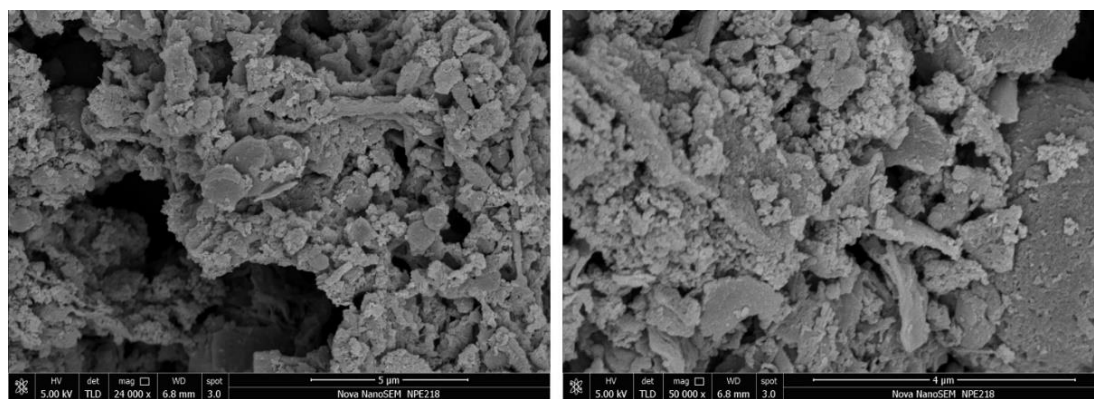


**Figure 13.** FE-SEM images of TAPT-DHTA-COF<sub>900</sub>.

PPZS<sub>900</sub> remained the sphere morphology, whereas the diameters was reduced to 600-830 nm (Figure 11). However, the morphology of the core-shell products was different with different thickness of the COF shell. For TAPT-DHTA-COF<sub>0.05</sub>@PPZS<sub>900</sub>, the shells were too thin to protect the core effectively, which were broken into fragments under thermal treatment (Figure 12 a-c). For TAPT-DHTA-COF<sub>0.1</sub>@PPZS<sub>900</sub>, the morphology changed into a nuts-like sphere (Figure 12 d-e). When the COF shell became further thicker, the surface of TAPT-DHTA-COF<sub>0.2</sub>@PPZS<sub>900</sub> was much smoother (Figure 12g-i). By contrast, TAPT-DHTA-

COF<sub>900</sub> was in aggregated bulks, and its original ribbon shape was totally collapsed (Figure 13).

The pore structure of TAPT-DHTA-COF was totally broken, the resultant carbon possessed nonporous structure, with a BET surface area of 21 m<sup>2</sup> g<sup>-1</sup> (Figure 4a, black). This is in a sharp decline of the TAPT-DHTA-COF precursor (2170 m<sup>2</sup> g<sup>-1</sup>), which was in accordance with morphology change. Otherwise, the product of direct pyrolysis of PPZS (PPZS<sub>900</sub>) achieved a high BET surface area of 609 m<sup>2</sup> g<sup>-1</sup> (Figure 14a, black). From the pore size distribution profiles, PPZS<sub>900</sub> had three different micropores with sizes of 0.77, 1.12, and 1.52 nm (Figure 14b, black) and pore volume of 0.26 cm<sup>3</sup> g<sup>-1</sup> (Figure 15). For the core-shell structure, the BET surface areas of TAPT-DHTA-COF<sub>0.05</sub>@PPZS<sub>900</sub> (blue), TAPT-DHTA-COF<sub>0.1</sub>@PPZS<sub>900</sub> (red), and TAPT-DHTA-COF<sub>0.2</sub>@PPZS<sub>900</sub> (green) were 533, 456 and 421 m<sup>2</sup> g<sup>-1</sup> respectively (Table 1). From the pore size distribution curves (Figure 14b, X = 0.05; blue, X = 0.1; red, and X = 0.2; green), TAPT-DHTA-COF<sub>X</sub>@PPZS<sub>900</sub> possessed only microporous structure, with pore size between 0.5 and 1.5 nm. The pore volumes of TAPT-DHTA-COF<sub>X</sub>@PPZS<sub>900</sub> exhibited decrease from 0.25, 0.22, and 0.20 cm<sup>3</sup> g<sup>-1</sup> (Figure 15) with increasing COF-carbon shell. From the pore structure analysis, higher COF content resulted in lower BET surface areas and smaller pore volume.

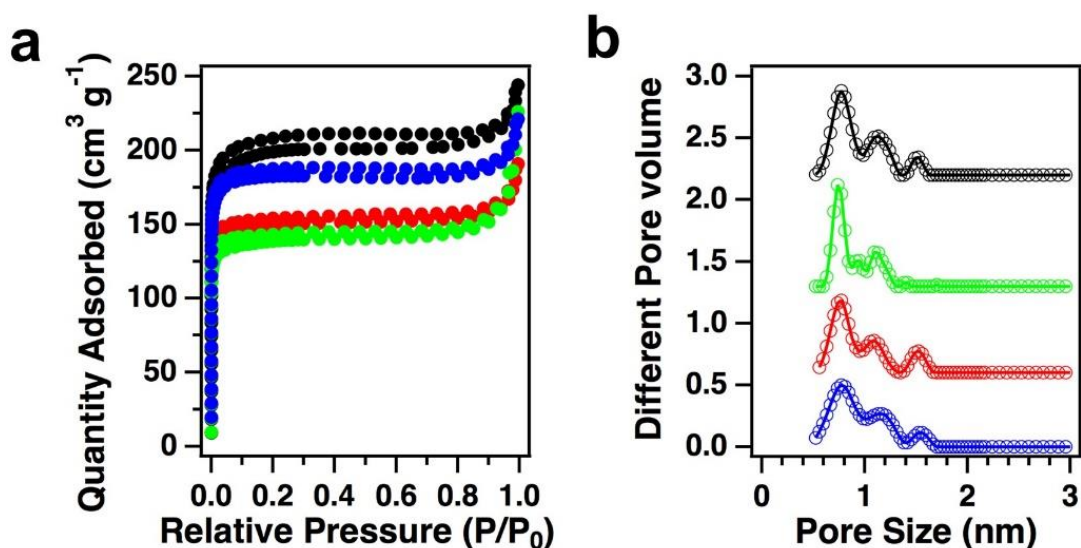


**Figure 14.** a) Nitrogen sorption isotherms, and b) pore size distribution profiles of PPZS<sub>900</sub> (black), TAPT-DHTA-COF<sub>0.05</sub>@PPZS<sub>900</sub> (blue), TAPT-DHTA-COF<sub>0.1</sub>@PPZS<sub>900</sub> (red), and TAPT-DHTA-COF<sub>0.2</sub>@PPZS<sub>900</sub> (green).

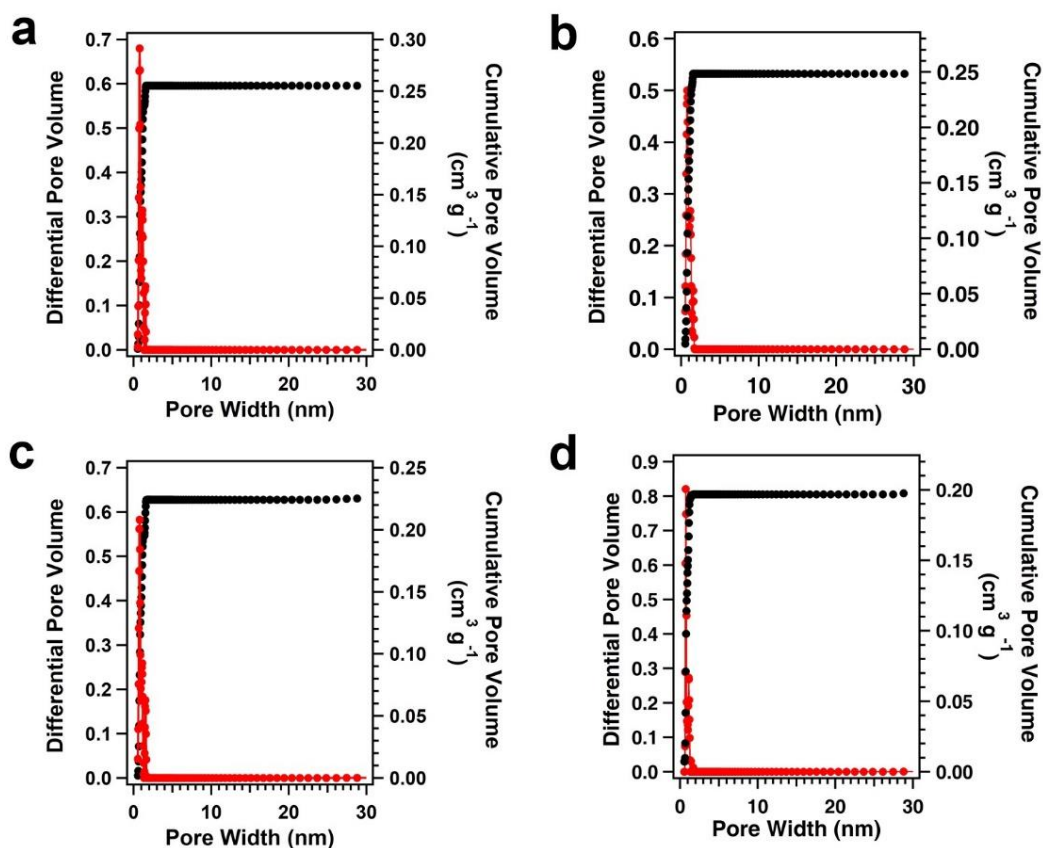


**Figure 15.** Pore size and distribution curves of a) PPZS<sub>900</sub>, b) TAPT-DHTA-COF<sub>0.05</sub>@PPZS<sub>900</sub>, c) TAPT-DHTA-COF<sub>0.1</sub>@PPZS<sub>900</sub>, and d) TAPT-DHTA-COF<sub>0.2</sub>@PPZS<sub>900</sub>.

**Table 1.** Pore structure of prepared materials.

Samples	BET surface areas (m <sup>2</sup> g <sup>-1</sup> )	Pore volume (cm <sup>3</sup> g <sup>-1</sup> )
TAPT-DHTA-COF <sub>0.05</sub> @PPZS	57	0.028
TAPT-DHTA-COF <sub>0.1</sub> @PPZS	156	0.065
TAPT-DHTA-COF <sub>0.2</sub> @PPZS	290	0.147
PPZS <sub>900</sub>	607	0.26
TAPT-DHTA-COF <sub>0.05</sub> @PPZS <sub>900</sub>	533	0.25
TAPT-DHTA-COF <sub>0.1</sub> @PPZS <sub>900</sub>	456	0.22
TAPT-DHTA-COF <sub>0.2</sub> @PPZS <sub>900</sub>	421	0.2

The chemical structure of the porous carbons was then investigated by Raman spectra. From Raman spectra, the D bands of TAPT-DHTA-COF<sub>x</sub>@PPZS<sub>900</sub> and PPZS<sub>900</sub> at 1347 cm<sup>-1</sup>, were from disordered carbons, whereas the G bands at 1601 cm<sup>-1</sup>, were assigned to ordered graphitic carbons (Figure 16). With increasing thickness of the shell, the corresponding intensity ratio of  $I_D/I_G$  for TAPT-DHTA-COF<sub>x</sub>@PPZS<sub>900</sub> was 1.04, 0.98, and 0.96, respectively. Thus, TAPT-DHTA-COF shell thickness resulted in higher degree of graphitization during pyrolysis. Notably, PPZS<sub>900</sub> exhibited a low graphitization, confirmed by a high  $I_D/I_G$  value (1.10). These results indicate that the COF-derived carbon shell promotes the formation of graphitic carbon, contributing to a good electrical conductivity as electrodes.<sup>8</sup>

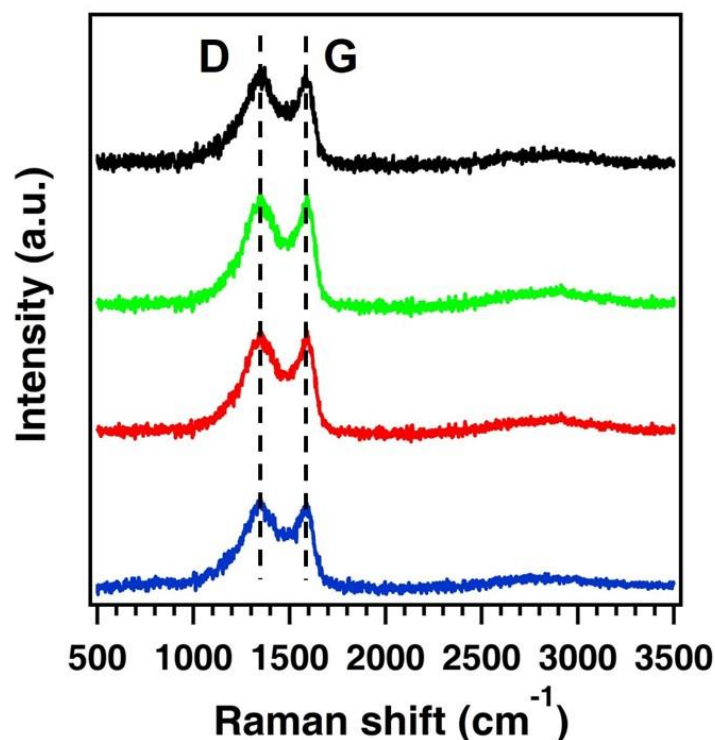


**Figure 16.** Raman spectra of PPZS<sub>900</sub> (black), TAPT-DHTA-COF<sub>0.05</sub>@PPZS<sub>900</sub> (blue), TAPT-DHTA-COF<sub>0.1</sub>@PPZS<sub>900</sub> (red), and TAPT-DHTA-COF<sub>0.2</sub>@PPZS<sub>900</sub> (green).

The chemical nature of hybrid carbons was further investigated by X-ray photoelectron spectroscopy (XPS). The peaks from C1s, N1s, O1s, S2p, and P2p, were clearly observed (Figure 17).<sup>9</sup> As shown in Table 2, the XPS analysis displayed that the ratio of heteroatoms (O, N, S, and P) was 12.38%, 12.21% and 7.37% for TAPT-DHTA-COF<sub>0.2</sub>@PPZS<sub>900</sub>, TAPT-DHTA-COF<sub>0.1</sub>@PPZS<sub>900</sub>, and TAPT-DHTA-COF<sub>0.05</sub>@PPZS<sub>900</sub>, which was higher than those of PPZS<sub>900</sub> (5.66%) and TAPT-DHTA-COF<sub>900</sub> (4.08%), respectively.

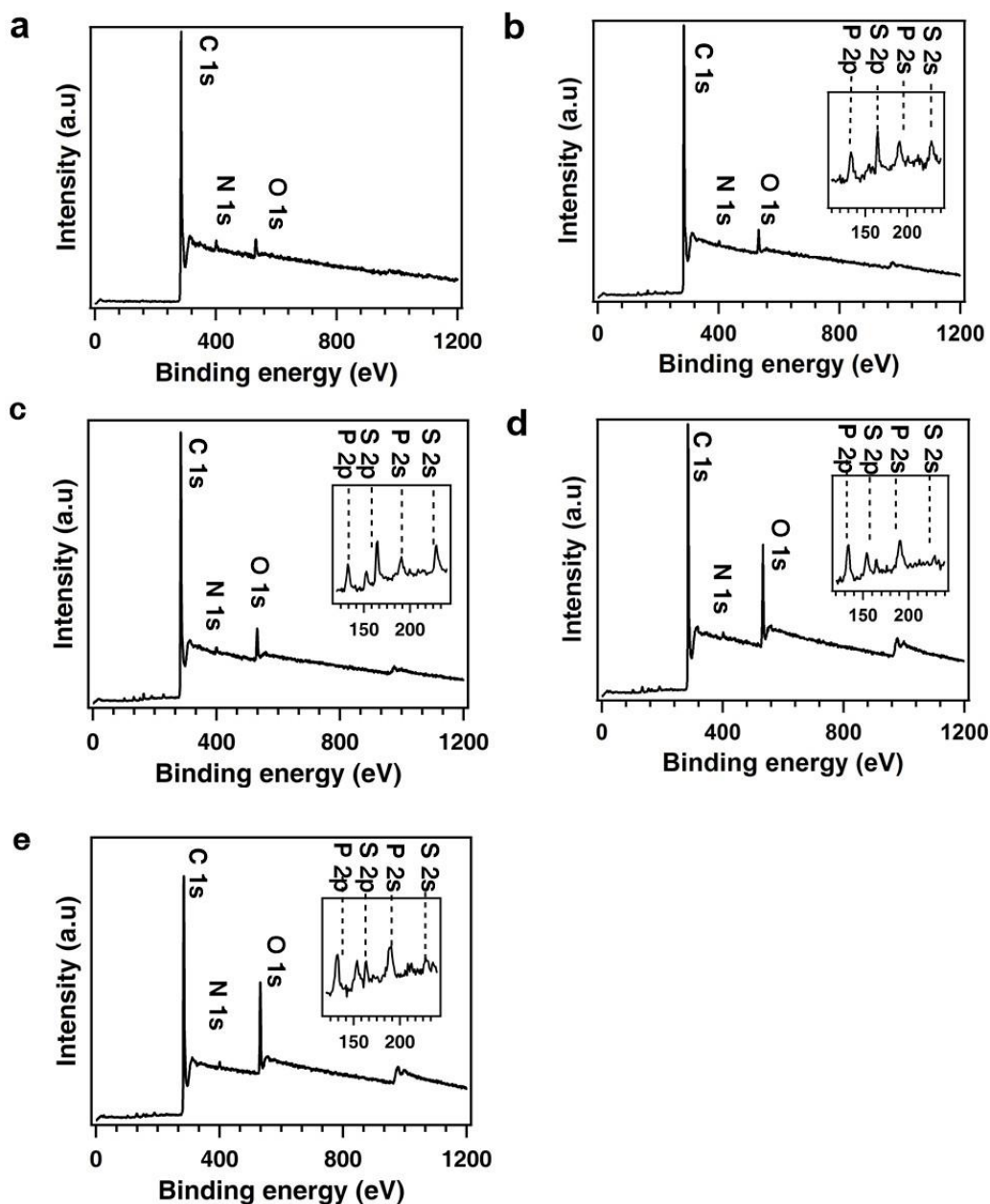


**Figure 17.** XPS pattern curves of a) TAPT-DHTA-COF<sub>900</sub>, b) PPZS<sub>900</sub>, c) TAPT-DHTA-COF<sub>0.05</sub>@PPZS<sub>900</sub>, d) TAPT-DHTA-COF<sub>0.1</sub>@PPZS<sub>900</sub> and e) TAPT-DHTA-COF<sub>0.2</sub>@PPZS<sub>900</sub>.

Thanks to the important roles of COF shell, the heteroatoms of PPZS bind with the COF shell during pyrolysis process, which leads to decrease the loss of heteroatoms effectively. And the broken shell of TAPT-DHTA-COF<sub>0.05</sub>@PPZS<sub>900</sub> leads to lower heteroatoms ratios. The XPS results were in correspondence with the observed FE-SEM morphology. Thus, the suitable COF-shell content is important: lower COF content leads to high surface areas and pore volume, but results in low heteroatom content, whereas higher COF content results to high heteroatom content and low pore volume.

**Table 2.** Elemental contents of PPZS<sub>900</sub>, TAPT-DHTA-COF<sub>900</sub>, TAPT-DHTA-COF<sub>0.05</sub>@PPZS<sub>900</sub>, TAPT-DHTA-COF<sub>0.1</sub>@PPZS<sub>900</sub>, and TAPT-DHTA-COF<sub>0.2</sub>@PPZS<sub>900</sub> according to the XPS analysis.

Samples	C at%	O at%	N at%	S at%	P at%
TAPT-DHTA-COF <sub>900</sub>	95.92	2.17	1.91	0	0
PPZS <sub>900</sub>	94.34	3.02	1.55	0.4	0.7
TAPT-DHTA-COF <sub>0.05</sub> @PPZS <sub>900</sub>	92.63	3.91	2.02	0.79	0.64
TAPT-DHTA-COF <sub>0.1</sub> @PPZS <sub>900</sub>	87.79	9.64	1.37	0.21	0.99
TAPT-DHTA-COF <sub>0.2</sub> @PPZS <sub>900</sub>	87.62	9.89	1.29	0.23	0.97

## 2.4 Capacitive Energy Storage Performance of Carbons

Adequate pore size (between 0.5 to 2 nm), high heteroatom content, and unique structure are key points to obtain high value of capacitance. Hence, the prepared TAPT-DHTA-COF<sub>x</sub>@PPZS<sub>900</sub>, hold promise for its application in electrochemical capacitors. The capacitive energy storage performance of these carbons as electrodes was evaluated in an aqueous alkaline solution (6 M KOH) by a three-electrode system. Cyclic voltammetry (CV) measurement was first conducted at a scan rate of 50 mV s<sup>-1</sup>. At -1 V, the current density of PPZS<sub>900</sub> (black curve) and TAPT-DHTA-COF<sub>900</sub> (Figure 18a, purple curve) was only 4.8 and 2.1 A g<sup>-1</sup> respectively. For the core-shell carbon materials, the current density was related with the thickness of the carbon shell. TAPT-DHTA-COF<sub>x</sub>@PPZS<sub>900</sub> exhibited a typical double layer capacitive behavior with a high current density of 7.5, 11.1 and 9.7 A g<sup>-1</sup> with X increasing from 0.05, 0.1 to 0.2. The higher current density indicated enhanced capacitive energy storage ability. Among the prepared carbons, the current density of TAPT-DHTA-COF<sub>0.1</sub>@PPZS<sub>900</sub> was the highest at different scan rates (Figure 19), indicating the best electrochemical capacitive energy storage ability.

In accordance with the changes of current density, the specific capacitance of carbon is also related to the core-shell structure (Figure 18b). The specific capacitance was obtained at different current density by galvanostatic charge/discharge method. At a current density of 1 A g<sup>-1</sup>, the specific capacitance of TAPT-DHTA-COF<sub>0.05</sub>@PPZS<sub>900</sub> was 178 F g<sup>-1</sup>, which was much higher than those of PPZS<sub>900</sub> (132 F g<sup>-1</sup>) and TAPT-DHTA-COF<sub>900</sub> (43.8 F g<sup>-1</sup>). Notably, the specific capacitance of TAPT-DHTA-

COF<sub>0.1</sub>@PPZS<sub>900</sub> achieved high to 287 F g<sup>-1</sup>, about 6.6 and 2.2 times of and TAPT-DHTA-COF<sub>900</sub> and PPZS<sub>900</sub>, respectively. And the specific capacitance of TAPT-DHTA-COF<sub>0.2</sub>@PPZS<sub>900</sub> was 255 F g<sup>-1</sup>. Moreover, the capacitance increased significantly with the decreased current density of 0.5 A g<sup>-1</sup>. The corresponding capacitance of TAPT-DHTA-COF<sub>0.1</sub>@PPZS<sub>900</sub> was high to 411 F g<sup>-1</sup> (Figure 18c). The capacitive performance was better than the COF-based and state-of-the-art carbon based capacitors (Table 3).

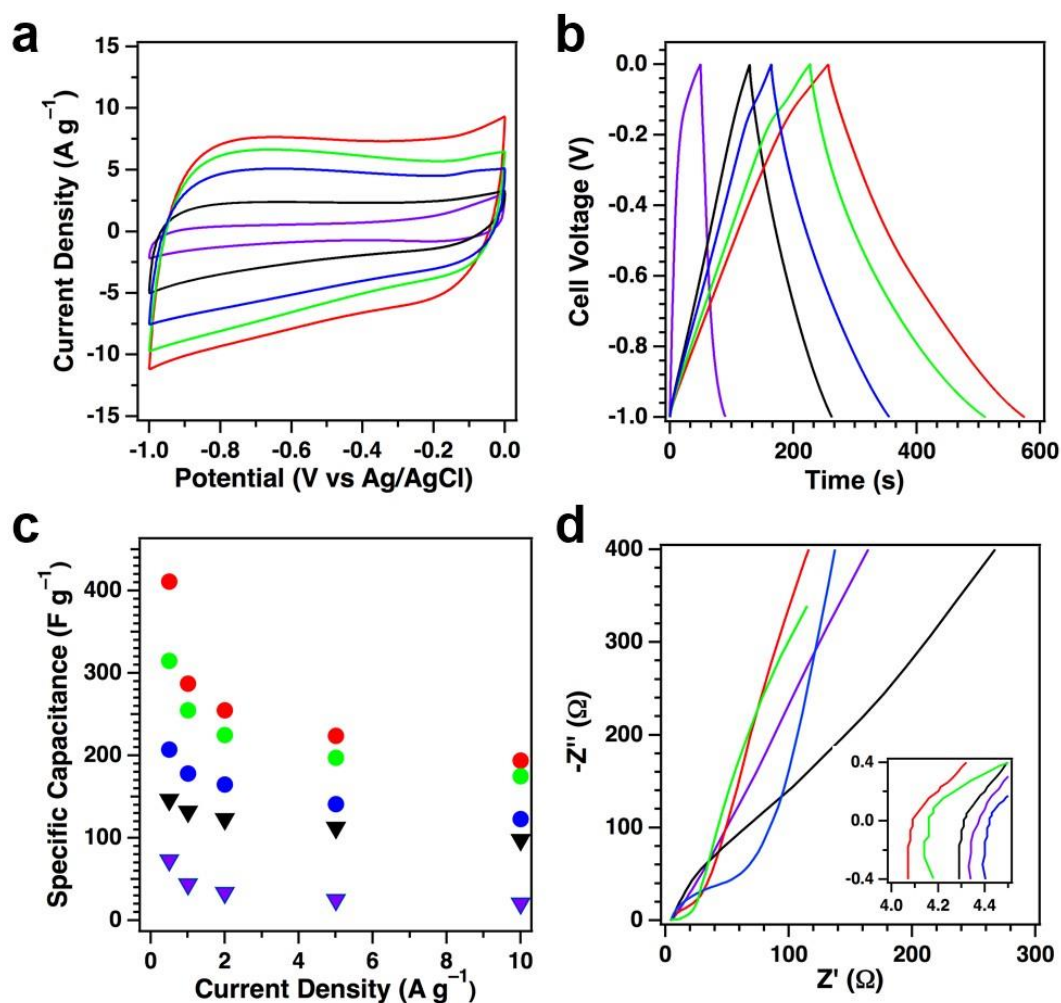


**Figure 18.** a) CV curves at 50 mV s<sup>-1</sup>, b) galvanostatic charge/discharge curves at 1 A g<sup>-1</sup>, c) capacitance at different current densities, and d) Nyquist plots of PPZS<sub>900</sub> (black), and TAPT-DHTA-COF<sub>900</sub> (purple), TAPT-DHTA-COF<sub>0.05</sub>@PPZS<sub>900</sub> (blue), TAPT-DHTA-COF<sub>0.1</sub>@PPZS<sub>900</sub> (red), TAPT-DHTA-COF<sub>0.2</sub>@PPZS<sub>900</sub> (green). Inset in (d) is enlarged semicircles.

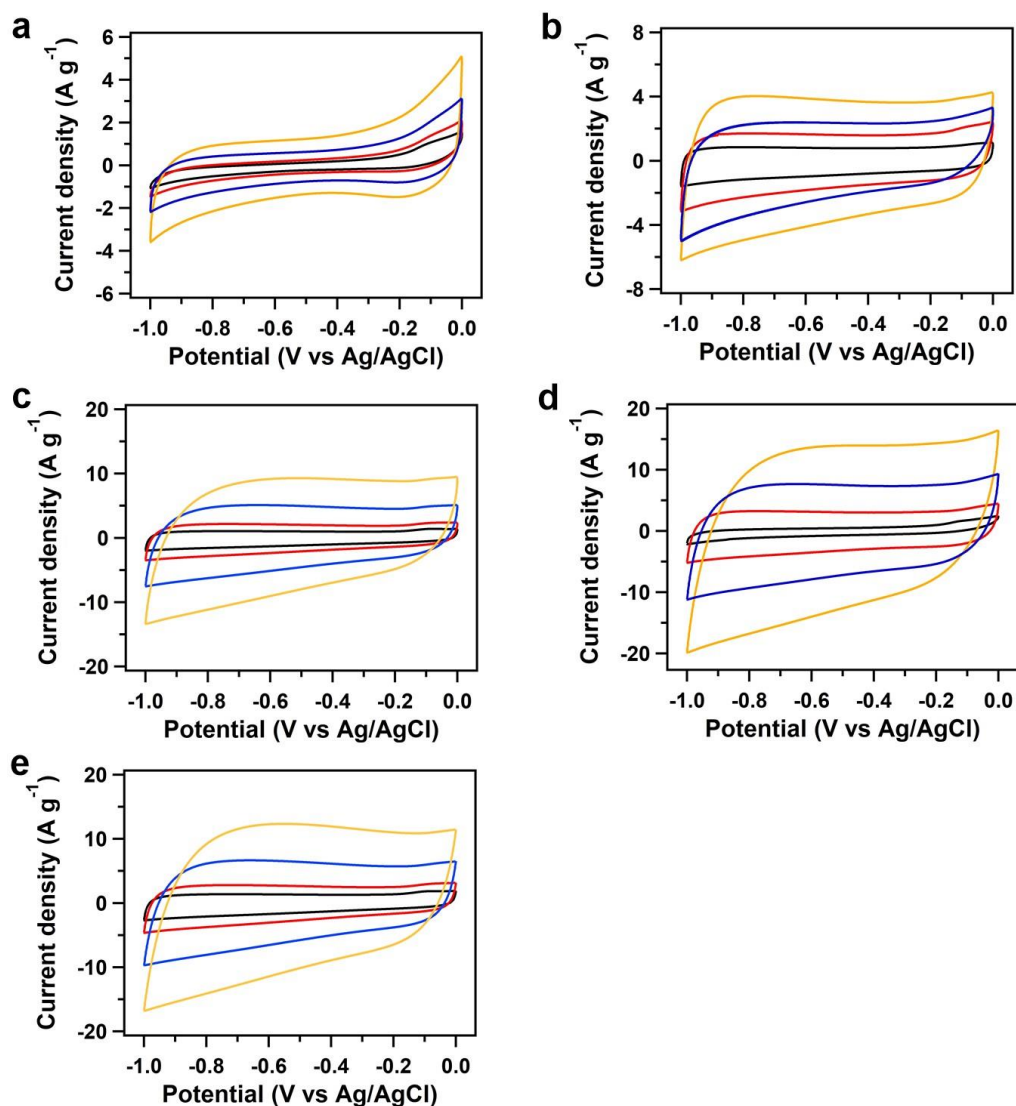


**Figure 19.** CV curves of a) TAPT-DHTA-COF<sub>900</sub>, b) PPZS<sub>900</sub>, c) TAPT-DHTA-COF<sub>0.05</sub>@PPZS<sub>900</sub>, d) TAPT-DHTA-COF<sub>0.1</sub>@PPZS<sub>900</sub> and e) TAPT-DHTA-COF<sub>0.2</sub>@PPZS<sub>900</sub> at different scan rates of 10 (black), 20 (red), 50 (blue) and 100 mV s<sup>-1</sup> (yellow).

High-rate performance revealed that TAPT-DHTA-COF<sub>0.1</sub>@PPZS<sub>900</sub> had capacitances of 235, 207, and 182 F g<sup>-1</sup> at different current densities of 2, 5, and 10 A g<sup>-1</sup>, respectively (Figure 18c, red circles). And TAPT-DHTA-COF<sub>0.2</sub>@PPZS<sub>900</sub> and TAPT-DHTA-COF<sub>0.05</sub>@PPZS<sub>900</sub> had the capacitance of 225 and 165 F g<sup>-1</sup> at 2 A g<sup>-1</sup>, 175 and 123 F g<sup>-1</sup> at 10 A g<sup>-1</sup>. In contrast, TAPT-DHTA-COF<sub>900</sub> (black circles) and PPZS<sub>900</sub> (blue circles) exhibited the capacitance of only 13.5 and 65 F g<sup>-1</sup>, respectively, at the same current density. Therefore, the resultant TAPT-DHTA-COF<sub>x</sub>@PPZS<sub>900</sub> exhibited better capacitive energy storage performance than PPZS<sub>900</sub> and TAPT-DHTA-COF<sub>900</sub>. Especially, TAPT-DHTA-COF<sub>0.1</sub>@PPZS<sub>900</sub> had a capacitance of

280% and 1350% enhancement as high as those of PPZS<sub>900</sub> and TAPT-DHTA-COF<sub>900</sub> at 10 A g<sup>-1</sup>.

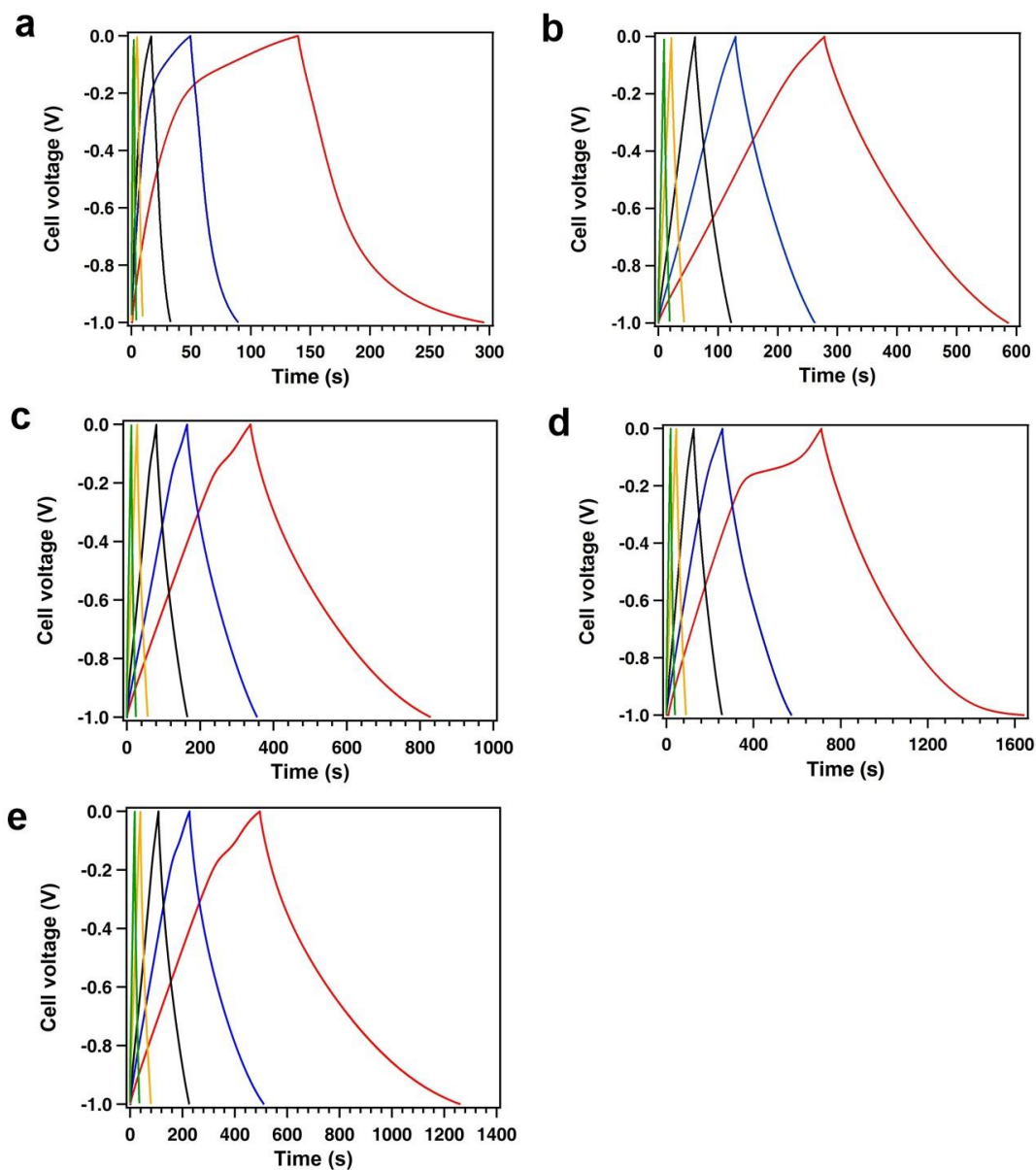


**Figure 20.** Galvanostatic charge-discharge curves of a) TAPT-DHTA-COF<sub>900</sub>, b) PPZS<sub>900</sub>, c) TAPT-DHTA-COF<sub>0.05</sub>@PPZS<sub>900</sub>, d) TAPT-DHTA-COF<sub>0.1</sub>@PPZS<sub>900</sub> and e) TAPT-DHTA-COF<sub>0.2</sub>@PPZS<sub>900</sub> at different current densities of 0.5 A g<sup>-1</sup> (red), 1 A g<sup>-1</sup> (blue), 2 A g<sup>-1</sup> (black), 5 A g<sup>-1</sup> (yellow) and 10 A g<sup>-1</sup> (green).

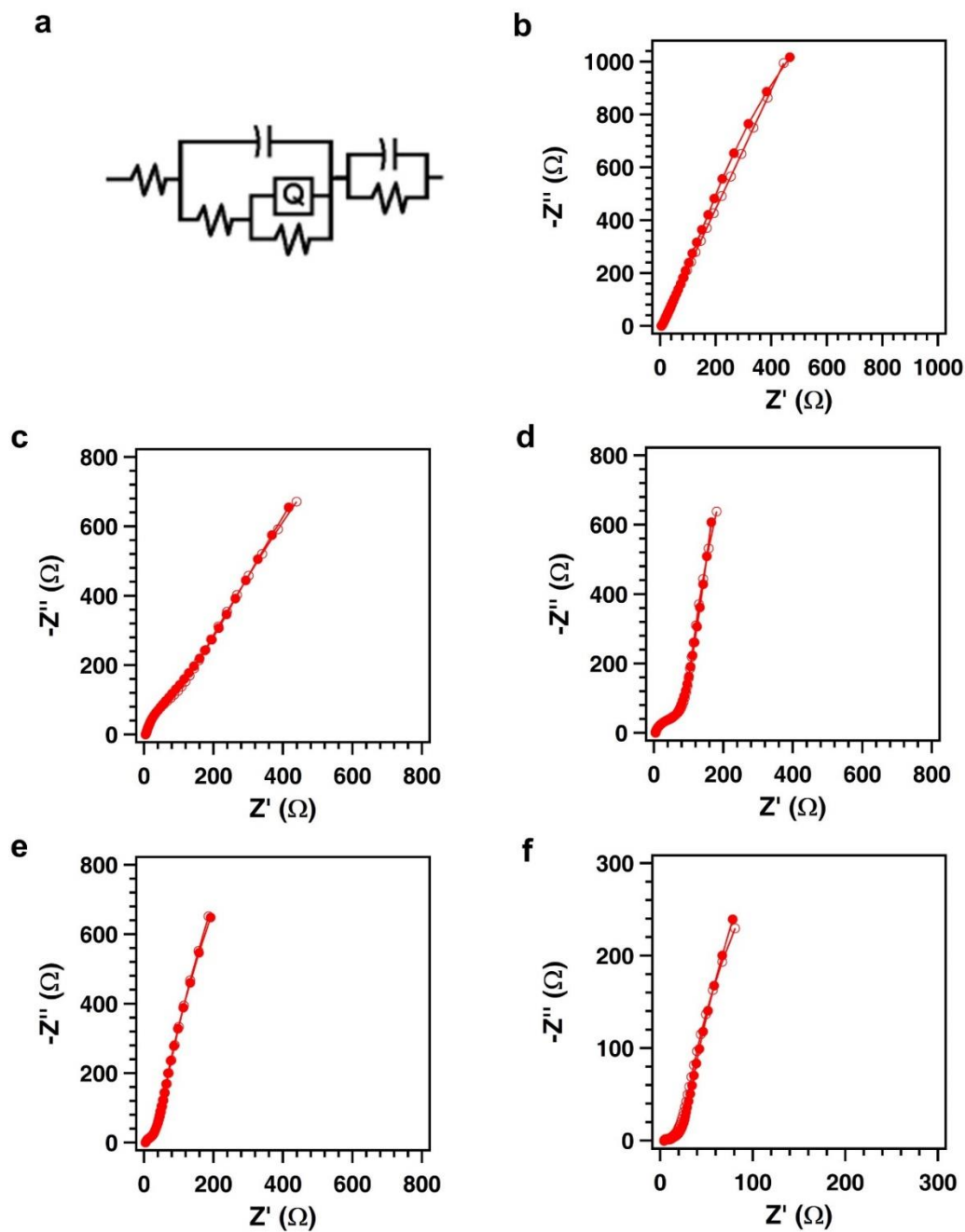


**Figure 21.** a) Equivalent circuit of the supercapacitors. Impedance spectra of supercapacitors based on b) TAPT-DHTA-COF<sub>900</sub>, c) PPZS<sub>900</sub>, d) TAPT-DHTA-COF<sub>0.05</sub>@PPZS<sub>900</sub>, e) TAPT-DHTA-COF<sub>0.1</sub>@PPZS<sub>900</sub>, and f) TAPT-DHTA-COF<sub>0.2</sub>@PPZS<sub>900</sub> (filled dots are the experiment data and open dots are the simulated data).

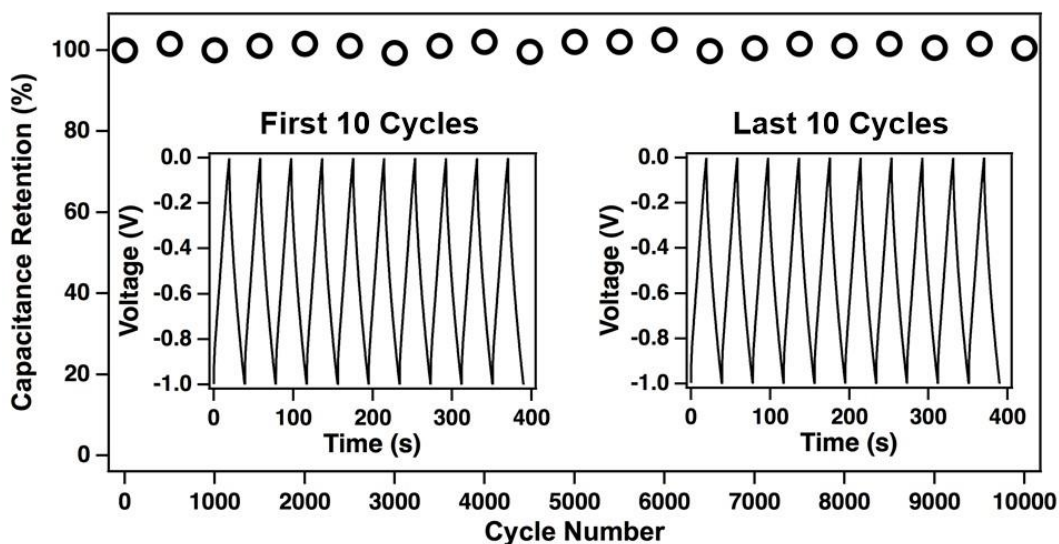


**Figure 22.** Cycle performance of TAPT-DHTA-COF<sub>0.1</sub>@PPZS<sub>900</sub>. Insets is charge-discharge curves.

As shown in Figure 21, the equivalent circuit was provided, and the impedance curves were simulated accordingly. From the semicircles in the impedance plots, the charge-transfer resistances of TAPT-DHTA-COF<sub>0.2</sub>@PPZS<sub>900</sub> (Figure 18d, green curve) and TAPT-DHTA-COF<sub>0.1</sub>@PPZS<sub>900</sub> (red curve) were about 25  $\Omega$ , which were smaller than those of TAPT-DHTA-COF<sub>0.05</sub>@PPZS<sub>900</sub> (40  $\Omega$ , blue curve) and PPZS<sub>900</sub> (46.4  $\Omega$ , black curve). Therefore, the carbon shell enabled to decrease the resistance of carbon effectively. From the low frequencies, the slope of TAPT-DHTA-COF<sub>0.1</sub>@PPZS<sub>900</sub> was larger than those of other prepared core-shell carbons, indicating the fastest ion diffusion in TAPT-DHTA-COF<sub>0.1</sub>@PPZS<sub>900</sub>. These mechanistic insights further confirmed the importance of the core-shell structure, which benefited facilitating ion transport and electron conduction. As a result, the core-shell carbons possessed better capacitive energy storage performance than only the carbon core (PPZS<sub>900</sub>) and carbon shell (TAPT-DHTA-COF<sub>900</sub>).

Cyclic stability is another critical issue of supercapacitor. The cyclic stability of TAPT-DHTA-COF<sub>0.1</sub>@PPZS<sub>900</sub> during galvanostatic charge-discharge cycles was investigated at the high rate of 10 A g<sup>-1</sup> (Figure 22). The capacitance ability of TAPT-DHTA-COF<sub>0.1</sub>@PPZS<sub>900</sub> was well maintained even after 10,000 cycles.

## 2.5 Conclusion

Based on the comparative studies on the template and direct pyrolysis, I demonstrated the first example that core-shell carbons were fabricated from COFs by template pyrolysis method. The template pyrolysis enabled the conversion of

conventional COFs into porous carbons. By fusing the advantages of the core and shell, the prepared core-shell materials possess better capacitive performance than the carbon derived from single precursors. Moreover, the template pyrolysis combines a set of exceptional properties, i.e. heteroatoms, conductivity, and microporosity, which are key to carbon materials for energy storage and catalysis. This strategy thus offers a platform for the conversion of various conventional COFs into heteroatom-doped functional carbons.

## 2.6 Experimental Sections

**Materials and Reagents.** 4,4'-Sulfonyldiphenol (BPS) and triethylamine (TEA) were purchased from TCI. Hexachlorocyclotriphosphazene (HCCP) was purchased from Sigma-aldrich. Mesitylene, dioxane, tetrahydrofuran (THF), and acetonitrile were purchased from Wako Chemicals. Potassium hydroxide (KOH) was purchased from Kanto Chemicals.

A JASCO model FT IR-6100 infrared spectrometer was used to conduct Fourier-transform infrared (FT IR) experiments. A Mettler-Toledo model TGA/SDTA851e was used for TGA measurements under nitrogen, by heating to 1000 °C at a rate of 10 °C min<sup>-1</sup>. A Rigaku model RINT Ultima III diffractometer was used for PXRD measurement, from  $2\theta = 1^\circ$  up to  $60^\circ$  with  $0.02^\circ$  increment. X-ray photoelectron spectroscopy (XPS) experiments were conducted on an AXIS Ultra DLD system from Kratos with Al K $\alpha$  radiation as X-ray source for radiation. Raman spectra were recorded on a SEN TERRA spectrometer (Bruker) employing a semiconductor laser ( $\lambda = 532$  nm). FE-SEM images were obtained on a FEI Sirion-200 field-emission scanning electron microscope at an electric voltage of 10 KV. Supersonicated reactions were conducted by using an ultrasonic cleaning machine using Sharp UT-305HS. TEM images were obtained on Hitachi H-7100 TEM at an electric voltage of 100 KV.

**Computational Calculations.** The crystalline structure of TAPT-DHTA-COF was calculated by the density-functional tight-binding (DFTB+) method including Lennard-Jones (LJ) dispersion. The calculations were conducted with the DFTB+ program package version 1.2.<sup>10</sup> The Coulombic interaction between partial atomic charges was determined using the self-consistent charge (SCC) formalism. Lennard-Jones type dispersion was employed in all calculations to describe van der Waals (vdW) and  $\pi$ -stacking interactions. The lattice dimensions were optimized simultaneously with the geometry. Standard DFTB parameters for X–Y element pair (X, Y = C, O, H, and N)

interactions were employed from the mio-0-1 set.<sup>11</sup>

**Pawley refinements.** Reflex, implemented in MS modeling version 4.4 (Accelrys Inc.) was used to conduct Molecular modeling and Pawley refinement.<sup>12</sup> First, dimensions of unit cell for both hexagonal and rhombic lattices were taken from the DFTB calculation and the space group for hexagonal and rhombic crystal system were selected as *P6*, respectively. Pawley refinement for hexagonal *S4* lattice was performed to optimize the lattice parameters iteratively until the  $R_{WP}$  value converges. The pseudo Voigt profile function was used for whole profile fitting and Berrar–Baldinozzi function was used for asymmetry correction during the refinement processes. A crystal system was deduced with lattice parameters of  $a = b = 37.1453 \text{ \AA}$ ,  $c = 3.49451 \text{ \AA}$ ,  $\alpha = \beta = 90^\circ$ , and  $\gamma = 120^\circ$  and the final  $R_{wp}$  and  $R_p$  values were 4.92% and 3.54%, respectively.

**Electrochemical Capacitance Measurements.** Electrochemical characterizations were carried on an EG & potentiostat/galvanostat Model 2273 advanced electrochemical system. A conventional cell of a three-electrode system was employed throughout this study. Working electrode was prepared by mixing resulting porous carbons with carbon black (Mitsubishi Chemicals, Inc.), and poly(vinyl difluoride) (PVDF) at a weight ratio of 85:10:5 and pasting the mixture on foaming nickel electrodes. A platinum foil was used as a counter electrode, whereas a Ag/AgCl worked as reference electrode. The experiments were carried out in 6 M KOH solution. The potential range was from  $-1$  to  $0 \text{ V}$  (Ag/AgCl) at different scan rates at the ambient temperature.

**Impedance Measurements.** Electrochemical impedance spectroscopic (EIS) measurements were performed under open circuit potential in an AC frequency range from 100,000 to 0.01 Hz with the excitation signal of 5 mV.

**Table 3.** Capacitances of TAPT-DHTA-COF<sub>0.1</sub>@PPZS<sub>900</sub>, COF-based materials, and state-of-the-art carbon materials.

Carbons	Electrolyte	Current Density	Capacitance (F g <sup>-1</sup> )	Reference
<b>TAPT-DHTA-COF<sub>0.1</sub>@PPZS<sub>900</sub></b>	6 M KOH	1 A/g 0.5 A/g	<b>287</b> <b>411</b>	<b>This work</b>
<b>GNrib</b>	1 M H <sub>2</sub> SO <sub>4</sub>	1 A/g	168	<i>Nat. Chem.</i> <b>2016</b> , 8, 718.
<b>HPG</b>	0.5 M H <sub>2</sub> SO <sub>4</sub>	0.5 A/g	225	<i>ACS Cent. Sci.</i> <b>2015</b> , 1, 68.
<b>NPC-F</b>	6 M KOH	1 A/g	284	<i>Adv. Mater.</i> <b>2016</b> , 28, 1981.
<b>Graphene (activated)</b>	BMIM <sub>4</sub> /AN	0.7 A/g	200	<i>Science</i> <b>2011</b> , 332, 1537.
<b>Lasers Cribbed Graphene</b>	1 M H <sub>2</sub> SO <sub>4</sub>	1 A/g	202	<i>Science</i> <b>2012</b> , 335, 1326.
<b>Hierarchical Carbon Material</b>	6 M KOH	175 mA/g	198	<i>Energy Environ. Sci.</i> <b>2011</b> , 4, 4504.
<b>HMCNs-180</b>	2 M H <sub>2</sub> SO <sub>4</sub>	5 mV/s	95	<i>Nano Lett.</i> <b>2013</b> , 13, 207.
<b>Carbon-L-950</b>	6 M KOH	0.1 A/g	228	<i>Adv. Mater.</i> <b>2014</b> , 26, 2047.
<b>CM-NF</b>	6 M KOH	0.1 A/g	189	<i>Nat. Commun.</i> <b>2015</b> , 6, 8503.
<b>PTF-700</b>	EMIMBF <sub>4</sub>	0.1 A/g	151.3	<i>J. Am. Chem. Soc.</i> <b>2015</b> , 137, 219.
<b>GNF</b>	EMIMBF <sub>4</sub>	0.5 A/g	193	<i>J. Am. Chem. Soc.</i> <b>2014</b> , 136, 2256.
<b>GCA</b>	6 M KOH	1 A/g	180	<i>Sci. Rep.</i> <b>2016</b> , 6, 3154.
<b>PAF-Carbon</b>	1 M H <sub>2</sub> SO <sub>4</sub>	0.5 A/g	173	<i>Sci. Rep.</i> <b>2015</b> , 5, 8307.

<b>NCCFs</b>	6 M KOH	1 A/g	240	<i>Sci. Rep.</i> <b>2015</b> , 5, 15388.
<b>DAAQ-TFP COFs</b>	1 M H <sub>2</sub> SO <sub>4</sub>	0.1 A/g	40	<i>J. Am. Chem. Soc.</i> , <b>2013</b> , 135, 16821.
<b>(TEMPO)<sub>100%</sub>- NiP-COF</b>	(C <sub>4</sub> H <sub>9</sub> ) <sub>4</sub> ClO <sub>4</sub>	2 A/g	113	<i>Angew. Chem. Int.</i> <i>Ed.</i> , <b>2015</b> , 54, 6814.
<b>TaPa-Py COF</b>	1 M H <sub>2</sub> SO <sub>4</sub>	0.5 A/g	209	<i>J. Mater. Chem. A</i> , <b>2016</b> , 4, 16312.
<b>NH<sub>2</sub>-f- MWCNT@COF<sub>TT</sub> A-DHTA</b>	1 M Na <sub>2</sub> SO <sub>4</sub>	0.4 A/g	127.5	<i>Chem. Commun.</i> , <b>2017</b> , 53, 6303.

**Table 4.** Atomistic coordinates for the AA-stacking mode of TAPT-DHTA-COF optimized by using DFTB+ method. Space group: *P6*; $a = 37.1453 \text{ \AA}$ ,  $b = 37.1453 \text{ \AA}$ ,  $c = 3.4951 \text{ \AA}$ .

Atom	$x/a$	$y/b$	$z/c$
C	0.2922	0.64329	0.49211
N	0.31502	0.62426	0.49198
C	0.24645	0.61732	0.49533
C	0.36498	0.58628	0.42002
C	0.38917	0.56728	0.42527
C	0.43207	0.5909	0.51263
C	0.45002	0.63402	0.58076
C	0.42563	0.65278	0.57325
N	0.45873	0.57437	0.519
C	0.44612	0.5356	0.58708
C	0.47434	0.51882	0.58307
C	0.45677	0.47516	0.58808
C	0.48135	0.45625	0.58038
H	0.33161	0.56781	0.35218
H	0.37467	0.53402	0.35473
H	0.48338	0.65255	0.64811
H	0.43973	0.68629	0.63103
H	0.41275	0.5126	0.65553
O	0.46061	0.41369	0.57763
H	0.57724	0.54494	0.59034
H	0.51959	0.59677	0.57403

**Table 5.** Atomistic coordinates for the refined unit cell parameters for TAPT-DHTA-COF via Pawley refinement. Space group: *P6*; $a = 37.255 \text{ \AA}$ ,  $b = 37.255 \text{ \AA}$ ,  $c = 3.5159 \text{ \AA}$ .

Atom	$x/a$	$y/b$	$z/c$
C	0.2922	0.64329	0.49211
N	0.31502	0.62426	0.49198
C	0.24645	0.61732	0.49533
C	0.36498	0.58628	0.42002
C	0.38917	0.56728	0.42527
C	0.43207	0.5909	0.51263
C	0.45002	0.63402	0.58076
C	0.42563	0.65278	0.57325
N	0.45873	0.57437	0.519
C	0.44612	0.5356	0.58708
C	0.47434	0.51882	0.58307
C	0.45677	0.47516	0.58808
C	0.48135	0.45625	0.58038
H	0.33161	0.56781	0.35218
H	0.37467	0.53402	0.35473
H	0.48338	0.65255	0.64811
H	0.43973	0.68629	0.63103
H	0.41275	0.5126	0.65553
O	0.46061	0.41369	0.57763
H	0.57724	0.54494	0.59034
H	0.51959	0.59677	0.57403

**Table 6.** Atomistic coordinates for the AB-stacking mode of TAPT-DHTA-COF optimized by using DFTB+ method. Space group:  $P63$ ;

$a = 37.4439 \text{ \AA}$ ,  $b = 37.4439 \text{ \AA}$ ,  $c = 6.0044 \text{ \AA}$ .

Atom	$x/a$	$y/b$	$z/c$
C	0.959	0.97765	0.26236
N	0.98085	0.95785	0.26232
C	0.9134	0.95263	0.26308
C	0.02881	0.91745	0.26628
C	0.05233	0.89802	0.26814
C	0.0959	0.92158	0.26657
C	0.11446	0.96504	0.26295
C	0.09076	0.98418	0.26131
N	0.12279	0.90558	0.26904
C	0.11111	0.86661	0.26895
C	0.14015	0.85113	0.27126
C	0.12398	0.808	0.27062
C	0.14924	0.79019	0.27077
H	0.99496	0.89882	0.2676
H	0.03658	0.86417	0.27116
H	0.14829	0.98388	0.26143
H	0.10579	0.01801	0.25868
H	0.07771	0.84207	0.26648
O	0.12966	0.74808	0.26964
H	0.24284	0.87908	0.27674
H	0.18303	0.92767	0.27286
C	0.37433	0.68903	0.26161
N	0.35246	0.7088	0.26156
C	0.41994	0.71409	0.26287
C	0.30395	0.74873	0.23068
C	0.28034	0.76805	0.23141

Chapter 2

---

C	0.23727	0.74487	0.26694
C	0.21917	0.70183	0.29829
C	0.24296	0.68279	0.29626
N	0.21039	0.76088	0.26689
C	0.22209	0.79981	0.27486
C	0.1931	0.81535	0.27284
C	0.20926	0.85847	0.27488
C	0.184	0.87628	0.27349
H	0.33742	0.76705	0.20282
H	0.2955	0.80146	0.20233
H	0.18574	0.6833	0.32595
H	0.22834	0.64929	0.32107
H	0.25548	0.82422	0.28539
O	0.20356	0.91841	0.27446
H	0.0904	0.7874	0.26954
H	0.15013	0.73875	0.27018

**References**

1. (a) Y. Wang, Y. Song, Y. Xia, *Chem. Soc. Rev.* **2016**, *45*, 5925-5950. (b) F. Xu, Z. Tang, S. Huang, L. Chen, Y. Liang, W. Mai, H. Zhong, R. Fu, D. Wu, *Nat. Commun.* **2015**, *6*, 7221, doi: 10.1038/ncomms8221. (c) X. D. Zhuang, D. Gehrig, N. Forler, H. Liang, M. Wagner, M. R. Hansen, F. Laquai, F. Zhang, X. L. Feng, *Adv. Mater.* **2015**, *27*, 3789-3796.
2. (a) W.-J. Liu, H. Jiang, H. -Q. Yu, *Chem. Rev.* **2015**, *115*, 12251-12285. (b) J.-S. M. Lee, T.-H. Wu, B. M. Alston, M. E. Briggs, T. Hasell, C.-C. Hu, A. I. Cooper, *J. Mater. Chem. A* **2016**, *4*, 7665-7673. (c) H. Liu, S. Li, H. Yang, S. Liu, L. Chen, Z. Tang, R. Fu, D. Wu, *Adv. Mater.* **2017**, *29*, 1700723.
3. (a) Q.-L. Zhu, W. Xia, T. Akita, R. Zou, Q. Xu, *Adv. Mater.* **2016**, *28*, 6391-6398. (b) Q.-L. Zhu, W. Xia, L.-R. Zheng, R. Zou, Z. Liu, Q. Xu, *ACS Energy Lett.* **2017**, *2*, 504-511. (c) W. Xia, A. Mahmood, R. Zou, Q. Xu, *Energy Environ. Sci.* **2015**, *8*, 1837-1866. (d) Y. Z. Chen, C. Wang, Z. Y. Wu, Y. Xiong, Q. Xu, S.-H. Yu, H. L. Jiang, *Adv. Mater.* **2015**, *27*, 5010-5016. (e) B. Liu, H. Shioyama, T. Akita, Q. Xu, *J. Am. Chem. Soc.* **2008**, *130*, 5390-5391. (f) H.-L. Jiang, B. Liu, Y.-Q. Lan, K. Kuratani, T. Akita, H. Shioyama, F. Zong, Q. Xu, *J. Am. Chem. Soc.* **2011**, *133*, 11854-11857. (g) P. Pachfule, D. Shinde, M. Majumder, Q. Xu, *Nat. Chem.* **2016**, *8*, 718-724.
4. (a) Q. Sun, B. Aguila, J. Perman, N. Nguyen, S. Ma, *J. Am. Chem. Soc.* **2016**, *138*, 15790-15796. (b) A. Halder, S. Kandambeth, B. P. Biswal, G. Kaur, N. C. Roy, M. Addicoat, J. K. Salunke, S. Banerjee, K. Vanka, T. Heine, S. Verma, R. Banerjee, *Angew. Chem. Int. ed.* **2016**, *55*, 7806-7810. (c) S. Lin, C. S. Diercks, Y. B. Zhang, N. Kornienko, E. M. Nichols, Y. B. Zhao, A. R. Paris, D. Kim, P. Yang, O. M. Yaghi, C. J. Chang, *Science* **2015**, *349*, 1208-1213. (d) H.-S. Xu, S.-Y. Ding, W.-K. An, H. Wu, W. Wang, *J. Am. Chem. Soc.* **2016**, *138*, 11489-11492. (e) N. Huang, P. Wang, D. Jiang, *Nat. Rev. Mater.* **2016**, *1*, 16068, doi: 10.1038/natrevmats2016.68. (f) H. Xu, S. Tao, D. Jiang, *Nat. Mater.* **2016**, *15*, 722-726. (g) H. Xu, J. Gao, D. Jiang, *Nat. Chem.* **2015**, *7*, 905-912. (h) E. Jin, M. Asada, Q. Xu, S. Dalapati, M. A. Addicoat, M. A. Brady, H. Xu, T. Nakamura, T. Heine, Q. Chen, D. Jiang, *Science* **2017**, *357*, 673-676.
5. (a) C. R. DeBlase, K. E. Silberstein, T. T. Truong, H. D. Abruna, W. R. Dichtel, *J. Am. Chem. Soc.* **2013**, *135*, 16821-16824. (b) C. R. Mulzer, L. Shen, R. P. Bisbey,

- J. R. McKone, N. Zhang, H. D. Abruna, W. R. Dichtel, *ACS Cent. Sci.* **2016**, *2*, 667-673. (c) C. R. DeBlase, K. Hernández-Burgos, K. E. Silberstein, G. G. Rodríguez-Calero, R. P. Bisbey, H. D. Abruña, W. R. Dichtel, *ACS Nano* **2015**, *9*, 3178-3183. (d) F. Xu, H. Xu, X. Chen, D. Wu, Y. Wu, H. Liu, C. Gu, R. Fu, D. Jiang, *Angew. Chem. Int. Ed.* **2015**, *54*, 6814-6818. (e) F. Xu, S. Jin, H. Zhong, D. Wu, X. Yang, X. Chen, H. Wei, R. Fu, D. Jiang, *Sci. Rep.* **2015**, *5*, 8225, doi: 10.1038/srep08225.
6. (a) Y.-B. Huang, P. Pachfule, J.-K. Sun, Q. Xu, *J. Mater. Chem. A* **2016**, *4*, 4273-4279. (b) G. Abellan, J. Romero, D. Rodriguez-San-Miguel, A. Ribera, R. Mas-Balleste, T. F. Otero, I. Manet, F. Liscio, F. Zamora, E. Coronado, *J. Mater. Chem. A* **2017**, *5*, 4343-4351. (c) L. Chen, L. Zhang, Z. Chen, H. Liu, R. Luque, Y. Li, *Chem. Sci.* **2016**, *7*, 6015-6020.
7. W. Wei, R. Lu, H. Xie, Y. Zhang, X. Bai, L. Gu, R. Da, X. Liu, *J. Mater. Chem. A* **2015**, *3*, 4314-4322.
8. (a) S. Gayathri, P. Jayabal, M. Kottaisamy, V. Ramakrishnan, *AIP Adv.* **2014**, *4*, 027116. (b) A. C. Ferrari, D. M. Basko, *Nat. Nanotechnol.* **2013**, *8*, 235-246. (c) H. Tian, Z. X. Lin, F. G. Xu, J. X. Zheng, X. D. Zhuang, Y. Y. Mai, X. L. Feng, *Small* **2016**, *12*, 3155-3163.
9. (a) F. Hu, J. Wang, S. Hu, L. Li, G. Wang, J. Qiu, X. Jian, *Nanoscale* **2016**, *8*, 16323-16331. (b) Y. Zhou, R. Ma, S. L. Candelaria, J. Wang, Q. Liu, E. Uchaker, P. Li, Y. Chen, G. Cao, *J. Power Sources* **2016**, *314*, 39-48. (c) J. Zhang, L. Qu, G. Shi, J. Liu, J. Chen, L. Dai, *Angew. Chem. Int. Ed.* **2016**, *55*, 2230-2234.
10. B. Aradi, B. Hourahine, T. Frauenheim, *J. Phys. Chem. A* **2007**, *111*, 5678-5684.
11. <http://www.dftb.org>.
12. Accelrys, Material Studio Release Notes, Release 4.4, Accelrys Software, San Diego 2008.

**Chapter 3. Template Conversion of Covalent Organic  
Frameworks into Two-Dimensional Conducting  
Nanocarbons for Catalyzing Oxygen Reduction Reaction**

## **Abstract**

Many effects in porous materials have been done on the design of metal-free carbon catalysts to replace platinum-loaded carbon catalysts in fuel cells. The carbon material must combine three functions, i.e. electrical conductivity for electron transport, optimal pores for ion motion and abundant heteroatom sites for catalysis. This requires a simultaneous yet nanoscopic control over carbon dimensionality, pore structure and heteroatom sites during pyrolysis. However, such a structural control remains challenging. Here I demonstrate the production of an ideal carbon catalyst by combining two strategies – the use of a two-dimensional porous precursor and the development of a suitable template to guide the pyrolysis. This technique produces nanosized two-dimensional carbon sheets with high conductivity, hierarchical porosity and abundant heteroatom catalytic edges. The catalyst achieves ultrahigh performance with exceptional onset and half-wave potentials, and high limit current density. These results reveal a novel material based on covalent organic frameworks for designing catalysts for high performance energy conversion systems.

### 3.1 Introduction

The oxygen reduction reaction (ORR) is the core electrochemical process of energy storage and conversion devices including rechargeable metal-air batteries and fuel cells.<sup>1</sup> Pt and Pt-based alloys are promising as catalysts for ORR, however, the reserve of Pt is limited and it hardly sustains enough numbers of batteries and fuel cells.<sup>2</sup> Intensive efforts over the past few decades have been made on pursuing alternate catalysts, including non-precious metal-based materials and recently metal-free carbon catalysts.<sup>3</sup> As catalysts for ORR, the carbon materials must merge three different functions, i.e. two-dimensional (2D) graphitic carbons with high electrical conductivity for quick electron transport, optimal pores for facilitated ion transport and abundant heteroatom sites for improved catalysis. The combination of these functions in one carbon material becomes possible when a simultaneous control at nanoscale precision over dimensionality, pores and heteroatom sites is realized during pyrolysis.<sup>4</sup> However, direct pyrolysis eventually gives rise to ill-controlled three-dimensional (3D) entangled carbon structures other than 2D graphitic carbons. Developing methodology to pyrolyze porous precursors into 2D carbons that combine high conductivity, large porosity and abundant heteroatom-doped edge sites is highly desired, but still under explored.

Covalent organic frameworks (COFs), a 2D crystalline porous polymer, enable the pre-designed integration of organic units with various heteroatoms into the ordered 2D layers and one-dimensional (1D) open channels.<sup>5</sup> By virtue of the diversity of topology design diagrams, the availability of building units and accessibility of linkages, various COFs with different topologies, skeletons and pores have been designed and synthesized. Their ordered skeletons and pores render COFs able to explore outstanding properties and functions such as semiconducting, ion conduction, heterogeneous catalysis and energy storage.<sup>6</sup> Given the features of two dimensionality, lightweight elements and abundant heteroatom sites in the skeletons, COFs are promising as precursors for pyrolyzed synthesis of heteroatom-doped 2D carbons with sufficient active sites on the edges. However, even though COFs are 2D layered materials, direct pyrolysis of COFs yielded only 3D carbon entanglements with the loss of their 2D structural and porous features.<sup>7</sup>

Herein, I reported a new strategy by carbonization of COFs into 2D carbons, which showed excellent performance in electrochemical catalysts. I demonstrated that the

production of such an ideal carbon catalyst was possible by combining two strategies – one was the use of a porous 2D COF precursor and the other was the development of a suitable template to guide the pyrolysis. This approach produced nanosized 2D graphitic carbon sheets with high conductivity, hierarchical micropores and mesopores and abundant N and P-doped catalytic edges. I highlighted that these nanosized-carbons function as catalysts in ORR that achieved ultrahigh performance with exceptional onset and half wave potentials, high limit current density and robust cyclic stability, which were far superior to those of benchmarked platinum and carbon.

### 3.2 Materials and Methods

**Synthesis of TAPT-DHTA-COF.** I added a mixture of dioxane/mesitylene (0.5 mL/0.5 mL), building blocks (TAPT (28 mg) and DHTA (20 mg)) and HAc solution (3 M, 0.2 mL) in a Pyrex tube (10 mL). And I degassed the tube by freeze-pump-thaw for three cycles. Then I sealed the tube and heated it at 120 °C for 3 days. I collected the precipitate by filtering, and then subjected to Soxhlet extraction with THF for 24 h. The sample was dried at 120 °C under vacuum overnight to obtain TAPT-DHTA-COF in a yield of 86%.

**Synthesis of PA@TAPT-DHTA-COF.** The TAPT-DHTA-COF sample (100 mg) was degassed under vacuum at 100 °C for 3 h and cooled down at 25 °C. Phytic acid (PA) (2 mL) was added to the TAPT-DHTA-COF sample and the mixture was heated at 90 °C for 12 h. The crude product was obtained by filtering and washed with anhydrous THF carefully. The solid was dried at 25 °C under vacuum to yield the PA@TAPT-DHTA-COF (156 mg).

**Synthesis of TAPT-DHTA-COF<sub>1000</sub>, PA@TAPT-DHTA-COF<sub>1000</sub> and PA@TAPT-DHTA-COF<sub>1000NH<sub>3</sub></sub>.** The PA@TAPT-DHTA-COF (300 mg) or TAPT-DHTA-COF (300 mg) samples were pyrolyzed at 1000 °C for 3 h (2 °C min<sup>-1</sup>) under nitrogen to yield PA@TAPT-DHTA-COF<sub>1000</sub> (122 mg) and TAPT-DHTA-COF<sub>1000</sub> (141 mg), respectively. The PA@TAPT-DHTA-COF<sub>1000</sub> sample (50 mg) was subjected to pyrolysis under NH<sub>3</sub> flow (60 mL min<sup>-1</sup>) at 900 °C for 0.5 h to yield the PA@TAPT-DHTA-COF<sub>1000NH<sub>3</sub></sub> (38 mg).

**Electrocatalytic Measurements.** The ORR catalysts (5mg; TAPT-DHTA-COF<sub>1000</sub>, PA@TAPT-DHTA-COF<sub>1000</sub> or PA@TAPT-DHTA-COF<sub>1000NH<sub>3</sub></sub>) were dispersed in a Nafion ethanol solution (0.25 wt%, 500 µL) and were sonicated for 2 h to yield a homogeneous ink. The catalyst ink (9 µL) was pipetted onto a glassy carbon electrode

(diameter = 5.00 mm, area = 0.196 cm<sup>2</sup>) with a content of 0.46 mg cm<sup>-2</sup>. The commercially available 20 wt% platinum on carbon black (Pt/C, BASF) was measured for comparison. The Pt/C sample (5 mg) was dispersed in a Nafion solution (0.25 wt %, 500  $\mu$ L) by sonication for 2 h to obtain a well-dispersed ink and the catalyst ink (9  $\mu$ L) was pipetted onto the glassy carbon electrode surface.

**ORR Performance Tests.** All the electrochemical measurements were carried out in a conventional three-electrode cell using the PINE electrochemical workstation (Pine Research Instrumentation, USA) at room temperature. The Ag/AgCl (3 M KCl) was used as an reference electrode, and platinum wire was used as a counter electrode, respectively. An RRDE electrode with a Pt ring and a glassy carbon disk served as the substrate for the working electrode for evaluating the ORR activity and selectivity of various catalysts. The electrochemical experiments were conducted in O<sub>2</sub> saturated aqueous solution of KOH (0.1 M) for the ORR. For the cyclic voltammetry (CV) tests, the potential range was circularly scanned between -1.0 and 0 V at a scan rate of 100 mV s<sup>-1</sup> after purging O<sub>2</sub> gas for 30 min. The electrolyte was deaerated by bubbling with nitrogen to estimate the double layer capacitance, and then the voltammogram was evaluated again in the deaerated electrolyte. The rotating disk electrode (RDE) measurements were conducted at different rotation rates from 400 to 1600 rpm. The rotating ring disk electrode (RRDE) measurements were conducted at a rotation rate of 1600 rpm with a sweep rate of 10 mV s<sup>-1</sup>. On the basis of ring and disk currents, the electron transfer number (*n*) and four electron selectivity of catalysts based on the H<sub>2</sub>O<sub>2</sub> yield (H<sub>2</sub>O<sub>2</sub> (%)) was calculated from the equations of  $n = 4 I_D / [(I_R/N) + I_D]$  and  $H_2O_2 (\%) = 200 (I_R/N) / [(I_R/N) + I_D]$ , where *I<sub>R</sub>* and *I<sub>D</sub>* are the disk and ring currents, respectively, and the ring collection efficiency *N* is 0.26. The Tafel slope was estimated by linear fitting of the polarization curves according to the Tafel equation ( $\eta = b \times \log j + a$ , where *j* is the current density and *b* is the Tafel slope).

**Stability Tests.** For the crossover methanol tolerance measurement, methanol (2%, v/v) was introduced into O<sub>2</sub>-saturated aqueous KOH solution (0.1 M) at around 300 s. The current-time chronoamperometric response of the PA@TAPT-DHTA-COF<sub>1000NH<sub>3</sub></sub> and Pt/C was tested at the potential of -0.8 V (vs. Ag/AgCl) for 20000 s in an O<sub>2</sub>-saturated aqueous KOH solution (0.1 M) at a rotation rate of 1600 rpm.

## 3.3 Molecular Design and Structural Characterization

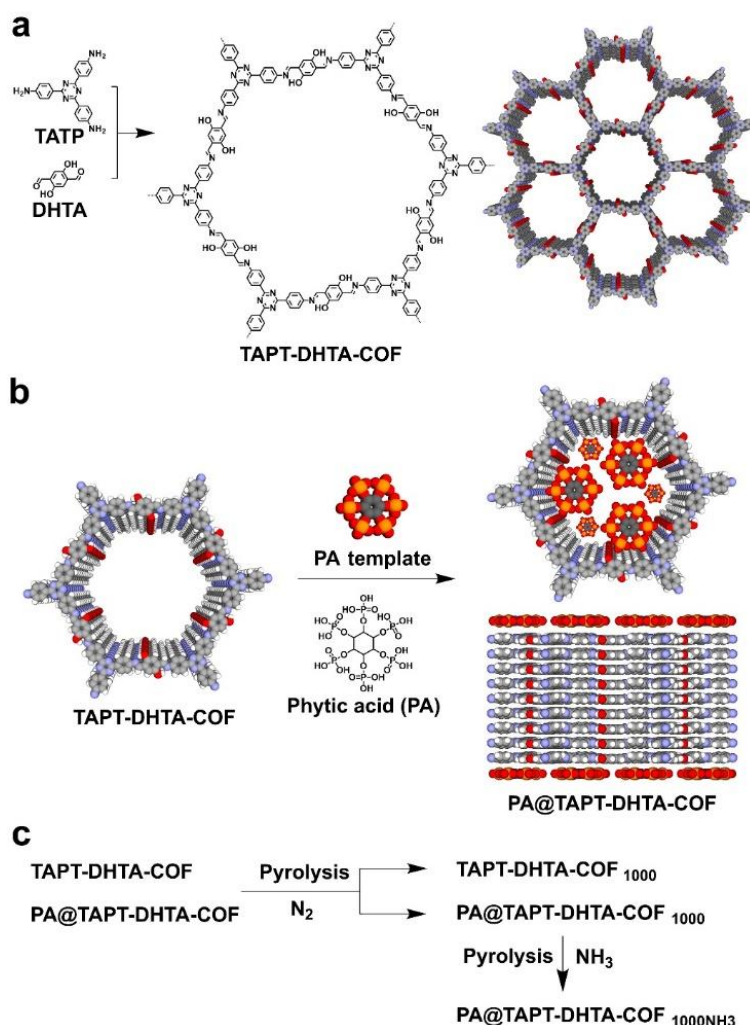


**Figure 1.** a) Structure and schematic for the synthesis of TAPT-DHTA-COF. b) Template synthesis of PA@TAPT-DHTA-COF by mixing TAPT-DHTA-COF with PA. The PA molecules occupy the pores (upper for top view) and separate COFs by coating on the surface (lower for side view). c) Template or non-template pyrolysis to convert COFs into carbons.

I employed PA as a template and treated a 2D COF (Figure 1, TAPT-DHTA-COF) with PA that enters into the 1D channels and layers. The function of PA is multifold. Firstly, PA exfoliates the heavily stacked layers of 2D COFs into a few layers that helps to form small-sized carbon sheets. Secondly, PA forms strong H-bonding networks that cover the surface of 2D COF layers and guide the conversion of 2D COF layers into 2D carbons during pyrolysis. Thirdly, the decomposition of PA networks helps to trigger porous structure of the resulting 2D carbons. Finally, PA dopes the 2D carbon sheets with P in addition to the N doping from imine linkages and triazine building blocks. I

observed that the layered structures of COFs are also essential for producing the 2D carbons; the carbonization of other amorphous precursors in the presence of PA results in amorphous carbons.<sup>8</sup>

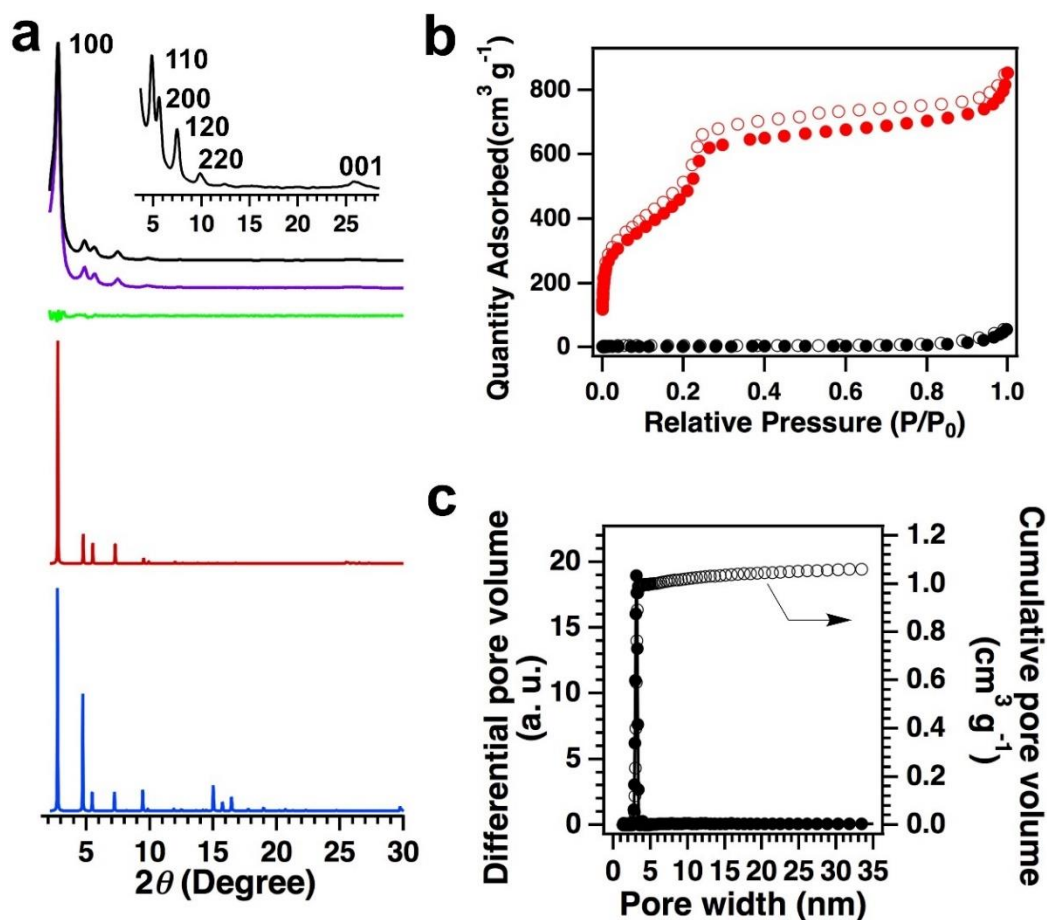


**Figure 2.** a) PXRD patterns of TAPT-DHTA-COF, experimentally observed (black), Pawley refined (purple), and their difference (green), simulated using AA (red) and AB-stacking modes (blue). b) Nitrogen sorption isotherm profiles of TAPT-DHTA-COF (red) and PA@TAPT-DHTA-COF (black). c) Pore size (filled circles) and pore size distribution (open circles) profiles of TAPT-DHTA-COF.

TAPT-DHTA-COF was synthesized by condensation of TAPT and DHTA under solvothermal condition (Figure 1a).<sup>9</sup> Powder X-ray diffraction (PXRD) measurements showed that TAPT-DHTA-COF was a crystalline polymer with the most intensive peak at  $2.78^\circ$ , and other five peaks at  $4.86$ ,  $5.68$ ,  $7.48$ ,  $9.80$ , and  $26.00^\circ$ , which were assigned to the (100), (110), (200), (120), (220), and (001) facets, respectively (Figure 2a, green curve). The Pawley-refined PXRD curve (purple curve) agreed well with the experimentally observed curve as confirmed by their negligible difference (black curve). TAPT-DHTA-COF at 77 K exhibited type-IV sorption isotherm curves, from

which the Brunauer–Emmett–Teller (BET) surface area was evaluated to be as high as  $2170 \text{ m}^2 \text{ g}^{-1}$  (Figure 2b, red curves). It consisted of mesopores with size of 3.1 nm, whereas the pore volume calculated by the nonlocal density functional theory method was  $1.08 \text{ cm}^3 \text{ g}^{-1}$  (Figure 2c; Table 1).

The morphology of TAPT-DHTA-COF was investigated by Field-emission scanning electron microscopy (FE-SEM) images and high-resolution transmission electron microscope (HR-TEM) images. FE-SEM images and HR-TEM images revealed TAPT-DHTA-COF was ribbons with elementary size of diameter of 40-50 nm and length of over  $1 \mu\text{m}$  (Figure 3).

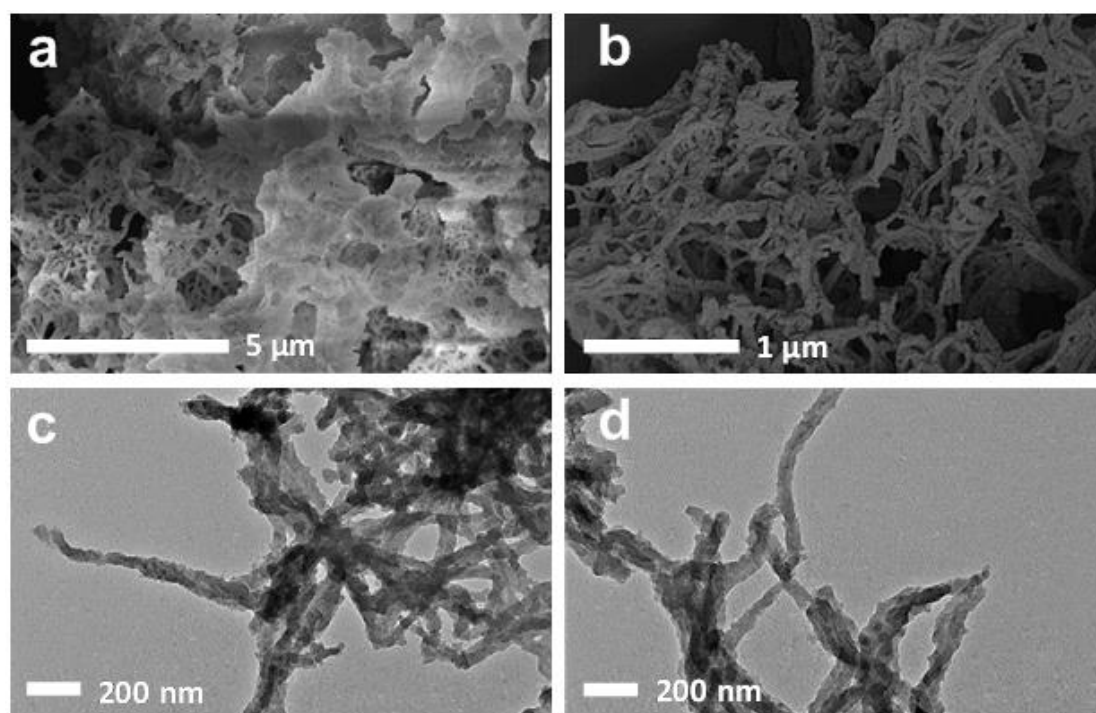


**Figure 3.** a, b) FE-SEM images of TAPT-DHTA-COF at different areas and magnification scales. c, d) TEM images of TAPT-DHTA-COF at different areas.

After loading PA into the pore channels, PA@TAPT-DHTA-COF was obtained. The BET surface area was obviously decreased to only  $21 \text{ m}^2 \text{ g}^{-1}$  (Figure 2b, black curves; Table 1), indicating almost all the pores were occupied by PA. From thermogravimetric analysis (Figure 4), TAPT-DHTA-COF was stable up to  $410 \text{ }^\circ\text{C}$  under nitrogen. PA@TAPT-DHTA-COF was thermally stable before  $250 \text{ }^\circ\text{C}$ , which was much higher than the boiling point ( $105 \text{ }^\circ\text{C}$ ) of PA. The chemical nature was further confirmed by Fourier-transform infrared spectroscopy (FT IR) (Figure 5). The new infrared adsorption bands at  $1180$ ,  $1060$ , and  $943 \text{ cm}^{-1}$  were assigned to vibrations of the P=O bond of PA while retaining all the peaks of the COF.<sup>8c,10</sup>

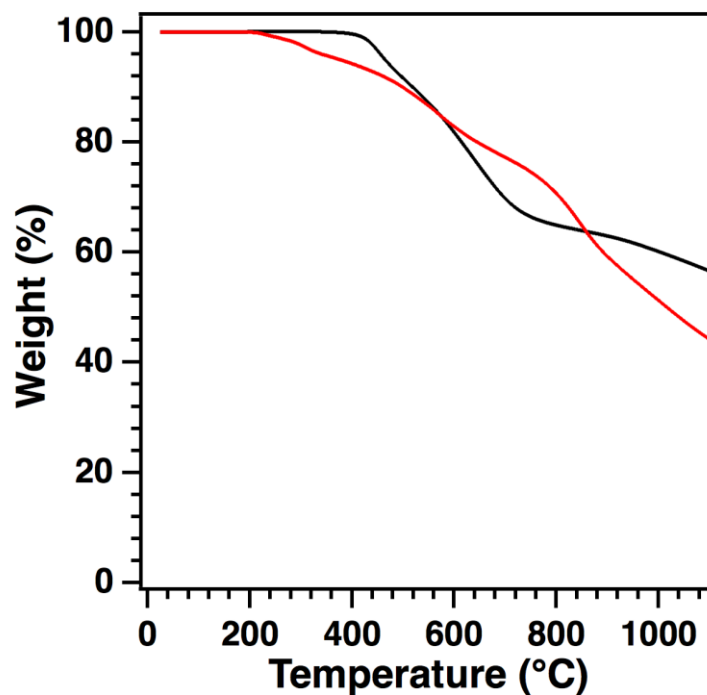


**Figure 4.** Thermogravimetric curves of TAPT-DHTA-COF (black) and PA@TAPT-DHTA-COF (red), measured from 25 to 1100 °C at a heating rate constant of 10 °C min<sup>-1</sup> under nitrogen.

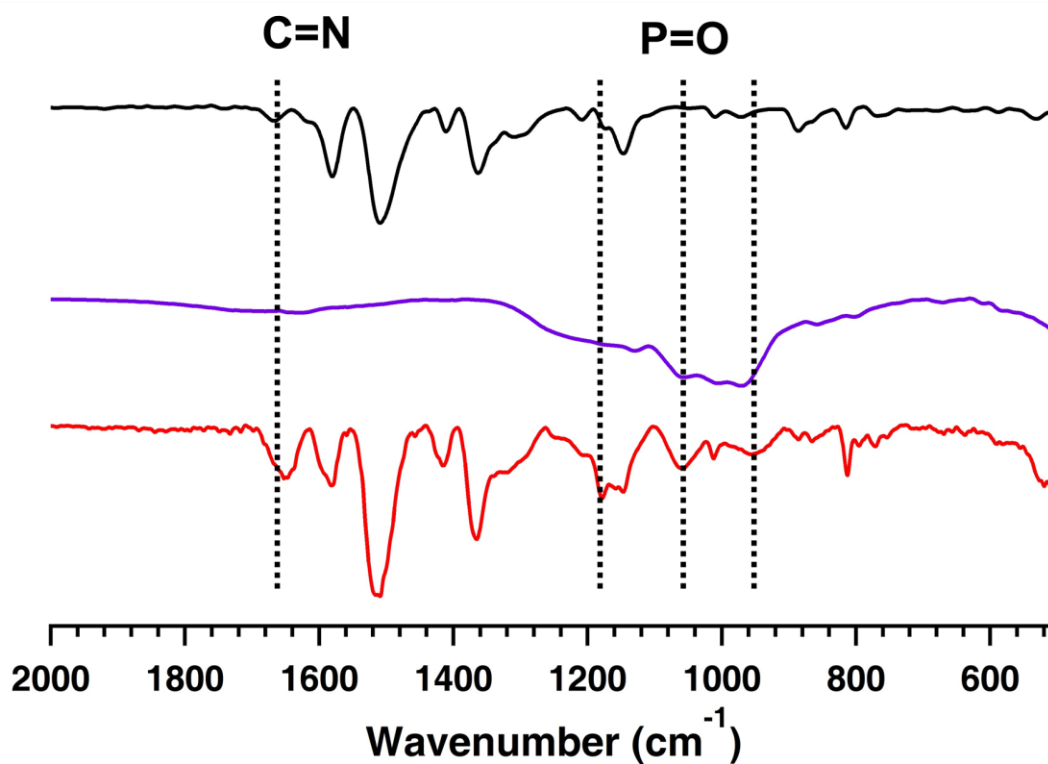


**Figure 5.** FT IR spectra of TAPT-DHTA-COF (black), PA (purple), and PA@TAPT-DHTA-COF (red).

The morphology of PA@TAPT-DHTA-COF changed from ribbons of TAPT-DHTA-COF to small particles of layered textures with the size of approximately 50 nm. This change was originated from the presence of PA networks on the COF surface that separate the layers (Figure 6).

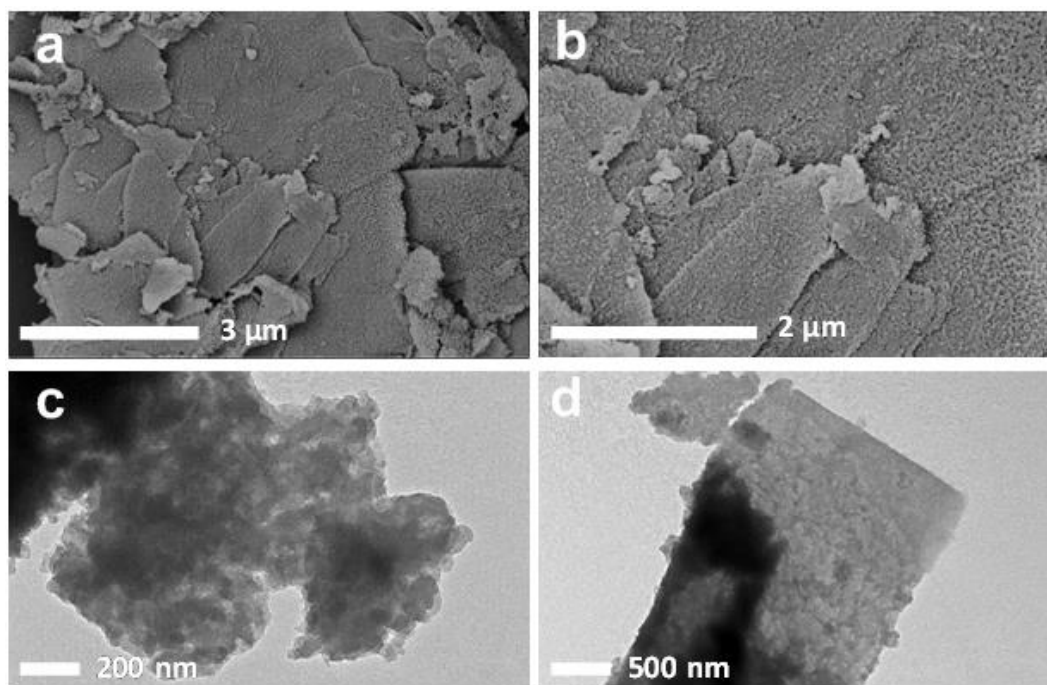


**Figure 6.** a, b) FE-SEM images of PA@TAPT-DHTA-COF at different magnification scales. c, d) TEM images of PA@TAPT-DHTA-COF at different areas.

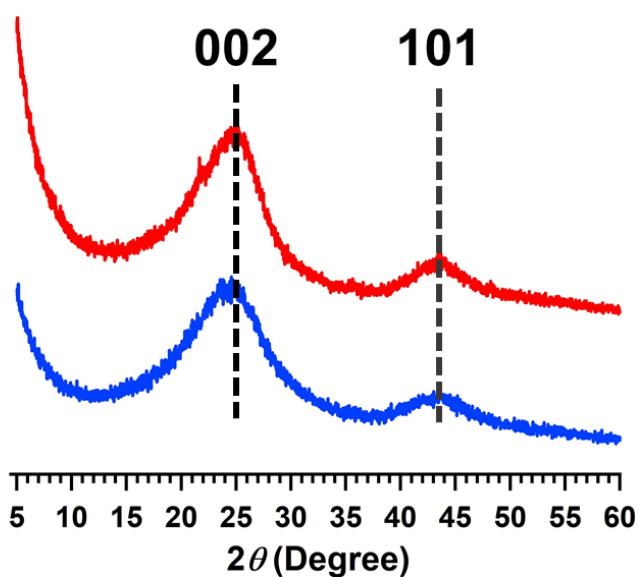


**Figure 7.** PXRD patterns of PA@TAPT-DHTA-COF<sub>1000</sub> (blue) and PA@TAPT-DHTA-COF<sub>1000NH3</sub> (red).

PA@TAPT-DHTA-COF was pyrolyzed at 1000 °C under nitrogen to yield N and P-co-doped PA@TAPT-DHTA-COF<sub>1000</sub> (Figure 1c). The PXRD profiles of the PA@TAPT-DHTA-COF<sub>1000</sub> revealed two intense peaks at 24° and 44° that were indexed to the (002) and (101) planes of graphite, respectively, suggesting highly crystal graphitic structure (Figure 7).

Pore structure of PA@TAPT-DHTA-COF<sub>1000</sub> was explored by nitrogen sorption isotherm at 77 K. The BET surface area was 495 m<sup>2</sup> g<sup>-1</sup> (Figure 8a, blue circles) and the pore volume was 0.22 cm<sup>3</sup> g<sup>-1</sup> (Figure 8b; Table 1). Notably, the pore size distribution profile indicated that PA@TAPT-DHTA-COF<sub>1000</sub> possessed only micropores with sizes between 0.7 nm to 1.6 nm (Figure 9b). However, the BET surface area of TAPT-DHTA-COF<sub>1000</sub> obtained from the direct thermolysis in the absence of PA under otherwise same conditions was only 20 m<sup>2</sup> g<sup>-1</sup> (Figure 9a, black circles), indicating the porous structure of the original COF was wholly collapsed.

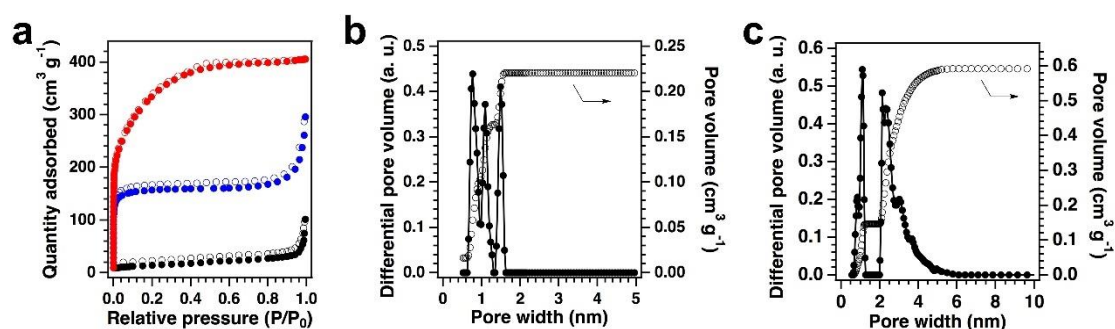


**Figure 8.** a) Nitrogen sorption isotherm profiles of TAPT-DHTA-COF<sub>1000</sub> (black), PA@TAPT-DHTA-COF<sub>1000</sub> (blue) and PA@TAPT-DHTA-COF<sub>1000</sub>NH<sub>3</sub> (red). b) Pore size (filled circles) and pore size distribution (open circles) profiles of PA@TAPT-DHTA-COF<sub>1000</sub>. c) Pore size (filled circles) and pore size distribution (open circles) profiles of PA@TAPT-DHTA-COF<sub>1000</sub>NH<sub>3</sub>.

The FE-SEM images and TEM images also certified their different architectures. PA@TAPT-DHTA-COF<sub>1000</sub> remained the 2D texture (Figure 9, 10), whereas TAPT-DHTA-COF<sub>1000</sub> assumed 3D aggregated bulks (Figure 11). Thus, the H-bonding networks of PA are the key to keep the 2D structural feature of COFs during pyrolysis. The FE-SEM elemental mapping analysis revealed that the carbon, nitrogen, oxygen and phosphorus atoms were uniformly distributed in PA@TAPT-DHTA-COF<sub>1000</sub> (Figure 12).

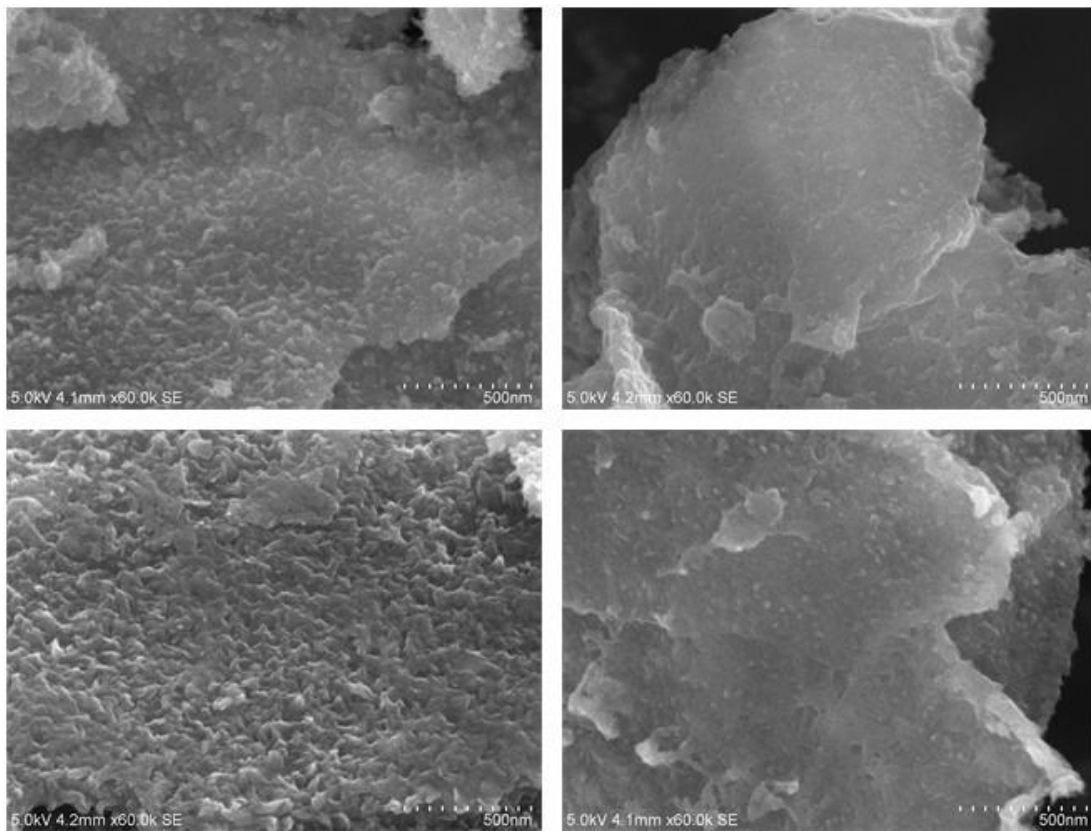


**Figure 9.** FE-SEM images of PA@TAPT-DHTA-COF<sub>1000</sub> at different areas and magnification scales.

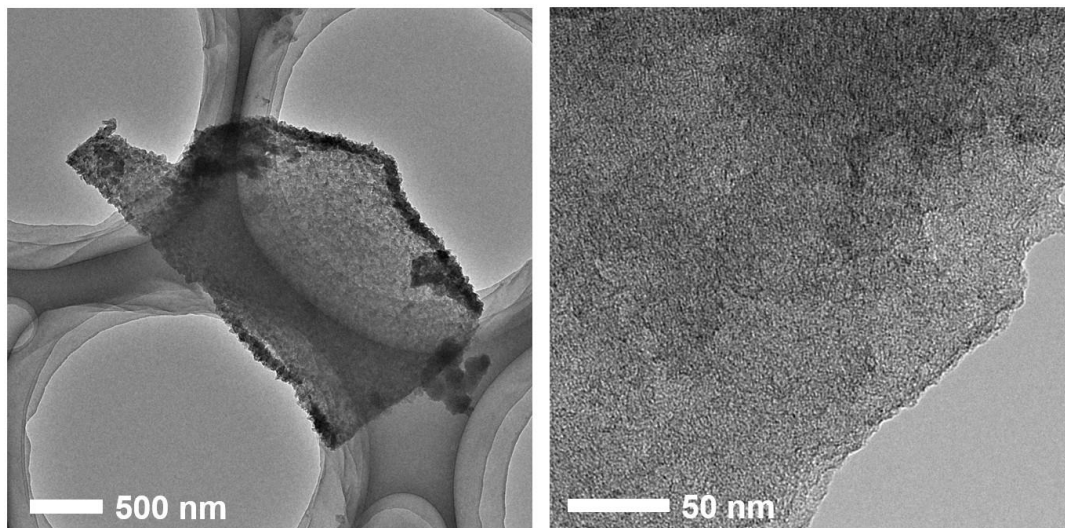


**Figure 10.** TEM images of PA@TAPT-DHTA-COF<sub>1000</sub> at different scales.

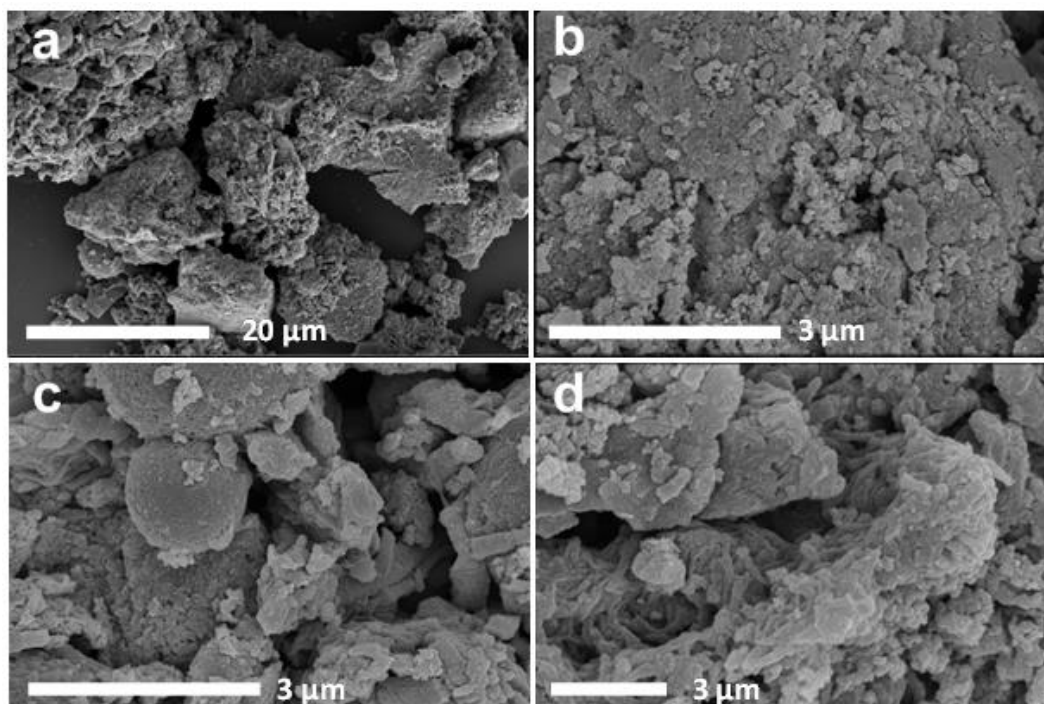


**Figure 11.** FE-SEM images of TAPT-DHTA-COF<sub>1000</sub> at different areas and magnification scales.

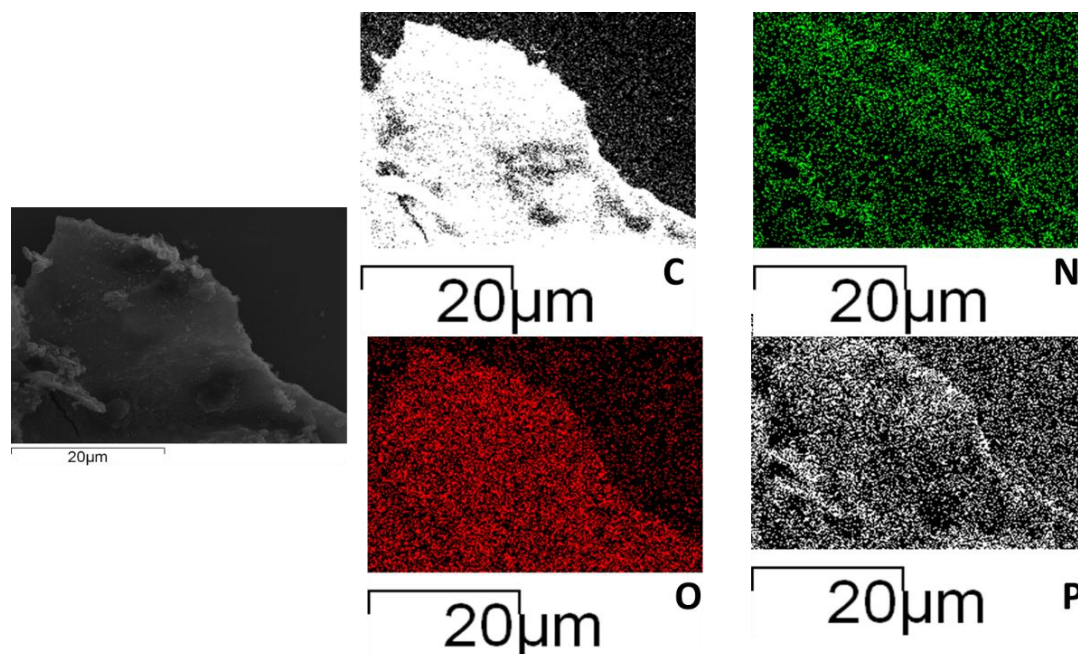


**Figure 12.** FE-SEM elemental mapping images of PA@TAPT-DHTA-COF<sub>1000</sub>.

The microstructure of PA@TAPT-DHTA-COF<sub>1000</sub> was investigated by HR-TEM (Figure 13a, b). The vertical graphene sheets in different direction with about two to ten layers were clearly observed.

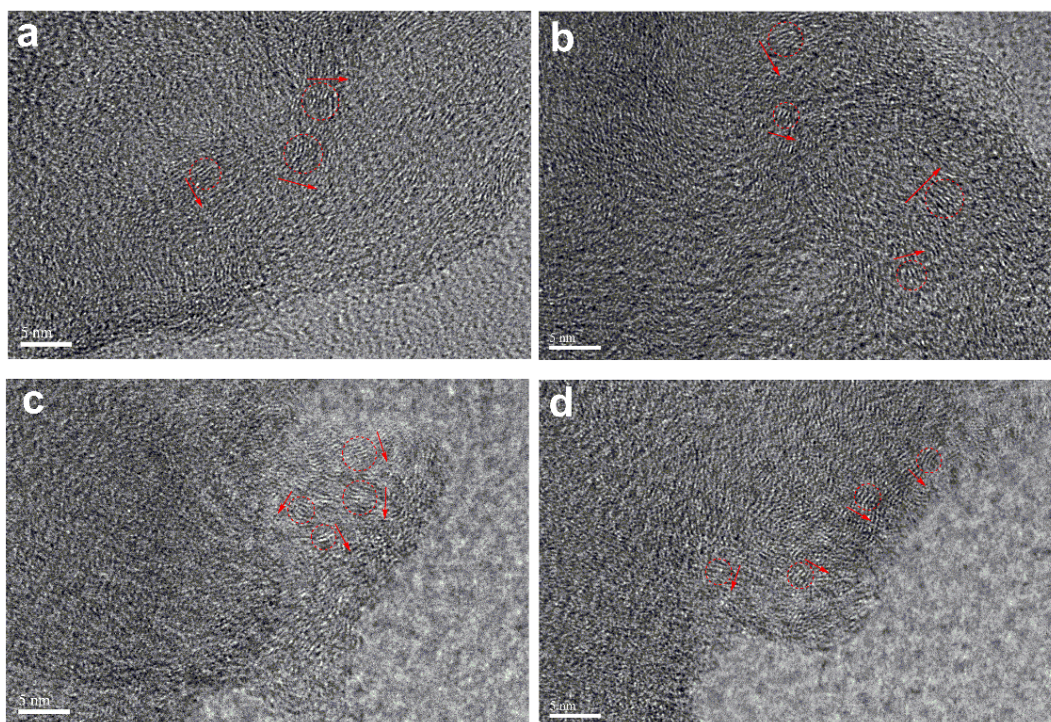


**Figure 13.** HR-TEM images of a, b) PA@TAPT-DHTA-COF<sub>1000</sub> and c, d) PA@TAPT-DHTA-COF<sub>1000NH3</sub> at different areas and magnification scales.

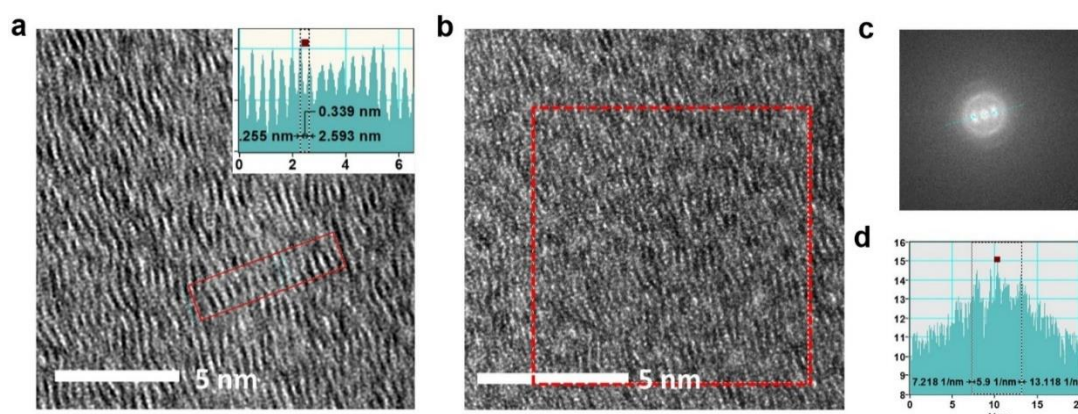


**Figure 14.** a, b) HR-TEM images at different scales. Inset in a is the lattice fringe distance measurement of the red region. c) FFT of the red square in b. d) The distance measurement of arcs in c.

From the enlarged HR-TEM images (Figure 14), the interlayer separation was 0.34 nm, which corresponded to the distance between 2D nanosheets. The fast Fourier Transform (FFT) of different lattice fringes was used to study the layer stacking and packing motifs. The FFT of red square region in Figure 14b generated two arcs (Figure 14c), and the distance between them was about 5.91 1/nm (Figure 14d), which was assigned to the (002) facet of graphene. These results reflected that carbon nanoflakes were aligned vertically with orientations.

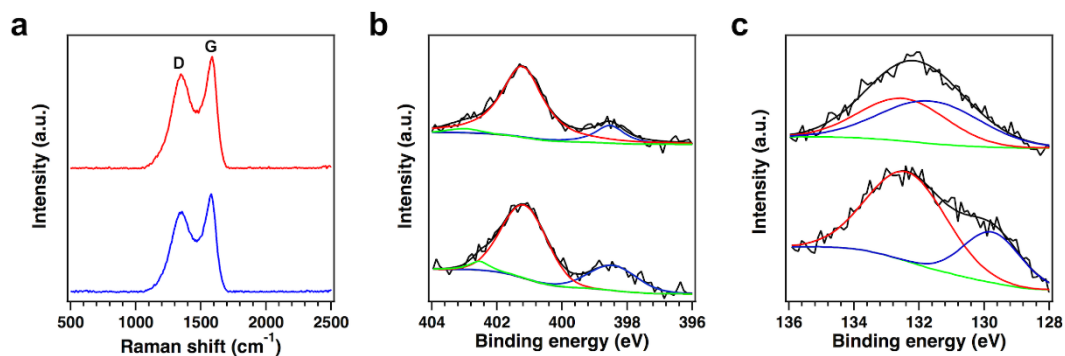


**Figure 15.** a) Raman spectra of PA@TAPT-DHTA-COF<sub>1000</sub> (blue) and PA@TAPT-DHTA-COF<sub>1000NH3</sub> (red). b) High-resolution XPS spectra of N 1s. The fitted peaks correspond to N 0 (green), N 1 (blue) and N 3 (red). c) High-resolution XPS spectra of P 2p. The fitted peaks correspond to the P–O (red) and P–C (blue) bonds. The upper is for PA@TAPT-DHTA-COF<sub>1000NH3</sub> and the lower is for PA@TAPT-DHTA-COF<sub>1000</sub>.

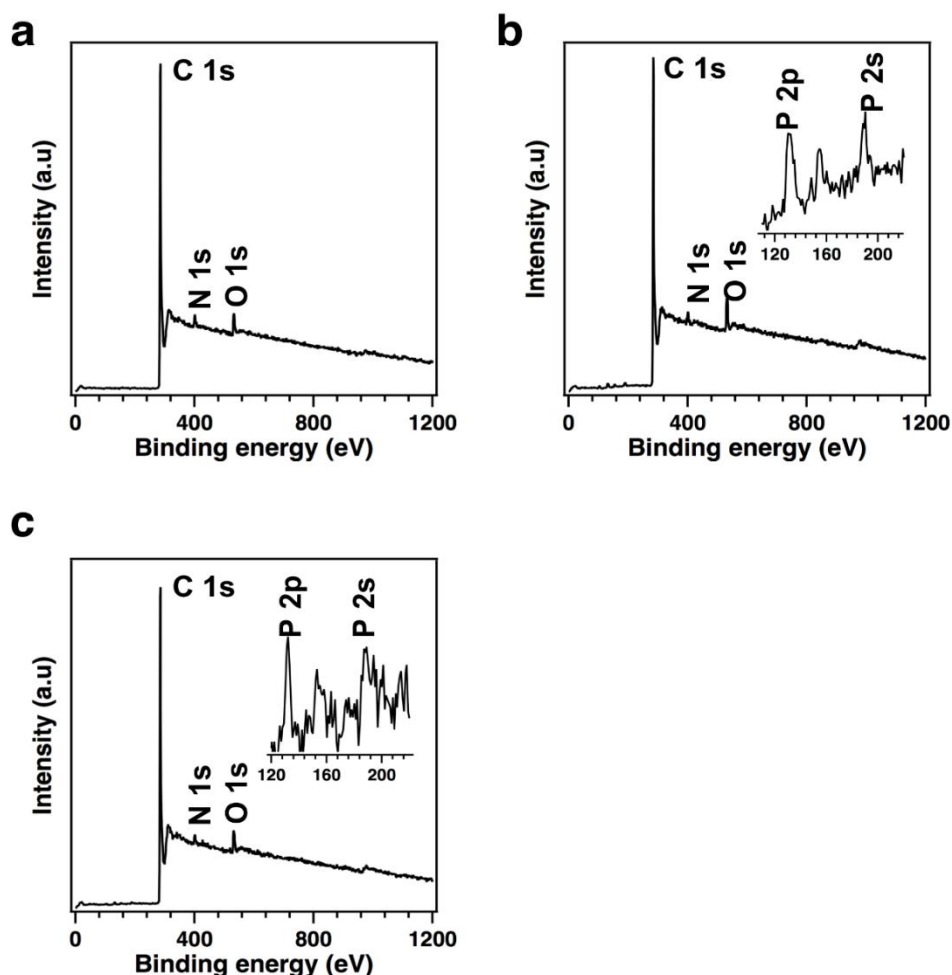


**Figure 16.** XPS spectra of a) TAPT-DHTA-COF<sub>1000</sub>, b) PA@TAPT-DHTA-COF<sub>1000</sub> and c) PA@TAPT-DHTA-COF<sub>1000NH3</sub>.

The chemical nature of PA@TAPT-DHTA-COF<sub>1000</sub> was further studied by using and X-ray photoelectron spectroscopy (XPS) and Raman spectroscopy. In Raman spectra, the G band is a characteristic feature of graphitic layers, while the D band corresponds to disordered carbons or defective graphitic structures.<sup>11</sup> The intensity ratio of these two bands ( $I_D/I_G$ ) reflects the degree of disorder for carbons. The  $I_D/I_G$  value was 0.81 for PA@TAPT-DHTA-COF<sub>1000</sub>, illustrating its high graphitization structure (Figure 15a, blue curve). In XPS spectrum, the peaks of N 1s, P 2s, P 2p, O 1s and C 1s were observed (Figure 16 and Table 2). The high-resolution N 1s spectroscopy was deconvoluted into three peaks at 398.4, 401.3 and 403.2 eV, which were assigned to corresponding pyridinic N (N 1), graphitic (N 3) and pyridinic N<sup>+</sup>-O<sup>-</sup> (N 0) nitrogen (Figure 15b).<sup>12</sup> Interestingly, the N 3 and N 1 contributed to 95.11% (68.62% for N 3 and 26.48% for N 1) of all nitrogen atoms. This exceptional content is important because these nitrogen sites enhance the conductivity of the materials, facilitate O<sub>2</sub> adsorption and weaken the O=O bonds during ORR process.<sup>1a,13</sup> Moreover, the high-resolution spectra of P 2p showed the P-C bond at 129.6 eV and the P-O bond at 132.3 eV, suggesting that P atoms were successfully doped in the 2D carbon sheets (Figure 15c).<sup>14</sup> Therefore, PA@TAPT-DHTA-COF<sub>1000</sub> was prepared as crystalline porous 2D carbon sheets with abundant edges. This unique structure originated from the PA networks that successfully template the conversion of COFs into 2D carbon sheets. Furthermore, the template PA networks created nanosized 2D layers other than aggregating or collapse. This unique 2D carbon structure offered sufficient numbers of heteroatom-doped active sites on edges that are key to ORR catalysis.

### 3.4 Electrocatalytic Performance

I investigated the ORR catalysis under alkaline conditions, because alkaline-type cells are more strategic that enable high efficiency, stability and low cost compared to proton-based fuel cells. To assess the ORR catalysis activity, cyclic voltammogram (CV) curves were recorded in an aqueous KOH solution (0.1 M) saturated with O<sub>2</sub> or nitrogen by using Ag/AgCl as the reference electrode, respectively (Figure 17a, blue curve). A cathodic peak at -0.23 V was observed for PA@TAPT-DHTA-COF<sub>1000</sub>, which reflected a catalytic activity in ORR under the O<sub>2</sub>-saturated conditions. By contrast, for the nitrogen-saturated systems under otherwise identical conditions, no obvious redox peak was observed (Figure 17a, black curve).

Based on the above results, the catalytic activity of ORR was investigated using RRDE systems in the O<sub>2</sub>-saturated aqueous KOH solution (0.1 M) at the rotation rate of 1600 rpm (Figure 17b). TAPT-DHTA-COF<sub>1000</sub> without template in the pyrolysis can catalyze ORR but had a quite low activity with an onset potential ( $E_0$ ) of  $-0.12$  V, halfwave potential ( $E_{1/2}$ ) of  $-0.29$  V and limiting diffusion current density ( $j_{\text{limit}}$ ) of  $4.0$  mA cm<sup>-2</sup>, respectively (Figure 17b, green curve; Table 1). As a control, I utilized the commercial Pt/C as the ORR catalyst under otherwise identical conditions. The Pt/C catalyst (Figure 17b, black curve) exhibited an  $E_0$  of  $-0.03$  V,  $E_{1/2}$  of  $-0.16$  V and  $j_{\text{limit}}$  of  $6.0$  mA cm<sup>-2</sup>, respectively. These comparative studies revealed that carbons formed upon direct pyrolysis of TAPT-DHTA-COF could catalyze ORR but it showed only a low catalytic activity. Unexpectedly, PA@TAPT-DHTA-COF<sub>1000</sub> (Figure 17b, blue curve; Table 1) constructed under template pyrolysis reached an  $E_0$  value at  $-0.02$  V,  $E_{1/2}$  at  $-0.19$  V and  $j_{\text{limit}}$  at  $6.5$  mA cm<sup>-2</sup>, respectively. The performance of PA@TAPT-DHTA-COF<sub>1000</sub> was close to or even better than that of the Pt/C, in terms of the current density.

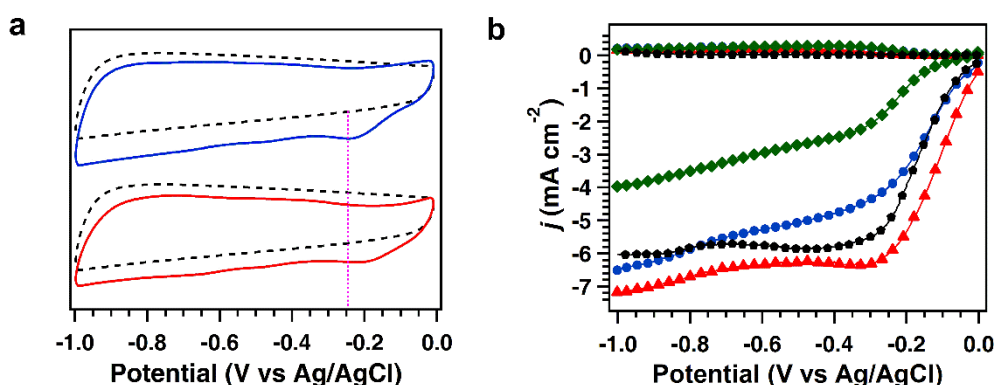


**Figure 17.** a) CV curves of PA@TAPT-DHTA-COF<sub>1000</sub> (blue) and PA@TAPT-DHTA-COF<sub>1000</sub>NH<sub>3</sub> (red) at a scan rate of  $100$  mV s<sup>-1</sup> under nitrogen (black) and O<sub>2</sub>. b) RRDE profiles at 1600 rpm by using TAPT-DHTA-COF<sub>1000</sub> (green), PA@TAPT-DHTA-COF<sub>1000</sub> (blue), PA@TAPT-DHTA-COF<sub>1000</sub>NH<sub>3</sub> (red) and Pt/C (black) electrodes in O<sub>2</sub>-saturated aqueous KOH solutions (0.1 M).

The outperformance of PA@TAPT-DHTA-COF<sub>1000</sub> originated from a synergistic structural effect. Firstly, the small-sized carbon sheets exposed numerous edges for loading enough active sites for ORR. Secondly, the high content of N 1 and N 3 improved the ORR activity drastically. Finally, the increased conductivity contributed to the fast electron transport from the electrode to catalytic sites.

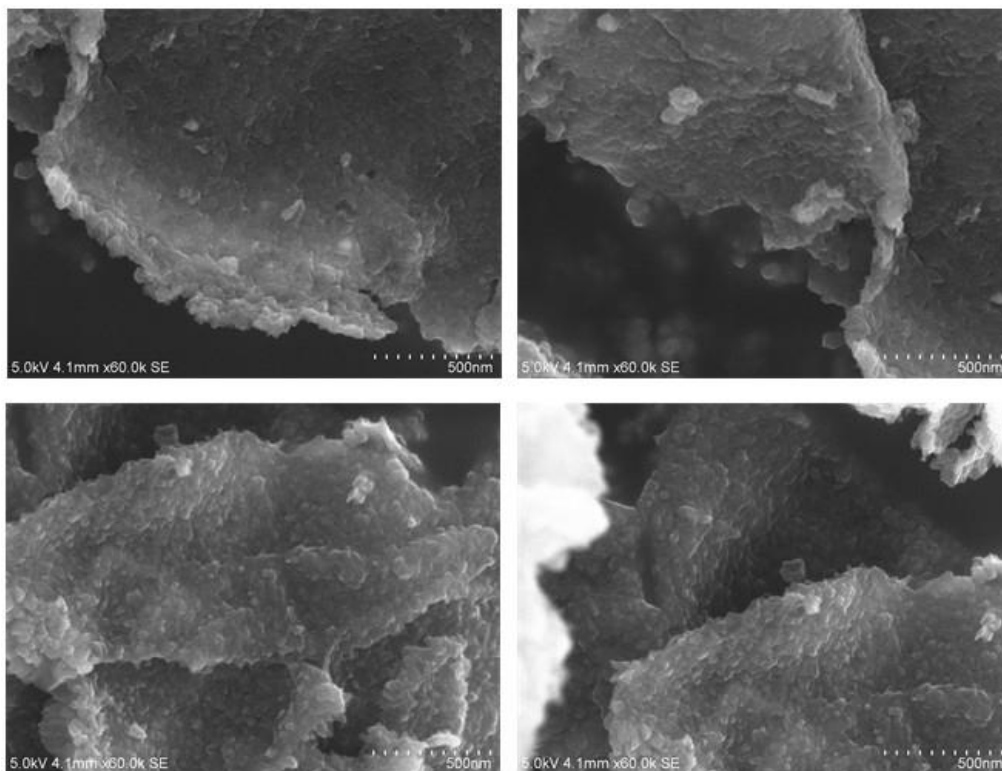


**Figure 18.** FE-SEM images of PA@TAPT-DHTA-COF<sub>1000</sub>NH<sub>3</sub> at different areas and scales.

In order to further improve the ORR activity, PA@TAPT-DHTA-COF<sub>1000</sub> was pyrolyzed in ammonia atmosphere at 900 °C to yield PA@TAPT-DHTA-COF<sub>1000</sub>NH<sub>3</sub>. The presence of ammonia in the pyrolysis could not only increase the active sites by reacting with the edge parts and oxygen on the surface but also reconstruct the porous structure.<sup>15</sup> Indeed, the effect is profound. Firstly, the atomic percentage of oxygen decreased from 2.90% to 2.37%. Secondly, the BET surface area increased from 495 to 1160 m<sup>2</sup> g<sup>-1</sup> (Figure 8a, red curve; Table 1), while the pore volume increased from 0.22 to 0.59 cm<sup>3</sup> g<sup>-1</sup> (Figure 8c). After a close look at the porosity, I observed that in contrast to PA@TAPT-DHTA-COF<sub>1000</sub> that possessed only micropores, PA@TAPT-DHTA-COF<sub>1000</sub>NH<sub>3</sub> constituted a hierarchical porous structure. PA@TAPT-DHTA-COF<sub>1000</sub>NH<sub>3</sub> consists of both micropores and mesopores (Figure 8c, filled dots; Table 1); the pore volume of micropores and mesopores was 0.14 and 0.45 cm<sup>3</sup> g<sup>-1</sup>, respectively (Figure 8c, open dots). Thirdly, in the presence of ammonia, the layered structure (Figure 13c-d, and Figure 18), and small-sized few-layer carbon sheets in different orientation were also well maintained (Figure 19).

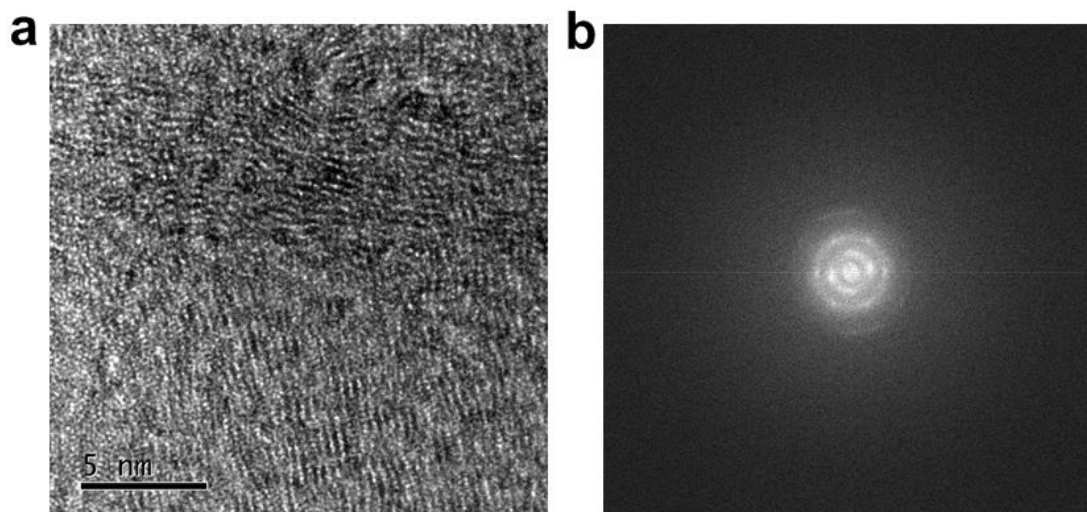


**Figure 19.** a) HR-TEM images of PA@TAPT-DHTA-COF<sub>1000NH<sub>3</sub></sub>, and b) FFT of a.

Moreover, in Raman spectra, the  $I_D/I_G$  value was almost the same (Figure 15a, red curve), which indicated the nanosized 2D graphitic structure was retained during the pyrolysis in the presence of ammonia. From the XPS analysis, the relative amount of N 3s was increased to 83.01% (Figure 15b). The high resolution XPS spectra of P 2p revealed that the proportion of P–C was increased from 29.2% to 53.5%, with the shift to higher energy position at 131.6 eV, demonstrating that the electron density of the P atoms became low and the P atoms were doped into the carbon sheets more efficiently (Figure 15c).

Surprisingly, PA@TAPT-DHTA-COF<sub>1000NH<sub>3</sub></sub> exhibited a reduction peak at  $-0.18$  V that was more positive than that ( $-0.23$  V) of PA@TAPT-DHTA-COF<sub>1000</sub> (Figure 17a, red curve), which suggested a greatly enhanced ORR catalytic activity of PA@TAPT-DHTA-COF<sub>1000NH<sub>3</sub></sub>. From the RRDE profiles (Figure 17b, red curve), the  $E_0$ ,  $E_{1/2}$  and  $j_{\text{limit}}$  values of PA@TAPT-DHTA-COF<sub>1000NH<sub>3</sub></sub> were 0 V,  $-0.11$  V and  $7.2$  mA cm<sup>-2</sup>, respectively. Thus, PA@TAPT-DHTA-COF<sub>1000NH<sub>3</sub></sub> achieved a more positive  $E_0$  by 30 mV, a higher  $E_{1/2}$  by 50 mV and a greatly enhanced  $j_{\text{limit}}$  by even  $1.2$  mA cm<sup>-2</sup> than those of Pt/C. This observation indicated that PA@TAPT-DHTA-COF<sub>1000NH<sub>3</sub></sub> that was derived from 2D COF was far superior to Pt/C in catalyzing ORR.

The superior performance of PA@TAPT-DHTA-COF<sub>1000NH<sub>3</sub></sub> compared to PA@TAPT-DHTA-COF<sub>1000</sub> likely originated from the different porous structures. The mesoporous structure in PA@TAPT-DHTA-COF<sub>1000NH<sub>3</sub></sub> acted as interconnected highways that could provide quick and full transport towards or from the catalytic sites for both reactant and products.<sup>16</sup>

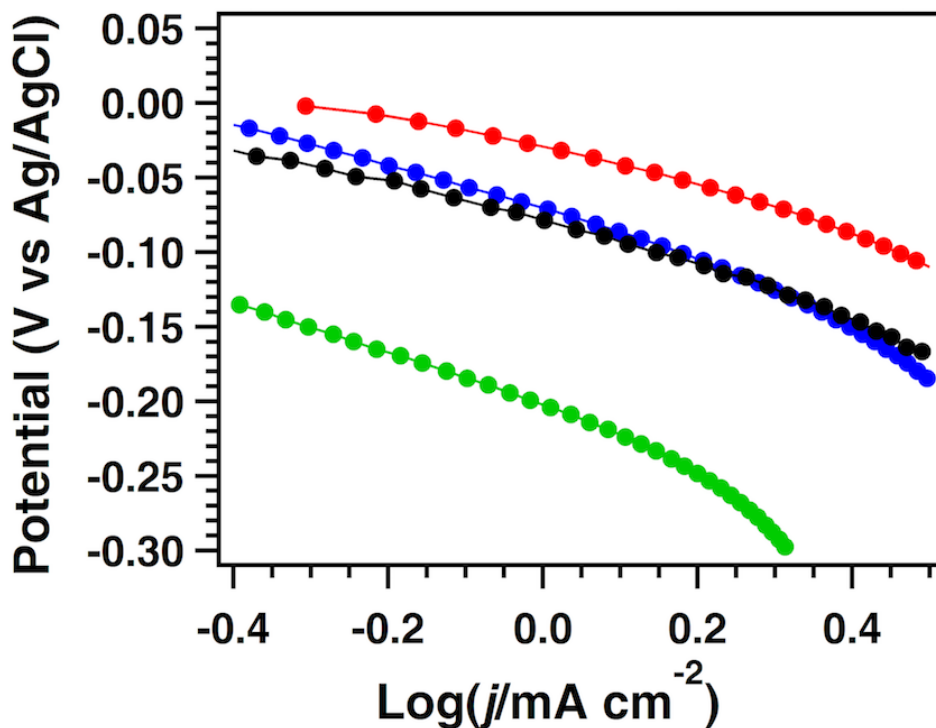


**Figure 20.** Tafel plots of PA@TAPT-DHTA-COF<sub>1000</sub>NH<sub>3</sub> (red), PA@TAPT-DHTA-COF<sub>1000</sub> (blue), Pt-C (black), and TAPT-DHTA-COF<sub>1000</sub> (green).

Along this line of study, I investigated the ORR activity using the Tafel slope (Figure 20). PA@TAPT-DHTA-COF<sub>1000</sub>NH<sub>3</sub> exhibited a much smaller Tafel slope of 110 mV decade<sup>-1</sup> (Table 1) than PA@TAPT-DHTA-COF<sub>1000</sub> (146 mV decade<sup>-1</sup>) and Pt-C (121 mV decade<sup>-1</sup>). This result again confirmed that PA@TAPT-DHTA-COF<sub>1000</sub>NH<sub>3</sub> was superior to Pt/C and of PA@TAPT-DHTA-COF<sub>1000</sub>. Table 3 summarized the ORR performance of carbon catalysts reported up to date. PA@TAPT-DHTA-COF<sub>1000</sub>NH<sub>3</sub> was far superior to previously reported carbon catalysts (Table 3).

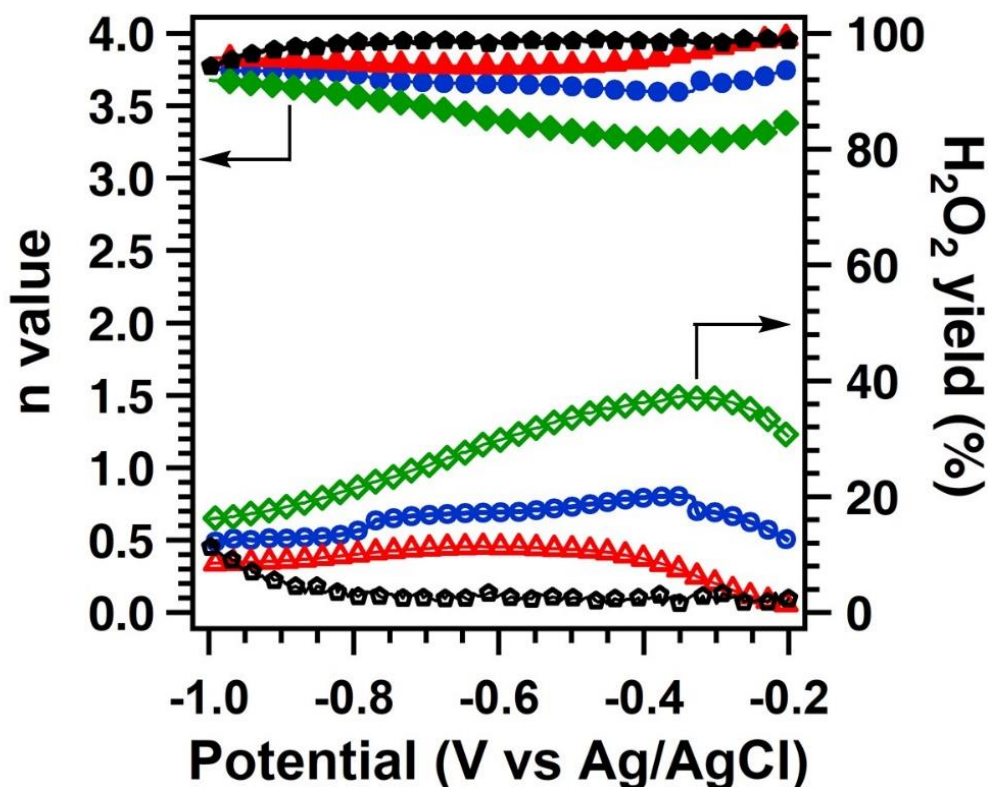


**Figure 21.** Number ( $n$ ) of electrons transferred, and  $\text{H}_2\text{O}_2$  yield plots for TAPT-DHTA- $\text{COF}_{1000}$  (green), PA@TAPT-DHTA- $\text{COF}_{1000}$  (blue), PA@TAPT-DHTA- $\text{COF}_{1000\text{NH}_3}$  (red) and Pt/C (black) calculated from the RRDE measurements.

To identify the ORR pathway, the electron transfer number ( $n$  value) was evaluated using the RRDE method. The  $n$  values of PA@TAPT-DHTA- $\text{COF}_{1000\text{NH}_3}$  were ranged from 3.77 to 3.98 (Table 1) with low  $\text{H}_2\text{O}_2$  yields (1.5%–11%) between  $-0.2$  and  $-1$  V (Figure 21, red curve), which are higher than PA@TAPT-DHTA- $\text{COF}_{1000}$  (Figure 21, blue curve) and TAPT-DHTA- $\text{COF}_{1000}$  (Figure 21, green curve). The linear scan voltammogram (LSV) curves showed the performance of the PA@TAPT-DHTA- $\text{COF}_{1000\text{NH}_3}$  at different rotation rates from 400 to 1600 rpm measured by RDE (Figure 22). Based on these LSV results, the Koutechy–Levich (K–L) plot (Figure 23) showed a linear relationship, and the  $n$  values were close to 4, which was similar to the values based on the RRDE measurements. Thus, these results clearly revealed a high selectivity of TAPT-DHTA- $\text{COF}_{1000\text{NH}_3}$  catalyst towards the four-electron reduction reaction of oxygen.

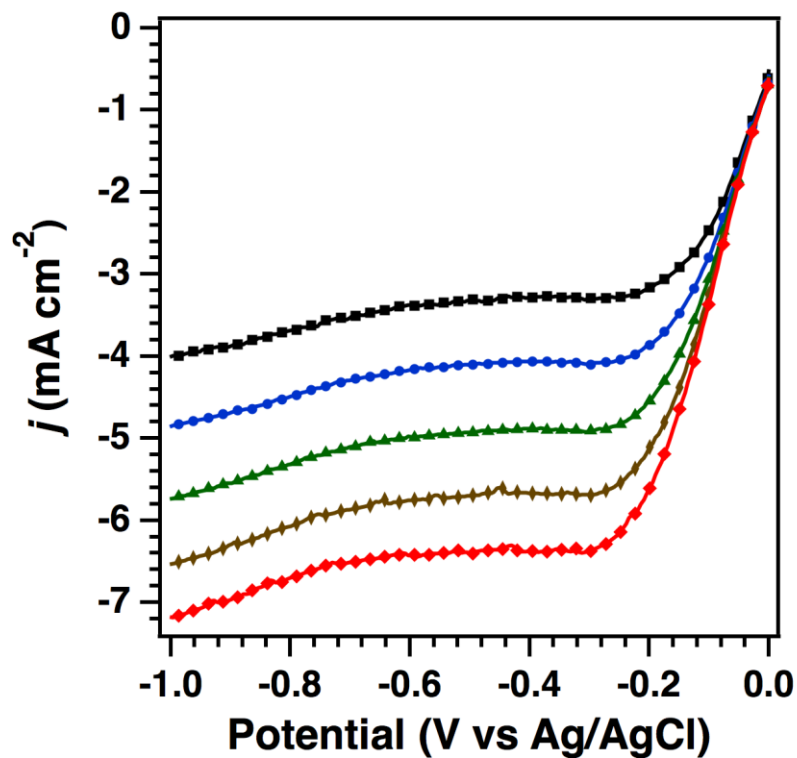


**Figure 22.** LSV curves of PA@TAPT-DHTA-COF<sub>1000NH3</sub> at different rotation rates of 400 (black), 625 (blue), 900 (green), 1225 (brown) and 1600 rpm (red) on RDE.

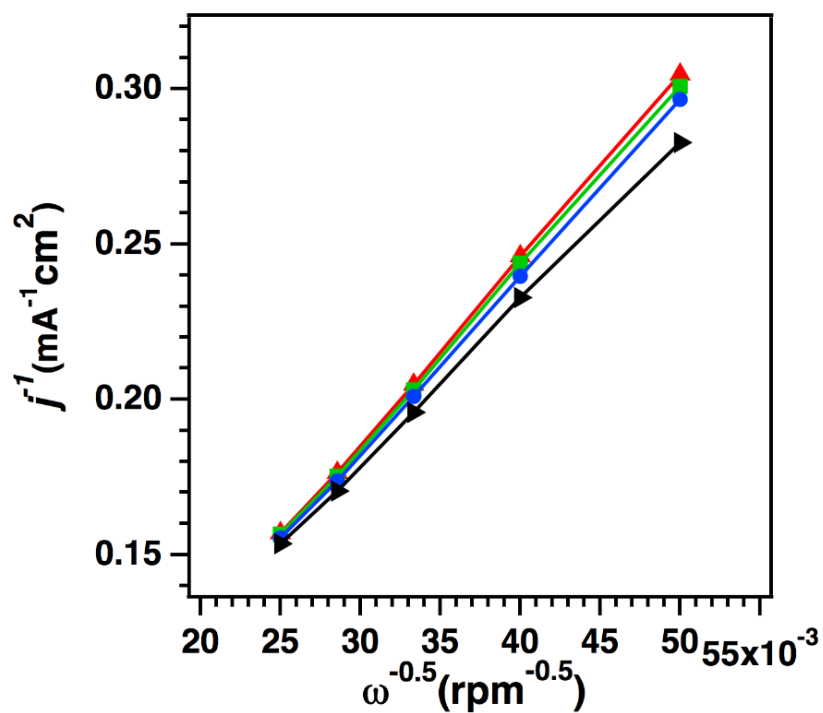


**Figure 23.** K-L plots of PA@TAPT-DHTA-COF<sub>1000NH3</sub> at different potentials, -0.4 V (red), -0.5 V (green), -0.6 V (blue) and -0.7 V (black).  $\omega$  is the angular rotation speed according to Figure 23.

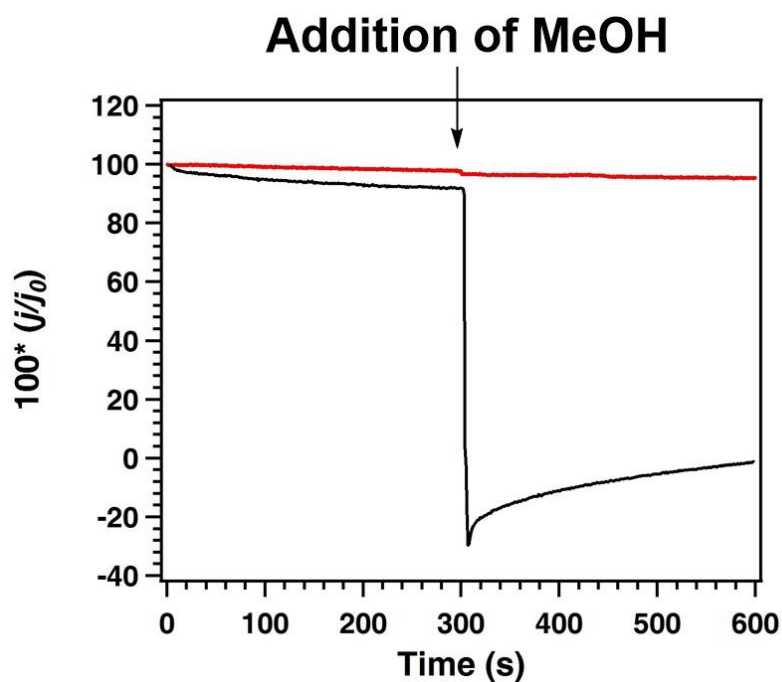


**Figure 24.** Chronoamperometric curves of PA@TAPT-DHTA-COF<sub>1000NH<sub>3</sub></sub> (red) and Pt/C (black) upon addition of methanol.

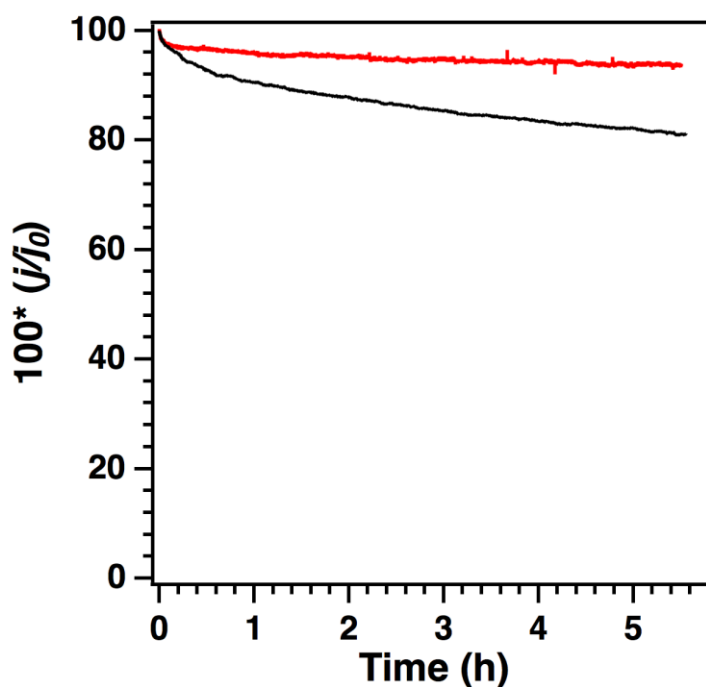


**Figure 25.** Chronoamperometric curves of PA@TAPT-DHTA-COF<sub>1000NH<sub>3</sub></sub> (red) and Pt/C (black) tested at the potential of  $-0.8$  V (vs Ag/AgCl) for 20000 s in O<sub>2</sub>-saturated aqueous KOH solution (0.1 M) at a rotation rate of 1600 rpm.

The durability and methanol-tolerance properties of the TAPT-DHTA-COF<sub>1000NH<sub>3</sub></sub> were evaluated. Upon addition of methanol, no obvious changes in the current density

were observed for the TAPT-DHTA-COF<sub>1000NH3</sub> catalyst. By contrast, under otherwise identical conditions, Pt/C exhibited a greatly decreased current density (Figure 24). Moreover, I compared the stability of TAPT-DHTA-COF<sub>1000NH3</sub> and Pt/C catalysts at  $-0.8$  V for 5.5 h at a rotation rate of 1600 rpm (Figure 25). TAPT-DHTA-COF<sub>1000NH3</sub> retained 95% of the original current density; however, Pt/C exhibited only 80% of the original current density. Therefore, TAPT-DHTA-COF<sub>1000NH3</sub> was also superior to the Pt/C catalyst in terms of methanol-tolerance ability and durability.

In addition to ORR, TAPT-DHTA-COF<sub>1000NH3</sub> serves as a catalyst that promotes the oxygen evolution reaction (OER). The OER performance was continuously investigated in an aqueous KOH solution (0.1 M). Figure 26 (red curve) showed the rapidly increased anodic current above 0.3 V, which is much lower than those of other metal-free OER catalysts<sup>17</sup> and metal-based OER catalysts, such as CoO/N-doped graphene<sup>18</sup> and Co<sub>3</sub>O<sub>4</sub>/N-doped-graphene<sup>19</sup>. TAPT-DHTA-COF<sub>1000NH3</sub> exhibited a current density of 10 mA cm<sup>-2</sup> at 0.97 V, which was 10 times higher than that 1.01 mA cm<sup>-2</sup> of Pt/C.

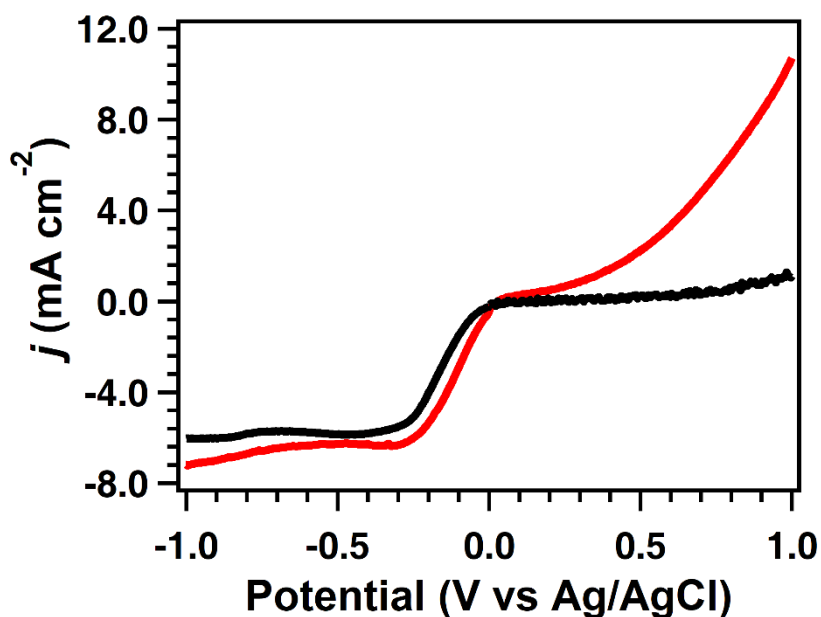


**Figure 26.** LSV curves of PA@TAPT-DHTA-COF<sub>1000NH3</sub> (red) and Pt/C (black) catalysts in OER on RDE at 1600 rpm in aqueous KOH solution (0.1 M).

### 3.5 Conclusion

In summary, I demonstrated that the merge of two strategies, i.e. the exploration of 2D COFs as porous precursors and the development of PA as a template for pyrolysis, enables the production of nanosized 2D carbons that possess high conductivity,

hierarchical porosity and abundant heteroatom catalytic edges. The COFs-derived carbons function as catalysts achieved ultrahigh performance with exceptional onset and half-wave potentials, and high limit current density and robust cyclic performance. Given with the predesignability and broad structural diversity of COFs, our results suggest a new materials platform for designing metal-free carbon catalysts that play important roles in next-generation energy storage and conversion devices.

### 3.6 Experimental Sections

**Characterizations.** A JASCO model FT IR-6100 infrared spectrometer was used to conduct Fourier-transform infrared (FT IR) experiments. A Mettler-Toledo model TGA/SDTA851e was used for TGA measurements under nitrogen, by heating to 1100 °C at a rate of 10 °C min<sup>-1</sup>. A Rigaku model RINT Ultima III diffractometer was used for PXRD measurement, from  $2\theta = 1^\circ$  up to  $60^\circ$  with  $0.02^\circ$  increment. At 77 K, nitrogen sorption isotherms were conducted on a 3Flex surface characterization analyzer with the Micrometrics Instrument Corporation model. X-ray photoelectron spectroscopy (XPS) experiments were carried out on an AXIS Ultra DLD system from Kratos with Al K $\alpha$  radiation as X-ray source for radiation. Raman spectra were obtained using a Bruker SEN TERRA spectrometer employing a semiconductor laser ( $\lambda = 532$  nm). FE-SEM images were obtained on a FEI Sirion-200 or Hitachi high technologies (SU-6600) field-emission scanning electron microscope at an electric voltage of 5 KV. EDX and elemental mapping were acquired using a NOVA Nano SEM 230 microscope (FEI, USA). Transmission Electron Microscopes (TEM) images were obtained by JEM-2100. HR-TEM images and FFT were obtained on a JEOL model of ARM200F.

**Reagents.** Mesitylene, dioxane, and tetrahydrofuran, (99.5%) were purchased from Wako Chemicals. Phytic acid solution (50%) was purchased from TCI. TAPT and DHTA were synthesized according to the report.<sup>20</sup>

**Table 1.** The porosity and electrochemical catalytic activity in ORR.

Sample	BET surface areas ( $\text{m}^2 \text{g}^{-1}$ )	Pore volume ( $\text{cm}^3 \text{g}^{-1}$ )	Pore size (nm)	$E_0$ (V)	$E_{1/2}$ (V)	$j_{\text{limit}}$ ( $\text{mA cm}^{-2}$ )	n value	$\text{H}_2\text{O}_2$ yield (%)	Tafel slope ( $\text{mV decade}^{-1}$ )
TAPA-DHTA-COF	2170	1.08	3.1	–	–	–	–	–	–
PA@TAPT-DHTA-COF	21	<0.01							
TAPT-DHTA-COF <sub>1000</sub>	20	<0.01		–0.12	–0.29	4.0	3.26-3.68	16-37	190
PA@TAPT-DHTA-COF <sub>1000</sub>	495	0.22	0.7-1.6	–0.02	–0.19	6.5	3.60-3.76	12-20	146
PA@TAPT-DHTA-COF <sub>1000NH3</sub>	1160	0.59	0.5- 6	0	–0.11	7.2	3.77-3.98	1.5-11	110
Pt-C	–	–	–	–0.03	–0.16	6.0	3.75-3.98	1.3-12	121

**Table 2.** Atomic elemental content and nitrogen ratios calculated from XPS results.

Samples	C atom%	O atom%	N atom%	P atom%	N0 pyridinic $\text{N}^+-\text{O}^- \text{N}$	N1 pyridinic N	N3 graphitic N
PA@TAPT-DHTA-COF <sub>1000</sub>	93.92	2.90	2.20	0.98	4.89%	26.48%	68.63%
PA@TAPT-DHTA-COF <sub>1000NH3</sub>	95.12	2.37	1.86	0.65	2.42%	14.57%	83.10%
TAPT-DHTA-COF <sub>1000</sub>	96.13	2.04	1.83	0	7.03%	20.53%	72.84%

**Table 3.** ORR parameters of state-of-the-art ORR carbon-based catalysts (also including metal-carbon catalysts) in O<sub>2</sub>-saturated aqueous KOH solutions (0.1 M) at a rate constant of 1600 rpm. Values in parenthesis are given by subtracting the corresponding values of the Pt/C control.

Catalysts	Onset potential (V)	Half-wave potential (V)	$j_{\text{limit}}$ (mA cm <sup>-2</sup> )	Reference
<b>PA@TAPT-DHTA-COF<sub>1000NH3</sub></b>	<b>0.98</b> (+30 mV)	<b>0.87</b> (+ 50 mV)	<b>7.2</b> (+ 1.2)	<b>This work</b>
Pt/C (Control)	0.95	0.82	6.0	
<b>Co<sub>3</sub>O<sub>4</sub>/rmGO</b>	0.88	0.79 (-70 mV)	<5	<i>Nat. Mater.</i> <b>10</b> , 780-786 (2011)
<b>Co<sub>3</sub>O<sub>4</sub>/N-rmGO</b>	0.88	0.83 (-30 mV)	5	
Pt/C (Control)	N/A	0.86	N/A	
<b>Fe-Pc-CNT</b>	N/A	0.915 (+35 mV)	<6 (0)	<i>Nat. Commun.</i> <b>4</b> , 2076 (2013).
Pt/C (Control)	N/A	0.88	<6	
<b>Mesoporous N-doped carbon</b>	N/A	0.87 (+ 20 mV)	<6 (0)	<i>Nat. Commun.</i> <b>5</b> , 4974 (2014)
Pt/C (Control)	N/A	0.85	<6	
<b>NPMC-1000</b>	0.94	0.85	6 (0)	<i>Nat. Nanotechnol.</i> <b>10</b> , 444-452 (2015)
Pt/C (Control)	N/A	N/A	6	
<b>NCNTF</b>	0.97	0.87 (+ 30 mV)	<6 (+1)	<i>Nature Energy</i> <b>1</b> , 15006 (2016).
Pt/C (Control)	N/A	0.84	<5	
<b>P-doped graphene</b>	0.92	N/A	4.18	<i>Adv. Mater.</i> <b>25</b> , 4932-4937 (2013)
Pt/C (Control)	0.95	N/A	N/A	
<b>CNTs/carbon hybrid</b>	0.92 (-60 mV)	0.82 (-30 mV)	5.5 (-0.5)	<i>Angew. Chem. Int. Ed.</i> <b>53</b> , 4102-4106 (2014)
Pt/C (Control)	0.98	0.85	6	
<b>NDCN-22</b>	0.97	0.86 (+ 30 mV)	5.45 (-0.33)	<i>Angew. Chem. Int. Ed.</i> <b>53</b> , 1570-1574 (2014)
Pt/C (Control)	0.96	0.83	5.78	
<b>Fe-N/C-800</b>	0.92 (-30 mV)	0.81 (-10 mV)	6.06 (+0.5)	<i>J. Am. Chem. Soc.</i> <b>136</b> , 11027-11033 (2014)
Pt/C (Control)	0.95	0.82	<5.5	
<b>C-COP-P-Co</b>	0.98	N/A	<6 (+0.5)	<i>Angew. Chem. Int. Ed.</i> <b>53</b> , 2433-2437 (2014)
Pt/C (Control)	0.98	N/A	<5	
<b>Zn(eIm)2TPIP</b>	0.91	0.78	<5.5	<i>Adv. Mater.</i> <b>26</b> , 1093-1097 (2014)
Pt/C (Control)	N/A	N/A	N/A	
<b>GNPCSS-800</b>	0.97	N/A	6	<i>Angew. Chem. Int. Ed.</i> <b>53</b> , 14235-39 (2014)
Pt/C (Control)	N/A	N/A	N/A	

<b>P-Z8-Te-1000</b>	0.88 (+10 mV)	0.79 (+30 mV)	6 (+0.5)	<i>J. Am. Chem. Soc.</i> <b>136</b> , 14385-14388 (2014)
Pt/C (Control)	0.87	0.76	5.5	
<b>NC-900</b>	0.83 (-120 mV)	N/A	4.0	<i>J. Am. Chem. Soc.</i> <b>136</b> , 6790-6793 (2014)
Pt/C (Control)	0.95	N/A	N/A	
<b>CIO-2</b>	0.8	0.74	6.5 (+1)	<i>J. Am. Chem. Soc.</i> <b>136</b> , 17530-17536 (2014)
Pt/C (Control)	N/A	N/A	5.5	
<b>CPM-99Fe/C</b>	0.95	0.80 (-20 mV)	<5.5 (+0.5)	<i>J. Am. Chem. Soc.</i> <b>137</b> , 2235-2238 (2015)
Pt/C (Control)	0.98	0.82	5	
<b>SG</b>	0.88	0.66	4.0	<i>Angew. Chem. Int. Ed.</i> <b>54</b> , 1888-1892 (2015)
Pt/C (Control)	N/A	N/A	N/A	
<b>Fe-N-CNFs</b>	0.96 (-30 mV)	0.84 (-20 mV)	5.12	<i>Angew. Chem. Int. Ed.</i> <b>54</b> , 8179-8183 (2015)
Pt/C (Control)	0.99	0.86	5.12	
<b>Co<sup>II</sup>-A-rG-O</b>	0.88 (-120 mV)	0.81 (-70 mV)	<5.5 (-0.5)	<i>Angew. Chem. Int. Ed.</i> <b>54</b> , 12622-12626 (2015)
Pt/C (Control)	1.0	0.88	<6	
<b>P-CNCo-20</b>	0.91 (-30 mV)	0.84 (+20 mV)	6.0 (+0.2)	<i>Adv. Mater.</i> <b>27</b> , 5010-5016 (2015)
Pt/C (Control)	0.94	0.82	5.8	
<b>NGM</b>	0.89 (-50 mV)	0.77 (-30 mV)	6.41 (+1.44)	<i>Adv. Mater.</i> <b>28</b> , 6845-6851 (2016)
Pt/C (Control)	0.94	0.80	4.97	
<b>Co-TA-800</b>	0.95 (+10 mV)	N/A	5.60 (0)	<i>Angew. Chem. Int. Ed.</i> <b>55</b> , 12470-12474 (2016)
Pt/C (Control)	0.94	N/A	5.6	
<b>Co<sub>3</sub>O<sub>4</sub>/NPGC</b>	0.97	0.84	5.84	<i>Angew. Chem. Int. Ed.</i> <b>55</b> , 4977-4982 (2016)
Pt/C (Control)	N/A	N/A	N/A	
<b>M-CMP2-800</b>	N/A	0.84 (-10 mV)	5.4 (-0.1)	<i>Angew. Chem. Int. Ed.</i> <b>55</b> , 6858-6863 (2016)
Pt/C (Control)	N/A	0.85	5.5	
<b>Bowl-like mesoporous carbon</b>	0.87	0.77	4.8 (-0.2)	<i>J. Am. Chem. Soc.</i> <b>138</b> , 11306-11311 (2016)
Pt/C (Control)	N/A	N/A	5	
<b>S, N-Fe/N/C-CNT</b>	N/A	0.85 (+30 mV)	6.68 (+0.68)	<i>Angew. Chem. Int. Ed.</i> <b>56</b> , 610-614 (2017)
Pt/C (Control)	N/A	0.82	6	

Ag/AgCl potential was converted to RHE using following Nerest equation:

$$E \text{ (RHE)} = E \text{ (Ag/AgCl)} + 0.059 \times \text{pH} + 0.205$$

**Reference**

1. (a) L. Dai, Y. Xue, L. Qu, H. J. Choi, J. B. Baek, *Chem. Rev.* **2015**, *115*, 4823-4892. (b) Y. Jiao, Y. Zheng, M. Jaroniec, S. Z. Qiao, *Chem. Soc. Rev.* **2015**, *44*, 2060-2086. (c) Y. Z. Chen, C. Wang, Z. Y. Wu, Y. Xiong, Q. Xu, S.-H. Yu, H.-L. Jiang, *Adv. Mater.* **2015**, *27*, 5010-5016. (d) M. Shao, Q. Chang, J. P. Dodelet, R. Chenitz, *Chem. Rev.* **2016**, *116*, 3594-3657. (e) Y.-J. Wang, N. Zhao, B. Fang, H. Li, X. T. Bi, H. Wang, *Chem. Rev.* **2015**, *115*, 3433-3467. (f) L. Jiao, Y. Hu, H. Ju, C. Wang, M.-R. Gao, Q. Yang, J. Zhu, S.-H. Yu, H.-L. Jiang, *J. Mater. Chem. A*, **2017**, *5*, 23170-23178. (g) W. Xia, A. Mahmood, R. Zou, Q. Xu, *Energy Environ. Sci.* **2015**, *8*, 1837-1866.
2. M. K. Debe, *Nature* **2012**, *486*, 43-51.
3. (a) W. Xia, A. Mahmood, Z. B. Liang, R. Q. Zou, S. J. Guo, *Angew. Chem. Int. Ed.* **2016**, *55*, 2650-2676. (b) M. Zhou, H.-L. Wang, S. Guo, *Chem. Soc. Rev.* **2016**, *45*, 1273-1307. (c) G. Huang, L. Yang, X. Ma, J. Jiang, S.-H. Yu, H.-L. Jiang, *Chem. Eur. J.* **2016**, *22*, 3470-3477. (d) A. Aijaz, N. Fujiwara, Q. Xu, *J. Am. Chem. Soc.* **2014**, *136*, 6790-6793. (e) Q.-L. Zhu, W. Xia, T. Akita, R. Zou, Q. Xu, *Adv. Mater.* **2016**, *28*, 6391-6398. (f) Q.-L. Zhu, W. Xia, L.-R. Zheng, R. Zou, Z. Liu, Q. Xu, *ACS Energy Lett.* **2017**, *2*, 504-511.
4. A. Shen, Y. Zou, Q. Wang, R. A. W. Dryfe, X. Huang, S. Dou, L. Dai, S. Wang, *Angew. Chem. Int. Ed.* **2014**, *53*, 10804-10808.
5. (a) N. Huang, P. Wang, D. Jiang, *Nat. Rev. Mater.* **2016**, *1*, 16068, doi: 10.1038/natrevmats2016.68. (b) X. Feng, X. Ding, D. Jiang, *Chem. Soc. Rev.* **2012**, *41*, 6010-6022. (c) E. Jin, M. Asada, Q. Xu, S. Dalapati, M. A. Addicoat, M. A. Brady, H. Xu, T. Nakamura, T. Heine, Q. Chen, D. Jiang, *Science* **2017**, *357*, 673-676. (d) S. Dalapati, M. Addicoat, S. Jin, T. Sakurai, J. Gao, H. Xu, S. Irle, S. Seki, D. Jiang, *Nat. Commun.* **2015**, *6*, 7786, doi: 10.1038/ncomm8786. (e) C. R. Mulzer, L. Shen, R. P. Bisbey, J. R. McKone, N. Zhang, H. D. Abruña, W. R. Dichtel, *ACS Cent. Sci.* **2016**, *2*, 667-673. (f) C. R. DeBlase, K. E. Silberstein, T. T. Truong, H. D. Abruña, W. R. Dichtel, *J. Am. Chem. Soc.* **2013**, *135*, 16821-16824. (g) V. S. Vyas, F. Haase, L. Stegbauer, G. Savasci, F. Podjaski, C. Ochsenfeld, B. V. Lotsch, *Nat. Commun.* **2015**, *6*, 8508, doi: 10.1038/ncomm9508.
6. (a) H. Xu, S. Tao, D. Jiang, *Nat. Mater.* **2016**, *15*, 722-726. (b) H. Xu, J. Gao, D. Jiang, *Nat. Chem.* **2015**, *7*, 905-912. (c) X. Chen, M. Addicoat, S. Irle, A. Nagai,

- D. Jiang, *J. Am. Chem. Soc.* **2016**, *135*, 546-549. (d) S. Lin, C. S. Diercks, Y.-B. Zhang, N. Kornienko, E. M. Nichols, Y. Zhao, A. R. Paris, D. Kim, P. Yang, O. M. Yaghi, C. J. Chang, *Science*, **2015**, *349*, 1208-1213. (e) H.-S. Xu, S.-Y. Ding, W.-K. An, H. Wu, W. Wang, *J. Am. Chem. Soc.* **2016**, *138*, 11489-11492.
7. (a) Y.-B. Huang, P. Pachfule, J.-K. Sun, Q. Xu, *J. Mater. Chem. A* **2016**, *4*, 4273-4279. (b) G. Abellan, J. Romero, D. Rodriguez-San-Miguel, A. Ribera, R. Mas-Balleste, T. F. Otero, I. Manet, F. Liscio, F. Zamora, E. Coronado, *J. Mater. Chem. A* **2017**, *5*, 4343-4351. (c) L. Chen, L. Zhang, Z. Chen, H. Liu, R. Luque, Y. Li, *Chem. Sci.* **2016**, *7*, 6015-6020.
8. (a) J. W. F. To, Z. Chen, H. Yao, J. He, K. Kim, H.-H. Chou, L. Pan, J. Wilcox, Y. Cui, Z. Bao, *ACS Cent. Sci.* **2015**, *1*, 68-76. (b) J. Zhang, L. Qu, G. Shi, J. Liu, J. Chen, L. Dai, *Angew. Chem. Int. Ed.* **2016**, *55*, 2230-2234. (c) J. Zhang, Z. Zhao, Z. Xia, L. Dai, *Nat. Nanotechnol.* **2015**, *10*, 444-452.
9. (a) A. Halder, S. Kandambeth, B. P. Biswal, G. Kaur, N. C. Roy, M. Addicoat, J. K. Salunke, S. Banerjee, K. Vanka, T. Heine, S. Verma, R. Banerjee, *Angew. Chem. Int. Ed.* **2016**, *55*, 7806-7810. (b) X. Chen, M. Addicoat, E. Jin, L. Zhai, H. Xu, N. Huang, Z. Guo, L. Liu, S. Irlle, D. Jiang, *J. Am. Chem. Soc.* **2015**, *137*, 3241-3247.
10. F. Razmjooei, K. P. Singh, E. J. Bae, J.-S. Yu, *J. Mater. Chem. A* **2015**, *3*, 11031-11039.
11. A. C. Ferrari, D. M. Basko, *Nat. Nanotechnol.* **2013**, *8*, 235-246.
12. D. Guo, R. Shibuya, C. Akiba, S. Saji, T. Kondo, J. Nakamura, *Science* **2016**, *351*, 361-365.
13. R. Liu, D. Wu, X. Feng, K. Müllen, *Angew. Chem. Int. Ed.* **2010**, *49*, 2565-2569.
14. (a) C. H. Choi, S. H. Park, S. I. Woo, *ACS Nano* **2012**, *6*, 7084-7091. (b) R. Li, Z. Wei, X. Gou, W. Xu, *RSC Adv.* **2013**, *3*, 9978-9984.
15. H. W. Liang, X. Zhuang, S. Bruller, X. Feng, K. Müllen, *Nat. Commun.* **2014**, *5*, 4973, doi: 101038/ncomm5973.
16. G. A. Ferrero, K. Preuss, A. B. Fuertes, M. Sevilla, M. M. Titirici, *J. Mater. Chem. A* **2016**, *4*, 2581-2589.
17. (a) T. Y. Ma, J. R. Ran, S. Dai, M. Jaroniec, S. Z. Qiao, *Angew. Chem. Int. Ed.* **2015**, *54*, 4646-4650. (b) T. Y. Ma, S. Dai, M. Jaroniec, S. Z. Qiao, *Angew. Chem. Int. Ed.* **2014**, *53*, 7281-7285.
18. X. Han, F. Cheng, T. Zhang, J. Yang, Y. Hu, J. Chen, *Adv. Mater.* **2014**, *26*, 2047-2051.

19. Y. Liang, Y. Li, H. Wang, J. Zhou, J. Wang, T. Regier, H. Dai, *Nat. Mater.* **2011**, *10*, 780-786.
20. (a) A. Halder, S. Kandambeth, B. P. Biswal, G. Kaur, N. C. Roy, M. Addicoat, J. K. Salunke, S. Banerjee, K. Vanka, T. Heine, S. Verma, R. Banerjee, *Angew. Chem. Int. Ed.* **2016**, *55*, 7806-7810. (b) X. Chen, M. Addicoat, E. Jin, L. Zhai, H. Xu, N. Huang, Z. Guo, L. Liu, S. Irlle, D. Jiang, *J. Am. Chem. Soc.* **2015**, *137*, 3241-3247.

**Chapter 4. Design and Synthesis of Covalent Organic  
Frameworks for Lithium Ion Conduction**

## Abstract

To solve the safety, leak and stability problems associated with liquid electrolytes in lithium ion batteries, a lot of efforts have been made about poly(ethylene oxide)-salt complexes (PEO). Most of studies focus on nonporous polymers to improve electrolyte performance of PEO, which are without special structure and lacking optimizing ion transport pathways. Here I design and synthesize all-solid lithium electrolytes based on two-dimensional (2D) COF by skeleton functional method, in which the one-dimensional (1D) pores enable the ordering of the oligoethylene oxide chains on the pore walls that provide a pathway for lithium ion conduction. The targeted COF (TPB-BMTP-COF) was synthesized by condensation of 2,5-bis ((2-methoxyethoxy) methoxy) terephthalaldehyde (BMTP) and 1,3,5-tri(4-aminophenyl) benzene (TPB) under solvothermal conditions. TPB-BMTP-COF exhibits a high Brunauer–Emmett–Teller (BET) surface of  $1750 \text{ m}^2 \text{ g}^{-1}$ . It consists of mesopores with size of 3.0 nm, whereas the pore value is  $0.96 \text{ cm}^{-3} \text{ g}^{-1}$ . In addition, TPB-BMTP-COF is thermally stable up to 300 °C under nitrogen. These oligoethylene oxide side chains are capable of formation complex with lithium ion and thus provide an aligned structure for the ion transport across the 1D channels.  $\text{LiClO}_4@$ TPB-BMTP-COF exhibited a high conductivity of  $6.9 \times 10^{-3} \text{ S cm}^{-1}$  at 100 °C. More importantly, the electrolyte shows excellent cyclic and thermal stability.

## 4.1 Introduction

Poly(ethylene oxide)-based (PEO) electrolytes are now becoming increasingly attractive for lithium ion batteries (LIBs), because of their excellent properties such as safety, mechanical properties, and flexibility.<sup>1</sup> Various attempts have been made to develop solid polymer electrolytes, and most of studies focus on nonporous polymers, such as synthesizing grafted PEO copolymers, preparing crosslinking networks or copolymers.<sup>2</sup> However, the resultant polymer electrolytes are without special structure, lacking optimizing ion diffusion pathway, resulting in hindering the lithium ion fast transport. On the other hand, the well-defined pore structure materials have already been adopted to improve the stability of LIBs by suppressing growth of lithium dendrites, including modifying electrodes with regular pores or channels, or loading electrolyte solvents into the pores for preparing solid-like electrolytes.<sup>3</sup> Nonetheless, these approaches could not enable to solve the leak and safety problems triggered from liquid electrolytes fundamentally. Thus, preparing solid electrolytes with well-defined pore structure provides an excellent method to resolve the drawbacks of electrolyte solvents and optimize the ion diffusion and transport pathways of PEO-based materials simultaneously. Unfortunately, it is difficult to dissociate and transport lithium ion for ordered porous polymers analogy PEO, which hinders them work as all solid-state electrolytes. Till now, fabrication of solid electrolytes from porous materials with straightforward channels is still under exploration.

Covalent organic frameworks (COFs) are linked by different functional organic building blocks with various linkages as expect. By virtue of the diversity of topology design diagram, availability of building units and accessibility of linkages, various COFs with different topologies, skeletons and pores have been designed and synthesized.<sup>4</sup> Their ordered skeletons and polygon pores render COFs able to explore outstanding properties and functions such as semiconducting, chemsensor, heterogeneous catalysis and energy storage.<sup>5</sup> Especially, the aligned channels of COFs enable to load proton carries and exhibit excellent proton conductivity.<sup>6</sup> Furthermore, the well-defined one-dimensional (1D) electronic pathways facilitate efficient electronic conduction, and enable to shorten the distance for lithium ion diffusion.<sup>7</sup> Accordingly, COFs are suitable candidates for outstanding lithium ion conductivity. However, the low ionic conductivity hampers the complexes of COFs and lithium ion carriers to work for solid lithium ion electrolytes.<sup>8</sup> It is crucial to reduce the resistances

and improve ionic conductivity for developing superior solid polymer electrolytes by fully taking advantages of 1D pore channels.

Herein, I demonstrated two COFs (TPB-DMTP-COF and TPB-BMTP-COF) for lithium ion conduction (Figure 1), both of them possess outstanding crystallinity and porosity. The Brunauer–Emmett–Teller (BET) surface areas of TPB-DMTP-COF and TPB-BMTP-COF were 2658 and 1746 m<sup>2</sup> g<sup>-1</sup>, with the pore volume of 1.34 cm<sup>3</sup> g<sup>-1</sup> and 0.96 cm<sup>3</sup> g<sup>-1</sup>. In addition, methoxy and oligoethylene oxide groups were incorporated in the walls of the two COFs, which enabled to donate electron to lithium ion. As a result, lithium ion can be conducted in the channels more easily. Moreover, oligoethylene oxide groups, as units of PEO, can further help the lithium hopping within the channels. The resultant materials exhibit superior lithium ion conductivity, and thermal stability.

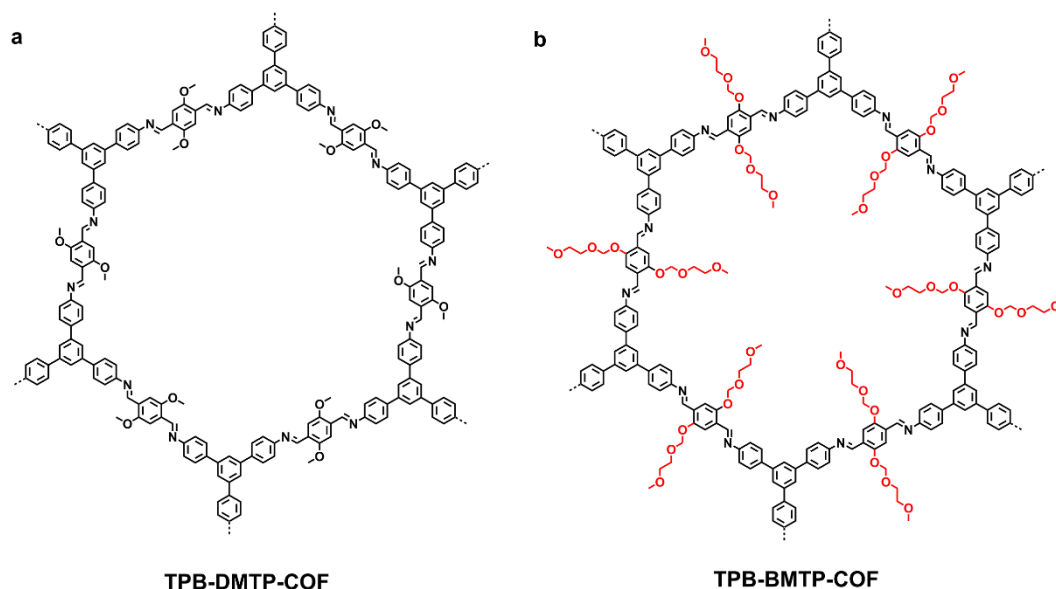


**Figure 1.** The chemical structure of a) TPB-DMTP-COF and b) TPB-BMTP-COF.

## 4.2 Materials and Methods

**Synthesis of TPB-DMTP-COF.** First, I added building blocks (TPB (28 mg, 0.08 mmol) and DMTP (23.3 mg, 0.12 mmol)) in a Pyrex tube (10 mL), and then added a mixture of BuOH/*o*-DCB (0.5 mL/0.5 mL), and HAc solution (6 M, 0.1 mL). I degassed the tube by freeze-pump-thaw for three cycles. The tube was sealed and heated at 120 °C for 3 days. I collected the precipitate by filtering, and then subjected to Soxhlet extraction with THF for 24 h. The sample was dried at 120 °C under vacuum overnight to obtain TPB-DMTP-COF in 82% yield (Figure 2).

**Synthesis of TPB-BMTP-COF.** First, I added monomers (TPB (28 mg, 0.08 mmol) and BMTP (41 mg, 0.12 mmol)) in a Pyrex tube (10 mL), then added solvents of BuOH/*o*-DCB (0.5 mL/0.5 mL), and HAc (6 M, 0.1 mL). The tube was then degassed by three freeze-pump-thaw cycles. I sealed the tube and kept it at 120 °C for 3 days. I collected the precipitate by filtering, and then subjected to Soxhlet extraction with THF for 24 h. The sample was dried at 120 °C under vacuum overnight to obtain TPB-BMTP-COF in 78% yield.

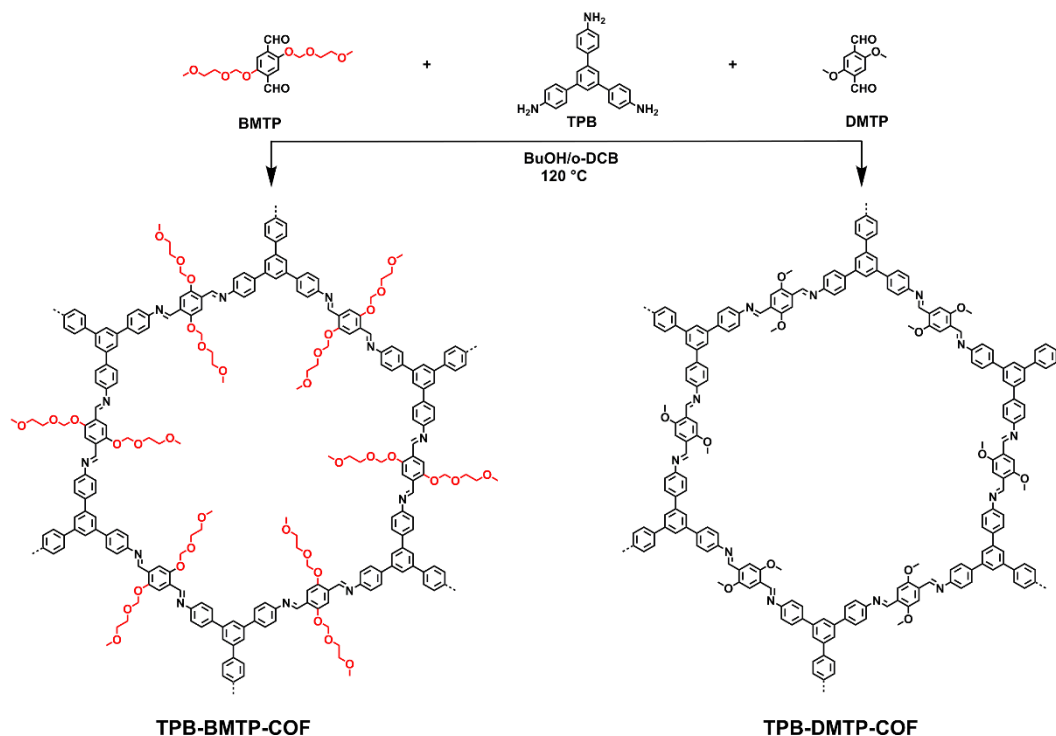


**Figure 2.** Synthesis of TPB-DMTP-COF and TPB-BMTP-COF by solvothermal method.

**Synthesis of TPB-TP-COF.** First, I added monomers (TPB (0.08 mmol, 28 mg) and TP (0.120 mmol, 16.1 mg)) in a Pyrex tube (10 mL), then added solvents of BuOH/*o*-DCB (0.5 mL/0.5 mL), and HAc (6 M, 0.1 mL). The tube was then degassed by three freeze-pump-thaw cycles. I sealed the tube and kept it at 120 °C for 3 days. I collected the precipitate by filtering, and then subjected to Soxhlet extraction with THF for 24 h. The powder was collected and then dried at 120 °C under vacuum overnight to give TPB-TP-COF in a yield of 83%.

**Synthesis of Li@TPB-DMTP-COF.** First, I degassed TPB-DMTP-COF (100 mg) under vacuum at 100 °C for 3 h, and then cooled down at 25 °C. I added LiClO<sub>4</sub> solution (324 mg in 2 mL MeOH) to the TPB-DMTP-COF sample and kept mixture stirring at

25 °C for 3 h. I removed MeOH under vacuum at 25 °C for 1 hour, 70 °C for 2 hours. The hybrid was then active at 90 °C overnight to prepare Li@TPB-DMTP-COF.

**Synthesis of Li@TPB-BMTP-COF.** First, I degassed TPB-BMTP-COF (100 mg) under vacuum at 100 °C for 3 h, and then cooled down at 25 °C. I added LiClO<sub>4</sub> solution (232 mg in 2 mL MeOH) to the TPB-BMTP-COF sample and kept mixture stirring at 25 °C for 3 h. I removed MeOH under vacuum at 25 °C for 1 hour, 70 °C for 2 hours. The hybrid was then active at 90 °C overnight to prepare Li@TPB-BMTP-COF.

**Synthesis of Li@TPB-TP-COF.** First, I degassed TPB-TP-COF (100 mg) under vacuum at 100 °C for 3 h, and then cooled down at 25 °C. I added LiClO<sub>4</sub> solution (24.2 mg in 1 mL MeOH) to the TPB-TP-COF sample and kept mixture stirring at 25 °C for 3 h. I removed MeOH under vacuum at 25 °C for 1 hour, 70 °C for 2 hours. The hybrid was then active at 90 °C overnight to prepare Li@TPB-TP-COF.

**Synthesis of Li&PEO@TPB-DMTP-COF.** First, I degassed TPB-DMTP-COF (100 mg) and PEO (Mn = 400, 81.7 mg) under vacuum at 100 °C for 3 h, and then cooled it down to 25 °C. I added LiClO<sub>4</sub> solution (114 mg in 2 mL MeOH) to the TPB-TP-COF sample and kept mixture stirring at 25 °C for 3 h. I removed MeOH under vacuum at 25 °C for 1 hour, 70 °C for 2 hours. The hybrid was then active at 90 °C overnight to prepare Li&PEO@TPB-DMTP-COF.

### 4.3 Characterization of COFs and Li@COFs

TPB-DMTP-COF and TPB-BMTP-COF were synthesized in the same condition. The pore structure of prepared COFs was investigated firstly. From the nitrogen-sorption isotherm curves, TPB-DMTP-COF exhibited a rapid uptake at a low pressure of  $P/P_0$ , followed by a sharp step between  $P/P_0 = 0.15$  and  $0.25$  (Figure 3a, blue curve). The isotherm was described as type-IV isotherm, confirming the mesoporous structure. The BET surface area of TPB-DMTP-COF was high to  $2658 \text{ m}^2 \text{ g}^{-1}$ . The pore size of the COF was 3.26 nm (Figure 3c), with a pore volume of  $1.34 \text{ cm}^3 \text{ g}^{-1}$  (Figure 3b).

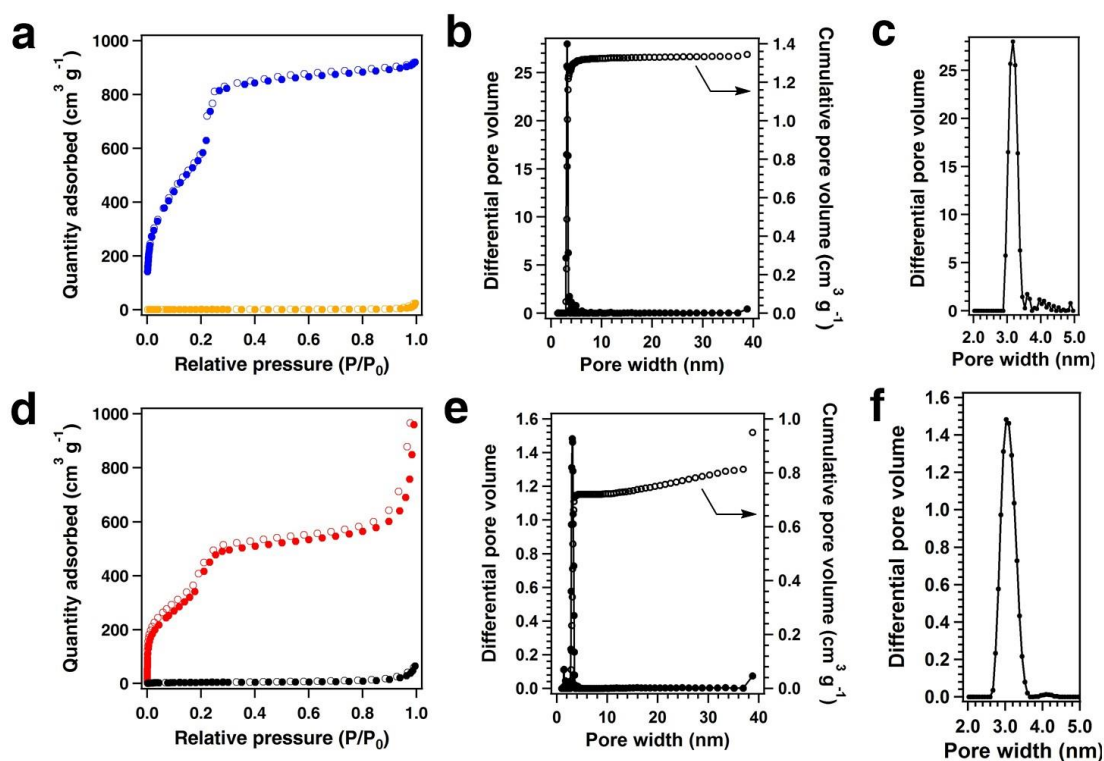


**Figure 3.** a) Nitrogen sorption isotherm profiles of TPB-DMTP-COF (blue) and Li@TPB-DMTP-COF (yellow). b) Pore size (black) and pore size distribution (red) profiles of TPB-DMTP-COF. c) The pore size distribution profiles of TPB-DMTP-COF from 2 to 5 nm. d) Nitrogen sorption isotherm profiles of TPB-BMTP-COF (red) and Li@TPB-BMTP-COF (black). e) Pore size (black) and pore size distribution (red) profiles of TPB-BMTP-COF. f) The pore size distribution profiles of TPB-BMTP-COF from 2 to 5 nm.

When the methoxy group was replaced by short ethylene oxide chains incorporated into the pore walls, TPB-BMTP-COF possessed typical mesoporous character from the nitrogen-sorption isotherm curves, corresponding to the pore structure of TPB-DMTP-COF. The BET surface area decreased to  $1746 \text{ m}^2 \text{ g}^{-1}$  (Figure 3d, red curve). Because of the existence of chains in the pores, the pore size reduced to 3.02 nm (Figure 3f), and the pore volume was  $0.96 \text{ cm}^3 \text{ g}^{-1}$  (Figure 3e).

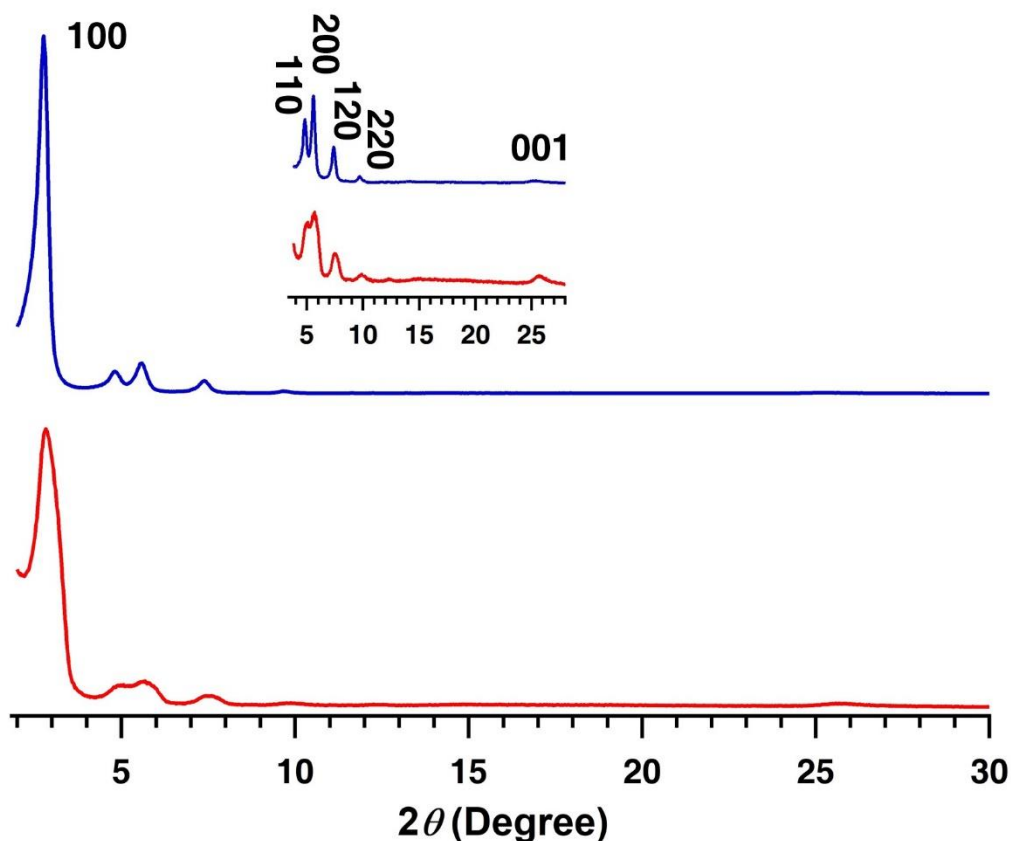


**Figure 4.** PXRD curves of TPB-DMTP-COF (blue) and TPB-BMTP-COF (red).

The crystallinity of COFs was investigated by powder X-ray diffraction (PXRD). From the PXRD patterns, peaks of TPB-DMTP-COF at  $2.76^\circ$ ,  $4.82^\circ$ ,  $5.60^\circ$ ,  $7.42^\circ$ ,  $9.70^\circ$ , and  $25.2^\circ$ , were from the (100), (110), (200), (210), (220), and (001) facets, respectively (Figure 4, blue curve). TPB-DMTP-COF adopted AA stacking model.<sup>6a</sup> With the long chains on the walls of channels, all of the corresponding peak positions of TPB-BMTP-COF (Figure 4, red curves) exhibited a positive shift, at  $2.82^\circ$ ,  $5.04^\circ$ ,  $5.73^\circ$ ,  $7.45^\circ$ ,  $9.97^\circ$ , and  $25.7^\circ$ , in accordance with the changes of pore size. The experimentally observed curve agreed well with the Pawley-refined PXRD curve as confirmed by their negligible difference (Figure 5; Table 1 and 2). Thus, TPB-BMTP-COF adopted the same AA stacking model as TPB-DMTP-COF. Therefore, TPB-DMTP-COF and TPB-BMTP-COF possessed high crystallinity and were stacked in the AA model.

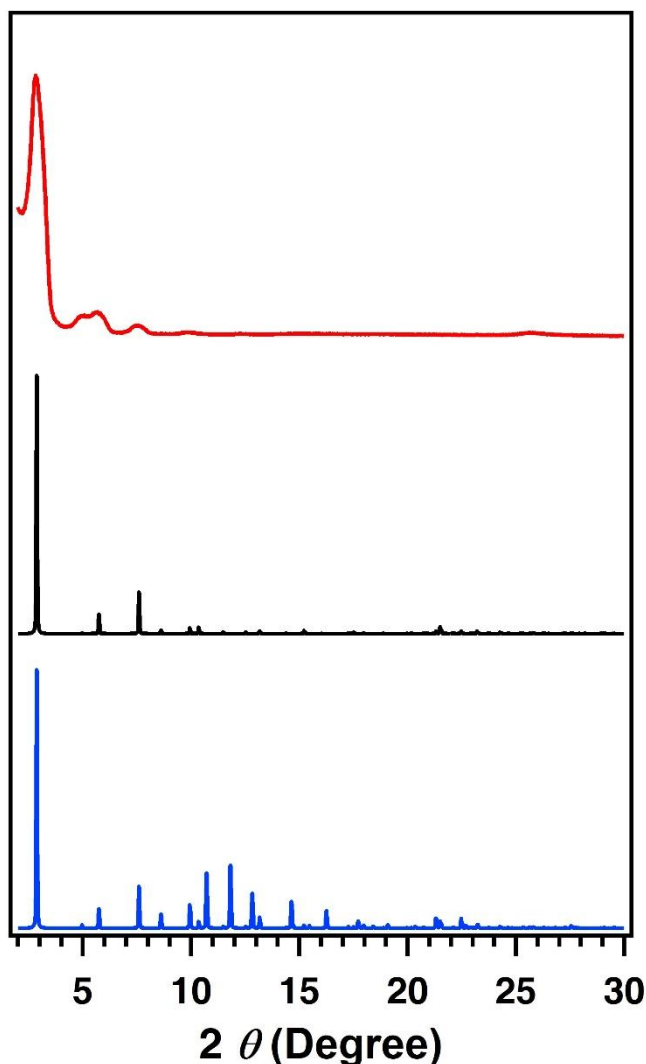


**Figure 5.** PXR D patterns of TPB-BMTP-COF, experimentally observed (red), simulated using AA (black) and AB stacking modes (blue), with  $R_{wp} = 6.32\%$ ,  $R_p = 4.56\%$ .

The thermal stability of the COFs was conducted by the thermogravimetric analysis (TGA) measurement under nitrogen. From TGA curves, TPB-DMTP-COF was thermal stable up to 400 °C (Figure 6), whereas there was no decomposition observed for TPB-BMTP-COF before 300 °C. The weaker thermal stability was from the decomposition of chains.

Thus, the two mesoporous COFs have high pore volume, thermal stability and crystallinity, while the 1D channels adapted with different functional groups. Such COFs are ideal platforms to load lithium salt, and the functional group on the walls promote effectively lithium ion fast transport.

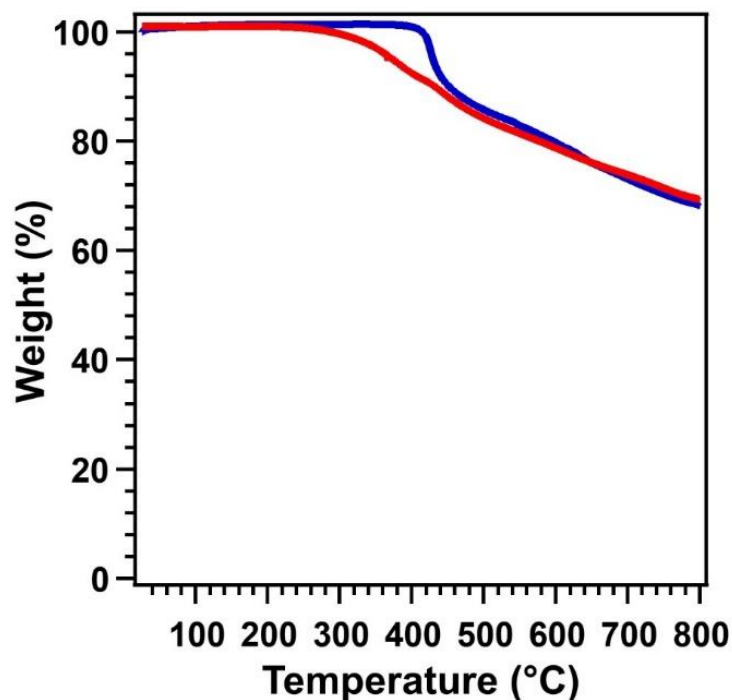


**Figure 6.** TGA curves of TPB-DMTP-COF (blue), and TPB-BMTP-COF (red).

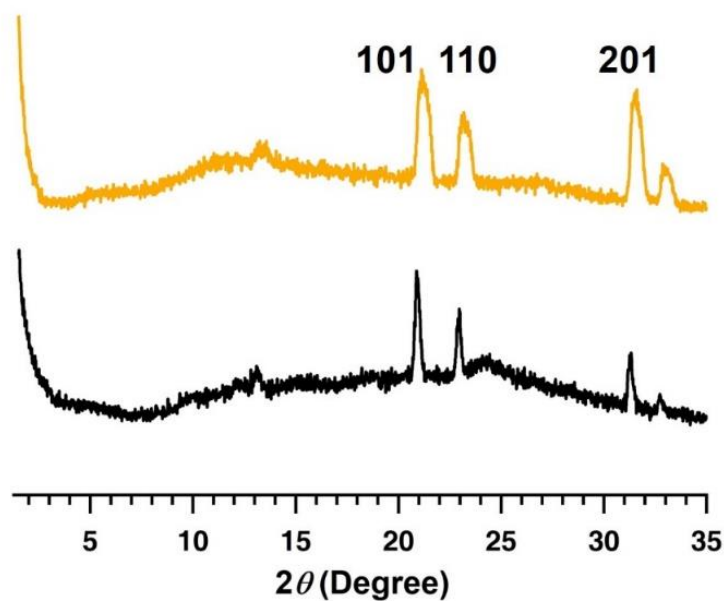


**Figure 7.** PXRD curves of Li@TPB-DMTP-COF (yellow) and Li@TPB-BMTP-COF (black).

On the basis of the 1D mesoporous channels, TPB-DMTP-COF and TPB-BMTP-COF can accommodate LiClO<sub>4</sub> in their pores. To investigate the LiClO<sub>4</sub> fully loaded in the pores, nitrogen sorption isotherm experiments were firstly conducted. Upon loading LiClO<sub>4</sub> in the COFs (Li@TPB-DMTP-COF and Li@TPB-BMTP-COF), the BET

surface areas declined to about  $20 \text{ m}^2 \text{ g}^{-1}$  for them (Figure 3a, yellow curve and Figure 3d, black curve), and almost no pores could be observed. From the PXRD results, the peak assigned to (100) faces disappeared, with arising peaks at  $21^\circ$ ,  $23^\circ$  and  $31^\circ$ , which were accompanied to (101), (110), and (201) faces of  $\text{LiClO}_4$  (Figure 7).<sup>9</sup>

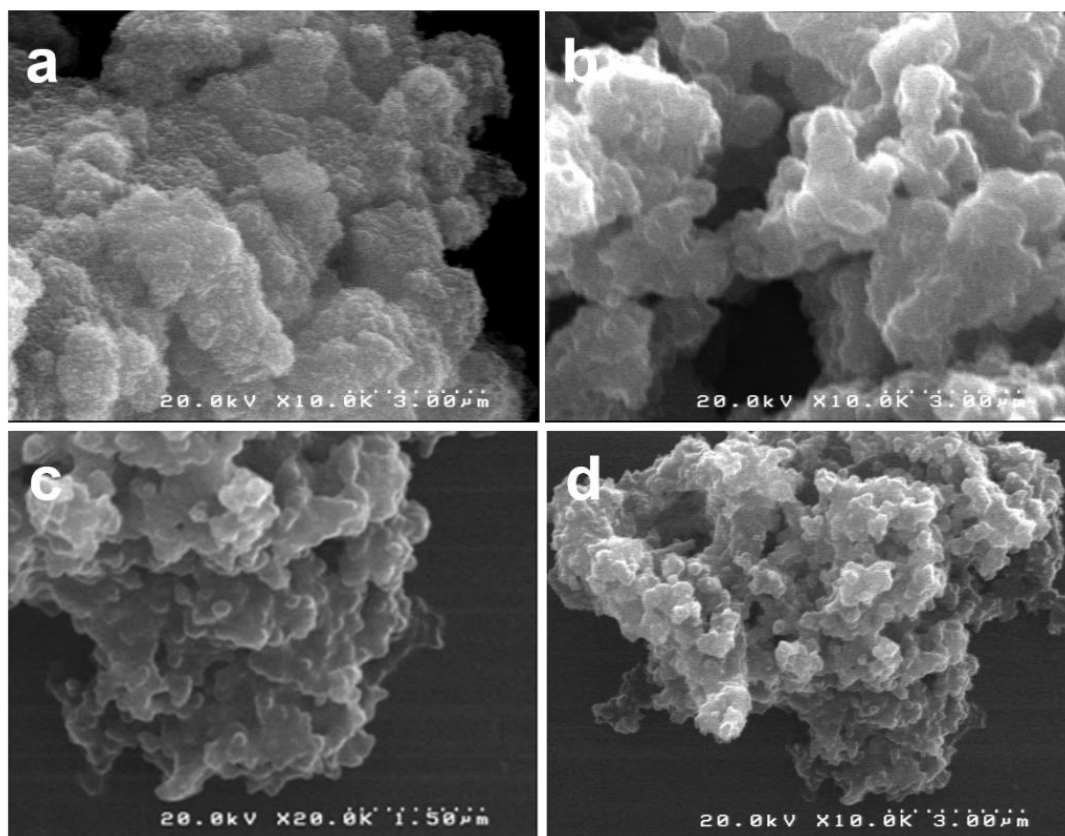


**Figure 8.** FE-SEM images of a) TPB-DMTP-COF, b) Li@TPB-DMTP-COF, c) TPB-BMTP-COF and d) Li@TPB-BMTP-COF.

From the Field-emission scanning electron microscopy (FE-SEM) images, the morphology of these two COFs did not change, and no free  $\text{LiClO}_4$  particles aggregated on the surface could be observed, further indicated all the lithium sources were successfully loaded in the pores (Figure 8). These results suggested that pore was fully occupied by lithium salt. Upon loading  $\text{LiClO}_4$ , Fourier-transform infrared (FT IR) spectra of Li@TPB-DMTP-COF and Li@TPB-BMTP-COF revealed the peak at about  $2900 \text{ cm}^{-1}$  assigned from aliphatic CH stretching ethylene oxide chains, or methoxy group (Figure 9a and 9b).<sup>9</sup> Moreover, the new bands at  $625$  and  $1089 \text{ cm}^{-1}$  were assigned to  $\text{ClO}_4^{-1}$ .

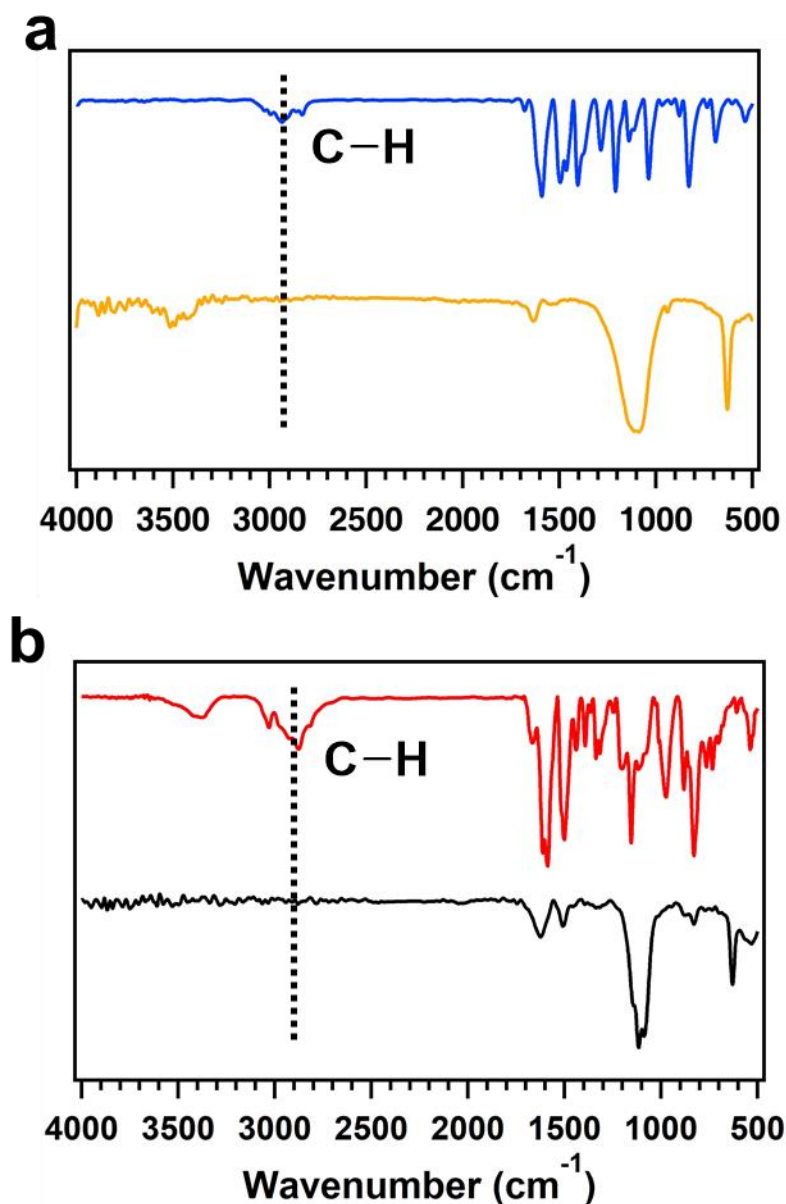


**Figure 9.** FT IR spectra of a) TPB-DMTP-COF (blue), Li@TPB-DMTP-COF (yellow) and b) TPB-BMTP-COF (red), Li@TPB-BMTP-COF (black).

In addition, Li@TPB-DMTP-COF and Li@TPB-BMTP-COF were thermal stability until 100 °C under nitrogen from TGA curves (Figure 10). More importantly, with loading LiClO<sub>4</sub> and keeping in the air for over one month, the BET surface areas of TPB-DMTP-COF and TPB-BMTP-COF exhibited just slightly decreased to about 2450 and 1600 m<sup>2</sup> g<sup>-1</sup> respectively (Figure 11). These results further verified the superior long-time stability of the complexes of lithium salt and COFs.

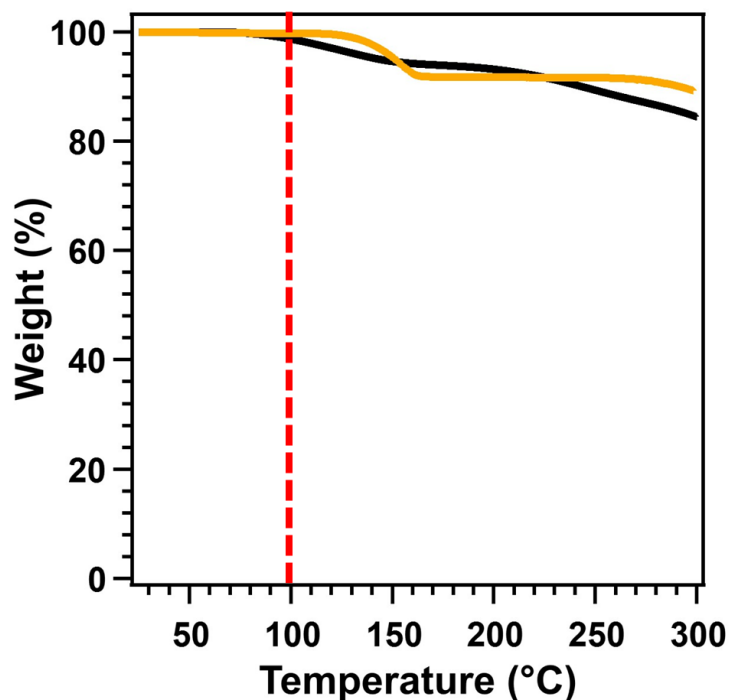


**Figure 10.** TGA curves of Li@TPB-DMTP-COF (yellow) and Li@TPB-BMTP-COF (black).

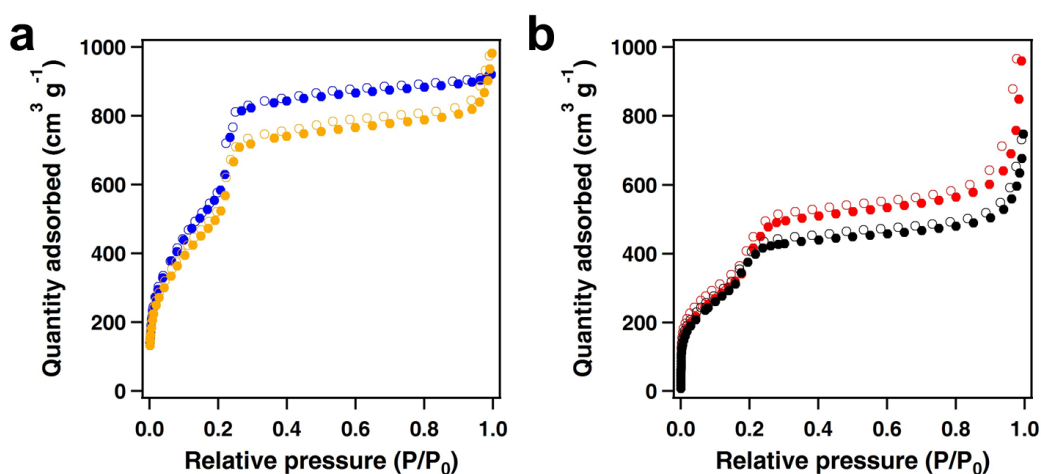


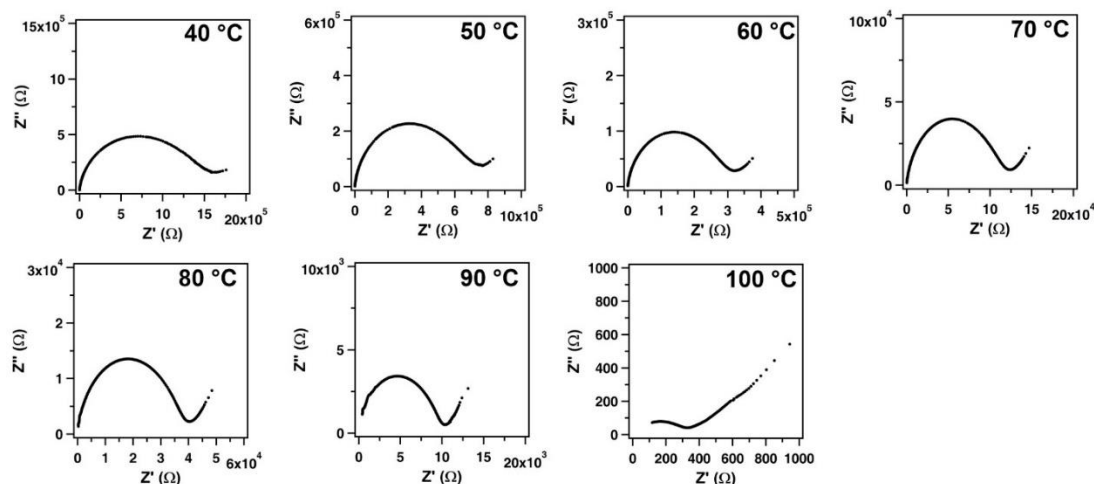
**Figure 11.** a) Nitrogen sorption isotherm profiles of TPB-DMTP-COF (blue) and TPB-DMTP-COF treated with LiClO<sub>4</sub> (yellow) at room temperature under air for 1 month. b) Nitrogen sorption isotherm profiles of TPB-DMTP-COF (red) and TPB-BMTP-COF treated with LiClO<sub>4</sub> (black) at room temperature under air for 1 month.

Thus, both of the prepared COFs have fully loaded the lithium salt in the pore channels, and the excellent stability meets the requirements of polymer electrolytes.

#### 4.4 Results and Discussion

With fully loading LiClO<sub>4</sub> in the channels, the Li@TPB-DMTP-COF and Li@TPB-

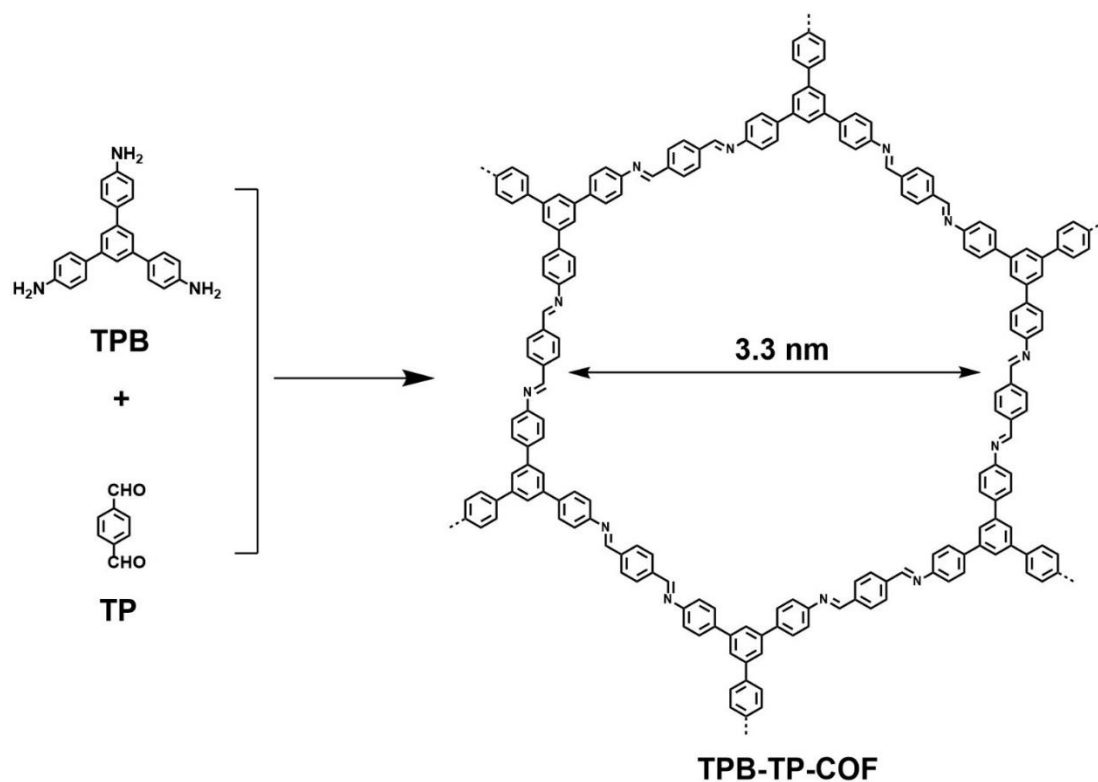
BMTP-COF were prepared for pellets for conductivity performance under over 40 MP for 2 hours. No crush could be observed, which indicated good mechanical strength of our materials. The conductivities of Li@TPB-DMTP-COF and Li@TPB-BMTP-COF were measured by using alternating-current impedance spectroscopy.



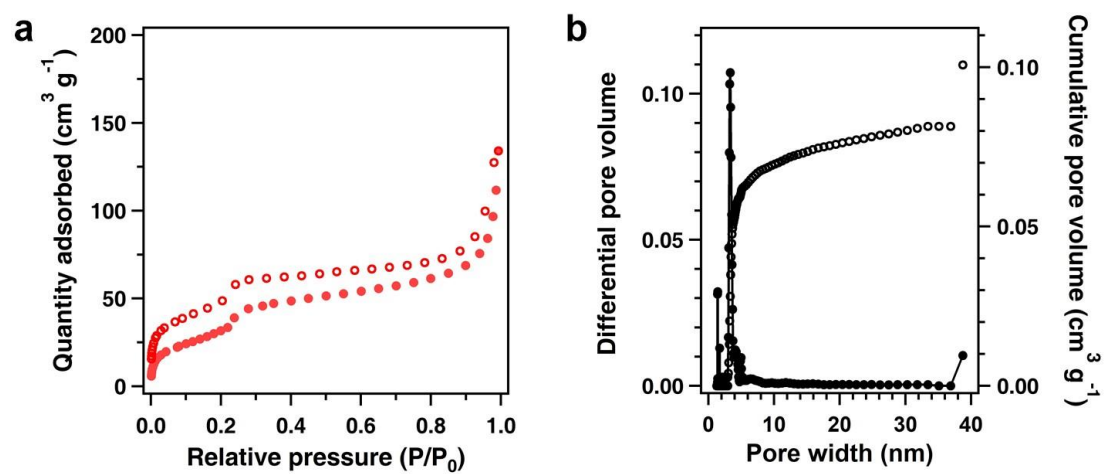
**Figure 12.** Nyquist plots of Li@TPB-DMTP-COF measured from 40 to 100 °C.

Figure 12 showed the Nyquist plots of Li@TPB-DMTP-COF under nitrogen atmosphere at temperature ranging from 40 to 100 °C. The impedance plots exhibited semicircular shape followed by a spike, suggesting typical of predominantly ionic conduction. where the plot of the real component ( $Z'$ ) versus the imaginary component ( $Z''$ ) of the complex impedance function displayed a semicircular shape followed by a spike. The conductivity was calculated according to the equation  $\sigma = L/(Z \times A)$ ,  $L$  is the thickness of samples (cm),  $A$  is the electrode area ( $\text{cm}^2$ ),  $\sigma$  is the conductivity ( $\text{S cm}^{-1}$ ) and  $Z$  is the impedance ( $\Omega$ ). The resistances of Li@TPB-DMTP-COF were  $1.59 \times 10^6$ ,  $7.31 \times 10^5$ ,  $3.21 \times 10^5$ ,  $1.24 \times 10^5$ ,  $4.02 \times 10^4$ ,  $1.03 \times 10^4$  and  $314 \Omega$  at 40, 50, 60, 70, 80, 90 and 100 °C, with the corresponding conductivities of  $1.36 \times 10^{-7}$ ,  $2.96 \times 10^{-7}$ ,  $6.74 \times 10^{-7}$ ,  $1.75 \times 10^{-6}$ ,  $5.37 \times 10^{-6}$ ,  $2.09 \times 10^{-5}$  and  $6.08 \times 10^{-4} \text{ S cm}^{-1}$ .

As for a control, I have synthesized TPB-TP-COF by condensation of TPB and TP in the same condition (Figure 13). Without methoxy group on the pore channels, the BET surface area decreased to  $145 \text{ m}^2 \text{ g}^{-1}$ . TPB-TP-COF had a similar pore size of 3.3 nm, but a low pore volume of  $0.1 \text{ cm}^3 \text{ g}^{-1}$  (Figure 14). Then  $\text{LiClO}_4$  was loaded in the pore channels.



**Figure 13.** Synthesis of TPB-TP-COF from TPB and TP under solvothermal condition.



**Figure 14.** a) Nitrogen sorption isotherm and b) pore size distribution profiles of TPB-TP-COF.

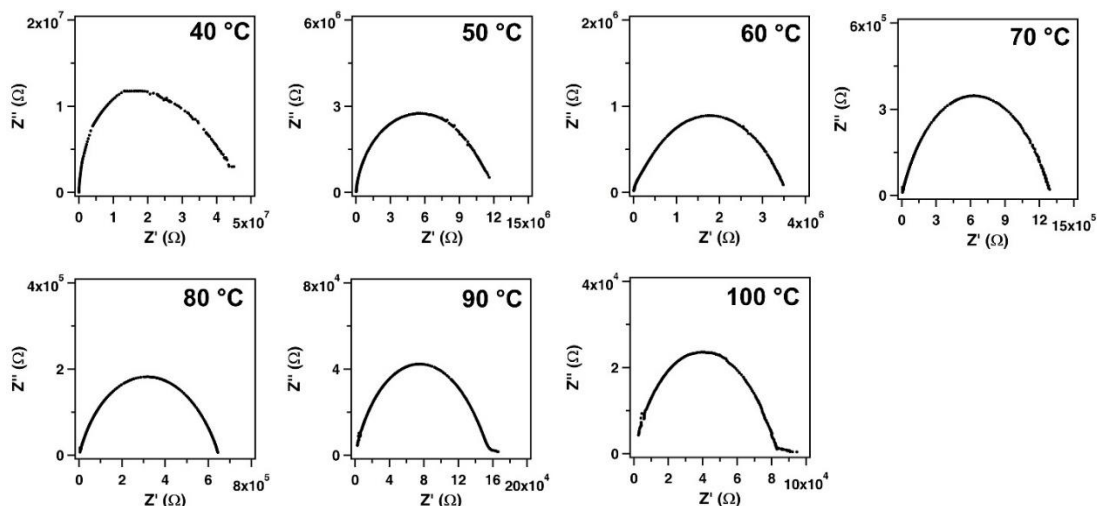


**Figure 15.** Nyquist plots of Li@TPB-TA-COF measured from 40 to 100 °C.

With increasing temperature from 40 to 100 °C, the resistances were decreased from  $4.5 \times 10^7$  to  $8.37 \times 10^5 \Omega$ . And the corresponding conductivities were  $3.25 \times 10^{-9}$ ,  $1.26 \times 10^{-8}$ ,  $4.21 \times 10^{-8}$ ,  $1.14 \times 10^{-7}$ ,  $2.27 \times 10^{-7}$ ,  $9.28 \times 10^{-7}$  and  $1.75 \times 10^{-6} \text{ S cm}^{-1}$  at 40, 50, 60, 70, 80, 90 and 100 °C (Figure 15), respectively, less than 10% of those of TPB-DMTP-COF. Especially, the conductivity was 2.3% of that of Li@TPB-DMTP-COF at 40 °C. The poor conduction performance was ascribed to the low lithium concentration in the pore channels.

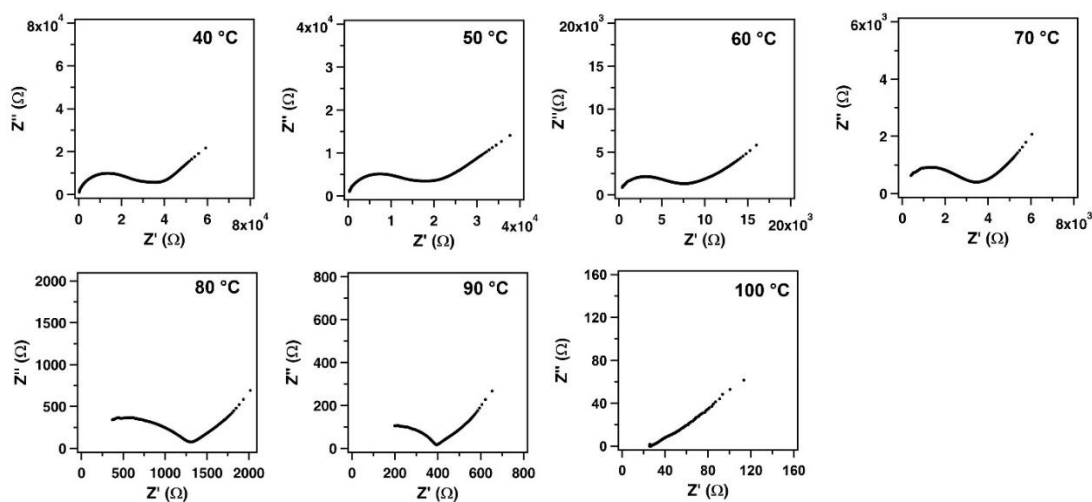


**Figure 16.** Nyquist plots of Li@TPB-BMTP-COF measured from 40 to 100 °C.

In order to improve lithium ion transport performance in the pore channels, the methoxy group was substituted with ethylene oxide groups. The short ethylene oxide chains can form the complexes with lithium ion. The Nyquist plots were obtained in the same condition (Figure 16). The resistances decreased from  $3.58 \times 10^4$  to  $31 \Omega$  from 40 to 100 °C. The conductivities were  $6.04 \times 10^{-6}$ ,  $1.21 \times 10^{-5}$ ,  $2.85 \times 10^{-5}$ ,  $6.28 \times 10^{-5}$ ,  $1.66$

$\times 10^{-4}$ ,  $5.49 \times 10^{-4}$  and  $6.94 \times 10^{-3}$  S  $\text{cm}^{-1}$ , which were more than 10 times higher than those of Li@TPB-DMTP-COF, respectively. The conductivity at 100 °C was just only less than 1 order of magnitude lower than common liquid electrolytes (from 4.5 to  $11.1 \times 10^{-3}$  S  $\text{cm}^{-1}$ ).<sup>3a</sup> Although the lithium ion concentration within TPB-DMTP-COF was higher because of higher pore volume, the conductivities were much lower than those of Li@TPB-BMTP-COF. The lower resistances and superior conductive ability of Li@TPB-BMTP-COF were caused by ethylene oxide chains on the channels: the flexible chains of TPB-BMTP-COF enhance the lithium ion solubility in the polymer matrix analogous to PEO-salt materials, helping the lithium ion interchain hopping in the confined 1D channels.

Apart from good ionic conductive performance, electrolytes must be an electronic insulator. The conduction of TPB-BMTP-COF was conducted in the same temperature period (Figure 17). From the impedance spectroscopy, no Nyquist behavior could be observed. Thus, TPB-BMTP-COF is a good ionic conductor and electronic insulator.

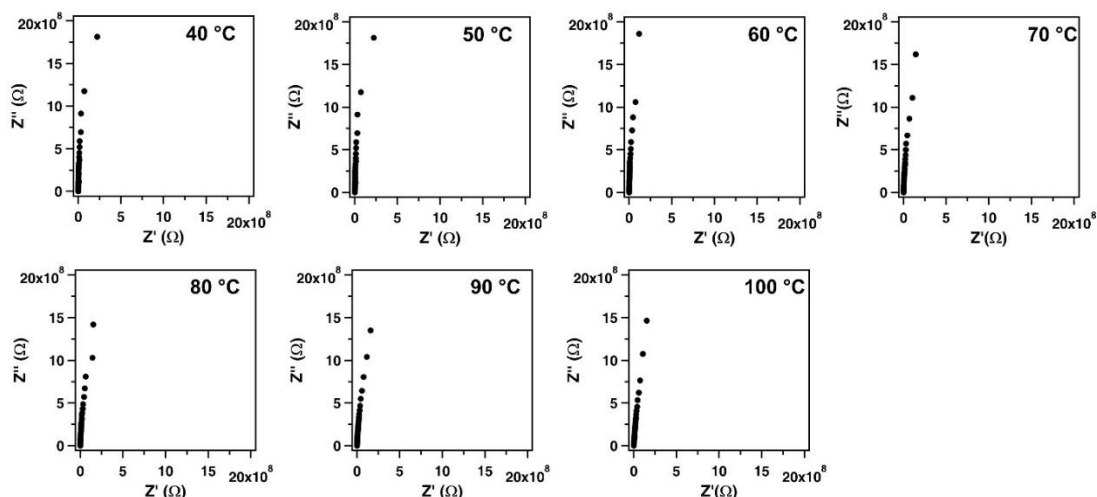


**Figure 17.** Nyquist plots of TPB-BMTP-COF measured from 40 to 100 °C.

The cyclic stability of polymer electrolytes at high temperature is another important issue. The cyclic stability of Li@TPB-BMTP-COF was measured at 100 °C for 24 h (Figure 18a). After 24 h, the resistance of Li@TPB-BMTP-COF was still low to 70  $\Omega$ , and the corresponding conductivity was high to  $3.5 \times 10^{-3}$  S  $\text{cm}^{-1}$ . Additionally, the pore structure and crystallinity of TPB-BMTP-COF exhibited slight decrease, even after treatment with LiClO<sub>4</sub> at 100 °C for 48 h (Figure 18b), which further confirmed the stability of the electrolytes.

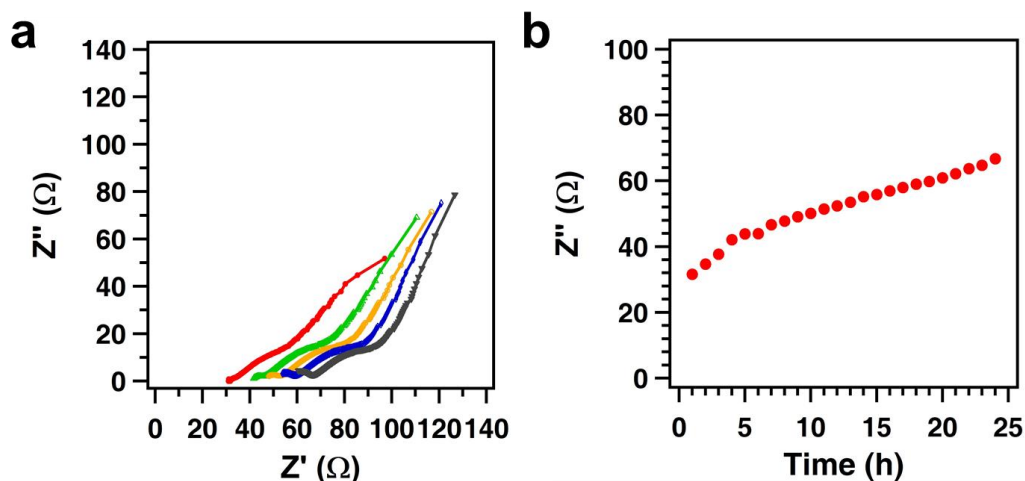


**Figure 18.** a) Nyquist plots of Li@TPB-BMTP-COF measured at 100 °C for 24 h. b) The resistances of Li@TPB-BMTP-COF for 24 h.

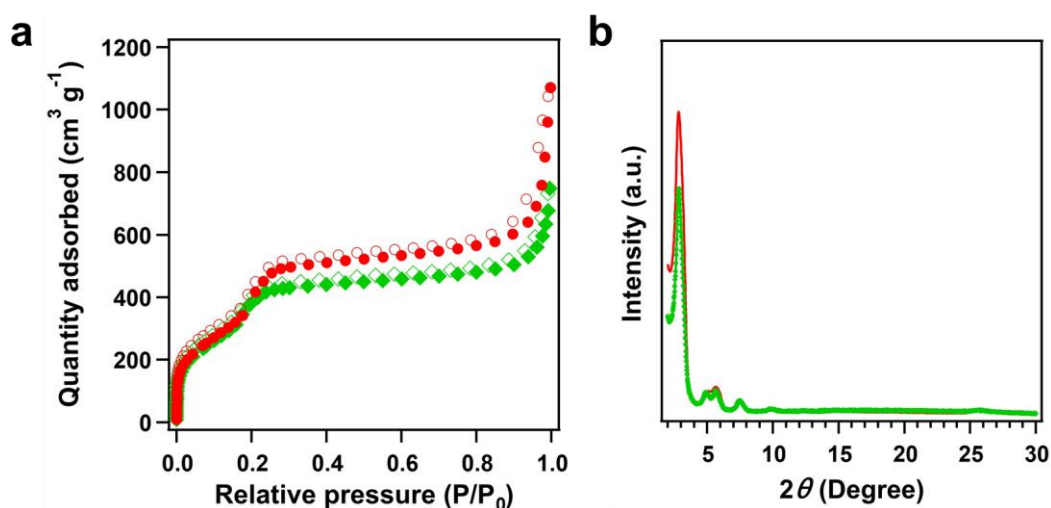


**Figure 19.** a) Nitrogen sorption isotherm profiles and b) PXRD curves of TPB-BMTP-COF before (red) and after (green) treatment with LiClO<sub>4</sub> at 100 °C for 48 h.

To investigate the conductivity mechanism for the lithium ion transport in the COFs, the conductive performance of Li@TPB-DMTP-COF, and Li@TPB-BMTP-COF was characterized as a function of temperature. The smaller activation energy ( $E_a$ ) implies that conductivity is less dependent on the temperature, favor to dissociate and transport lithium ions in the channels, indicating high-rate transport over a wide temperature range.<sup>10</sup> In Figure 20a, the conductivities of Li@TPB-DMTP-COF exhibited a typical Arrhenius-type behavior, and their  $E_a$  was calculated as 0.96 eV. And the  $E_a$  of Li@TPB-BMTP-COF was 0.87 eV (Figure 20b), smaller than that of Li@TPB-DMTP-COF, which confirmed the longer chains promoted lithium ion transport. The similar  $E_a$  indicated the equal conductive mechanism: lithium ion hopping intrachains along

the pore channels using forming or breaking Li-O bonds, because of the coordination interaction between of the lithium ion and oxygen from pore channels.<sup>2a, 11</sup>

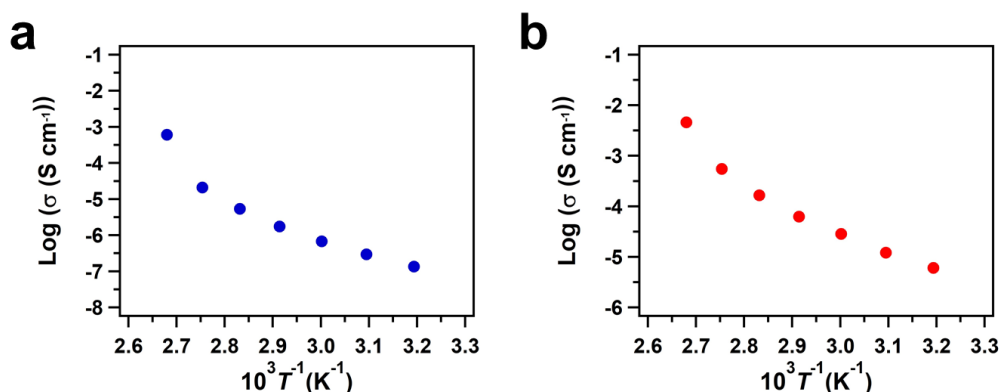


**Figure 20.** Temperature dependence of conductivities a) Li@TPB-DMTP-COF and b) Li@TPB-BMTP-COF.

To confirm the hopping mechanism, I loaded half theoretical amount of  $\text{LiClO}_4$  within the pore channels, which resulted in larger space between lithium sources and chains within the channels, and made it difficult for lithium ion hopping interchains along the channels. The resistances were from  $5.82 \times 10^6$  to  $2.06 \times 10^4 \Omega$  from 40 to 100 °C (Figure 21). The corresponding conductivities were  $3.55 \times 10^{-8}$  and  $1.0 \times 10^{-5} \text{ S cm}^{-1}$  at 40 and 100 °C, less than 1% of conductivities with Li@TPB-BMTP-COF. The poor conductivity performance was from the free space in the channels block the lithium ion fast transport.

For comparisons, I have loaded the complexes of  $\text{LiClO}_4$  and polyethylene oxide (PEO) in the pore channels of TPB-DMTP-COF to obtain Li&PEO@TPB-DMTP-COF. With increasing temperature from 30 to 70 °C, the resistances changed from 4400 to 1120  $\Omega$ , with corresponding conductivities increasing from  $7.93 \times 10^{-5}$  and  $2.48 \times 10^{-4} \text{ S cm}^{-1}$  at 30 and 70 °C (Figure 22). Although the conductivities were better than those of Li@TPB-BMTP-COF at the same temperature, the cyclic stability limited the application. After conducting impedance measurement at 70 °C for 1 h, the resistance increased obviously to 3500  $\Omega$ . Thus, linking short ethylene oxide chains on the wall of channels can enhance the cyclic and thermal stability.

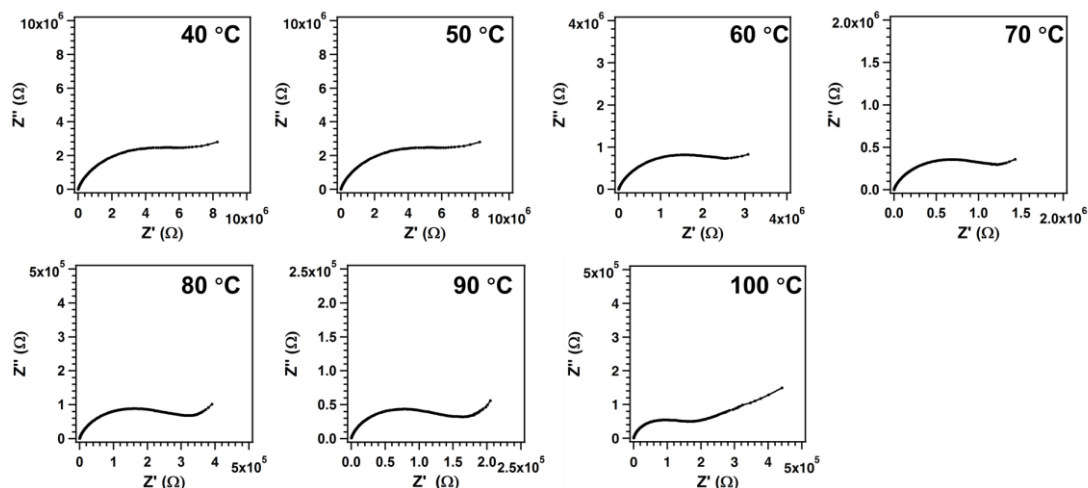


**Figure 21.** Nyquist plots of Li@TPB-BMTP-COF measured from 40 to 100 °C, with loading half theoretical amount of LiClO<sub>4</sub>.

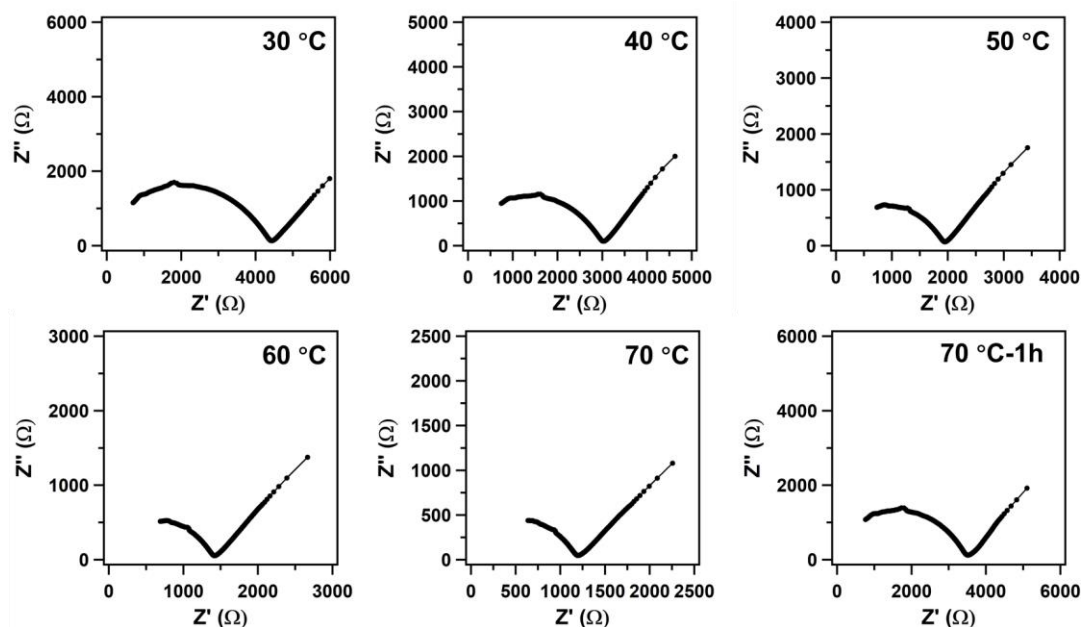


**Figure 22.** Nyquist plots of Li&PEO@TPB-DMTP-COF measured from 40 to 70 °C.

## 4.5 Conclusion

By developing highly crystalline and stable COFs with methoxy or short ethylene oxide groups incorporated in the walls, I have successfully shown fast lithium ion conduction across the 1D channels. The prepared solid electrolytes possess good mechanical strength and thermal stability. The results display that the electrolytes are promisingly ionic conductor, with ethylene oxide groups. The TPB-BMTP-COF integrates the advantages of ionic conductivity of PEO and 1D ion transport pathways of COFs, which results higher conductivity than other polymer-based electrolytes, and even comparable to liquid electrolytes. The innovative strategy renders COFs to be

applied in the future solid-state batteries.

## 4.6 Experimental Sections

**Characterizations.** A JASCO model FT IR-6100 infrared spectrometer was used to conduct Fourier-transform infrared (FT IR) experiments. A Mettler-Toledo model TGA/SDTA851e was used for TGA measurements under nitrogen, by heating to 800 °C at a rate of 10 °C min<sup>-1</sup>. A Rigaku model RINT Ultima III diffractometer was used for PXRD measurement, from  $2\theta = 1^\circ$  up to  $60^\circ$  with  $0.02^\circ$  increment. At 77 K, nitrogen sorption isotherms were conducted on a 3Flex surface characterization analyzer with the Micrometrics Instrument Corporation model. FE-SEM images were obtained on a FEI Sirion-200 or Hitachi high technologies (SU-6600) field-emission scanning electron microscope at an electric voltage of 5 KV.

**Computational Calculations.** The crystalline structure of TAPT-DHTA-COF was determined using the density-functional tight-binding (DFTB+) method including Lennard-Jones (LJ) dispersion. The calculations were carried out with the DFTB+ program package version 1.2.<sup>12</sup> DFTB is an approximate density functional theory method based on the tight binding approach and utilizes an optimized minimal LCAO Slater-type all-valence basis set in combination with a two-center approximation for Hamiltonian matrix elements. The Coulombic interaction between partial atomic charges was determined using the self-consistent charge (SCC) formalism. Lennard-Jones type dispersion was employed in all calculations to describe van der Waals (vdW) and  $\pi$ -stacking interactions. The lattice dimensions were optimized simultaneously with the geometry. Standard DFTB parameters for X–Y element pair (X, Y = C, O, H, and N) interactions were employed from the mio-0-1 set.<sup>13</sup>

**Pawley refinements.** Molecular modeling and Pawley refinement were carried out using Reflex, a software package for crystal determination from XRD pattern, implemented in MS modeling version 4.4 (Accelrys Inc.).<sup>14</sup> Initially, unit cell dimensions for both hexagonal and rhombic lattices were taken from the DFTB calculation and the space group for hexagonal and rhombic crystal system were selected as *P6*, respectively. I performed Pawley refinement for hexagonal *S4* lattice to optimize the lattice parameters iteratively until the  $R_{WP}$  value converges. The pseudo Voigt profile function was used for whole profile fitting and Berrar–Baldinozzi function was used for asymmetry correction during the refinement processes. A crystal system was deduced with lattice parameters of  $a = b = 35.5832 \text{ \AA}$ ,  $c = 4.2857 \text{ \AA}$ ,  $\alpha = \beta = 90^\circ$ , and  $\gamma$

= 120° and the final  $R_{wp}$  and  $R_p$  values were 6.32% and 4.56%, respectively.

**Conductivity Measurement:** Impedance analyses were performed on lithium salt loaded COF powders. The powders were obtained by grinding Li@COFs. The resultant powders were added into a 10-mm standard die and then slowly increased pressure to 100 kN and kept for 30 min to prepare pellets. Measurements were performed using an impedance analyzer (IM3570, HIOKIE. E. Co.), with a two-Ag-probe over the frequency range from 4 Hz to 5 MHz and with an input voltage amplitude of 100 mV. The cell was filled with nitrogen before conducting the measurements. The proton conductivities were obtained from equation:  $\sigma = L / (Z \times A)$ , where conductivity ( $S\ cm^{-1}$ ) was represented by  $\sigma$ , thickness of sample (cm) was showed by  $L$ , electrode area ( $cm^2$ ) was represented by  $A$  and impedance ( $\Omega$ ) was indicated by  $Z$ .

**Reagents.** 1,3,5-Tri(4-aminophenyl) benzene (TPB), terephthalaldehyde (TP), and 1,4-dimethoxybenzene were bought from TCI. Acetic acid, *o*-Dichlorobenzene (*o*-DCB), tetrahydrofuran (THF), and n-Butanol (BuOH) were bought from Kanto Chemicals.  $LiClO_4$ , polyethylene glycol 400 (PEO), anhydrous MeOH were brought from Aldrich. 2,5-Dimethoxyterephthalaldehyde (DMTP),<sup>15</sup> and 2,5-bis((2-methoxyethoxy)methoxy) terephthalaldehyde (BMTP)<sup>16</sup> were synthesized according to reports.

**Table 1.** Atomistic coordinates for the AA-stacking mode of TPB-BMTP-COF optimized by using DFTB+ method. Space group:  $P6_3$ ;

$a = 35.5832 \text{ \AA}$ ,  $b = 35.5832 \text{ \AA}$ ,  $c = 4.2857 \text{ \AA}$

C	1.64593	-0.71223	0.56889
C	1.69136	-0.68731	0.57276
C	1.62522	-0.75882	0.49613
C	1.5908	-0.77635	0.27702
C	1.57416	-0.81837	0.16445
C	1.59166	-0.84391	0.27253
C	1.62585	-0.82667	0.4943
C	1.64242	-0.78449	0.60468
N	1.57678	-0.88599	0.16198
C	1.53731	-0.90906	0.06492
C	1.51935	-0.95447	-0.0189
C	1.47386	-0.98074	-0.0371
C	1.45441	-1.02597	-0.04048
H	1.57815	-0.756	0.1839
H	1.54863	-0.83084	-0.01709
H	1.63883	-0.84698	0.58128
H	1.66912	-0.77106	0.77729
H	1.58942	1.48656	1.07201
O	0.53682	0.59009	0.94957
C	0.58249	0.61545	0.896
O	0.59069	0.65854	0.84265
C	0.63556	0.68737	0.75631
C	0.64057	0.73084	0.67492
O	0.68528	0.75923	0.58019
C	0.69211	0.80113	0.48796
H	1.45428	-0.96479	-0.02428
H	0.59253	0.6032	0.68281
H	0.60149	0.61437	1.10865
H	0.64436	0.67363	0.54943

Chapter 4

---

H	0.65729	0.69003	0.95694
H	0.63257	0.74504	0.88276
H	0.61832	0.72781	0.47765
H	0.67132	0.79831	0.28263
H	0.72643	0.82147	0.42118
H	0.68457	0.81678	0.68655
H	0.2894	0.70362	1.55719

**Table 2.** Atomistic coordinates for the AB-stacking mode of TPB-BMTP-COF optimized by using DFTB+ method. Space group: *P63*;

$a = 35.5832 \text{ \AA}$ ,  $b = 35.5832 \text{ \AA}$ ,  $c = 8.5714 \text{ \AA}$

C	-0.02373	-0.04594	0.33446	0
C	0.02187	-0.02334	0.33877	0
C	-0.04826	-0.09368	0.30119	0
C	-0.08764	-0.11232	0.21725	0
C	-0.10745	-0.15523	0.16584	0
C	-0.08779	-0.18032	0.19323	0
C	-0.05026	-0.16312	0.28394	0
C	-0.03073	-0.12042	0.33802	0
N	-0.10431	-0.22292	0.12966	0
C	-0.13205	-0.23993	0.01629	0
C	-0.14732	-0.2849	-0.03051	0
C	-0.19188	-0.31224	-0.05724	0
C	-0.20909	0.64284	-0.0775	0
H	-0.10261	-0.0936	0.18364	0
H	-0.13766	-0.16815	0.10275	0
H	-0.03541	-0.18266	0.30774	0
H	-0.00124	-0.10832	0.40446	0
H	-0.07639	0.14636	-0.03889	0
O	-0.13289	0.25354	-0.10399	0
C	-0.08786	0.28374	-0.08439	0
O	-0.08125	0.32559	-0.11532	0
C	-0.03667	0.35677	-0.10248	0
C	-0.0304	0.40088	-0.14646	0
O	0.0142	0.4322	-0.13575	0
C	0.02061	0.47295	-0.18346	0
H	-0.21274	-0.29828	-0.05316	0
H	-0.06897	0.27593	-0.16909	0
H	-0.07832	0.28174	0.03816	0
H	-0.01651	0.34961	-0.18343	0

Chapter 4

H	-0.02488	0.35876	0.01935	0
H	-0.05009	0.40849	-0.06503	0
H	-0.04289	0.39849	-0.26748	0
H	0.01141	0.47247	-0.30794	0
H	0.05568	0.49732	-0.17319	0
H	0.00266	0.48404	-0.10746	0
H	-0.3718	0.37524	0.20783	0
C	-0.30956	0.37889	0.21358	0
C	-0.35499	0.35698	0.21601	0
C	-0.28533	0.42585	0.18053	0
C	-0.25458	0.4417	0.05957	0
C	-0.23518	0.48504	0.01386	0
C	-0.24621	0.51329	0.08912	0
C	-0.27636	0.49764	0.21105	0
C	-0.29585	0.45424	0.257	0
N	-0.2283	0.55777	0.04522	0
C	-0.19739	0.57943	-0.0544	0
C	-0.18065	0.62613	-0.07071	0
C	-0.13576	0.65397	-0.06011	0
C	-0.11839	-0.30107	-0.04055	0
H	-0.24696	0.42007	-0.00429	0
H	-0.21276	0.49562	-0.08274	0
H	-0.28504	0.51935	0.26843	0
H	-0.31959	0.4426	0.35024	0
H	-0.25469	0.17979	-0.10901	0
O	-0.19835	0.07334	-0.02898	0
C	-0.24232	0.04438	-0.07158	0
O	-0.24929	0.00173	-0.07107	0
C	-0.29079	-0.0268	-0.13373	0
C	-0.29922	-0.07295	-0.12731	0
O	-0.34052	-0.10047	-0.19317	0
C	-0.35187	-0.14421	-0.17117	0

Chapter 4

---

H	-0.11514	0.63973	-0.05757	0
H	-0.24819	0.05325	-0.19052	0
H	-0.26422	0.04688	0.01556	0
H	-0.29283	-0.01903	-0.25831	0
H	-0.31701	-0.02573	-0.06597	0
H	-0.29744	-0.08105	-0.00277	0
H	-0.27329	-0.07456	-0.19489	0
H	-0.32695	-0.15118	-0.21963	0
H	-0.38264	-0.16529	-0.23484	0
H	-0.35775	-0.15334	-0.04565	0
H	0.03889	-0.04121	0.33667	0

**References**

1. (a) Z. Gadjourova, Y. G. Andreev, D. P. Tunstall, P. G. Bruce, *Nature* **2001**, *412*, 520-523. (b) J. M. Tarascon, M. Armand, *Nature* **2001**, *414*, 359-367. (c) L. Yue, J. Ma, J. Zhang, J. Zhao, S. Dong, Z. Liu, G. Cui, L. Chen, *Energy Storage Mater.* **2016**, *5*, 139-164. (d) P. Lightfoot, M. A. Mehta, P. G. Bruce, *Science* **1993**, *262*, 883-885. (e) R. Khurana, J. L. Schaefer, L. A. Archer, G. W. Coates, *J. Am. Chem. Soc.* **2014**, *136*, 7395-7402.
2. (a) Z. Xue, D. He, X. Xie, *J. Mater. Chem. A* **2015**, *3*, 19218-19253. (b) X. Lin, M. Salari, L. M. R. Arava, P. M. Ajayan, M.W. Grinstaff, *Chem. Soc. Rev.* **2016**, *45*, 5848-5887. (c) R. Bouchet, S. Maria, R. Meziane, A. Aboulaich, L. Lienafa, J.-P. Bonnet, T. N. T. Phan, D. Bertin, D. Gigmes, D. Devaux, R. Denoyel, M. Armand, *Nat. Mater.* **2013**, *12*, 452-457. (d) N. Liu, J. Liu, P.-C. Sun, Y. Hsu, H.-W. Li, Y. Lee, *Nano Lett.* **2015**, *15*, 2740-2745. (e) D. H. C. Wong, A. Vitale, D. Devaux, A. Taylor, A. A. Pandya, D. T. Hallinan, J. L. Thelen, S. J. Mecham, S. F. Lux, A. M. Lapidés, P. R. Resnick, T. J. Meyer, R. M. Kostecki, N. P. Balsara, J. M. DeSimone, *Chem. Mater.* **2015**, *27*, 597-603. (f) Q. Ma, H. Zhang, C. W. Zhou, L. P. Zheng, P. F. Cheng, J. Nie, W. F. Feng, Y. S. Hu, H. Li, X. J. Huang, L. Q. Chen, M. Armand, Z. B. Zhou, *Angew. Chem. Int. Ed.* **2016**, *55*, 2521-2525.
3. (a) W. Liu, D. Lin, A. Pei, Y. Cui, *J. Am. Chem. Soc.* **2016**, *138*, 15443-15450. (b) J. Zhang, Y. Bai, X.-G. Sun, Y. Li, B. Guo, J. Chen, G. M. Veith, D. K. Hensley, M. P. Paranthaman, J. B. Goodenough, S. Dai, *Nano Lett.* **2015**, *15*, 3398-3402. (c) G. Zheng, S. W. Lee, Z. Liang, H.-W. Lee, K. Yan, H. Yao, H. Wang, W. Li, S. Chu, Y. Cui, *Nat. Nanotech.* **2014**, *9*, 618-623. (d) Z. Tu, Y. Kambe, Y. Lu, L. A. Archer, *Adv. Energy Mater.* **2014**, *4*, 1300654. doi: 10.1002/aenm.201300654.
4. (a) N. Huang, P. Wang, D. Jiang, *Nat. Rev. Mater.* **2016**, *1*, 16068, doi: 10.1038/natrevmats2016.68. (b) X. Feng, X. Ding, D. Jiang, *Chem. Soc. Rev.* **2012**, *41*, 6010-6022. (c) J. L. Segura, M. J. Mancheno, F. Zamora, *Chem. Soc. Rev.* **2016**, *45*, 5635-5671. (d) J. Zhou, B. Wang, *Chem. Soc. Rev.* **2017**, *46*, 6927-6945. (e) P. J. Waller, F. Gándara, O. M. Yaghi, *Acc. Chem. Res.* **2015**, *48*, 3053-3063.
5. (a) E. Jin, M. Asada, Q. Xu, S. Dalapati, M. A. Addicoat, M. A. Brady, H. Xu, T. Nakamura, T. Heine, Q. Chen, D. Jiang, *Science* **2017**, *357*, 673-676. (b) S. Dalapati, M. Addicoat, S. Jin, T. Sakurai, J. Gao, H. Xu, S. Irle, S. Seki, D. Jiang, *Nat. Commun.* **2015**, *6*, 7786, doi: 10.1038/ncomm8786. (c) C. R. Mulzer, L. Shen,

- R. P. Bisbey, J. R. McKone, N. Zhang, H. D. Abruña, W. R. Dichtel, *ACS Cent. Sci.* **2016**, *2*, 667-673. (d) C. R. DeBlase, K. E. Silberstein, T. T. Truong, H. D. Abruña, W. R. Dichtel, *J. Am. Chem. Soc.* **2013**, *135*, 16821-16824. (e) V. S. Vyas, F. Haase, L. Stegbauer, G. Savasci, F. Podjaski, C. Ochsenfeld, B. V. Lotsch, *Nat. Commun.* **2015**, *6*, 8508, doi: 10.1038/ncomm9508.
6. (a) H. Xu, S. Tao, D. Jiang, *Nat. Mater.* **2016**, *15*, 722-726. (b) H. Ma, B. Liu, B. Li, L. Zhang, Y.-G. Li, H.-Q. Tan, H.-Y. Zang, G. Zhu, *J. Am. Chem. Soc.* **2016**, *138*, 5897-5903. (c) S. Chandra, T. Kundu, S. Kandambeth, R. BabaRao, Y. Marathe, S. M. Kunjir, R. Banerjee, *J. Am. Chem. Soc.* **2014**, *136*, 6570-6573. (d) S. Chandra, T. Kundu, K. Dey, M. Addicoat, T. Heine, R. Banerjee, *Chem. Mater.* **2016**, *28*, 1489-1494. (e) Y. Peng, G. Xu, Z. Hu, Y. Cheng, C. Chi, D. Yuan, H. Cheng, D. Zhao, *ACS Appl. Mater. Interfaces.* **2016**, *8*, 18505-18512.
7. Y. Sun, N. Liu, Y. Cui, *Nature Energy* **2016**, *1*, 16071. doi: 10.1038/nenergy.2016.71.
8. D. A. Vazquez-Molina, G. S. Mohammad-Pour, C. Lee, M. W. Logan, X. Duan, J. K. Harper, F. J. Uribe-Romo, *J. Am. Chem. Soc.* **2016**, *138*, 9767-9770.
9. K. Kesavan, S. Rajendran, C. M. Mathew, *Polym. Compos.* **2015**, *36*, 302-311.
10. J. H. Park, K. Suh, M. R. Rohman, W. Hwang, M. Yoon, K. Kim, *Chem. Commun.* **2015**, *51*, 9313-9316.
11. B. M. Wiers, M. L. Foo, N. P. Balsara, J. R. Long, *J. Am. Chem. Soc.* **2011**, *133*, 14522-14525.
12. B. Aradi, B. Hourahine, T. Frauenheim, *J. Phys. Chem. A* **2007**, *111*, 5678-5684.
13. <http://www.dftb.org>.
14. Accelrys, Material Studio Release Notes, Release 4.4, Accelrys Software, San Diego 2008.
15. H. Xu, J. Gao, D. Jiang, *Nat. Chem.* **2015**, *7*, 905-912.
16. Y. Okada, M. Sugai, K. Chiba, *J. Org. Chem.* **2016**, *81*, 10922-10929.

**Chapter 5. Design and Synthesis of Covalent Organic  
Frameworks for Polymer Electrolytes by Pore Surface  
Engineering Method**

## **Abstract**

Poly(ethylene oxide)-lithium complexes have been extensively studied as the solid polymer electrolytes that solve the safety, leak and stability issues of liquid electrolytes. However, ionic transport is extremely sluggish in poly(ethylene oxide) because it tends to crystallize and impedes ion motion. Design of a solid polymer electrolyte with high conductivity remains a challenge. Here I report a series of solid polymer electrolytes based on covalent organic frameworks with one-dimensional open channels that provide a predesigned pathway for ion conduction. The frameworks are designed to anchor short ethylene oxide chains free of crystallinity on the walls, so that the chains retain high motion flexibility to facilitate ion conduction. By virtue of tuning the pore channels, length and content of ethylene oxide chains on the walls of frameworks accurately, the lithium ion conductivity achieves higher than  $10^{-5}$  S cm<sup>-1</sup> at 40 °C, and  $10^{-3}$  S cm<sup>-1</sup> at 100 °C with a small activation energy of 0.68 eV.

## 5.1 Introduction

Many efforts have been done to develop solid electrolytes for solid-state batteries (SSBs), as potentially safe and stable high-energy storage systems. Solid electrolytes have a large electrochemical stability window and excellent safety in comparison to traditional organic liquid electrolytes with leakage, flammability and poor chemical stability issues.<sup>1</sup> More importantly, solid electrolytes enable to possess promising cyclic stability by suppressing lithium metal dendrites effectively. Solid electrolytes can be classified into two kinds, inorganic materials and organic polymer materials.<sup>2</sup> In comparison to inorganic materials, polymer electrolytes (SPEs, combination of polymer and lithium salt) based on polymer poly(ethylene oxide) (PEO) can offer many advantages, including flexibility, light weight and low-cost processing.<sup>3</sup> Nevertheless, the highly crystalline tendency of polymers below glass transition temperature restricts a suitable temperature range and results in a low conductivity at room temperature, which limits the practical application. Till now, various attempts have been made to address these problems by synthesizing PEO-based copolymers, composite polymers and crosslinking networks.<sup>4</sup> Unfortunately, the resulting electrolytes are still low in ion conduction because of their disordered structure. To overcome the bottleneck, a composite polymer electrolyte with well-aligned inorganic nanowires has been reported.<sup>5</sup> The resultant material showed improved conduction performance, because of a fast ion conducting pathway. However, the nanowires were prepared under high temperature (800 °C). Thus, preparing a polymer electrolyte feasibly to enable fast ion transport is of great significance.

Covalent organic frameworks (COFs), as an emerging class of crystalline porous polymers, are consist of ordered organic building blocks and linked with robust covalent bonds. By virtue of the diversity of topology design diagram, the availability of building units and the accessibility of linkages, various COFs with different topologies, skeletons and pores have been designed and synthesized.<sup>6</sup> Apart from designable, another important feature of COFs is pore surface engineering.<sup>7</sup> The capability of designing pore channels renders COFs able to design outstanding properties ranging from heterogeneous catalysis to gas absorption and energy storage.<sup>8</sup> Especially, the aligned channels and mesoporous play vital roles in loading proton carries<sup>9</sup> or lithium resources<sup>10</sup> and triggering excellent proton conductivity. Thus, COFs

may be an ideal candidate to overcome the disadvantages of conventional polymer electrolytes.

In this study, I described the design and synthesis of a series of solid polymer electrolytes based on COFs by pore surface engineering method (COFs structure shown in Figure 1). Different from synthesis of COFs by skeleton function method, the ethylene oxide chains are controllable to link the pore channels of the frameworks by click reactions. The ethylene oxide chains on the pore walls retained high motion flexibility that can facilitate ion transport across the channels. Moreover, the COFs were allowed for the precise tune of pores and control over the length and content of ethylene oxide chains on the pore walls. The resulting COFs, upon loading of lithium ions, served as polyelectrolytes that enabled high rate transport of lithium ion, demonstrating the importance of ordered channels and ordered electrolyte sites in facilitating ion conduction.

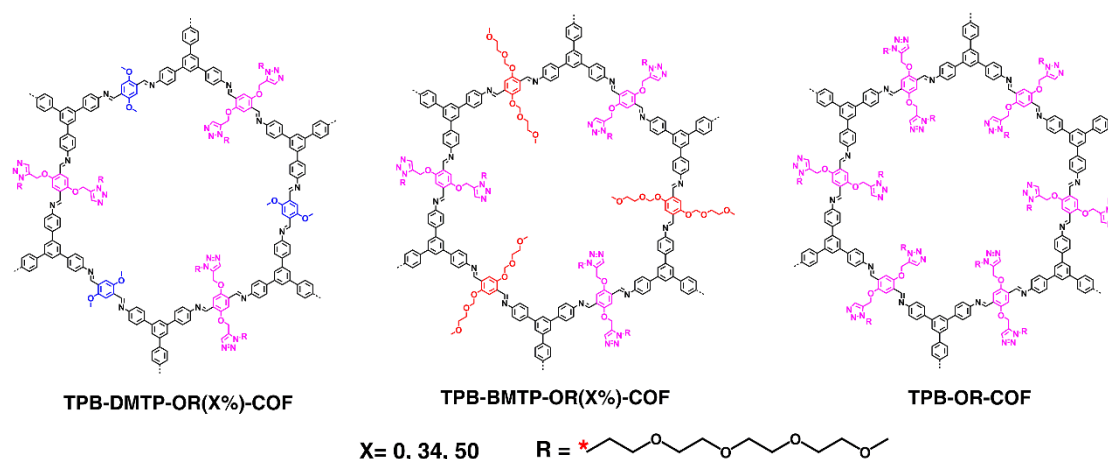


**Figure 1.** Chemical structure of polymer electrolytes based on 2D COFs by pore surface engineering method.

## 5.2 Materials and Methods

**Synthesis of TPB-DMTP-BPTA(X%)-COF and TPB-DMTP-COF.** First, I added building blocks (TPB (28 mg, 0.08 mmol), BPTA ( $X\% \times 0.12$  mmol), and DMTP ( $(100-X)\% \times 0.12$  mmol)) into a Pyrex tube (10 mL), then added a mixture of BuOH/*o*-DCB (0.5 mL/0.5 mL), and HAc (6 M, 0.1 mL). The tube was degassed by freeze-pump-thaw for three cycles. Then I sealed the tube and kept it at 120 °C for 3 days. I collected the precipitate by filtering, and then subjected to Soxhlet extraction with THF for 24 h. The powder was collected and then dried at 120 °C under vacuum overnight



for 3 days. I collected the precipitate by filtering, and then subjected to Soxhlet extraction with THF for 24 h. The powder was collected and then dried at 120 °C under vacuum overnight to give TPB-BPTA-COF (Figure 2b) in a yield of 77%.

**Synthesis of TPB-BMTP-BPTA(X%)-COF, and TPB-BMTP-COF.** A mixture of BuOH/*o*-DCB (0.5 mL/0.5 mL), TPB (28 mg, 0.08 mmol), BPTA ( $X\% \times 0.12$  mmol), BMTP ( $(100-X)\% \times 0.12$  mmol), and HAc (6 M, 0.1 mL) was degassed in a Pyrex tube (10 mL) by freeze-pump-thaw for three cycles. Then I sealed the tube and kept it at 120 °C for 3 days. I collected the precipitate by filtering, and then subjected to Soxhlet extraction with THF for 24 h. The powder was collected and then dried at 120 °C under vacuum overnight to give TPB-BMTP-BPTA(X%)-COF in yields of 83% ( $X=34$ ) and 78% ( $X = 50$ ) (Figure 2b). When  $X$  is 0, the product was TPB-BMTP-COF.

**Synthesis of TPB-DMTP-OR(X%)-COF.** A mixture of THF/CH<sub>3</sub>CN (0.4 mL/3.6 mL), TPB-DMTP-BPTA(X%)-COF, CuI (3 mg), N, N-diisopropylethylamine (DIPEA) (0.1 ml) and 13-azido-2,5,8,11-tetraoxatridecane (36 mg for  $X = 34$ , and 60 mg for  $X = 50$ ) was degassed in a Pyrex tube (10 mL) by three freeze-pump-thaw cycles. The tube was sealed and stirring at room temperature for 24 h. I collected the precipitate by filtering, washed with acetone, CH<sub>3</sub>CN, and THF. The residues were then dried at 90 °C under vacuum overnight to obtain TPB-DMTP-OR(X%)-COF (Figure 2a). The yields of TPB-DMTP-OR(X%)-COF were 94% ( $X = 34$ ), and 88% ( $X = 50$ ) respectively.

**Synthesis of TPB-OR-COF.** A mixture of THF/CH<sub>3</sub>CN (0.4 mL/3.6 mL), TPB-BPTA-COF, CuI (3 mg), DIPEA (0.1 ml) and 13-azido-2,5,8,11-tetraoxatridecane (120 mg) was added in a Pyrex tube (10 mL). Then I degassed it by three freeze-pump-thaw cycles. I sealed the tube and kept it stirring at room temperature for 24 h. I collected the precipitate by filtering, washed with acetone, CH<sub>3</sub>CN, THF, and then dried at 90 °C under vacuum overnight to obtain TPB-OR-COF (Figure 2b) in a yield of 79%.

**Synthesis of TPB-BMTP-OR(X%)-COF.** A mixture of THF/CH<sub>3</sub>CN (0.4 mL/3.6 mL), TPB-BMTP-BPTA(X%)-COF, CuI (3 mg), DIPEA (0.1 ml) and 13-azido-2,5,8,11-tetraoxatridecane (36 mg for  $X = 34$  and 60 mg for  $X = 50$ ) was added in a Pyrex tube (10 mL). Then I degassed it by three freeze-pump-thaw cycles. I sealed the tube and kept it stirring at room temperature for 24 h. I collected the precipitate by filtering, washed with acetone, CH<sub>3</sub>CN, THF, and then dried at 90 °C under vacuum overnight to obtain TPB-BMTP-OR(X%)-COF (Figure 2b). The corresponding yields were 92% ( $X = 34$ ) and 87% ( $X = 50$ ).

**Synthesis of Li@TPB-DMTP-OR(X%)-COF.** The TPB-DMTP-OR(X%)-COF (100 mg) were firstly degassed under vacuum at 100 °C for 3 h. The COFs were then cooled down at 25 °C. Then I added LiClO<sub>4</sub> solution (171 mg with X = 34, and 65 mg with X = 50, in 2 mL MeOH) to COFs sample, and kept them stirred at 25 °C for 3 h. I removed MeOH under vacuum at 25 °C for 1 h, 70 °C for 2 h. The hybrids were then active at 90 °C overnight to prepare Li@TPB-DMTP-OR(X%)-COF.

**Synthesis of Li@TPB-OR-COF.** The prepared COF (100 mg) was degassed under vacuum at 100 °C for 3 h and cooled down at 25 °C. Then I added LiClO<sub>4</sub> solution (15 mg in 2 mL MeOH) to COF sample, and kept them stirring at 25 °C for 3 h. I removed MeOH under vacuum at 25 °C for 1 h, 70 °C for 2 h. The hybrid was then active at 90 °C overnight to prepare Li@TPB-OR-COF.

**Synthesis of Li@TPB-BMTP-OR(X%)-COF.** The TPB-BMTP-OR(X%)-COF (100 mg) were degassed under vacuum at 100 °C for 3 h and cooled down at 25 °C. Then I added LiClO<sub>4</sub> solution (87 mg with X = 34, 22 mg with X = 50, in 2 mL MeOH) to the TPB-BMTP-OR(X%)-COF samples and kept them stirring at 25 °C for 3 h. I removed MeOH under vacuum at 25 °C for 1 h, 70 °C for 2 h. The hybrids were then active at 90 °C overnight to prepare Li@TPB-BMTP-OR(X%)-COF.

### 5.3 Characterization of Polymer Electrolytes

TPB-DMTP-COF and TPB-BMTP-COF were synthesized by condensation of TPB and DMTP or BMTP under solvothermal conditions. I employed the three-component system with 2,5-bis(prop-2-yn-1-yloxy)terephthalaldehyde (BPTA) and DMTP or BMTP respectively as edge units to synthesize TPB-DMTP-BPTA(X%)-COF and TPB-BMTP-BPTA(X%)-COF (Figure 2), where X is the percentage of functional groups as a fraction of the groups linking the pore walls. When X is 100, the prepared COF was TPB-BPTA-COF. After a quantitative azide-ethynyl click reaction, the TPB-DMTP-BPTA(X%)-COF, TPB-BPTA-COF and TPB-BMTP-BPTA(X%)-COF were converted into TPB-DMTP-OR(X%)-COF, TPB-OR-COF, and TPB-BMTP-OR(X%)-COF, in which the chains were anchored onto the walls through triazoles rings.

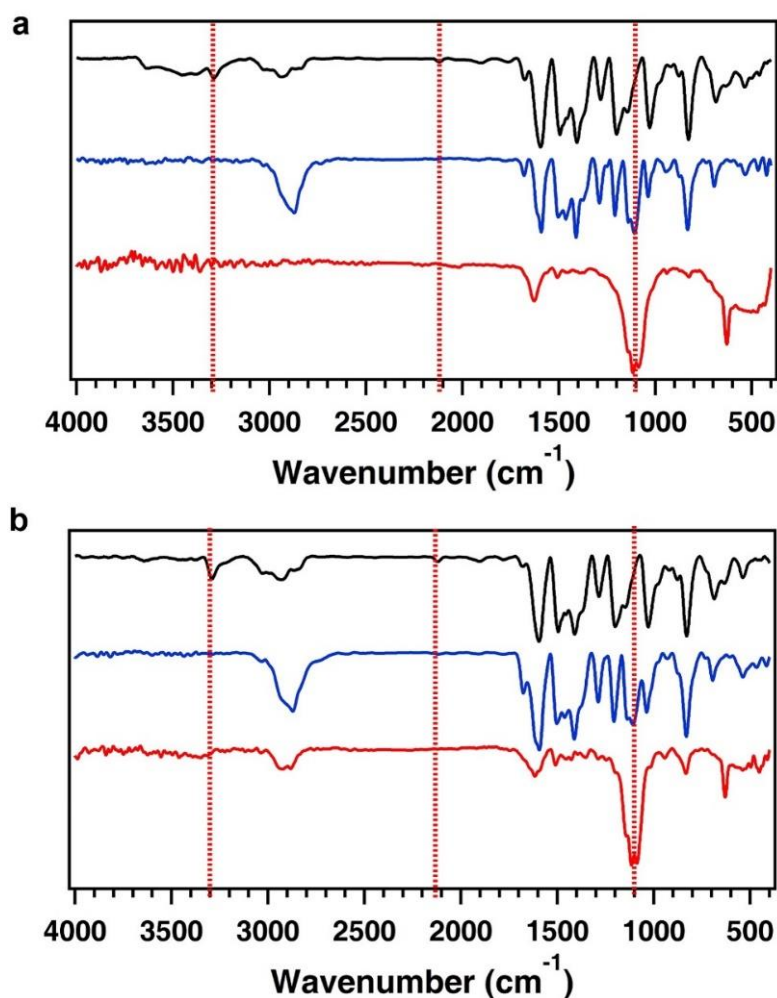


**Figure 3.** FT IR spectra of a) TPB-DMTP-BPTA(34%)-COF (black), TPB-DMTP-OR(34%)-COF(blue) and Li@TPB-DMTP-OR(34%)-COF (red), and b) TPB-DMTP-BPTA(50%)-COF (black), TPB-DMTP-OR(50%)-COF (blue) and Li@TPB-DMTP-OR(50%)-COF (red).

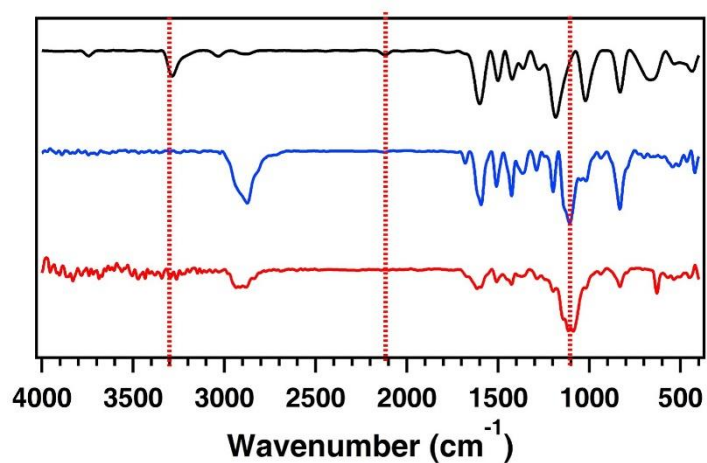


**Figure 4.** FT IR spectra of TPB-BPTA-COF (black), TPB-OR-COF (blue) and Li@TPB-OR-COF (red).

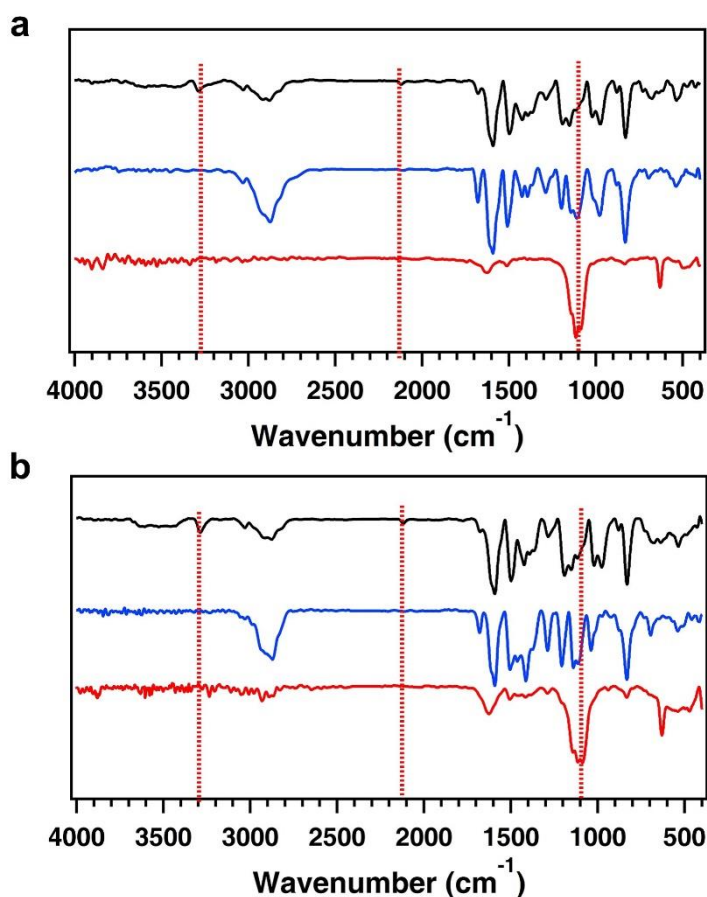


**Figure 5.** FT IR spectra of a) TPB-BMTP-BPTA(34%)-COF (black), TPB-BMTP-OR(34%)-COF (blue) and Li@TPB-BMTP-OR(34%)-COF (red), and b) TPB-BMTP-BPTA(50%)-COF (black), TPB-BMTP-OR(50%)-COF (blue) and Li@TPB-BMTP-OR(50%)-COF (red).

The Fourier-transform infrared (FT IR) spectra of TPB-BMTP-BPTA(X%)-COF revealed the chains were successfully linked onto the walls (Figure 3). The peaks at 2100 and 3300  $\text{cm}^{-1}$  were from  $\text{C}\equiv\text{C}$  and  $\text{C}\equiv\text{C}-\text{H}$  of BPTA units of COFs. After conducting click reactions, these peaks disappeared, whereas the peak intensity at 1100 and 2900  $\text{cm}^{-1}$  assigned to C-O-C symmetric and asymmetric stretching and aliphatic CH stretching was enhanced obviously.<sup>11</sup> More importantly, the peaks assigned to imine linkage at about 1700  $\text{cm}^{-1}$  were well maintained. Therefore, the triple-bonds were fully anchored by ethylene oxide chains along the pore surface by click reactions, and the COFs structure was well maintained. The similar results were able to be observe for TPB-BPTA-COF (Figure 4) and TPB-BMTP-BPTA(X%)-COF (Figure 5).

The precious chemical structure of the prepared COFs was further confirmed by element analysis. From the element analysis results, there was slight difference between the theoretical and observed content (Table 1).

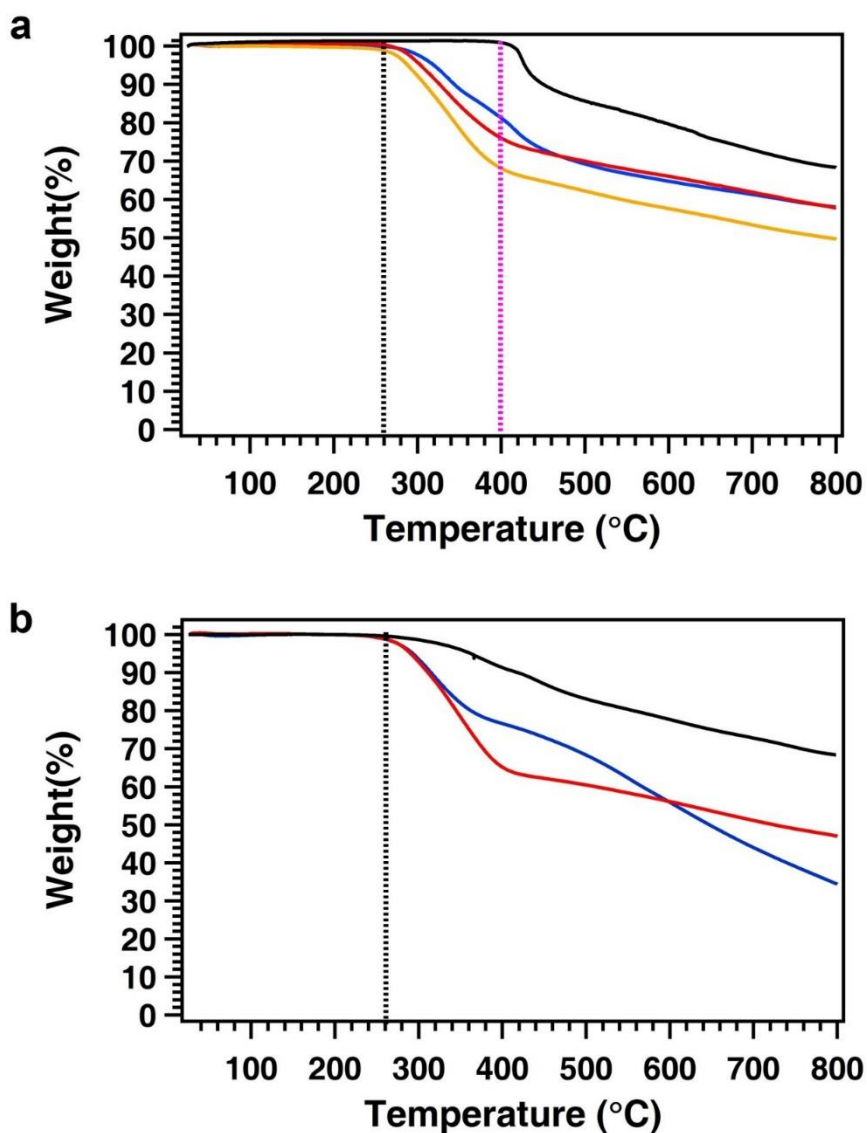


**Figure 6.** Thermogravimetric curves of a) TPB-DMTP-COF (black), TPB-DMTP-OR(34%)-COF (blue), TPB-DMTP-OR(50%)-COF (red), TPB-OR-COF (yellow), and b) TPB-BMTP-COF (black), TPB-BMTP-OR(34%)-COF (blue), and TPB-BMTP-OR(50%)-COF (red) measured over the temperature from 25 to 800 °C at a heating rate constant of 10 °C min<sup>-1</sup> under nitrogen.

The thermal stability of the prepared TPB-DMTP-COF, TPB-DMTP-OR(X%)-COF, TPB-OR-COF, TPB-BMTP-COF and TPB-BMTP-OR(X%)-COF were investigated by thermogravimetric analysis (TGA) under nitrogen. From TGA results, TPB-DMTP-COF was thermal stable before 400 °C (Figure 6a). With anchoring flexible chains onto the wall, no decomposition of TPB-DMTP-OR(X%)-COFs could be observed before 260 °C. The weight losses between 260 to 400 °C were from decomposition of ethylene oxide chains. Thus, the weight fraction of chains was able to be estimated according to

the TGA results. The weight percentages of chains were 18.7%, 23.1% and 32.1% for TPB-DMTP-OR(33%)-COF, TPB-DMTP-OR(50%)-COF and TPB-OR-COF, which were close to the theoretical amount (17.4%, 23.6% and 36.9%, respectively). From TGA curves, TPB-BMTP-COF was stable until 300 °C (Figure 6b). And the start decomposition temperature of TPB-BMTP-OR(X%)-COF were 260 °C, which was the same as that of the TPB-DMTP-OR(X%)-COFs.

From nitrogen-sorption isotherm curves at 77 K, TPB-DMTP-COF measured at 77 K exhibited a type-IV isotherm, rapid uptake at a low pressure of  $P/P_0$ , followed by a sharp step between  $P/P_0 = 0.15$  and 0.25 (Figure 7a). The Brunauer–Emmett–Teller (BET) surface area was 2756 m<sup>2</sup> g<sup>-1</sup> (Table 2). The pore size distribution profile revealed that the COF had a pore volume of 1.34 cm<sup>3</sup> g<sup>-1</sup>, with a pore size of 3.26 nm. With changing the percentages of BPTA, the BET surface areas and pore structure changed. The resultant BET surface areas of TPB-DMTP-BPTA(34%)-COF and TPB-DMTP-BPTA(50%)-COF were 2560, 2620 m<sup>2</sup> g<sup>-1</sup>. The corresponding pore volume of TPB-DMTP-BPTA (34%, 50%)-COF were 1.24, and 1.36 cm<sup>3</sup> g<sup>-1</sup>, with pore size of 3.10, 3.09 nm (Figure 7b and c, and Table 2). Whereas the BET surface area of TPB-BPTA-COF was 2008 m<sup>2</sup> g<sup>-1</sup> (Figure 7a, yellow curve), and the pore size reduced to 2.88 nm with pore volume of 0.91 cm<sup>3</sup> g<sup>-1</sup>. Accompanied with the ethylene oxide chains on the wall, the surface areas decreased obviously to 1502 and 477 m<sup>2</sup> g<sup>-1</sup> for TPB-DMTP-OR (34% and 50%)-COF (Figure 7d), whereas the pore volume was 0.71 and 0.27 cm<sup>3</sup> g<sup>-1</sup> respectively, with decreased pore size of 2.88 and 2.78 nm (Figure 7e and f). For TPB-OR-COF, almost nonporous structure was maintained, with low BET surface area (48 m<sup>2</sup> g<sup>-1</sup>) and ignored pore volume (0.06 cm<sup>3</sup> g<sup>-1</sup>) (Figure 7f, yellow). The decreased surface areas and pore volume were ascribed to the chains in the pore channels.

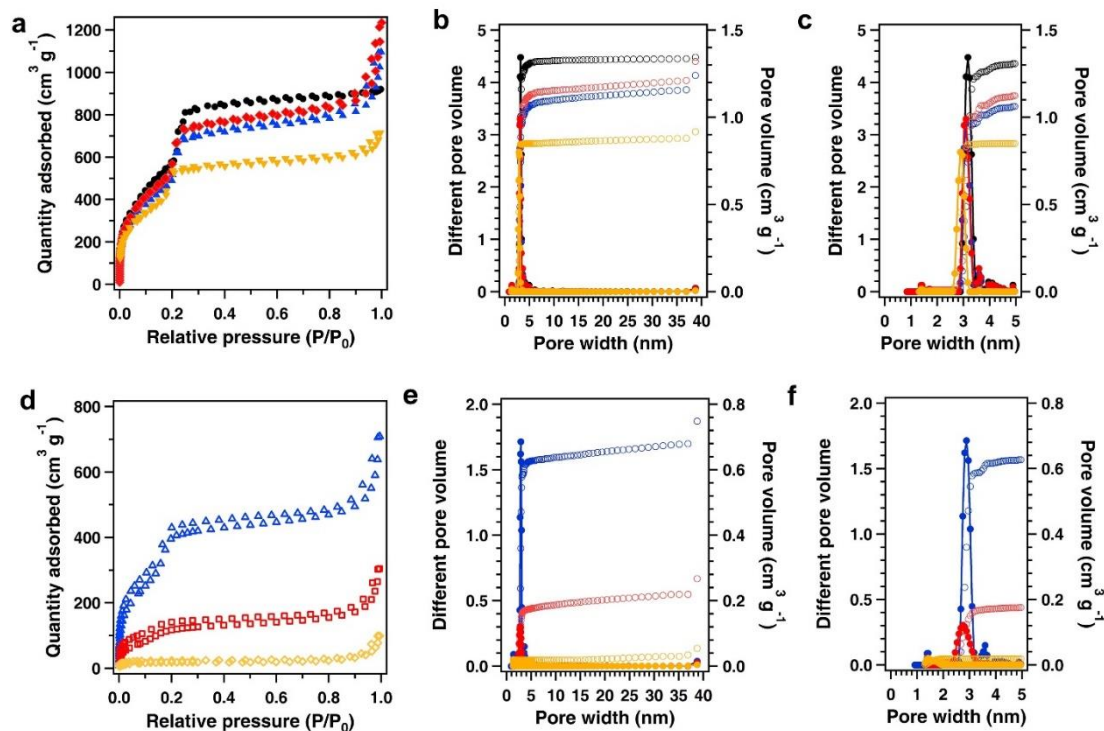


**Figure 7.** a) Nitrogen sorption isotherm profiles, b) pore size distribution profiles, and c, f) pore size distribution profiles from 0 to 5 nm, of TPB-DMTP-COF (black), of TPB-DMTP-BPTA(34%)-COF (blue), TPB-DMTP-BPTA(50%)-COF (red), and TPB-BPTA-COF (yellow). d) Nitrogen sorption isotherm profiles, e) pore size distribution profiles, and f) pore size distribution profiles from 0 to 5 nm TPB-DMTP-OR(34%)-COF (blue), TPB-DMTP-OR(50%)-COF (red), and TPB-OR-COF (yellow).

When the methoxy group of DMTP was replaced by short ethylene oxide chains of BMTP incorporated into the pore walls, TPB-BMTP-COF possessed the same mesoporous character from the nitrogen-sorption isotherm curves, corresponding to the pore structure of TPB-DMTP-COF. The BET surface area decreased to  $1746 \text{ m}^2 \text{ g}^{-1}$  (Figure 8a, black curve). Because of the existence of short ethylene oxide chains in the pores, the pore size also reduced to 3.02 nm, and the pore volume was  $0.96 \text{ cm}^3 \text{ g}^{-1}$  (Figure 8b, Table 2). The BET surface areas of TPB-BMTP-BPTA(34% and 50%)-COF were 2042 and  $1963 \text{ m}^2 \text{ g}^{-1}$ , whereas the pore volume was 1.04 and  $1.01 \text{ cm}^3 \text{ g}^{-1}$ . And the corresponding pore size of TPB-BMTP-BPTA(34%)-COF and TPB-BMTP-BPTA(50%)-COF was the same as 2.95 nm (Figure 8c). With longer ethylene oxide chains on the wall, the surface areas decreased to 633 and  $78 \text{ m}^2 \text{ g}^{-1}$  (Figure 8d), and the pore volume was declined to 0.39 and  $0.09 \text{ cm}^3 \text{ g}^{-1}$ , respectively, with pore size of 2.73 and 2.67 nm (Figure 8e and f, and Table 2).

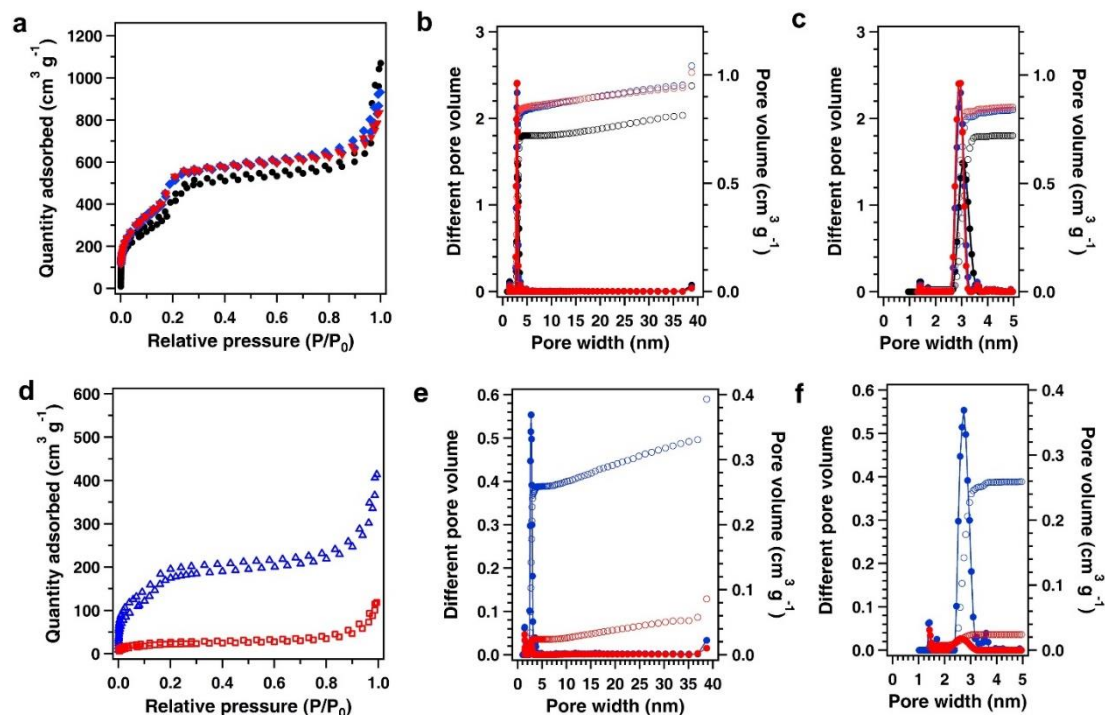


**Figure 8.** a) Nitrogen sorption isotherm profiles, b) pore size distribution profiles, and c) pore size distribution profiles from 0 to 5 nm of TPB-BMTP-COF (black), of TPB-BMTP-BPTA(34%)-COF (blue), and TPB-BMTP-BPTA(50%)-COF (red). d) Nitrogen sorption isotherm profiles, e) pore size distribution profiles, and f) pore size distribution profiles from 0 to 5 nm TPB-BMTP-OR(34%)-COF (blue), and TPB-BMTP-OR(50%)-COF (red).

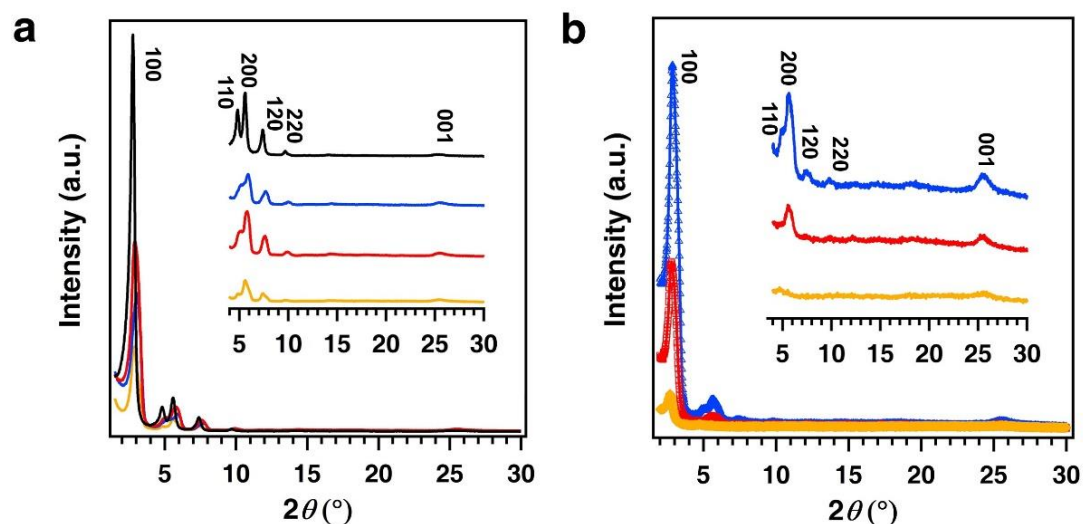


**Figure 9.** a) PXRD patterns of TPB-DMTP-COF (black), TPB-DMTP-BPTA(34%)-COF (blue), TPB-DMTP-BPTA(50%)-COF (red) and TPB-BPTA-COF (yellow). b) PXRD patterns of TPB-DMTP-OR(34%)-COF (blue), TPB-DMTP-OR(50%)-COF (red), and TPB-OR-COF (yellow).

Powder X-ray diffraction (PXRD) measurements showed that TPB-DMTP-COF was a crystalline polymer with the most intensive peak at  $2.76^\circ$  and other five peaks at  $4.82$ ,  $5.60$ ,  $7.42$ ,  $9.70$ , and  $25.2^\circ$ , which were assigned to the (100), (110), (200), (210), (220), and (001) facets, respectively (Figure 9a). All the corresponding peaks were observed for TPB-DMTP-BPTA(X%)-COF, and TPB-BPTA-COF. With linking longer chains of TPB-DMTP-OR(X%)-COF and TPB-OR(X%)-COF, the corresponding intensity of PXRD peaks was declined (Figure 9b), whereas the peaks from (100) and (001) facets of all the prepared COFs were clearly identified.

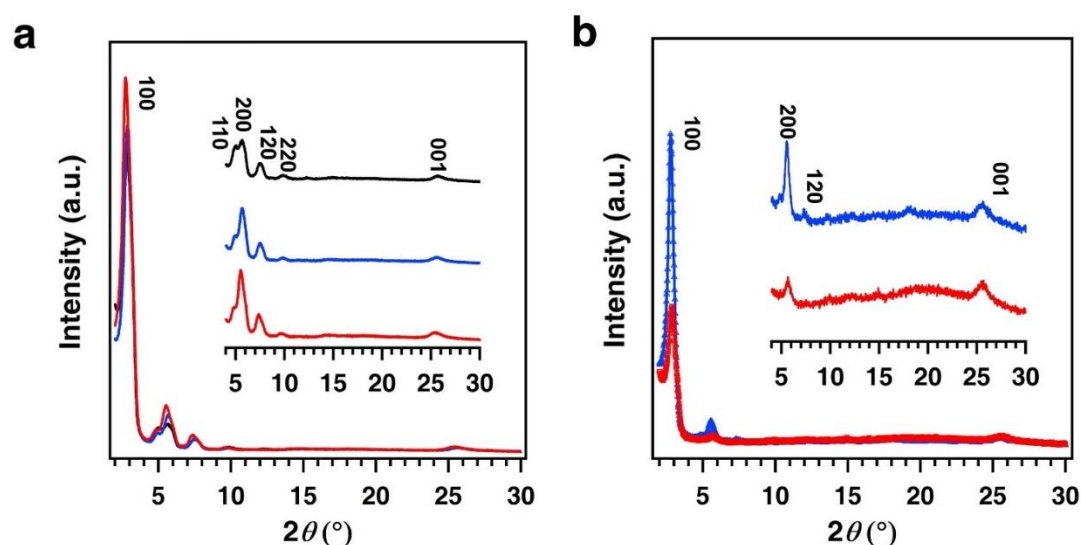


**Figure 10.** a) PXRD patterns of TPB-BMTP-COF (black), TPB-BMTP-BPTA(34%)-COF (blue), and TPB-BMTP-BPTA(50%)-COF (red). b) PXRD patterns of TPB-BMTP-OR(34%)-COF (blue) and TPB-DMTP-OR(50%)-COF (red).

Similarly, peaks of TPB-BMTP-COF at  $2.82$ ,  $5.04$ ,  $5.73$ ,  $7.45$ ,  $9.97$ , and  $25.7^\circ$  (Figure 10a) were from (100), (110), (200), (210), (220), and (001) facets (Figure 10b). These peaks were also clearly identified for three component COFs, TPB-BMTP-BPTA(X%)-COF. With linking longer ethylene chains by click reactions, the peaks from (100), (200), and (001) facets were also observed, indicating the high crystallinity of prepared COFs.

Therefore, the prepared COFs have high surface areas, thermal stability, and crystallinity, while the 1D channels adopted with different chain content. Increasing the content and length of the ethylene oxide chains results in lower surface areas, pore volume, and crystallinity. 1D pore channels of COFs provide the fast pathway for lithium ion transport and diffusion, and the functional groups on the walls promote effectively lithium ion fast transport. Thus, these COFs are potentially working as

polymer electrolytes, and overcoming the disadvantages of traditional polymer electrolytes, including thermal and dimensional stability, and low conductive performance.

Based on the 1D mesoporous channels, the prepared COFs can accommodate  $\text{LiClO}_4$  in their pores. Upon loading  $\text{LiClO}_4$  in the COFs (TPB-DMTP-OR(X%)-COF, TPB-OR-COF, and TPB-BMTP-OR(X%)-COF), the complexes of lithium and COFs (Li@TPB-DMTP-OR(X%)-COF, Li@TPB-OR-COF, and Li@TPB-BMTP-OR(X%)-COF) were prepared. To investigate the  $\text{LiClO}_4$  was fully in the pores, nitrogen sorption isotherm experiments were firstly conducted. The BET surface areas of the hybrid were declined to about  $10 \text{ m}^2 \text{ g}^{-1}$  (Figure 11), and almost no pores could be observed. Thus, all the pore channels were fully loaded by lithium sources.

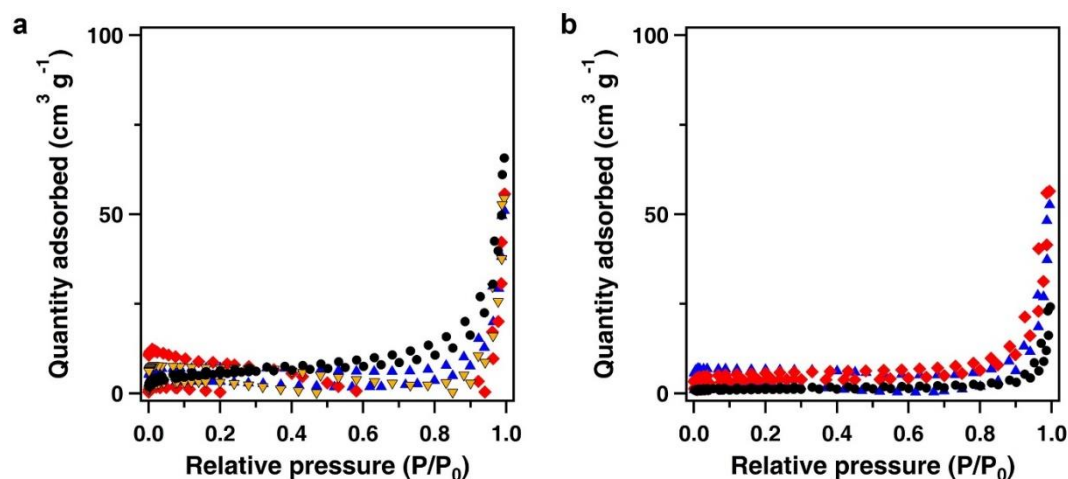


**Figure 11.** a) Nitrogen sorption isotherm profiles of Li@TPB-DMTP-COF (black), Li@TPB-DMTP-OR(34%)-COF (blue), Li@TPB-DMTP-OR(50%)-COF (red), and Li@TPB-OR-COF (yellow). b) Nitrogen sorption isotherm profiles of Li@TPB-BMTP-COF (black), of Li@TPB-BMTP-OR(34%)-COF (blue), and Li@TPB-BMTP-OR(50%)-COF (red).

From the PXRD results, with additional of  $\text{LiClO}_4$ , the peaks of all the COFs assigned to (100) faces disappeared. Whereas peaks at  $21^\circ$ , and  $23^\circ$  were arising, which were accompanied to (101), and (110) faces of  $\text{LiClO}_4$  (Figure 12). The intensity of Li@TPB-OR-COF and Li@TPB-BMTP-OR(50%)-COF was weaker than Li@TPB-DMTP-OR(34%, and 50%)-COF and Li@TPB-BMTP-OR(34%)-COF, which were from the smaller amount of  $\text{LiClO}_4$ .

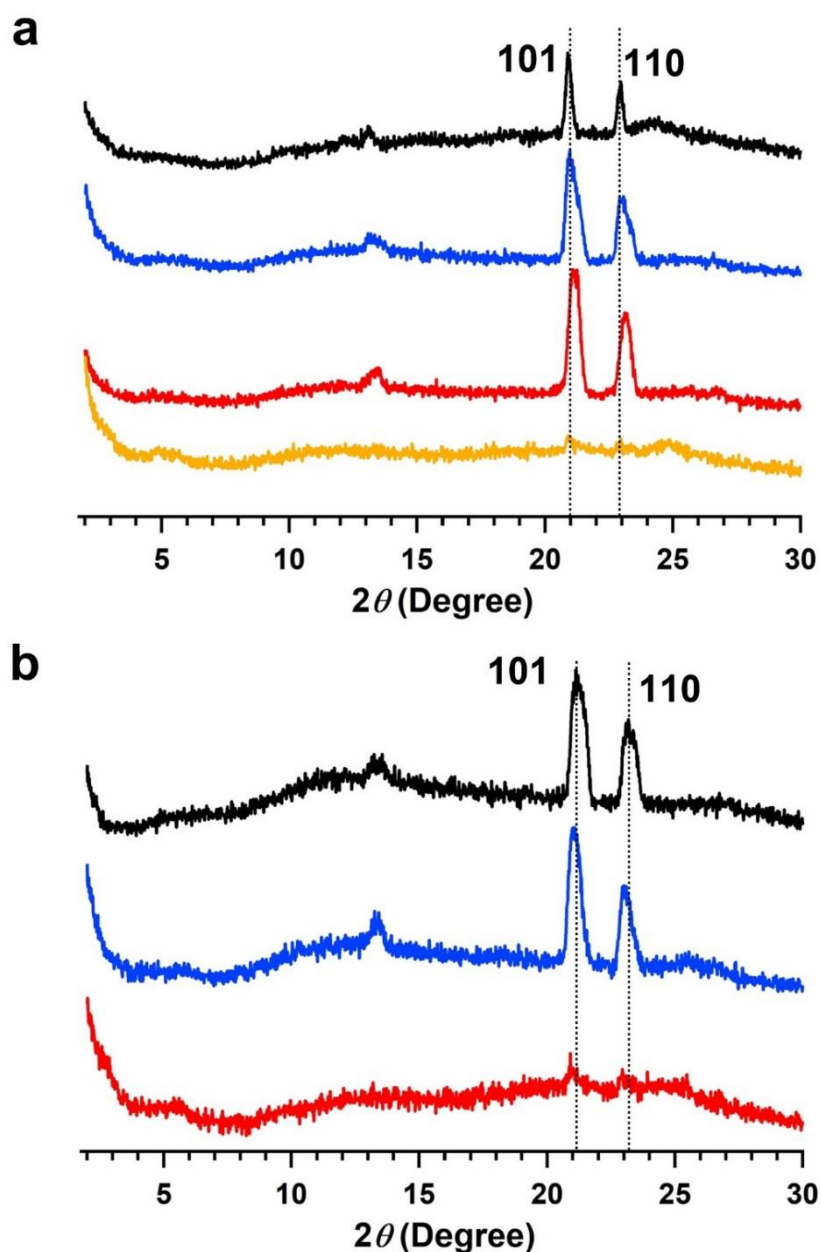


**Figure 12.** a) PXRD patterns of Li@TPB-DMTP-COF (black), Li@TPB-DMTP-OR(34%)-COF (blue), Li@TPB-DMTP-OR(50%)-COF (red), and Li@TPB-OR-COF (yellow). b) PXRD patterns of Li@TPB-BMTP-COF (black), Li@TPB-BMTP-OR(34%)-COF (blue), Li@TPB-BMTP-OR(50%)-COF (red).

From the Field-emission scanning electron microscopy (FE-SEM) images, the morphology of these COFs did not change, and no free  $\text{LiClO}_4$  particles aggregated on the surface could be observed, further indicated all the lithium sources were successfully loaded in the pores (Figure 13 and 14). Upon loading  $\text{LiClO}_4$ , FT IR spectra revealed that a new peak at  $625\text{ cm}^{-1}$  was assigned to  $\text{ClO}_4^{-1}$  anions (Figure 3, 4 and 5, red curve).<sup>11</sup> Thus, lithium sources were fully loaded in the 1D channels.

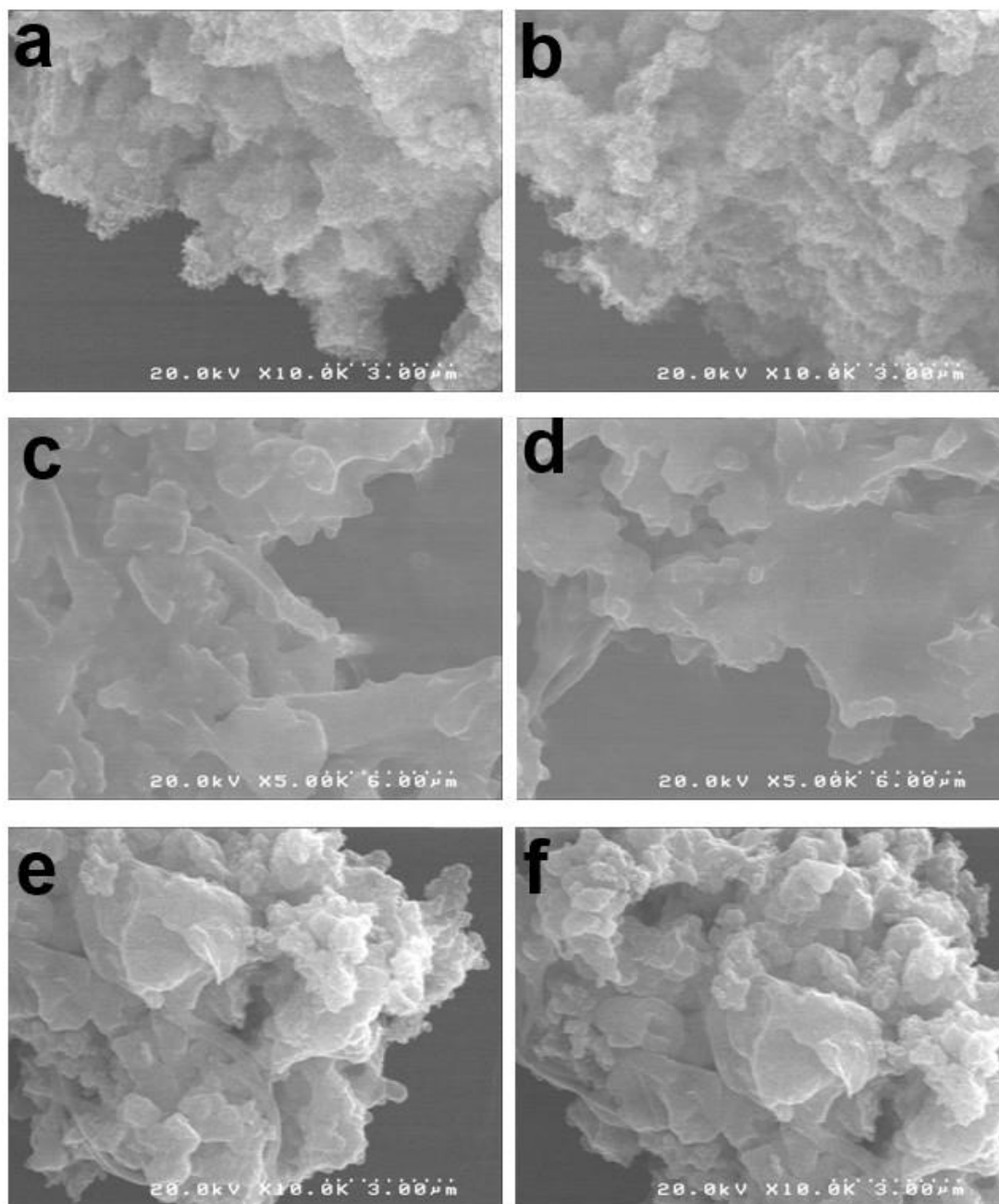


**Figure 13.** FE-SEM images of a) TPB-DMTP-OR(34%)-COF, b) Li@TPB-DMTP-OR(34%)-COF, c) TPB-DMTP-OR(50%)-COF, d) Li@TPB-DMTP-OR(50%)-COF, e) TPB-OR-COF and f) Li@TPB-OR-COF.

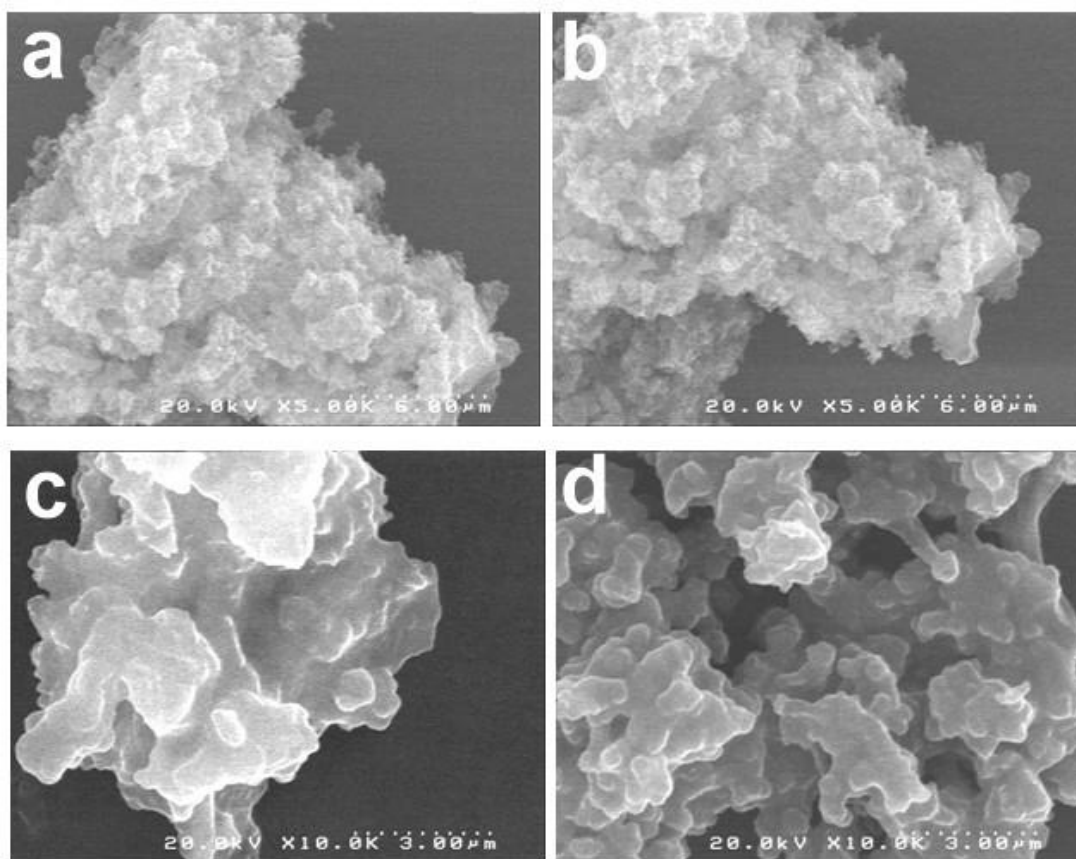


**Figure 14.** FE-SEM images of a) TPB-BMTP-OR(34%)-COF, b) Li@TPB-BMTP-OR(34%)-COF, c) TPB-BMTP-OR(50%)-COF and d) Li@TPB-BMTP-OR(50%)-COF.

## 5.5 Results and Discussion

The prepared complexes of  $\text{LiClO}_4$  and COFs were prepared for pellets for conductivity performance under over 40 MP pressure for 2 hours. No crush could be observed, which indicated good mechanical strength of our materials. The conductivities of Li@COFs were measured by using alternating-current impedance spectroscopy.

Nyquist plots of pellets were obtained under a nitrogen atmosphere at temperatures between 40 and 100 °C. These impedance plots were typical of predominantly ionic conduction, where the plot of the real component ( $Z'$ ) versus the imaginary component ( $Z''$ ) of the complex impedance function displayed a semicircular shape followed by a spike.<sup>12</sup> The conductivity was calculated according to the equation  $\sigma = L/(Z \times A)$ , in which  $\sigma$  is the conductivity ( $\text{S cm}^{-1}$ ),  $L$  is the sample thickness (cm),  $Z$  is the impedance ( $\Omega$ ) and  $A$  is the electrode area ( $\text{cm}^2$ ). Increasing temperature leads to high motion ability of chains on the walls, which makes higher conduction performance. The

resistances of Li@TPB-DMTP-OR(34%)-COF were  $1.96 \times 10^4$ ,  $7.92 \times 10^3$ ,  $3.68 \times 10^3$ , 1709, 745, 273 and  $23 \Omega$  at 40, 50, 60, 70, 80, 90 and  $100 \text{ }^\circ\text{C}$ , with the corresponding conductivities of  $7.77 \times 10^{-6}$ ,  $1.93 \times 10^{-5}$ ,  $4.15 \times 10^{-5}$ ,  $8.94 \times 10^{-5}$ ,  $2.05 \times 10^{-4}$ ,  $5.58 \times 10^{-4}$  and  $6.46 \times 10^{-3} \text{ S cm}^{-1}$ .

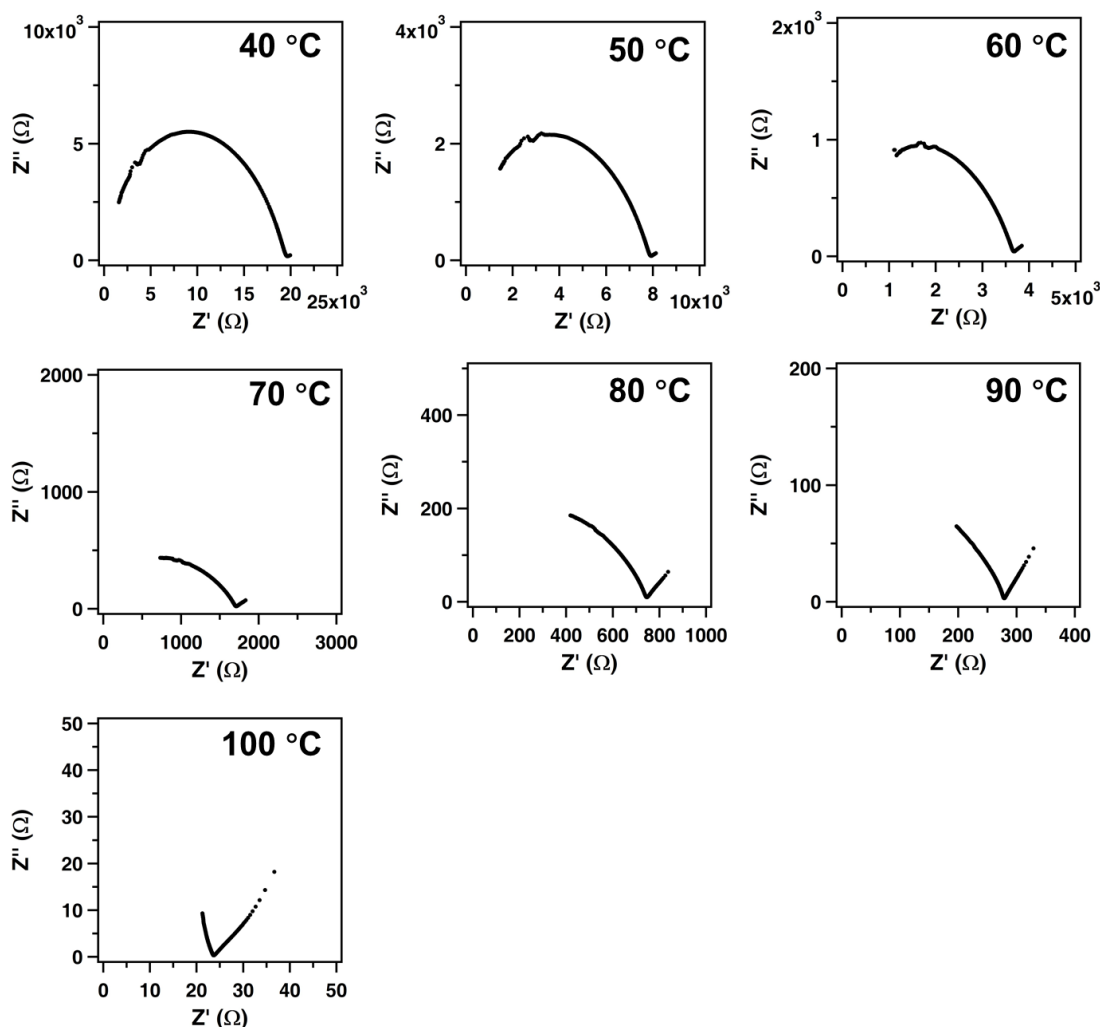


**Figure 15.** Nyquist plots of Li@TPB-DMTP-OR(34%)-COF at different temperature.

To better understand the roles of the ethylene oxide chains density on the pore channels, the percentage of ethylene oxide chains increased from 34% to 50%. The resistances of TPB-DMTP-OR(50%)-COF decreased to  $1.07 \times 10^4$ ,  $4.06 \times 10^3$ ,  $1.91 \times 10^3$ , 1060, 563, 299 and  $61 \Omega$  at 40, 50, 60, 70, 80, 90 and  $100 \text{ }^\circ\text{C}$ , with the corresponding conductivities of  $1.31 \times 10^{-5}$ ,  $3.45 \times 10^{-5}$ ,  $7.32 \times 10^{-5}$ ,  $1.32 \times 10^{-4}$ ,  $2.49 \times 10^{-4}$ ,  $4.68 \times 10^{-4}$  and  $2.26 \times 10^{-3} \text{ S cm}^{-1}$  (Figure 16). As for a control, the resistances of TPB-DMTP-COF were  $1.59 \times 10^6$ ,  $7.31 \times 10^5$ ,  $3.21 \times 10^5$ ,  $1.24 \times 10^5$ ,  $4.02 \times 10^4$ ,  $1.03 \times 10^4$  and  $314 \Omega$  at 40, 50, 60, 70, 80, 90 and  $100 \text{ }^\circ\text{C}$  (Figure 17), with the corresponding conductivities of  $1.36 \times 10^{-7}$ ,  $2.96 \times 10^{-7}$ ,  $6.74 \times 10^{-7}$ ,  $1.75 \times 10^{-6}$ ,  $5.37 \times 10^{-6}$ ,  $2.09 \times 10^{-5}$

and  $6.08 \times 10^{-4} \text{ S cm}^{-1}$ . Notably, compared with TPB-DMTP-COF, the TPB-DMTP-OR(34%)-COF and TPB-DMTP-OR(50%)-COF had a much smaller pore volume ( $0.71$  and  $0.27 \text{ cm}^3 \text{ g}^{-1}$  than  $1.36 \text{ cm}^3 \text{ g}^{-1}$ ), but the complexes of  $\text{LiClO}_4$  and COFs exhibited much better conduction performance (56 and 96 times of TPB-DMTP-OR(34%)-COF and TPB-DMTP-OR(50%)-COF higher than TPB-DMTP-COF at  $40 \text{ }^\circ\text{C}$ ).

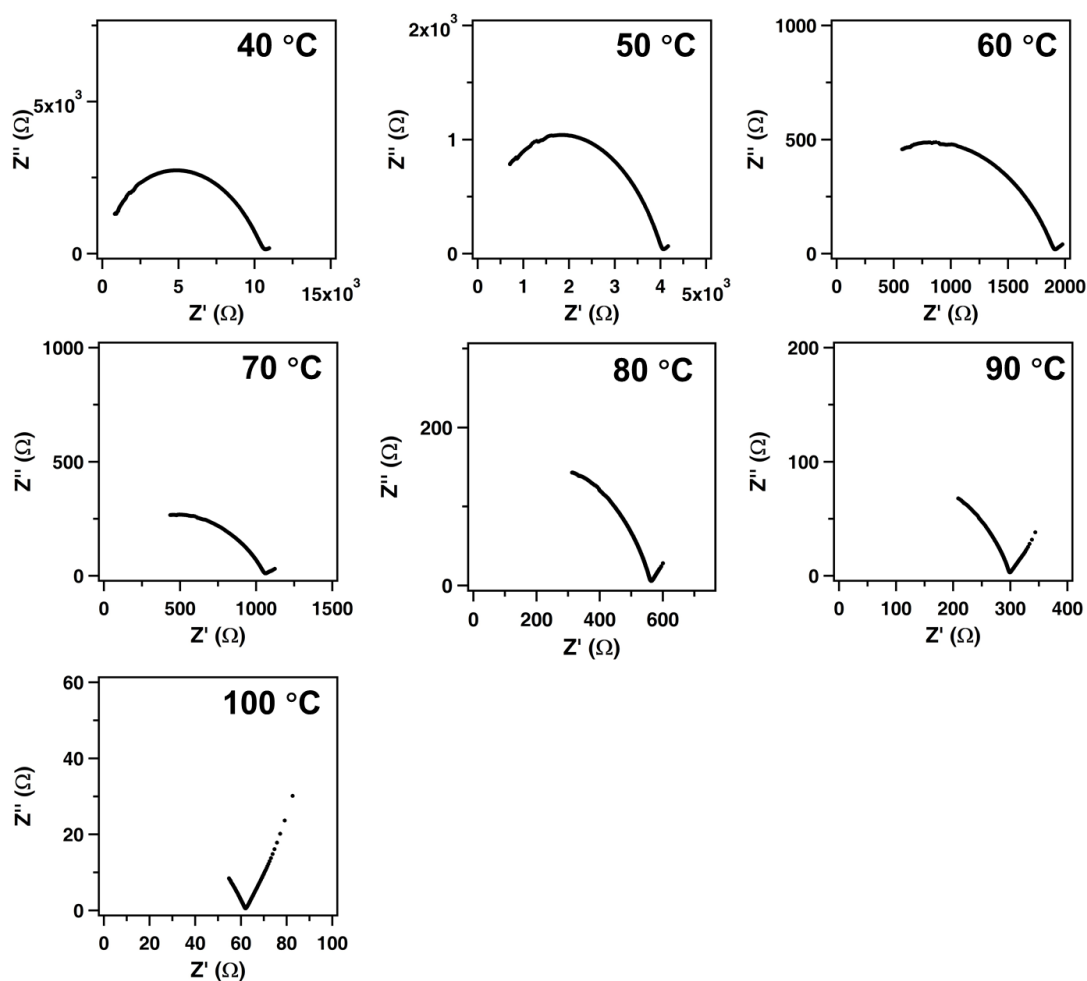


**Figure 16.** Nyquist plots of Li@TPB-DMTP-OR(50%)-COF at different temperature.

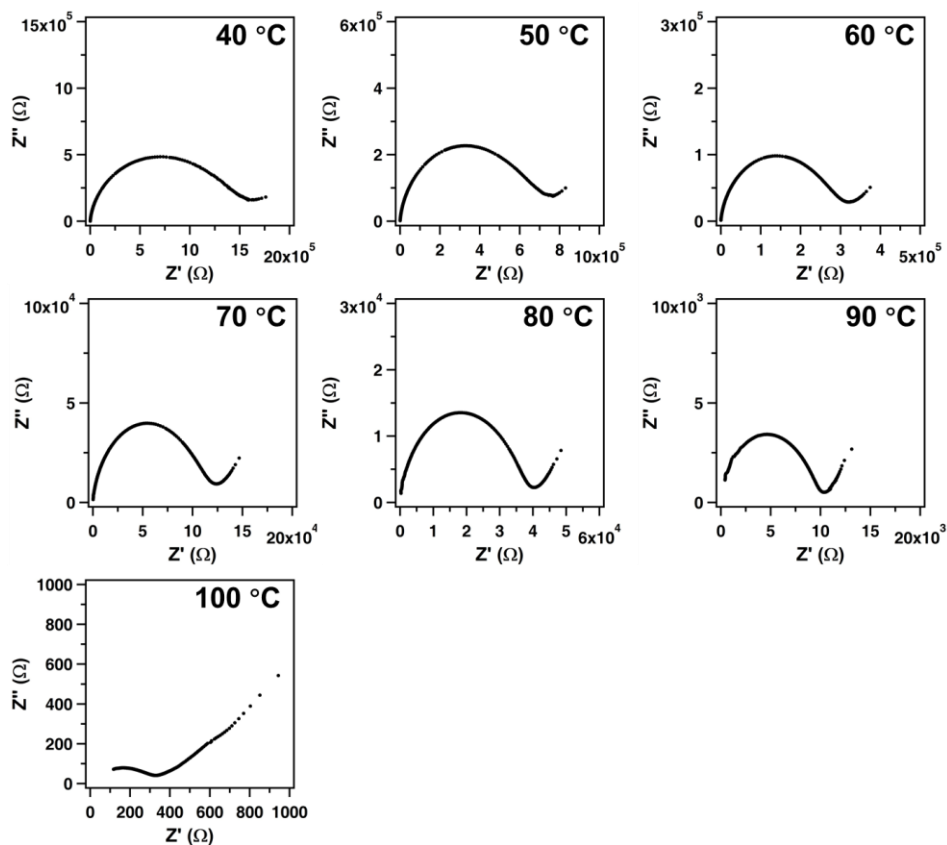


**Figure 17.** Nyquist plots of Li@TPB-DMTP-COF at different temperature.

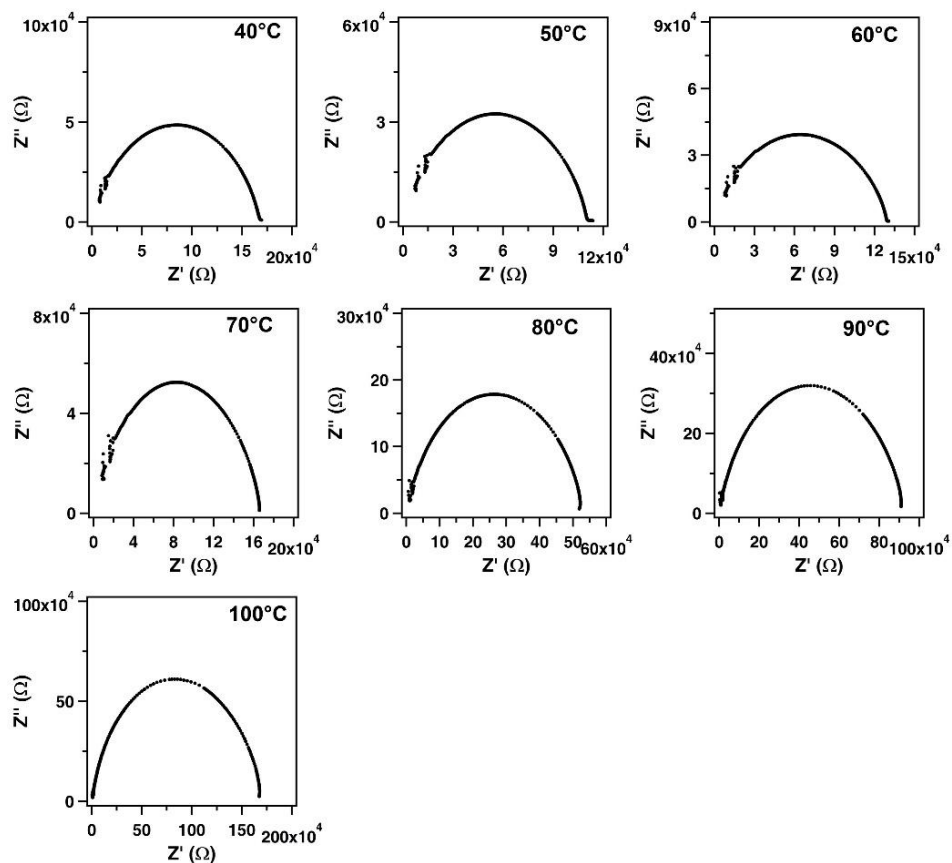


**Figure 18.** Nyquist plots of Li@TPB-OR-COF at different temperature.

The percentage of ethylene oxide chains was further increased to 100% along the pore channels the resultant polymer almost had no pores ( $0.06 \text{ cm}^3 \text{ g}^{-1}$ ). Thus, it was difficult to accommodate enough lithium salt in the channels, even though the chain density was 2 times of TPB-DMTP-OR(50%)-COF. As a result, the increased resistances were  $1.69 \times 10^5$ ,  $1.13 \times 10^5$ ,  $1.30 \times 10^5$ ,  $1.63 \times 10^5$ ,  $5.21 \times 10^5$ ,  $9.00 \times 10^5$  and  $1.64 \times 10^6 \Omega$  from 40 to 100 °C. And the conductivities were  $9.04 \times 10^{-7}$ ,  $1.35 \times 10^{-6}$ ,  $1.17 \times 10^{-6}$ ,  $9.35 \times 10^{-7}$ ,  $2.93 \times 10^{-7}$ ,  $1.70 \times 10^{-7}$  and  $9.29 \times 10^{-8} \text{ S cm}^{-1}$ . The conductivities were even decreased, while increasing temperature (above 50 °C). The poor thermal stability was because that  $\text{LiClO}_4$  was not able without confining into pores. Thus, the high pore volume is important to load sufficient lithium ion sources, whereas the chains play more important roles to improve lithium ion conduction in channels.

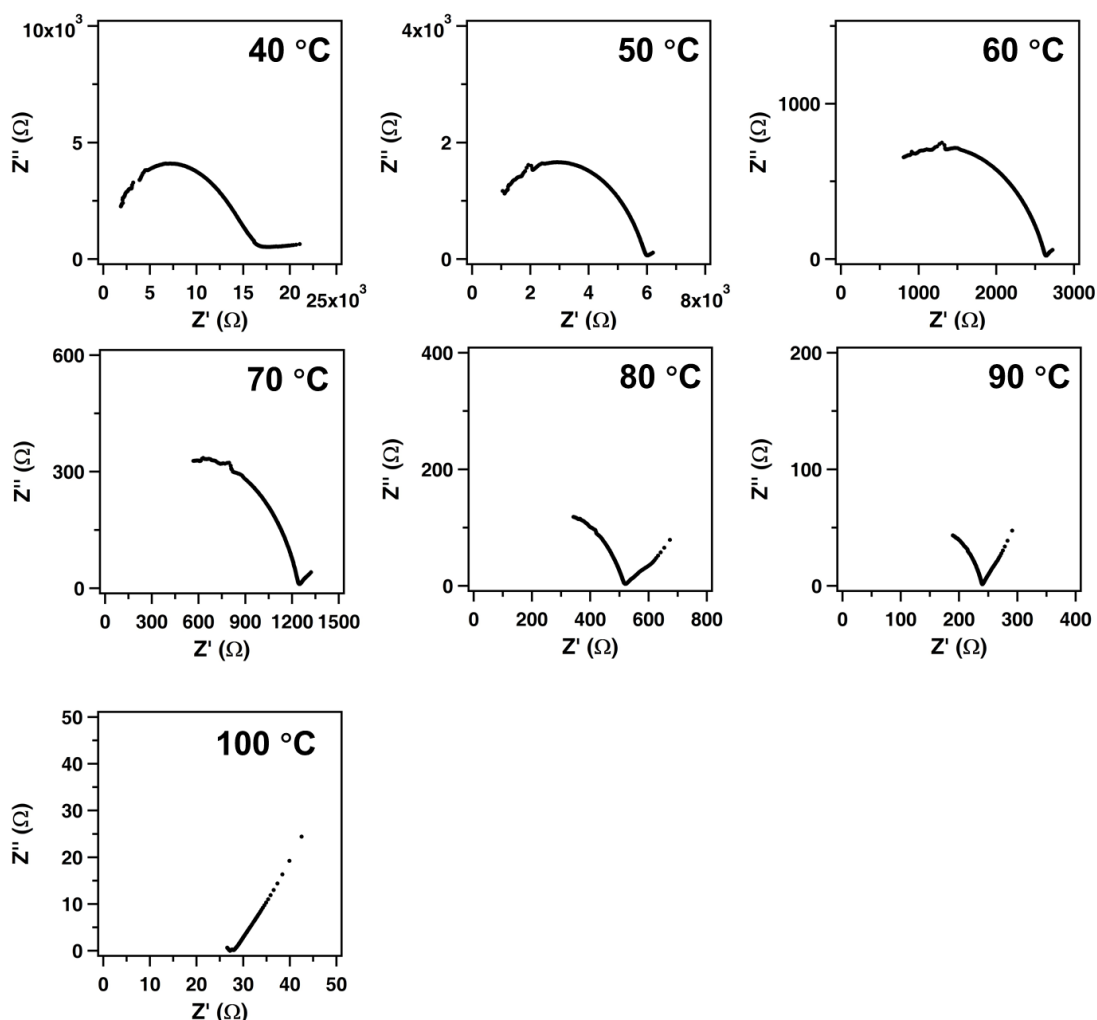


**Figure 19.** Nyquist plots of Li@TPB-BMTP-OR(34%)-COF at different temperature.

Apart from lithium ion concentration and ethylene oxide chains density along the pore channels, the length of chains is another important effect for conduction

performance. When the BMTP units of TPB-BMTP-COF were substituted by longer chains (OR group), the conduction was further investigated in the same condition. The resistances of TPB-BMTP-OR(34%)-COF were  $1.66 \times 10^4$ ,  $6.01 \times 10^3$ ,  $2.64 \times 10^3$ , 1247, 520, 239 and  $27 \Omega$  at 40, 50, 60, 70, 80, 90 and  $100 \text{ }^\circ\text{C}$ , respectively. The corresponding conductivities were  $8.43 \times 10^{-6}$ ,  $2.33 \times 10^{-5}$ ,  $5.33 \times 10^{-5}$ ,  $1.12 \times 10^{-4}$ ,  $2.69 \times 10^{-4}$ ,  $5.84 \times 10^{-4}$  and  $5.01 \times 10^{-3} \text{ S cm}^{-1}$  respectively (Figure 19). The conduction performance was superior to those of TPB-BMTP-COF, which were  $6.04 \times 10^{-6}$ ,  $1.21 \times 10^{-5}$ ,  $2.85 \times 10^{-5}$ ,  $6.28 \times 10^{-5}$ ,  $1.66 \times 10^{-4}$ ,  $5.49 \times 10^{-4}$  and  $6.94 \times 10^{-3} \text{ S cm}^{-1}$  from 40 to  $100 \text{ }^\circ\text{C}$  (Figure 20). The enhanced conductivity confirmed the longer chains benefited lithium ion conduction, in despite of decreasing pore volume of COFs.

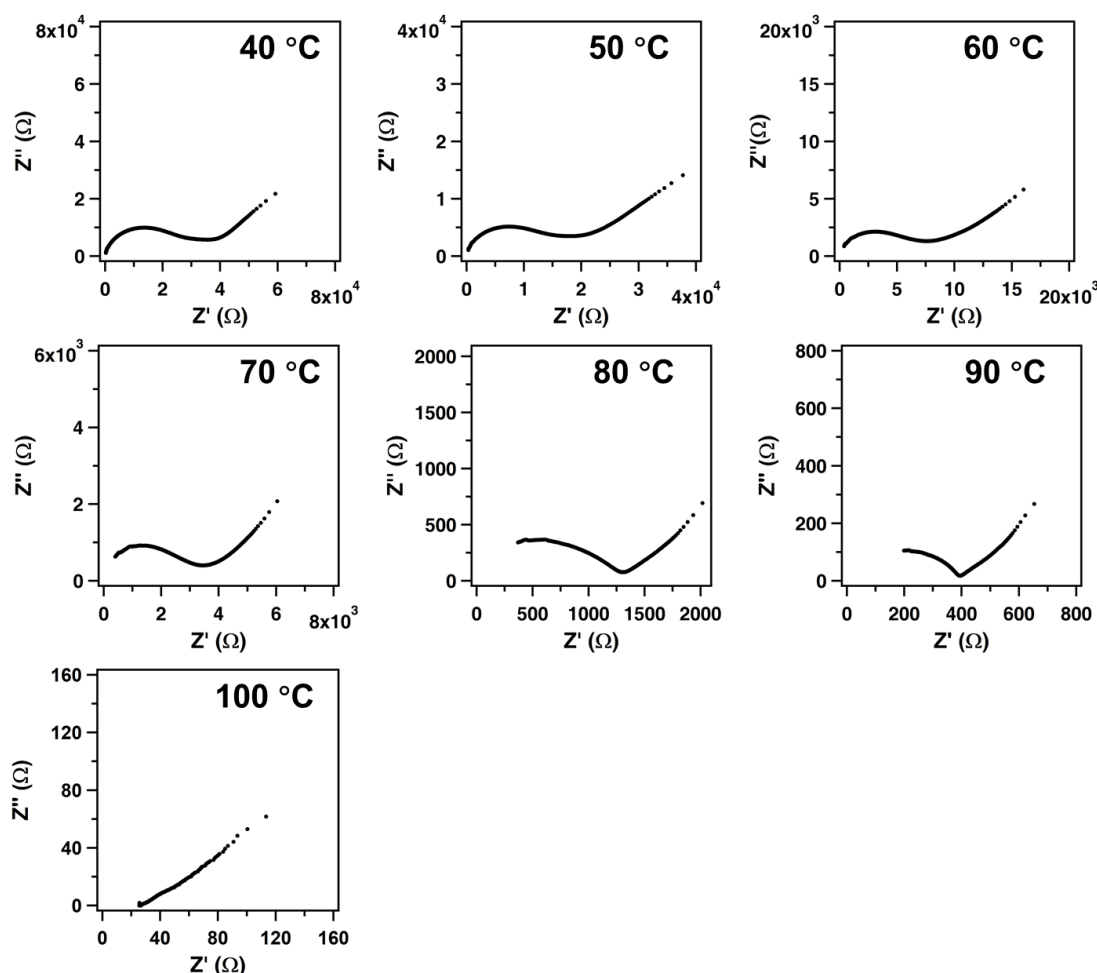


**Figure 20.** Nyquist plots of Li@TPB-BMTP-COF at different temperature.

The longer chains (OR) percentage was further increased to 50%, which made the TPB-BMTP-OR(50%)-COF had very limited pore volume ( $0.09 \text{ cm}^3 \text{ g}^{-1}$ ). There was limited space for lithium salt. And the resultant conductivities were  $5.51 \times 10^{-6}$ ,  $1.64 \times 10^{-5}$ ,  $2.77 \times 10^{-5}$ ,  $3.85 \times 10^{-5}$ ,  $3.79 \times 10^{-5}$ ,  $3.18 \times 10^{-5}$  and  $1.74 \times 10^{-5} \text{ S cm}^{-1}$  from 40 to

100 °C (Figure 21). The thermal stability was from the limited lithium sources in the pores.

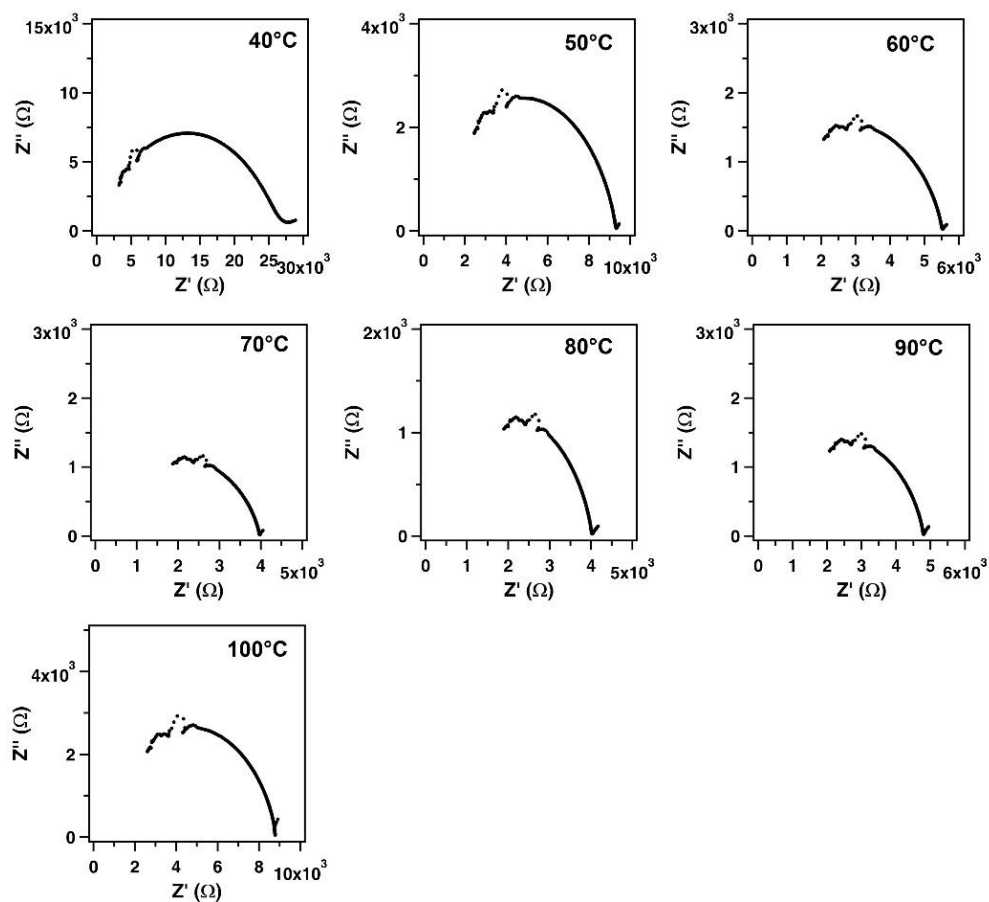


**Figure 21.** Nyquist plots of Li@TPB-BMTP-OR(50%)-COF at different temperature.

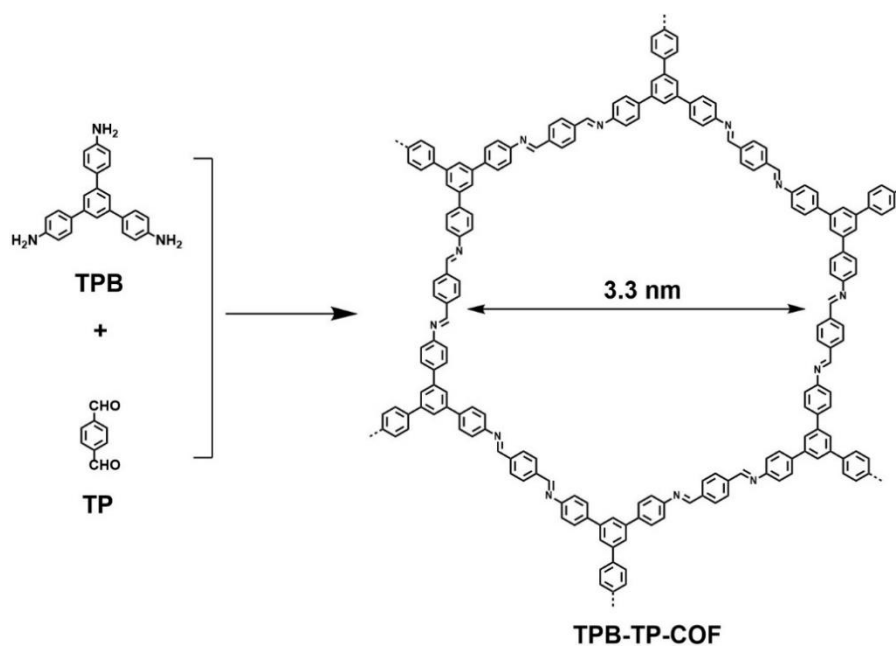


**Figure 22.** Synthesis and chemical structure of TPB-TP-COF.

The lithium ion concentration and flexible chains are two crucial factors which influence lithium ion conduction performance. To exclude the ion concentration effects, I have calculated the relative conductivities of prepared polymer electrolytes at 40 °C. The conductivity of Li@TPB-TP-COF (Figure 22) was set as 1, whose pore volume was 0.1 cm<sup>3</sup> g<sup>-1</sup>, with pore size of 3.3 nm. And all the corresponding conductivities were calculated in the same lithium ion concentrations as Li@TPB-TP-COF. The relative conductivity of Li@TPB-DMTP-COF was 3.07, which is higher than TPB-TP-COF, indicating the methoxy group helps lithium ion transport in the pore channels (Figure 23). The relative conductivities were greatly improved to 336 and 1490 of Li@TPB-DMTP-OR(34%)-COF and Li@TPB-DMTP-OR(50%)-COF, indicating higher ethylene oxide chains density leads to better conduction performance. And the relative conductivities were 193, 664, and 1880 of Li@TPB-BMTP-COF, Li@TPB-BMTP-OR(34%)-COF, and Li@TPB-BMTP-OR(50%)-COF. Compared to the methoxy group, the functional group of TPB-BMTP-COF could promote lithium ion transport more effectively. With lengthening chains, the relative conduction was amended. And the relative conductivity of Li@TPB-OR-COF (463) was lower than TPB-BMTP-OR(50%)-COF (1880), which was because lithium salt was difficult to bind with ethylene oxide chains in the pores because of nonporous structure.

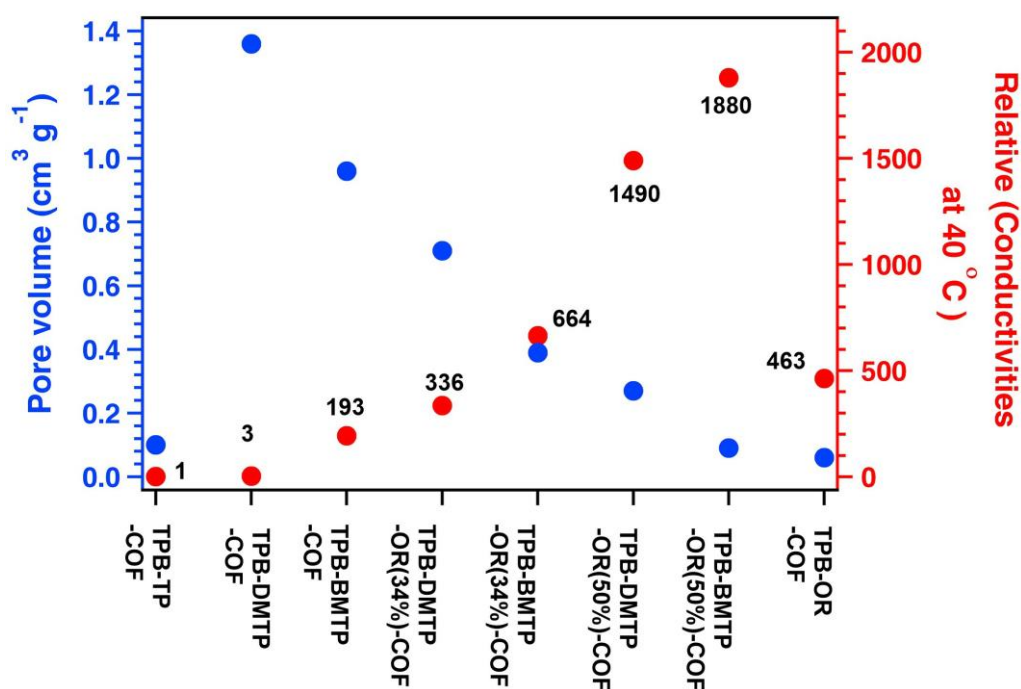


**Figure 23.** The relative conductivities of prepared polymer electrolytes at 40 °C and pore volumes with different chains on the COFs.

To investigate the conductivity mechanism for the lithium ion transport in the COFs, conductivities of Li@COFs were characterized as a function of temperature. In Figure 24a, the conductivities of Li@TPB-DMTP-COF, Li@TPB-DMTP-OR(34%)-COF, Li@TPB-DMTP-OR(50%)-COF exhibited a typical Arrhenius-type behavior, and their activation energies ( $E_a$ ) were calculated as 0.96, 0.78 and 0.68 eV. The smaller  $E_a$  implies that conductivity is less dependent on the temperature, favor to dissociate and transport lithium ion in the channels, suggesting high-rate transport over a wide temperature range.<sup>9a,12</sup> The  $E_a$  of Li@TPB-BMTP-COF and Li@TPB-BMTP-OR(34%)-COF were 0.87 and 0.82 eV, respectively (Figure 24b). The similar  $E_a$  of our materials indicated the equal conductive mechanism: lithium ion is hopping intrachains or interchains within the pore channels of the framework, since the coordination roles between lithium ion and oxygen atoms from the ethylene oxide chains along the pore channels. Thus, by balancing the lithium ion concentration, ethylene oxide chains content and length, the prepared TPB-DMTP-OR(50%)-COF exhibited best conduction performance ( $1.31 \times 10^{-5} \text{ S cm}^{-1}$  at 40 °C) with the lowest activation energy (0.68 eV).

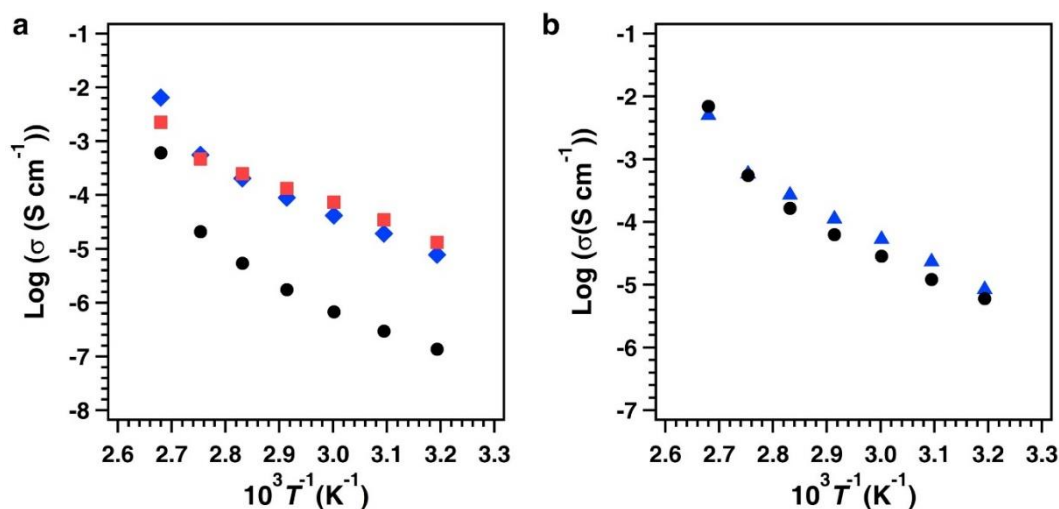


**Figure 24.** a) Temperature dependence of conductivities Li@TPB-DMTP-COF (black), Li@TPB-DMTP-OR-(34%)-COF (blue), and Li@TPB-DMTP-OR(50%)-COF (red). b) Temperature dependence of conductivities of Li@TPB-BMTP-COF (black) and Li@TPB-BMTP-OR(34%)-COF (blue).

As an electrolyte, it must be a good ionic conductor and electronic insulator. The bulk TPB-DMTP-OR(50%)-COF pellet displayed no Nyquist behavior, indicating that the conductivity observed is due to confined  $\text{LiClO}_4$  in the material (Figure 25). Thus,

the prepared COF is good ionic conductor and electronic insulator, which meets basic requirement for electrolytes.

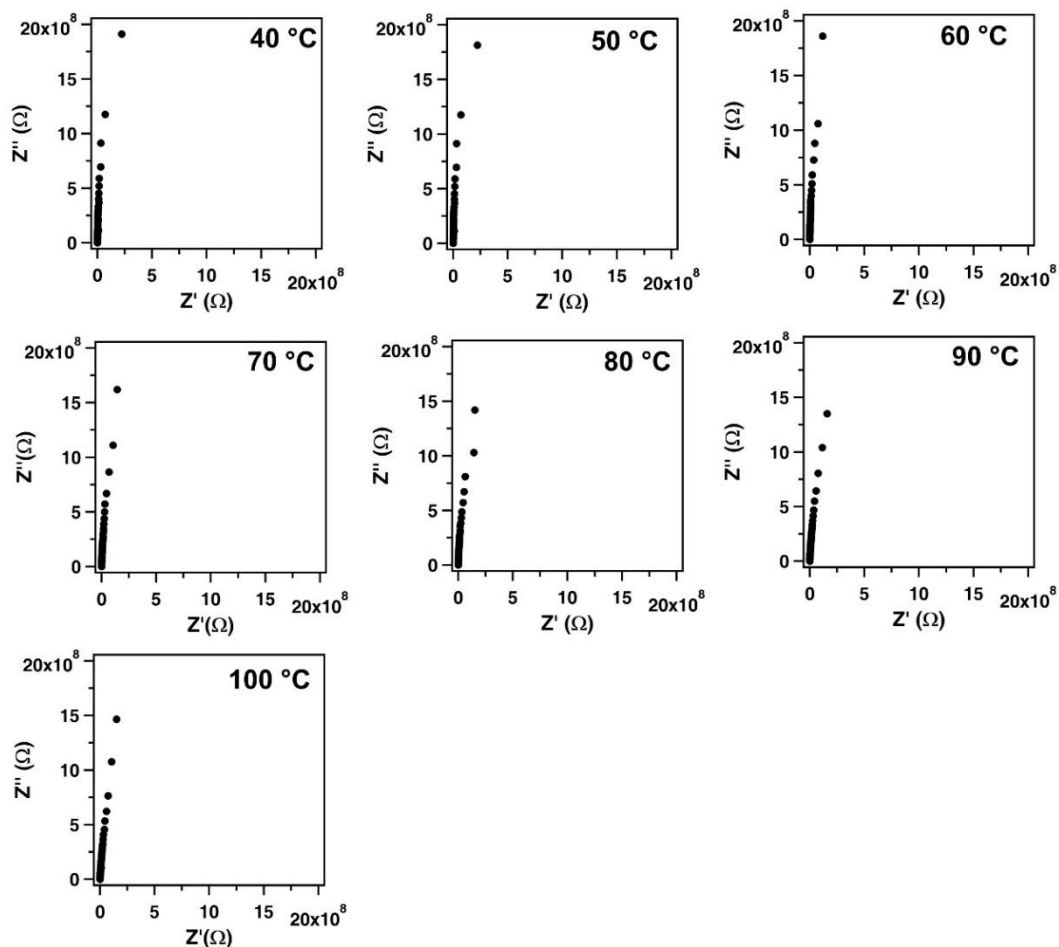


**Figure 25.** Nyquist plots of TPB-DMTP-OR(50%)-COF at different temperature.

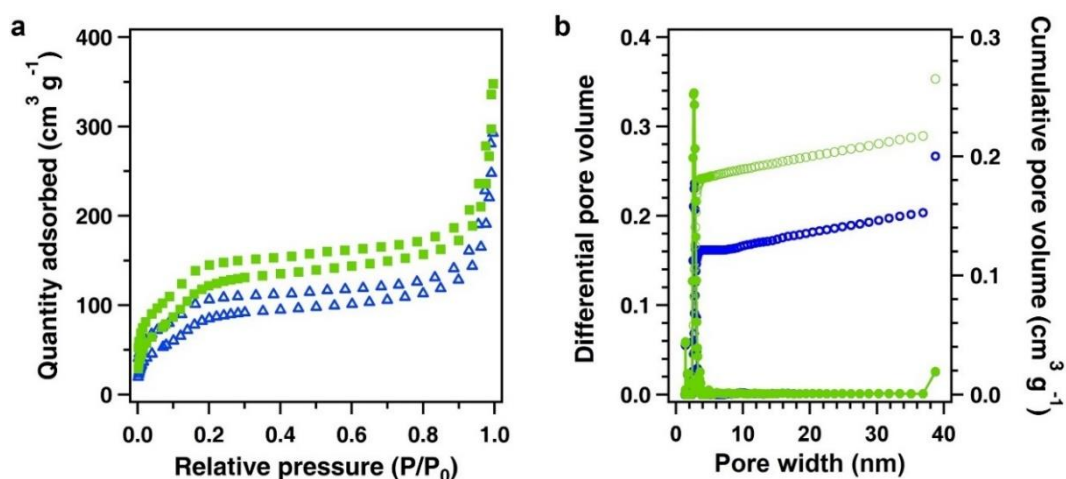


**Figure 26.** a) Nitrogen sorption isotherm profiles and b) the corresponding pore size and pore distribution profiles, of TPB-DMTP-OR(50%)-COF treated with  $\text{LiClO}_4$  at room temperature for 1 week (green curves) and  $100\text{ }^\circ\text{C}$  for 24 hours (blue curves).

The cyclic and thermal stability of the polymer electrolytes is another critical issue. I have treated TPB-DMTP-OR(50%)-COF with  $\text{LiClO}_4$  at room temperature for 1 week, or at  $100\text{ }^\circ\text{C}$  for 24 hours. The BET surface areas were 488 (Figure 26a, green curve) and  $322\text{ m}^2\text{ g}^{-1}$  (Figure 26a, blue curve), with the pore volume of  $0.27$  and  $0.20\text{ cm}^3\text{ g}^{-1}$  respectively (Figure 26b). And the crystallinity was also well maintained (Figure 27).

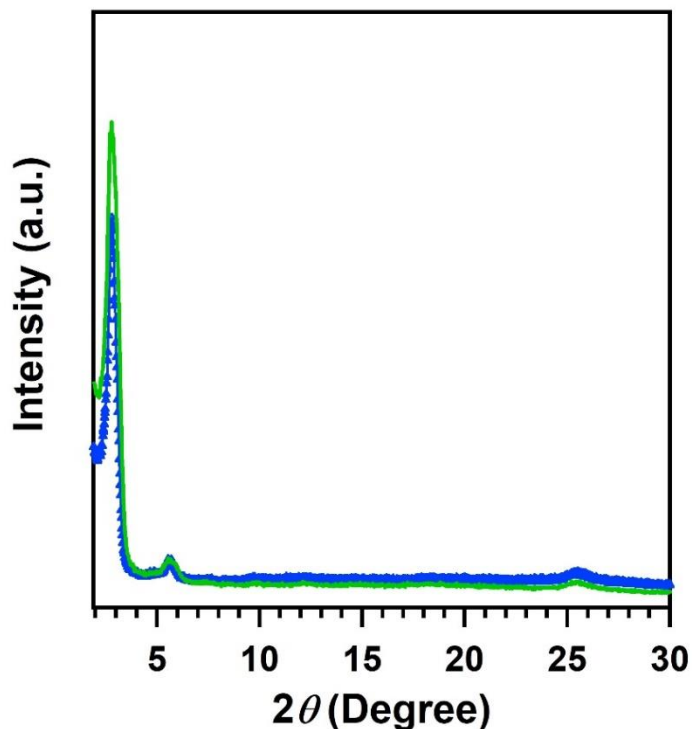


**Figure 27.** PXRD curves of TPB-DMTP-OR(50%)-COF treated with  $\text{LiClO}_4$  at room temperature for 1 week (green curves) and  $100\text{ }^\circ\text{C}$  for 24 hours (blue curves).

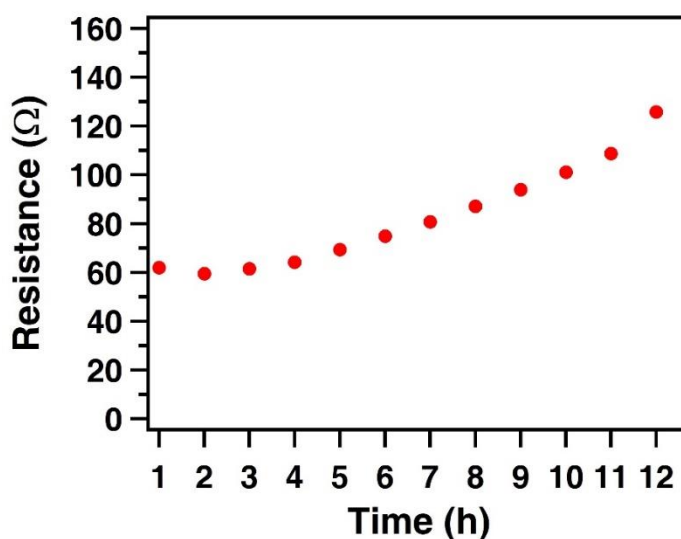


**Figure 28.** Cyclic stability of  $\text{Li@TPB-DMTP-OR(50%)-COF}$  at  $100\text{ }^\circ\text{C}$  for 12 hours.

More importantly, I have conducted the lithium ion conduction of Li@TPB-DMTP-OR(50%)-COF under nitrogen at 100 °C for 24 hours. After 12 hours, the conduction was high to  $1.11 \times 10^{-3} \text{ S cm}^{-1}$  (Figure 28). Therefore, the polymer electrolyte possessed excellent thermal and cyclic stability.

## 5.6 Conclusion

By developing a series of highly crystalline and stable COFs with different ethylene oxide chains incorporated in the walls, I have successfully shown fast lithium ion conduction across the 1D channels. The results help us to investigate the roles of the channels, flexible chain length and content, respectively. As a 2D porous polymer for electrolytes, it is better to possess high ethylene oxide chains contents along the wall, and enough pore volume to accommodate lithium sources simultaneously. Among all the prepared polymer electrolytes, TPB-DMTP-OR(50%)-COF possesses the best conduction performance: high conduction ( $1.31 \times 10^{-5} \text{ S cm}^{-1}$  at 40 °C) with the lowest activation energy of 0.68 eV. The COFs with distributed flexible chains anchored on the wall integrate the advantages of ionic conductivity of PEO and 1D ion transport fast pathways of COFs, which results in higher conductivity than other polymer-based electrolytes. The innovative strategy renders COFs to be applied in the future solid-state batteries.

## 5.6 Experimental Sections

**Characterizations.** A JASCO model FT IR-6100 infrared spectrometer was used to conduct Fourier-transform infrared (FT IR) experiments. A Mettler-Toledo model TGA/SDTA851e was used for TGA measurements under nitrogen, by heating to 800 °C at a rate of  $10 \text{ °C min}^{-1}$ . A Rigaku model RINT Ultima III diffractometer was used for PXRD measurement, from  $2\theta = 1^\circ$  up to  $60^\circ$  with  $0.02^\circ$  increment. At 77 K, nitrogen sorption isotherms were conducted on a 3Flex surface characterization analyzer with the Micrometrics Instrument Corporation model. FE-SEM images were obtained on a FEI Sirion-200 or Hitachi high technologies (SU-6600) field-emission scanning electron microscope at an electric voltage of 5 KV.

**Conductivity Measurement:** Impedance analyses were performed on lithium salt loaded COF powders. The powders were obtained by grinding Li@COFs. The resultant powders were added into a 10-mm standard die and then slowly increased pressure to 100 kN and kept for 30 min to prepare pellets. Measurements were performed using an impedance analyzer (IM3570, HIOKIE. E. Co.), with a two-Ag-probe over the

frequency range from 4 Hz to 5 MHz and with an input voltage amplitude of 100 mV. The cell was filled with nitrogen before conducting the measurements. The proton conductivities were obtained from equation:  $\sigma = L/(Z \times A)$ , where conductivity ( $\text{S cm}^{-1}$ ) was represented by  $\sigma$ , thickness of sample (cm) was showed by  $L$ , electrode area ( $\text{cm}^2$ ) was represented by  $A$  and impedance ( $\Omega$ ) was indicated by  $Z$ .

**Reagents.** 1,3,5-Tri(4-aminophenyl) benzene (TPB), benzene-1,4-diamine (TA), 13-azido-2,5,8,11-tetraoxatridecane, hydrobromic acid (47%), N, N-diisopropylethylamine (DIPEA), propargyl bromide, and 1,4-dimethoxybenzene were bought from TCI. Acetic acid, *o*-Dichlorobenzene (*o*-DCB), tetrahydrofuran (THF), acetonitrile ( $\text{CH}_3\text{CN}$ ), copper iodide (CuI), and n-Butanol (BuOH) were bought from Kanto Chemicals.  $\text{LiClO}_4$ , anhydrous MeOH were brought from Aldrich.

2,5-Dimethoxyterephthalaldehyde (DMTP),<sup>8b</sup> 2,5-bis(prop-2-yn-1-yloxy)terephthalaldehyde (BPTA),<sup>8b</sup> and 2,5-bis((2-methoxyethoxy)methoxy)terephthalaldehyde (BMTP)<sup>14</sup> were synthesized according to reports.

**Table 1.** The element analysis results of synthesized COFs.

COFs		C %	N %	H %
TPB-BMTP-COF	Calcd.	72	5.25	4.75
	Found	71.34	6.048	5.007
TPB-DMTP-BPTA(34%)-COF	Calcd.	81.72	6.97	3.32
	Found	77.45	6.63	4.71
TPB-DMTP-BPTA(50%)-COF	Calcd.	82.08	6.84	3.26
	Found	77.95	6.5	4.53
TPB-BPTA-COF	Calcd.	83.07	6.46	3.07
	Found	79.49	5.87	4.48
TPB-BMTP-BPTA(34%)-COF	Calcd.	75.20	5.60	4.27
	Found	73.59	5.985	5.075
TPB-BMTP-BPTA(50%)-COF	Calcd.	76.96	5.79	4
	Found	76.18	6.52	4.25
TPB-DMTP-OR(34%)-COF	Calcd.	71.85	10.05	4.67
	Found	70.74	9.64	5.25
TPB-DMTP-OR(50%)-COF	Calcd.	69.12	10.89	5.03
	Found	68.78	10.82	7.84
TPB-OR-COF	Calcd.	68.10	9.64	5.89
	Found	64.27	9.611	5.71
TPB-BMTP-OR(34%)-COF	Calcd.	68.36	8.54	5.19
	Found	64.63	8.16	5.48
TPB-BMTP-OR(50%)-COF	Calcd.	67.00	9.77	5.35
	Found	66.10	9.94	5.72

**Table 2.** Summary of the pore structure of synthesized COFs.

COFs	BET Surface areas ( $\text{m}^2 \text{g}^{-1}$ )	Pore volume ( $\text{cm}^3 \text{g}^{-1}$ )	Pore size (nm)
TPB-DMTP-COF	2756	1.36	3.3
TPB-DMTP-BPTA(34%)-COF	2565	1.24	3.1
TPB-DMTP-BPTA(50%)-COF	2620	1.36	3.09
TPB-BPTA-COF	2008	0.91	2.88
TPB-DMTP-OR(34%)-COF	1502	0.71	2.88
TPB-DMTP-OR(50%)-COF	477	0.27	2.78
TPB-OR-COF	48	0.06	No
TPB-BMTP-COF	1750	0.96	3.03
TPB-BMTP-BPTA(34%)-COF	2042	1.04	2.95
TPB-BMTP-BPTA(50%)-COF	1963	1.01	2.95
TPB-BMTP-OR(34%)-COF	633	0.39	2.73
TPB-BMTP-OR(50%)-COF	78	0.09	2.67

**References**

1. (a) Z. Gadjourova, Y. G. Andreev, D. P. Tunstall, P. G. Bruce, *Nature* **2001**, *412*, 520-523. (b) J. M. Tarascon, M. Armand, *Nature* **2001**, *414*, 359-367. (c) L. Yue, J. Ma, J. Zhang, J. Zhao, S. Dong, Z. Liu, G. Cui, L. Chen, *Energy Storage Mater.* **2016**, *5*, 139-164. (d) P. Lightfoot, M. A. Mehta, P. G. Bruce, *Science* **1993**, *262*, 883-885. (e) R. Khurana, J. L. Schaefer, L. A. Archer, G. W. Coates, *J. Am. Chem. Soc.* **2014**, *136*, 7395-7402. (f) J. Janek, W. G. Zeier, *Nature Energy* **2016**, *1*, 1614, doi: 10.1038/nenergy.2016.141.
2. (a) R. Chen, W. Qu, X. Guo, L. Li, F. Wu, *Mater. Horiz.* **2016**, *3*, 487-516. (b) R. C. Agrawal, G. P. Pandey, *J. Phys. D: Appl. Phys.* **2008**, *41*, 223001. (c) X.-B. Cheng, R. Zhang, C.-Z. Zhao, Q. Zhang, *Chem. Rev.*, **2017**, *117*, 10403–10473.
3. (a) Z. Xue, D. He, X. Xie, *J. Mater. Chem. A* **2015**, *3*, 19218-19253. (b) X. Lin, M. Salari, L. M. R. Arava, P. M. Ajayan, M. W. Grinstaff, *Chem. Soc. Rev.* **2016**, *45*, 5848-5887. (c) R. Bouchet, S. Maria, R. Meziane, A. Aboulaich, L. Lienafa, J.-P. Bonnet, T. N. T. Phan, D. Bertin, D. Gimes, D. Devaux, R. Denoyel, M. Armand, *Nat. Mater.* **2013**, *12*, 452-457. (d) D. H. C. Wong, A. Vitale, D. Devaux, A. Taylor, A. A. Pandya, D. T. Hallinan, J. L. Thelen, S. J. Mecham, S. F. Lux, A. M. Lapidés, P. R. Resnick, T. J. Meyer, R. M. Kostecki, N. P. Balsara, J. M. DeSimone, *Chem. Mater.* **2015**, *27*, 597-603.
4. (a) C. Sun, J. Liu, Y. Gong, D. P. Wilkinson, J. Zhang, *Nano Energy* **2017**, *33*, 363-386. (b) D. Lin, W. Liu, Y. Liu, H. R. Lee, P.-C. Hsu, K. Liu, Y. Cui, *Nano Lett.* **2016**, *16*, 459-465. (c) S. Choudhury, R. Mangal, A. Agrawal, L. A. Archer, *Nat. Commun.* **2015**, *6*, 10101, doi:10.1038/ncomms10101. (d) W. Liu, N. Liu, J. Sun, P.-C. Hsu, Y. Li, H.-W. Lee, Y. Cui, *Nano Lett.* **2015**, *15*, 2740-2745.
5. W. Liu, S. W. Lee, D. Lin, F. Shi, S. Wang, A. D. Sendek, Y. Cui, *Nature Energy* **2017**, *2*, 17035, doi:10.1038/nenergy.2017.35.
6. (a) N. Huang, P. Wang, D. Jiang, *Nat. Rev. Mater.* **2016**, *1*, 16068, doi: 101038/natrevmats2016.68. (b) X. Feng, X. Ding, D. Jiang, *Chem. Soc. Rev.* **2012**, *41*, 6010-6022. (c) J. L. Segura, M. J. Mancheno, F. Zamora, *Chem. Soc. Rev.* **2016**, *45*, 5635-5671. (d) J. Zhou, B. Wang, *Chem. Soc. Rev.*, **2017**, *46*, 6927-6945. (e) P. J. Waller, F. Gándara, O. M. Yaghi, *Acc. Chem. Res.* **2015**, *48*, 3053-3063.
7. A. Nagai, Z. Guo, X. Feng, S. Jin, X. Chen, X. Ding, D. Jiang, *Nat. Commun.* **2011**, *2*, 536, doi:10.1038/ncomms1542.

8. (a) F. Xu, H. Xu, X. Chen, D. Wu, Y. Wu, H. Liu, C. Gu, R. Fu, D. Jiang, *Angew. Chem. Int. Ed.*, **2015**, *54*, 6814-6818. (b) N. Huang, R. Krishna, D. Jiang, *J. Am. Chem. Soc.* **2015**, *137*, 7079-7082. (c) H. Xu, J. Gao, D. Jiang, *Nat. Chem.* **2015**, *7*, 905-912. (e) S. B. Alahakoon, C. M. Thompson, G. Occhialini, R. A. Smaldone, *ChemSusChem* **2017**, *10*, 2116-2129. (f) L. Meri-Bofi, S. Royuela, F. Zamora, M. L. Ruiz-Gonzalez, J. L. Segura, R. Munoz-Olivas, M. J. Mancheno, *J. Mater. Chem. A*, **2017**, *5*, 17973-17981.
9. (a) H. Xu, S. Tao, D. Jiang, *Nat. Mater.* **2016**, *15*, 722-726. (b) H. Ma, B. Liu, B. Li, L. Zhang, Y.-G. Li, H.-Q. Tan, H.-Y. Zang, G. Zhu, *J. Am. Chem. Soc.* **2016**, *138*, 5897-5903. (c) S. Chandra, T. Kundu, S. Kandambeth, R. BabaRao, Y. Marathe, S. M. Kunjir, R. Banerjee, *J. Am. Chem. Soc.* **2014**, *136*, 6570-6573. (d) S. Chandra, T. Kundu, K. Dey, M. Addicoat, T. Heine, R. Banerjee, *Chem. Mater.* **2016**, *28*, 1489-1494. (e) Y. Peng, G. Xu, Z. Hu, Y. Cheng, C. Chi, D. Yuan, H. Cheng, D. Zhao, *ACS Appl. Mater. Interfaces.* **2016**, *8*, 18505-18512.
10. (a) D. A. Vazquez-Molina, G. S. Mohammad-Pour, C. Lee, M. W. Logan, X. Duan, J. K. Harper, F. J. Uribe-Romo, *J. Am. Chem. Soc.* **2016**, *138*, 9767-9770; (b) C. Montoro, D. Rodríguez-San-Miguel, E. Polo, R. Escudero-Cid, M. L. Ruiz-González, J. A. R. Navarro, P. Ocón, F. Zamora, *J. Am. Chem. Soc.* **2017**, *139*, 10079-10086.
11. K. Kesavan, S. Rajendran, C. M. Mathew, *Polym. Compos.* **2015**, *36*, 302-311.
12. M. E. Orazem, B. Tribollet, *Electrochemical Impedance Spectroscopy, 1st ed.*; Wiley-Interscience: New York, **2008**.
13. B. M. Wiers, M. L. Foo, N. P. Balsara, J. R. Long, *J. Am. Chem. Soc.* **2011**, *133*, 14522-14525.
14. Y. Okada, M. Sugai, K. Chiba, *J. Org. Chem.* **2016**, *81*, 10922-10929.

## **Chapter 6. Summary and Perspectives**

Covalent organic frameworks (COFs), are a class of crystalline porous polymers, which are linked by stable chemical bonds and possess chemical and thermal stability. The geometry and dimensions of the building blocks can be designed and controlled to synthesize COFs with different pore structure and characters. As a result, COFs can be used in different applications such as optoelectronic, chemical sensors, charge separation and charge carrier conduction, and catalysts. There are two kinds of methods for preparing functional COFs. The first is functional skeleton method, which uses different functional building blocks to synthesize COFs by the bottom-up method. The other is pore surface engineering method. The pore channels of COFs are able to be functionalized by linking different functional groups using this method. The functional skeleton method and pore surface engineering method endow the frameworks with outstanding physicochemical properties. Especially, Their thermal and chemical stability, ordering pore channels, and designable features, make COFs show superior performance in electrochemical energy storage and conversion devices, such as capacitors, fuel cells and batteries.

In chapter 1, I summarized the development of COFs in recent years. I illustrated the chemical science including design principle based on topology diagram, the diversity of building blocks, the variety of linkages and synthesis conditions and methods. Additionally, the major progress of COFs in the field of electrochemical energy storage and conversation, such as capacitors, lithium-ion batteries, lithium-sulfur batteries, and fuel cells were summarized. Furthermore, the evolution of COF-derived carbons were subsequently summarized, which have been used in supercapacitor, catalysts and electrochemical catalysts.

In chapter 2, I described a general strategy for converting conventional COFs into high-performance carbons based on template pyrolysis. COFs were grown as a shell on crosslinked polymer spheres to form a thickness-tunable core-shell structure in which a synergistic structural effect enabled the pyrolysis formation of carbons that combine conductivity, microporosity and heteroatom density, which were attractive for carbon electrodes in energy storage. The capacitor achieved exceptional capacitance, high-rate charge and discharge, and stable performance.

In chapter 3, I demonstrated the production of an ideal carbon catalysts by combining two strategies: the use of a 2D porous precursor and the development of a suitable template to guide the pyrolysis. This technique produced carbon sheets with high conductivity, hierarchical porosity and abundant heteroatom catalytic edges. These

carbons served as metal-free electrochemical catalysts for oxygen reduction reactions, and achieved ultrahigh performance with exceptional onset and half-wave potentials, and high limit current density.

In chapter 4, I have designed, and synthesized all-solid lithium ion electrolytes based on 2D COFs by skeleton functional method, in which the 1D pores enabled the ordering of the oligoethylene oxide chains on the pore walls that provided a pathway for lithium ion conduction. The targeted COF (TPB-BMTP-COF) was synthesized under solvothermal condition. TPB-BMTP-COF exhibited a high surface area and thermally stability. With loading lithium salt in the pore channels, the complexes (LiClO<sub>4</sub>@TPB-BMTP-COF) achieved high conduction at 100 °C, with excellent cyclic stability to retained a high conductivity.

In chapter 5, I described the design and synthesis of a series of solid polymer electrolytes based on COFs by pore surface engineering method. By this approach, different short ethylene oxide chains were successfully linked on the pore surface accurately. The short chains on the pore walls were free of crystallinity, and retained high motion flexibility, which were helpful to promote lithium ion conduction in the channels. The complexes of the resulting COFs and lithium salt, provided high rate transport pathway for lithium ion, and achieved high conductivity at low temperature. The results confirmed the importance of ordered channels and ordered electrolyte sites in facilitating ion conduction.

COFs comprise mainly of carbons and are versatile for integrating heteroatoms such as B, O and N to the skeletons. The designable structure and abundant composition render COFs useful as precursors for the pyrolytic synthesis of heteroatom-doped porous carbons. During my three-year experience, I design and synthesize functional porous carbons based on a series of 2D COFs for electrochemical storage and conversion, including supercapacitor, and electrochemical catalysts in fuel cells. Subsequently, I use 2D COFs in lithium ion conduction by functional skeleton method. Along this way, the COFs are further modified by pore surface engineering method for polymer electrolytes. The order pore channels and designable chemical structure make COFs widely used in energy storage and conversion fields in the future.

## **List of Publications**

1. **Q. Xu**, Y. Tang, L. Zhai, Q. Chen, D. Jiang, Pyrolysis of Covalent Organic Frameworks: A General Strategy for Template Converting Conventional Skeletons into Conducting Microporous Carbons for High-Performance Energy Storage. *Chemical Communications*, **2017**, *53*, 11690-11693.
2. **Q. Xu**, Y. Tang, X. Zhang, Y. Oshima, Q. Chen, and D. Jiang, Template Conversion of Covalent Organic Frameworks into 2D Conducting Nanocarbons for Catalyzing Oxygen Reduction Reaction. *Adv. Mater.* Accepted.
3. **Q. Xu**, S. Dalapati, D. Jiang, Charge Up in Wired Covalent Organic Frameworks. *ACS Central Science*, **2016**, *2*, 586-587.
4. E. Jin, M. Asada, **Q. Xu**, S. Dalapati, M. A. Addicoat, M. A. Brady, H. Xu, T. Nakamura, T. Heine, Q. Chen, D. Jiang, Two-dimensional sp<sup>2</sup> carbon-conjugated covalent organic frameworks. *Science*, **2017**, *357*, 673-676.

## **Presentations in Symposiums**

1. Qing Xu, Donglin Jiang. Carbonization Covalent Organic Frameworks for Oxygen Reduction Reaction. Japan-China Joint Symposium on Functional Supramolecular Architecture @ *Okazaki, Japan, January 2016*, Poster Presentation.
2. Qing Xu, Shanshan Tao, Donglin Jiang. Ultrafast Lithium Ion Transport in Covalent Organic Frameworks as Solid Polymer Electrolytes. *The 97<sup>th</sup> Chemical Society of Japan Annual Meeting @ Yokohama, Japan, March 2017*, Oral Presentation.
3. Qing Xu, Donglin Jiang. A Two-dimensional COF for All Solid-State Lithium Ion Conductivity. *The 66<sup>th</sup> Society of Polymer Science, Japan Annual Meeting @ Chiba, Japan, May 2017*, Oral Presentation.

## **Acknowledgements**

I wrote my thesis with a fully thankful heart. During the past three years at IMS and JAIST, I received countless amounts of help and support from many people.

Firstly, I would like to thank my supervisors, Prof. Donglin Jiang. Three years ago, I came to IMS to conduct my Ph.D. degree. I have never conducted chemical research work about porous polymers. Prof. Jiang guided me how to conduct chemical research work in a right way. He told me how to conduct chemical experiments, take research notebooks, prepare group meetings, and summarize research results. Discussing with Prof. Jiang is the best method to solve the problems in my research work. From Prof. Jiang, I learnt how to design functional materials by top-to-down methods and synthesize materials by bottom-up methods. Moreover, Prof. Jiang directed me conduct research projects at a high level, which is important for me to better understand projects. Additionally, Prof. Jiang supported me to join academic conferences such as SPSJ and CSJ, which make me learn to communicate with others from different fields. As a Ph.D. candidate, I am skillful conducting chemical research work from synthesis, to characterization and application of porous polymers. And I am confidence in conduct academic research independently. I want to express my acknowledgment to my supervisor for his guidance.

I also want to show my gratitude to Prof. Yokoyama, Toshihiko. At April 2016, I moved to JAIST as special research student following Prof. Jiang to continue my PhD study. During this period, Prof. Yokoyama patiently helped me with all the complicated issues required by two universities so that I can focus on my research work. In JAIST, I needed to go IMS for class or research work, Prof. Yokoyama helped me to arrange research work and helped me prepare documents for thesis. In the doctoral thesis and defense process, Prof. Yokoyama gave me a lot valuable instruction and advice. Without his kind help, it is difficult for me to finish my research work on time and come to the final defense.

I also owe my sincere gratitude to my lab mates, Dr. Cheng Gu, Dr. Hong Xu, Dr. Ning Huang, Dr. Yang Wu, Dr. Jia Gao, Dr. Enquan Jin, Dr. Qihong Chen, Dr. Yu Feng, Dr. Juan Li, Dr. Ping Wang, Dr. Lipeng Zhai, Dr. Shanshan Tao, Mr. Zhongping Li, Mr. Chao Yang, Mr. Zhanzhao Li, Mr. Weiming Jiang, Miss Yuan Zhao. I enjoyed discussing with them about research work in the group meeting, and I have learnt a lot from their experience. With them, the research work becomes more interesting. And I

## *Acknowledgements*

---

want to thank secretary Ms. Sayuri Suzuki (IMS), Ms. Junko Aoki (IMS) for their kind help. It is unforgettable experience for me to study and live in Japan.

XU Qing

January 2018